UNIVERSITÄT DUISBURG ESSEN

Open-Minded

Silver-based nanoparticles

Synthesis and characterization of bimetallic silver-platinum and silver-gold nanoparticles

Dissertation

Zur Erlangung des akademischen Grades eines

Doktors der Naturwissenschaften

Dr. rer. nat.

vorgelegt von

Viktoria Grasmik

Fakultät für Chemie

Institut für Anorganische Chemie

Universität Duisburg-Essen

2018

Die vorliegende Arbeit wurde im Zeitraum von April 2015 bis Mai 2018 im Arbeitskreis von Prof. Dr. Matthias Epple am Institut der Anorganischen Chemie der Universität Duisburg-Essen angefertigt.

Gutachter:	Prof. Dr. Matthias Epple
	Prof. Dr. Malte Behrens
Vorsitzender:	PD Dr. Holger Somnitz

Tag der Disputation: 04.09.2018

List of contents

Index of abbreviations

Abbreviation	Meaning
AAS	Atomic absorption spectrometry
at%	Atom percent
bcc	Body-centered cubic
bco	Body-centered orthorhombic
bct	Body-centered tetragonal
BSE	Back scattered electron
CNTs	Carbon nanotubes
CV	Cyclic voltammetry
Da	Dalton
DCS	Differential centrifugal sedimentation
DFG	Deutsche Forschungsgemeinschaft
DLS	Dynamic light scattering
DLVO	Derjagin, Landau, Verwey, Overbeek
EDX	Energy dispersive X-ray spectroscopy
fcc	Face-centered cubic
FWHM	Full width at half maximum
GCE	Glassy carbon electrode
HAADF	High-angle annular dark field
hcp	Hexagonal close packed
HeLa	Henrietta Lacks
hMSC	Human mesenchymal stem cells
HOMO	Highest occupied molecular orbital
HTAB	Hexadecyl-trimethyl-ammonium bromide
ICP	Inductively coupled plasma
ISO	International Organization for Standardization
K	Kelvin
LUMO	Lowest unoccupied molecular orbital
min	Minutes
mol%	Mole percent
mPEGthiol	Poly(ethylene glycol) methyl ether thiol

Abbreviation	Meaning
11-MUA	11-mercaptoundecanoic acid
MWCO	Molecular weight cutoff
p.a.	*Pro analysi*, analytical reagent grade
PDF	Powder diffraction file
PDI	Poly dispersity index
PE	Primary electrons
PEI	Poly(ethyleneimine)
PTFE	Poly(tetrafluoroethylene)
PVA	Poly(vinyl alcohol)
PVP	Poly(*N*-vinylpyrrolidone)
PXRD	Powder X-ray diffraction
ref	Reference
ROS	Reactive oxygen species
rpm	Revolutions per minute
RT	Room temperature
SCCP	Scientific Committee on Consumer Products
SE	Secondary electron
SEM	Scanning electron microscopy
SPR	Surface plasmon resonance
STEM	Scanning transmission electron microscopy
TDDFT	Time dependent density functional theory
TEM	Transmission electron microscopy
UPD	Underpotential deposition
UV/vis	Ultraviolet/visible
wt%	Weight percent

Abstract

Nanomaterials are widely applied nowadays. They are employed in electronics, fuel cells, in the (photo-)catalysis as well as in cosmetics and medicine. Nanoparticles are interesting because their physical and chemical properties, such as melting behavior, coloration, and reactivities, differ from bulk materials.

In this work, bimetallic silver-platinum and silver-gold nanoparticles were synthesized and characterized. One of the goals was to study the alloy properties of silver-platinum nanoparticles because of their limited miscibility. For this purpose, synthesis parameters like the pH and temperature were varied. It could be shown that at pH 3, a mixture of hollow alloyed particles and dense silver-core platinum-shell particles is received. With an increasing silver fraction, a higher percentage of hollow alloyed particles is obtained. If the pH is raised to 10, dense particles are formed because of an inhibition of the galvanic exchange reaction. Depending on the composition, alloyed or core-shell particles are the result.

Silver-gold nanoparticles with a diameter of 35 nm were studied according to their element distribution within single particles. It could be shown that the outermost layer of the nanoparticles consists of silver atoms only. Furthermore, the gradient character of 35 nm sized nanoparticles with a gold-rich core and a silver-rich shell is more pronounced than the gradient character of 7 nm sized bimetallic nanoparticles. High-temperature X-ray diffraction experiments with alloyed and pure silver and gold nanoparticles revealed a greater unit cell expansion of the alloys compared to the pure metals.

Silver release studies out of silver-platinum and silver-gold nanoparticles of different compositions showed a non-linear dependency between dissolution and silver content. It was found that at a molar fraction above 50 mol% of the nobler metal, i.e. platinum or gold, the silver dissolution was significantly lowered.

Moreover, autofluorescent silver-platinum and palladium nanoclusters could be synthesized at ambient conditions.

Deutscher Abstract

Nanomaterialien finden heutzutage eine sehr weite Verbreitung. Sie werden beispielsweise sowohl in der Elektrotechnik, in Brennstoffzellen, in der (Photo-)Katalyse als auch in Kosmetika oder in der Medizin eingesetzt. Nanopartikel sind sehr interessant, weil sie andere physikalische und chemische Eigenschaften, wie Schmelzverhalten, Färbungen und Reaktivitäten als Bulkmaterialien ausweisen.

In dieser Arbeit wurden bimetallische Silber-Platin und Silber-Gold Nanopartikel synthetisiert und charakterisiert. Das Ziel war es unter anderem, die Legierungseigenschaften von Silber-Platin Nanopartikeln zu untersuchen, da Silber-Platin ein begrenzt mischbares System darstellt. Dazu wurden die Syntheseparameter hinsichtlich des pH-Wertes und der Temperatur variiert. Es konnte gezeigt werden, dass bei pH 3 eine Mischung aus hohlen legierten Partikeln und kompakten Silber-Kern/Platin-Schale Partikeln vorliegt. Mit zunehmendem Silberanteil in der Zusammensetzung wurden prozentual mehr hohle legierte Partikel erhalten. Die Erhöhung des pH-Wertes auf 10 führt zu kompakten Partikeln, da die galvanische Auflösung inhibiert wird. Es bilden sich je nach Zusammensetzung legierte Partikel oder Kern-Schale Partikel aus.

Silber-Gold Nanopartikel mit einer Größe von 35 nm wurden hinsichtlich ihrer Elementverteilung innerhalb eines Partikels untersucht. Es konnte gezeigt werden, dass legierte Silber-Gold Nanopartikel dieser Größe eine stärkere Gradientenstruktur (goldreicher Kern, silberreiche Schale) aufweisen als 7 nm große Nanopartikel und dass sich ausschließlich Silberatome an der Partikeloberfläche befinden. Experimente mittels Hochtemperatur-röntgenbeugung an legierten und reinen Silber- und Gold-Nanopartikeln zeigten eine stärkere Ausdehnung der Elementarzelle der Legierungen im Vergleich zu den reinen Metallen.

Untersuchungen der Silberfreisetzung aus den Silber-Platin- und Silber-Gold-Nanopartikeln unterschiedlicher Zusammensetzungen zeigten einen nicht linearen Zusammenhang zwischen Auflösung und Silbergehalt. Es wurde festgestellt, dass ein höherer Anteil (> 50 mol%) des edleren Metalls Platin oder Gold die Silberauflösung maßgeblich verlangsamt.

Weiterhin konnten autofluoreszierende Silber-Platin- und Palladium-Nanocluster bei Raumtemperatur synthetisiert werden.

1. Introduction

Nanomaterials are materials in the nanometer (10^{-9} m) range and can consist of organic or inorganic compounds as well as mixtures of both. Thin films with thicknesses on the nanometer scale represent one-dimensional nanomaterials with applications in electronics or in fuel cells.[1] Two-dimensional nanomaterials are, for example, carbon nanotubes (CNTs)[2] which find their application in reinforced composites, sensors, nanoelectronics, or display devices because of their mechanically strong and flexible properties.[1] Another group of two-dimensional nanomaterials are nanowires. Semiconductor nanowires made of silicon, gallium nitride, and indium phosphide are used for high-density data storage or as electronic/opto-electronic devices.[1] Three-dimensional nanomaterials are represented by nanoparticles and quantum dots. A well-known group of organic nanomaterials are polymer nanoparticles[3] which are widely used in medicine. Examples for inorganic nanomaterials are titanium dioxide nanoparticles,[4] zinc oxide nanoparticles[5], and metallic nanoparticles, only to mention a few. Titanium dioxide and zinc oxide nanoparticles are used in sunscreens.[1] Quantum dots find their application in composites, solar cells, and as fluorescent biological labels.[1] Combinations of organic and inorganic compounds can be inorganic nanoparticles coated with polymers[6] or biomolecules.[7-8] For example, calcium phosphate nanoparticles, loaded with biomolecules, can be used in biomedicine as drug delivering agents.[7-8] Anti-bacterial properties of titanium dioxide, zinc oxide, silver, copper, gold, gallium, and clay nanoparticles as well as of CNTs are useful for the textile industry, and therefore applied in this branch.[9]

Nanoparticles exhibit different chemical and physical properties than bulk materials. Those are different dissolution rates or distinct catalytic and optical properties compared to the bulk[10]. Particles on the nanometer scale have a high surface area to volume ratio which makes them attractive for catalysis.[11-14] Classic metallic catalysts are the platinum metals, platinum, palladium, iridium, ruthenium, and rhodium. Not solely platinum can be used as the catalytic agent as described by Cui et al.,[13] Narayanan et al.,[15] and Wang et al.,[16] but also gold and silver nanoparticles which are immobilized on oxides as reported by Campbell et al.[12] and Wittstock et al.[14] The combination of catalytic properties with optical properties yields new materials which was described by Antosiewicz et al.[11] In their work, they immobilized silver nanoparticles, serving as an antenna, on classic catalytic metals like platinum, rhodium, or ruthenium to enhance their catalytic activity by the absorption of visible light. Especially metallic nanoparticles appear in different colors than bulk metals which is due to the surface

plasmon resonance. That is why dispersed spherical gold nanoparticles appear red, spherical silver nanoparticles yellow, and platinum nanoparticles brown.

Many nanoparticulate systems are well characterized. This is the case for gold particles,[17-19] silver particles,[20-22] and bimetallic silver-gold particles.[23-25] They can be synthesized with different reducing agents such as trisodium citrate, trisodium citrate/tannic acid, sodium borohydride, or ethylene glycol which may influence the nanoparticle size. Bimetallic silver-gold nanoparticles, synthesized by a co-reduction method, can show a gradient structure with an enrichment of gold in the core and a silver-enrichment in the shell.[25-29] Because of their unlimited miscibility, silver and gold form alloys even on the nanometer scale. Upon heating, metals show an expansion in length. This effect is described by the linear thermal expansion coefficient α which is a material specific constant that depends on the temperature. Only a few publications are accessible showing the thermal behavior of nanoparticulate silver and gold including their thermal expansion coefficients.[30-31] No references for the thermal expansion coefficient of alloyed silver-gold nanoparticles could be found so far.

Silver in the form of ions is cytotoxic, and therefore silver nanoparticles are used in medicine as bactericidal agents[32-33] where silver ions are released from the particles upon dissolution. Gold nanoparticles find their application in imaging[34-35] as contrast agents, as markers for cancer cells,[36-37] in photothermal therapy as treatment of cancers[38-40] or bacterial infections,[41] and as drug and gene delivering agents.[42] Silver-gold nanoalloys also show a cytotoxic effect on HeLa cells and human mesenchymal stem cells (hMSC) as reported by Ristig et al.[23] In their work, they incubated the mentioned cell lines with nanoparticles of different molar compositions of silver and gold. The composition of 80 mol% silver and 20 mol% gold showed the highest cytotoxicity. Therefore, several questions arise: Does the composition of alloyed silver-gold particles influence the dissolution kinetics of silver? Do alloyed silver-gold nanoparticles synthesized with different reducing agents show distinct element distributions within a particle? Of which element does the outermost layer consist? Are there any differences between those particles? How is the crystal structure of alloyed silver-gold nanoparticles affected by a temperature increase? Is there any change of crystallinity? And is it possible to obtain linear thermal expansion coefficients?

Silver-gold nanoparticles build up not the only bimetallic system. There are various others of which the silver-platinum system shall be mentioned that is the subject of controversial scientific discussion. Silver and platinum form a peritectic system with a wide miscibility gap.[43-44] Therefore, several authors believe that silver and platinum in one nanoparticle will form core-shell structures because no alloying is possible.[45-47] Depending on the reaction

conditions, the core can be made up of silver or of platinum. Other authors report successfully synthesized alloyed silver-platinum nanoparticles[48-54] of which some show hollow structures that are interesting for the catalysis.[48-49, 53-54] The pH of the reaction mixture seems to play a crucial role for the nanoparticle size. Bock et al.[55] showed with the PtRu system that higher pH in a synthesis with ethylene glycol as reducing agent yields smaller nanoparticles than using lower pH. Papa et al.[47] suggest the addition of sodium hydroxide and consequently the increase of the pH to improve the morphological control of the nanoparticles. Krishnan et al.[54] report an influence of the pH on the character of bimetallic nanoparticles. At lower pH they obtained hollow alloyed structures, whereas at higher pH dense core-shell particles were received. Now the questions are whether it is possible to synthesize alloyed silver-platinum nanoparticles over the whole composition range neglecting the miscibility gap. What will the nanoparticles look like? Will they be hollow or dense? Which crystallographic properties will they have? And which new plasmonic and dissolution properties will those nanoparticles show?

To answer the posed questions, the work is divided in two sections. In section one it is to synthesize and characterize alloyed silver-platinum nanoparticles over the whole composition range (Ag10Pt90 – Ag90Pt10) with different routes and perform dissolution kinetic experiments. In addition, silver-platinum nanoclusters in the whole composition range shall be synthesized and compared to the already known silver-gold nanocluster system characterized by Ristig et al.[24] and a new palladium nanocluster system will be introduced as another platinum group metal. Section two will deal with the synthesis and characterization of alloyed silver-gold nanoparticles with different compositions. The influence of the reducing agents trisodium citrate/tannic acid versus trisodium citrate on the nanoparticles will be analyzed. Dissolution kinetic experiments shall reveal the dissolution rate of silver. Comparison between both systems, silver-platinum and silver-gold, will show whether there is an effect of the alloyed metal on the silver dissolution. Also, further structural characterization will be performed by X-ray diffraction at room temperature and at elevated temperatures as well as with electrochemical methods.

2. Theoretical background

2.1 Colloids, nanoclusters, and nanoparticles – a definition

Colloids describe a two-phase system of substances with different aggregate phases. The dispersed phase, which consists of the suspended particles (sol), is found in the continuous phase that is the medium of suspension.[56] According to size, colloids lie in the range of 10^{-4} m and 10^{-9} m that is 1 nm to 100 µm. Table 1 shows representative materials which can be attributed to colloidal systems.

Table 1: Examples of materials which can be assigned to colloidal systems. Adapted from ref[56].

	Medium		
Dispersed phase	Gas	Liquid	Solid
Gas	---	Foam	Solid foam
Liquid	Liquid aerosol	Liquid emulsion	Solid emulsion
Solid	Solid aerosol	Sol	Solid sol

Staudinger divided the group of colloids in three sub-groups.[57] Those are dispersion colloids, molecular colloids, and association/micellar colloids (Fig. 1). Dispersion colloids are thermodynamically unstable, hydrophobic colloids with a polydisperse size distribution and with different morphologies. Representatives of this sub-group are metallic nanoparticles. Unlike dispersion colloids, molecular colloids are thermodynamically stable, hydrophilic colloids which are built of polymers that take balled shapes. Association or micellar colloids are also thermodynamically stable, hydrophilic colloids which are formed spontaneously through reversible association of tensides leading to micelles.

Nanoclusters are built up of a group of atoms with well-defined compositions and lie in the size range comparable to the Fermi wavelength of an electron (~ 0.5 nm for gold and silver).[58] Usually, particles with sizes between 1 nm and 2 nm which corresponds to clusters of 10 – 200 atoms are referred to as nanoclusters. They form a bridge between atoms and nanoparticles which leads to different properties from both, atoms and nanoparticles. Quantum effects are responsible for the new electronic, chemical, and optical properties which comprise magnetism, fluorescence, and catalytic activity. Nanoclusters of semiconductor materials are called quantum dots.[59] The term nanoparticle has several definitions of which the definition by the International Organization for Standardization (ISO) shall be mentioned. It says, a nanoparticle is a particle which spans 1 nm – 100 nm in diameter.[60] Other definitions add that at least one

dimension of the particle has to be in the nanometer range like the definition by the Scientific Committee on Consumer Products (SCCP).[60] Both, nanoclusters and nanoparticles are unified under the term nanomaterial. Those nanomaterials have high numbers of atoms at the surface compared to the total atom number which provides them with a higher chemical reactivity and probable lower melting points than bulk materials.[59] Because of this high surface area to volume ratio, nanoparticles tend to minimize the surface area, hence agglomerate easily if not stabilized.

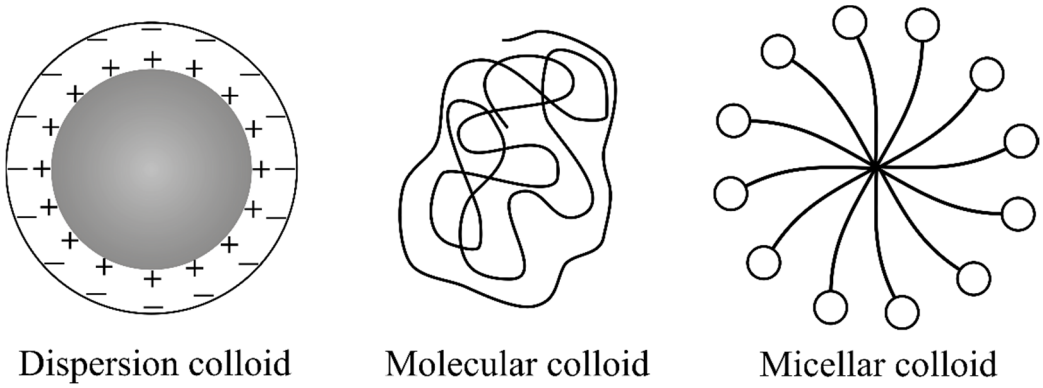

Figure 1: Simplified depiction of the three sub-groups of colloids. Dispersion colloid (left), molecular colloid (center), and association/micellar colloid (right). Adapted from ref.[57]

2.2 Stabilization of nanoparticles

Nanoparticles are considered as colloidally stable when they stay well dispersed in the continuous phase.[56] Because of their high surface energy, nanoparticles tend to agglomerate in favor of energy minimization. The agglomeration is driven by van der Waals forces when two particles in dispersion are attracted by each other.[59] To prevent the particles from agglomeration, thus to stabilize them, counter forces should be applied to the van der Waals attraction. There are two main possibilities for nanoparticle stabilization which are the electrostatic and the steric stabilization. To describe the electrostatic stabilization, the DLVO theory is used which was developed by Derjagin, Landau, Verwey, and Overbeek.[61-62] Every particle has a characteristic surface charge which allows counter ions from the dispersion medium to adsorb on the nanoparticle surface. The ions build up an electrochemical double layer with a rigid Stern layer consisting of counter ions and a diffuse layer comprised of counter ions and ions with the same charge as the particle itself. The nanoparticle appears neutral on the outside. The diffuse layer is confined by a slipping plane which is stripped upon particle migration. The charge of the slipping plane is called Zeta potential (Fig. 2). It refers to the

stability of the electrochemical double layer and is dependent on the ion concentration of the electrolytes. Electrostatically stable systems show Zeta potentials above ± 20 mV.[56-57]

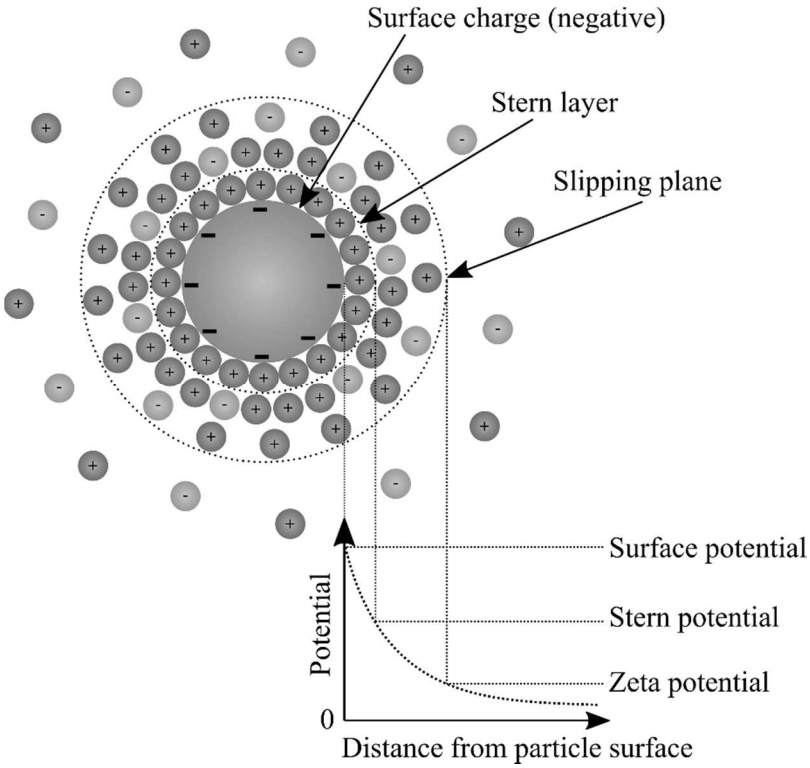

Figure 2: A schematic depiction of a negatively charged particle, its electrochemical double layer, and the three different potentials: surface, Stern, and Zeta potential.

When two particles approach each other, repulsive forces because of equal charge prevail the van der Waals forces and the particles are repelled from each other (Fig. 3, left). An increase of the electrolyte concentration in the dispersion leads to the shrinking of the double layer and as a consequence, the nanoparticles agglomerate (Fig. 3, right) as was shown by Schulze[63-64] and Hardy.[65-66] To depict the interaction potential between two particles as a sum of repulsive and attractive forces, the DLVO theory uses the model of the Lennard-Jones potential. There, repulsive forces possess positive, whereas attractive forces take on negative values.[57] Figure 3 shows two examples of a stable and an unstable dispersion. When the thickness of the double layer is large enough, repulsive forces predominate the attractive forces and the nanoparticles are stabilized. On the other hand, when the thickness of the double layer is small, attractive forces will prevail and the particles will agglomerate. A widely used electrostatic stabilizer is trisodium citrate which is a rather weak capping agent.[59]

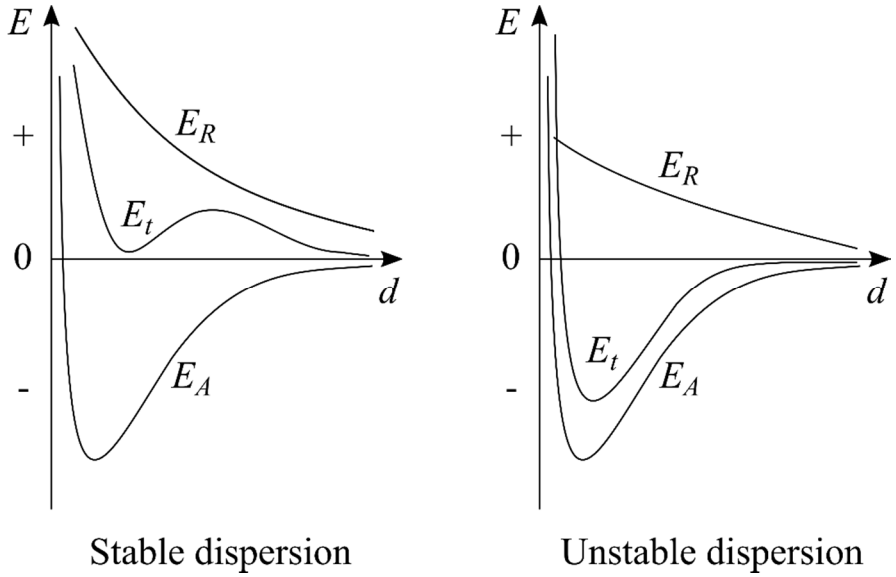

Figure 3: Energy versus distance functions of a stable dispersion (left) and an unstable dispersion (right). E_R means repulsive energy, E_A means attractive energy, and E_t stands for the total energy as a sum of E_R+E_A.

Steric stabilization of nanoparticles is ensured by the addition of polymers with polar side groups like poly(*N*-vinylpyrrolidone) (PVP) or poly(vinyl alcohol) (PVA) into the system[59] which adsorb on the particle surface. Because of the bulky molecules on the particle surface, agglomeration becomes unfavorable. The polymer concentration plays a crucial role in the colloid stability. This effect is depicted in Figure 4. If the concentration is too low, so-called bridging flocculation will occur. In contrary, steric stability is ensured at moderate polymer concentrations. The increase of the polymer concentration yields depletion flocculation and a further increase results in depletion stabilization.[67]

Also, a combination of electrostatic and steric stabilizations, the so called electrosteric stabilization, exists.[59] It combines both principles and uses charged polymers like poly(ethyleneimine) (PEI) under acidic conditions or long alkyl chains with functional groups like 11-mercaptoundecanoic acid under basic conditions. Protonation and deprotonation of the functional groups results in a charge and bulky parts contribute to the steric stabilization.

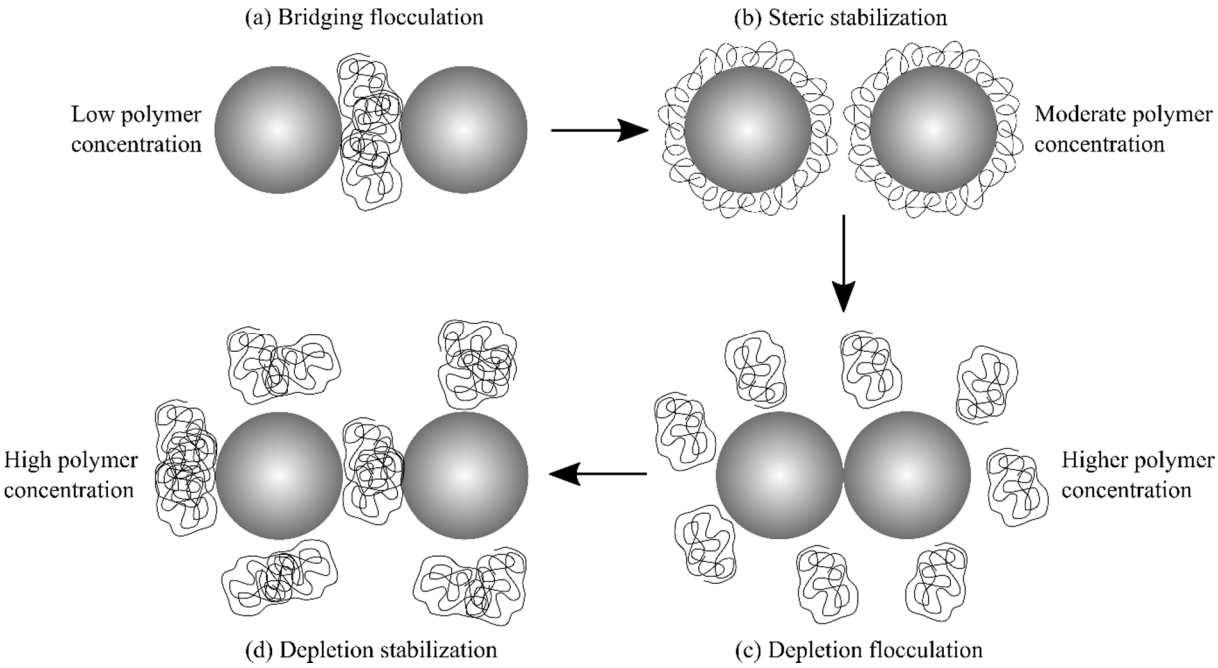

Figure 4: The influence of the increase of polymer concentration on the stability of dispersed nanoparticles. (a) Bridging flocculation, (b) steric stabilization, (c) depletion flocculation, (d) depletion stabilization.

2.3 Synthesis routes and crystallization processes

Two main approaches exist for the synthesis of nanoparticles. Those are the top-down and the bottom-up routes. The top-down synthesis uses a bulk starting material which is ground to yield small particles. The main disadvantage is the poor particle size control and the resulting polydispersity.[57] Another physical way to yield nanoparticles is laser ablation where a bulk metal or oxide target is put into a liquid and irradiated with a pulsed laser beam creating nanoparticles.[68-70] A chemical approach of the top-down synthesis is the etching of bigger nanoparticles by ligands such as thiols or poly(ethyleneimine) resulting in nanoclusters.[58] The bottom-up route uses ions as starting material which are reduced to atoms that form seeds and crystallize to nanoparticles. Stabilizers prevent agglomeration or further growth. The crystallization pathway was described by LaMer et al.[71-72] and is shown in Figure 5. The reduced ions form atoms which are dissolved in the solution (I). As the reduction proceeds, the atom concentration increases until a critical concentration is reached[71-72] (C_{min}). Once the critical concentration is exceeded, nucleation of the atoms starts (II). This step is characterized as the limiting state of supersaturation. The formed nuclei lead to a decrease of saturation and the atom concentration falls below C_{min}. No nuclei are formed anymore, but the system is still

supersaturated. Thus, atoms diffuse to the nuclei and the particles grow (III). Nucleation is the rate-limiting step of particle formation. To yield a monodisperse system, this step must be very short. The crystallization process is reversible and gives way to dissolution. In polydisperse systems, smaller particles are dissolved faster than bigger ones because they have a high surface energy which is not favorable. The atoms originated from dissolution diffuse to the bigger particles and crystallize on their surface. This process is called Ostwald ripening[56-57, 73] and might lead to a collapse of a colloidal system when the particles grow too big to stay well dispersed. The process is size, temperature, substance, and diffusion coefficient dependent. Ostwald ripening is slow in monodisperse systems and does not exist in a hypothetical case of particles with just one size.

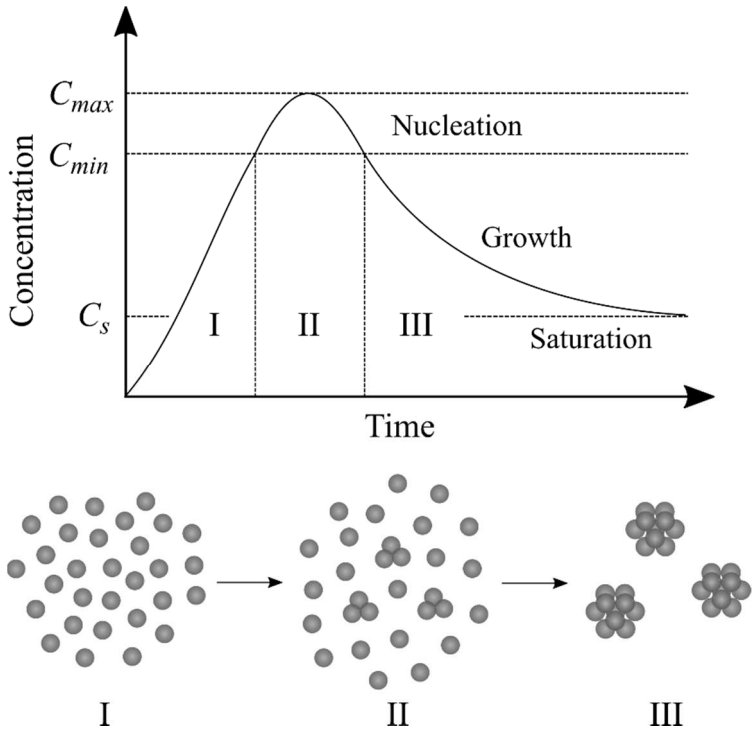

Figure 5: Schematic depiction of the nucleation and nucleus growth. I: Reduction of ions to atoms and increasing concentration of atoms in solution, II: Nucleation after reaching the critical concentration, III: Growth of particles.

To control the velocity of nucleation, several reducing agents might be used which differ in their reducing potential. Common reducer are sodium borohydride,[24, 46, 51, 74] hydrazine,[75] tannic acid,[73, 76-77] ascorbic acid,[48, 54] glucose,[78-79] ethylene glycol (polyol),[80-81] and trisodium citrate.[19, 45, 82] They are divided in strong and weak reductants of which sodium borohydride or hydrazine represent a strong and trisodium citrate represents a weak reducing agent. Strong reducer lead to the formation of more nuclei than weak reducer which results in smaller nanoparticles.

Bimetallic nanoparticles or particles consisting of more than one compound show various element or compound distributions within one particle. Alloyed particles are synthesized by a simultaneous reduction of both metal precursors and exhibit a statistical distribution of both metals in one particle.[25, 28] Take silver-gold nanoparticles as an example. Because gold has a higher redox potential than silver (at pH = 0, Au^{3+}/Au: +1.498 V and Ag^{+}/Ag: +0.7991 V), gold ions are reduced faster than silver ions which results in a gold rich core and a silver rich shell, but nevertheless in an alloy.[25, 83] To obtain core-shell particles with a core consisting of one metal and a shell built up of another metal, the seeded-growth method is applied. In the first step, nanoparticles of the core material are synthesized to be covered by the shell material in a second step.[54, 84] If the shell metal is nobler than the core metal, a dissolution of the core may occur. The particles will become hollow alloyed structures.[48, 54] To avoid this case, it is possible to adjust the concentration of the reducing agent and the pH which changes the redox potential. Another kind of nanoparticles are Janus particles which have two different surfaces. To obtain such kind of particles, several methods are published. The precursor particle is masked on one side and treated with surfactants on the unmasked side. Then, the mask is washed away and a particle with two differently functionalized sides is obtained. For example one side is hydrophobic, whereas the other is hydrophilic.[85] Other possibilities are the protection of one side by placing the precursor particle on a substrate and applying reactive fluxes, fields, or stamping. The last option is to work at the interface where a partial contact with a reactive medium is enabled.[86]

Spherical nanoparticles show the lowest surface energy, and therefore are readily obtained. However, spherical morphologies are not the only ones that exist. There are for example platelets[87-88] or triangles/prisms[87, 89] which appear often in one sample. Other morphologies are rods,[90] cubes,[91] dendrites,[92] capped columns,[88] or tripods.[93] Particle morphology can be controlled using certain routes. For instance, silver nanorods are synthesized using cubic silver chloride seeds. At the vertices, silver nanorods can grow. The silver chloride seeds are removed upon dissolution in ammonia[90]. Another mechanism of morphology control is the use of special ligands which adsorb on specific facets of the nanocrystal. Those facets are blocked, so that an anisotropic growth occurs. Widely applied surfactants are PVP that adsorbs on the (100) facet,[81, 94-95] trisodium citrate which blocks the (111) facet,[96] and hexadecyl-trimethyl-ammonium bromide (HTAB) that, depending on the concentration, yields cubes, spheres, rods, or prisms.[97-98]

2.4 Optical properties of metallic nanoparticles

Nanoparticles show optical properties differing from bulk materials which can be measured by UV/vis spectroscopy. Dispersed spherical silver particles appear yellow and show an absorption band at around 400 nm. Gold nanoparticle sols have a red color and an absorption at 530 nm, whereas dispersed spherical palladium particles appear black and have no absorption maximum in the visible region, but in the UV region.[99] The black color is due to a continuous high absorption of the whole visible spectrum. Calculations from Mie theory for 8 nm palladium particles predicted an absorption at 225 nm.[99] Mie theory describes the elastic scattering of light by spherical nanoparticles which have their size in the wavelength range. It enables the calculation of the optical behavior of particles which are irradiated with light by summing up the scattering and the absorption of light to yield the extinction.[100]

Nanoparticles with different morphologies show other absorptions than spherical particles. For example, gold nanorods with different lengths show shifted absorption bands as is the case for 40 nm, 55 nm, and 74 nm long rods which absorb at 653 nm, 728 nm, and 846 nm, respectively (only the main absorption band stated).[101] The absorption of nanoparticles is size, shape, composition, and dielectric constant dependent.[99] UV/vis spectra give information about the width of the particle size distribution and the presence of agglomerates.[46, 102-105] But why do nanoparticles exhibit different colors? To answer this question quantum effects of nanoparticles shall be considered. The energy splitting of small particles lies in between those of atoms and bulk materials.[106] Nanoclusters and nanoparticles show discrete energy levels because the number of atoms in a cluster or particle is finite. The band gap between the highest occupied molecular orbital (HOMO) and lowest unoccupied molecular orbital (LUMO) decreases as the particle size increases[58, 107] (Fig. 6). Nanoclusters have a bigger energy gap than nanoparticles, and therefore they appear colorless because the absorption and electron excitation occurs in the UV region. Nanoparticles, on the other hand, have a smaller band gap and absorb visible light and appear colorful. Bulk metals have no band gap because the HOMO and LUMO, also called valence band and conduction band, overlap. Only the characteristic metallic luster is observed. Some metals in the size of nanoclusters show autofluorescence, as is the case for gold clusters smaller than 3 nm.[108-109] This property is again caused by the electronic structure and the HOMO – LUMO gap as well as the ligands on the surface.[110]

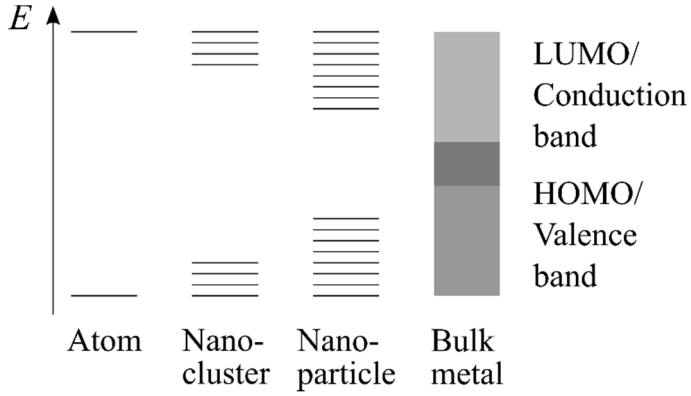

Figure 6: Energy levels of an atom, a nanocluster, a nanoparticle, and a bulk metal. The valence and conduction band overlap in the bulk material.

Another effect, which is responsible for the coloring of nanoparticles, is the surface plasmon resonance (SPR). It describes the collective motion of conduction band electrons (electron gas) relative to the core, caused by the electric field component of incident light and Coulomb attraction between electrons and the nucleus.[102, 107, 111] As a consequence, a dipole is induced (Fig. 7). The oscillation frequency of the electron gas is determined by the density of electrons, the effective electron mass, and the size and shape of the charge distribution. The particle must be smaller than the light wavelength. Because silver has less electrons than gold, the electron gas oscillates faster in silver nanoparticles than in gold nanoparticles causing an absorption at lower wavelengths for silver than for gold. Anisotropic nanoparticles show more than one absorption band which is caused by the SPR oscillation of each different surface area. Therefore, silver nanorods, for instance, show two absorption maxima in the UV/vis spectrum. The band at lower wavelengths is caused by the electron gas oscillation of the transversal surface, whereas the absorption at higher wavelengths is induced by the longitudinal surface.[94] Ligands on the nanoparticle surface also influence the surface plasmon oscillation because they change the electron density of the electron gas.[108]

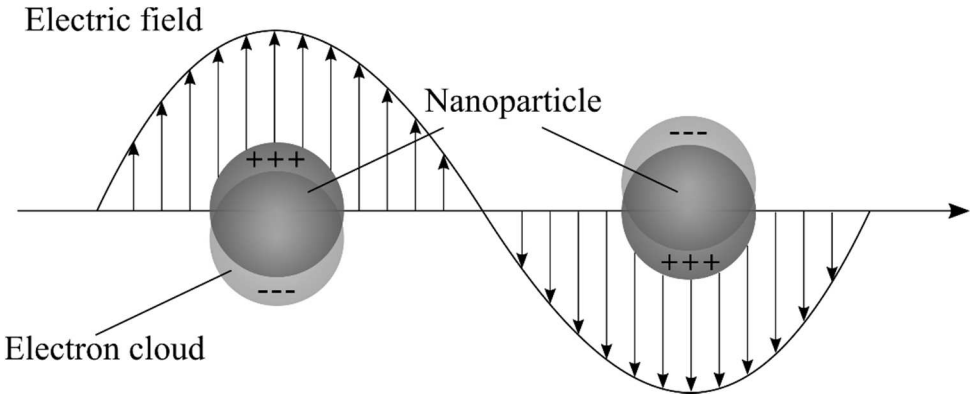

Figure 7: Schematic depiction of the dipole induction and oscillation of the electron gas in a nanoparticle by the electric field component of the incident light leading to surface plasmon resonance.

2.5 Employed metals and their properties

This work concentrates on the group 10 and group 11 metals palladium, platinum, silver, and gold. Those metals are denoted as noble metals. Palladium and platinum belong to the so-called platinum metals which include ruthenium, osmium, rhodium, and iridium. Of those platinum metals, palladium and platinum are the most reactive ones. Both adsorb hydrogen, and therefore are readily applied as catalysts in hydrogenation reactions.[112] Palladium is soluble in nitric acid and *aqua regia*. Widely used palladium nanoparticle precursors are palladium(II) nitrate ($Pd(NO_3)_2$) and hexachloridopalladic(IV) acid ($H_2[PdCl_6]$) and its salts. Under basic conditions, hexachlorido-palladate(IV) undergoes a ligand exchange to $[Pd(OH)_6]^{2-}$ which yields PdO_2 upon drying.[113] Palladium nanoclusters of sizes less than 3 nm are reported to be more toxic against bacteria than palladium ions. Especially the gram positive bacterium S*taphylococcus aureus* was affected more than the gram negative bacterium *Escherichia coli.*[114] In cells, palladium ions show a disturbance in the cell functions by accumulating in mitochondria leading to a high release of reactive oxygen species (ROS) and a resulting oxidative stress.[115]

46 Pd	47 Ag
78 Pt	79 Au

Platinum is applied in automobile exhaust purification, in jewelry fabrication, and in medicine as cisplatin for cancer treatment.[116] Elemental platinum is stable in nitric acid up to 100 °C and soluble in *aqua regia* yielding hexachloridoplatinic(IV) acid ($H_2[PtCl_6]$). This compound and its salts are also used as precursors for platinum nanoparticles. Those particles can be taken up by cells, but are not found in the nucleus or mitochondria and show no significant cytotoxicity.[117] Like hexachloridopalladate(IV), hexachloridoplatinate(IV) reacts under basic conditions to $[Pt(OH)_6]^{2-}$ and to PtO_2 when acidified and dried. With silver nitrate, hexachloridoplatinic(IV) acid reacts to silver hexachloridoplatinate(IV) ($Ag_2[PtCl_6]$) which precipitates in water.[113]

Silver is a soft metal which is alloyed with copper to ensure a sufficient hardness for an application in jewelry production, in household as mirrors, or in electronics. With thiols, silver reacts very easily to silver sulfide. Silver is not toxic for humans, but shows toxic effects on microorganisms and cells.[22, 118-121] Silver ions inhibit the activity of thiol enzymes by binding to them. Therefore, materials composed of silver are widely applied in the medicine in the form of colloids, foils, ointments, or tablets as bactericidal or fungicidal agents. In aqueous solution, silver ions form a tetra aqua silver ion ($[Ag(H_2O)_4]^+$). With chloride, silver ions react to silver chloride which is not soluble in water, but in ammonia, sodium thiosulfate, or potassium

cyanide solutions. Formation of silver hydroxide occurs in basic solutions with a further reversible reaction to silver oxide (brown precipitate). Under light irradiation, silver oxide is reduced to silver nanoparticles. Silver hydroxide precipitates in alcoholic solutions.[113] A widely used precursor for the synthesis of silver nanoparticles is silver nitrate.

Gold shows a twofold higher density than its lighter homologues copper and silver because of its smaller atomic radius. The reason lies in the lanthanoide contraction. The inner electrons are bound more tightly to the core and yield a smaller atomic radius. Application of gold is found in jewelry production, dentures, and electrical engineering. Bulk gold does not show any catalytic activity. Concerning nanoparticles, it was found that gold nanoparticles show hydrogen, oxygen, and carbon monoxide adsorption[122-124] which makes them attractive as catalyst for hydrogenation and oxidation reactions. Nanoparticles, deposited on a reducible oxide substrate, oxidize carbon monoxide to carbon dioxide.[125-127] In ion form, gold (+) ions disproportionate to elemental gold and gold (3+) ions. Also, ions show a high oxidation potential and enable the oxidation of water to oxygen. Because of its high positive redox potential of +1.498 V (Au^0/Au^{3+}), bulk gold does not react with oxygen. The precursor for the preparation of nanoparticles is tetrachloridoauric acid ($H[AuCl_4]$) and its salts. In biomedicine, gold nanoparticles have various applications. Because of the surface plasmon resonance and the ability to absorb visible light, gold nanoparticles are used in photothermal therapy[40] to destroy targeted carcinoma cells. Another advantage of SPR is the change of absorption wavelength of antibody conjugated gold particles, while in cancerous cells compared to non-cancerous cells.[36] Additionally, gold nanoclusters are used as drug-delivery systems for chemotherapeutic drugs.[128]

Table 2 shows oxidation numbers, melting points, thermal expansion coefficients, crystal systems, lattice parameters, redox potentials, and atomic radii of palladium, platinum, silver, and gold in comparison.

Table 2: Some important properties of palladium, platinum, silver, and gold in direct comparison. If not noted separately, all data were taken from reference[113]. The bold oxidation numbers state the preferred ones. Fcc means face-centered cubic.

Element	Palladium	Platinum	Silver	Gold
Oxidation numbers	**+II**, +IV	**+II**, **+IV**	**+I**, +II	+I, **+III**
Melting point / °C	1554	1772	962	1064
Thermal expansion coefficient / K^{-1}	$11.8 \cdot 10^{-6}$ [129]	$8.8 \cdot 10^{-6}$ [129]	$18.9 \cdot 10^{-6}$ [129]	$14.2 \cdot 10^{-6}$ [129]
Crystal system	fcc	fcc	fcc	fcc
Lattice parameter *a* / Å	3.991[130]	3.923[131]	4.0862[132]	4.0786[133]
Redox potential at pH = 0 / V	Pd^0/Pd^{2+}: +0.62 Pd^{2+}/Pd^{4+}: +1.47	$Pt^0/[PtCl_4]^{2-}$: +0.758 $[PtCl_4]^{2-}/[PtCl_6]^{4-}$: +0.726 Pt^0/Pt^{2+}: +1.188 [134]	Ag^0/Ag^+: +0.799	Au^0/Au^+: +1.691 Au^+/Au^{3+}: +1.401 Au^0/Au^{3+}: +1.498
Atomic radius / Å	1.376	1.373	1.445	1.442

All four metals crystallize in the face centered cubic (fcc) crystal structure (Table 2). Beside the fcc structure, some authors report the presence of a body-centered tetragonal (bct) phase in silver nanowires[135] or gold platelets.[136] Also, body-centered orthorhombic (bco) and hexagonal close packed (hcp) structures are described in the literature for gold nanoparticles.[136-138] Those findings are supported by molecular dynamics calculations for gold nanowires[139] and palladium nanowires.[140] The bct phase is found if penta-twinning or stacking faults occur which lead to stress within the particle. There is a spontaneous, reversible transition from fcc to bct. Annealing of the nanostructures to high temperatures relieves the stress between crystallites and a transition from bct back to fcc takes place.

2.5.1 The binary silver-gold system

The binary silver-gold system is one of the most characterized ones. Because silver and gold crystallize both in the fcc structure, have very similar lattice parameters (Table 2), and show close melting points, they are completely miscible over the entire composition range. Figure 8 shows the binary phase diagram of silver-gold which gives information on the composition dependent melting temperatures of the alloy. The solidus and liquidus lines are narrow and allow just a small area for the existent liquidus plus solid solution phase. Upon heating, metals show an expansion in length. This effect is described by the linear thermal expansion coefficient α which is a material specific constant that depends on the temperature. The length variation ΔL is calculated by multiplying the linear thermal expansion coefficient α, the initial length of the material L, and the temperature change ΔT. Linear thermal expansion coefficients of bulk silver and gold at room temperature are[129]: $\alpha(Ag) = 18.9 \cdot 10^{-6}\ K^{-1}$ and $\alpha(Au) = 14.2 \cdot 10^{-6}\ K^{-1}$.

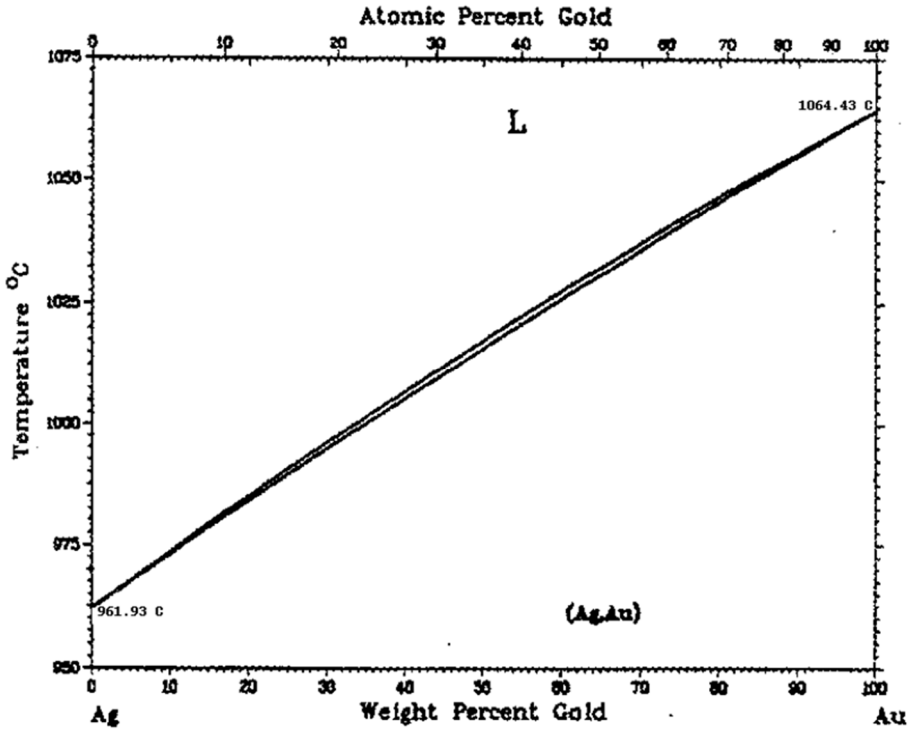

Figure 8: Phase diagram of the binary silver-gold system showing a melting point versus amount of gold dependence of the alloy.[141]

In the crystallographic aspect, silver-gold nanoparticles present a very interesting system. Investigations by Vegard[142-143] showed that if a crystal consists of two atom types A and B, of which B is the bigger atom, the lattice parameters of the unit cell will increase linearly with a higher B content. This is called Vegard`s law. In the case of silver-gold, a negative deviation

from Vegard`s law was found which had its maximum at the silver 50 mol%, gold 50 mol% composition. This effect is larger for nanoparticles than for bulk materials as described by Ristig et al.,[25] Lubarda et al.,[144] and Petkov et al.[145] Alloying of silver (a less noble metal) with gold (a noble metal) increases the oxidation potential of silver[83, 146] which is observable in cyclic voltammetry measurements. Because of a synergetic effect, new chemical and physical properties can be created by the preparation of bimetallic nanoparticles. Studies[147-148] on gold-palladium and gold-platinum nanoparticles showed an increased catalytic activity than in pure metal particles. The alloying of silver with gold into one nanoparticle enables the tuning of the surface plasmon resonance upon the molar composition.[149-150] It is possible not only to synthesize alloyed silver-gold nanoparticles, as reported by Ristig et al.[25] and Mahl et al.,[28] but core-shell particles as well. The core can be either made up of silver or of gold with the corresponding shell of either gold or silver.[151-152]

Biological experiments of silver-gold nanoparticles with *Daphnia magna*, a test model for effluent release of pollutants into water, showed that the introduction of gold into silver nanoparticles lowers the environmental impact by decreasing the released silver amount.[29] In their studies, Li et al. tested gold nanoparticles, silver nanoparticles with different sizes as well as alloyed silver 80 mol%, gold 20 mol% and silver 20 mol%, gold 80 mol% nanoparticles. Alissawi et al.[153] probed the dissolution of silver-gold nanoparticles in water which were deposited on polytetrafluoroethylene. They used pure silver nanoparticles as well as silver-gold nanoparticles with molar compositions of Ag:Au 90:10, 70:30, and 50:50 to conclude an improvement of oxidation resistance upon alloying of silver nanoparticles with gold. Grade et al.[154] investigated the antibacterial and cytotoxic effects of alloyed silver-gold nanoparticles using *Staphylococcus aureus* and human gingival fibroblasts (HGFib). They trialed silver nanoparticles, gold nanoparticles, and alloyed silver-gold nanoparticles with molar compositions of Ag:Au 80:20 and 50:50. With the increasing gold fraction in the silver-gold nanoparticles, the cytotoxic effect was reduced stronger than expected. Experiments with hMSC and HeLa cells, incubated with alloyed silver-gold nanoparticles of different compositions, showed no cytotoxicity for the silver 50 mol%, gold 50 mol% composition against hMSC.[23, 28] Only nanoparticles with higher silver content (above 60 mol% silver) exposed a cytotoxic effect on hMSC. The composition with 80 mol% silver showed the highest toxicity of all compositions already after 24 h. In contrary, the effect on HeLa cells was already visible for silver amounts of 40 mol%.[23] Those findings were ascribed to the dissolution of silver because of the silver ion toxicity.

2.5.2 The binary silver-platinum system

The binary system of silver-platinum is more complicated than the silver-gold system because the melting points of silver (962 °C) and platinum (1772 °C) lie widely apart, a peritectic at 1188 °C at 40 at% platinum, and several intermediate phases exist which indicate a wide miscibility gap (Fig. 9). Additionally, an intermediate compound with a defined composition of 47 at% silver and 53 at% platinum is found which transforms into a stoichiometric undefined phase above 803 °C. Peng et al.[50] reported a phase transition or segregation above 700 °C for silver-platinum nanoalloys. No data for the behavior of silver-platinum below 400 °C is found.

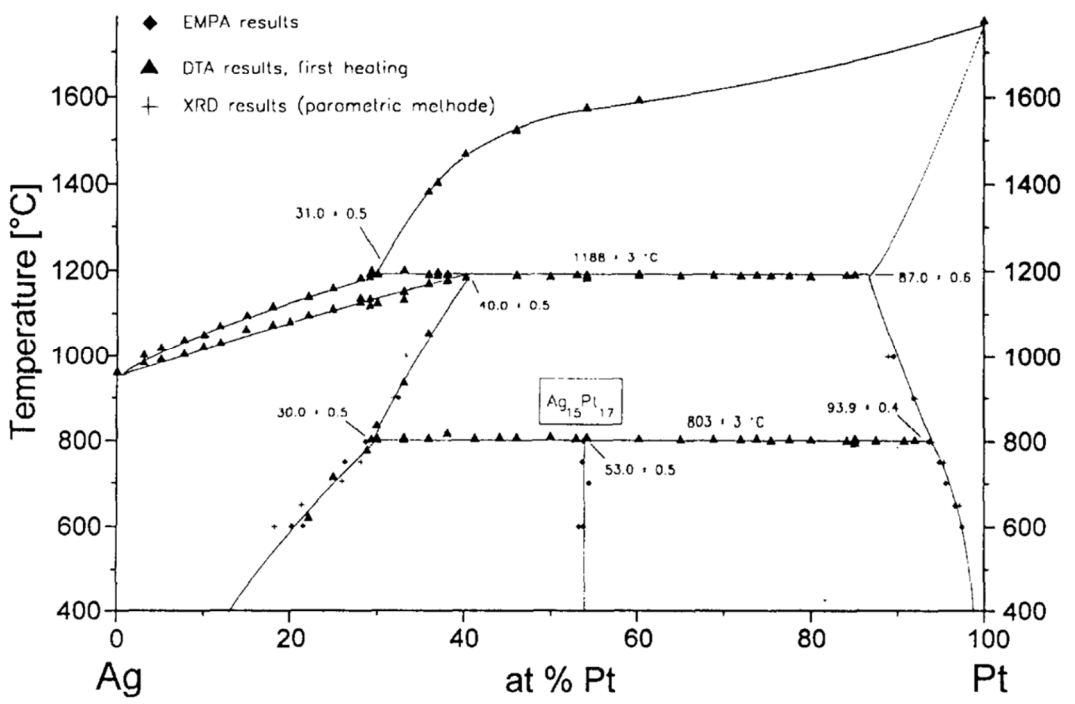

Figure 9: Phase diagram of the binary silver-platinum system showing a peritectic at 40 at% platinum and several intermediate phases.[43]

From the crystallographic point of view, a solid solution (alloy) of silver-platinum should be accessible because the lattice constants have a mismatch of just 4 % and the atomic radii mismatch lies at 5 % (for exact values see Table 2). Several authors believe that silver and platinum do not form nanoalloys.[45-47] Instead, core-shell systems are formed that have either silver or platinum as core. On the other hand, authors report successfully synthesized alloyed silver-platinum nanoparticles.[48-54] Some of them show hollow structures which are interesting for the catalysis.[48-49, 53-54] The hollow alloy and core-shell structures could be confirmed by energy dispersive X-ray spectroscopy (EDX) where single particles were investigated.[48, 53-54, 155-159] Although publications about silver-platinum nanoparticles go back to 1995, only after

2013 publications containing EDX mapping or line scan analysis can be found. In respect of the alloy character and from the crystallographic point of view, Karakaya et al.[44] reported a negative deviation from Vegard`s law after investigating the whole composition range of silver-platinum nanoparticles. Other authors[51, 160-162] only stated that the reflexes of silver-platinum particles in a powder X-ray diffraction pattern lie between the reflexes of the pure metals. Peng et al.[50] showed a linear shape of calculated lattice parameters following Vegard`s law, although the values did not lie perfectly on the theoretical curve, but slightly underneath. It is reported in the literature[163-166] that 6 nm large silver, gold, and platinum particles could have up to 0.5 % deviation in lattice parameters compared to their bulk material.

A potential use of silver-platinum alloys in the medicine lies in the coating of orthodontic appliances[167] where biological studies showed a release of silver ions in phosphate-buffered saline which led to an antimicrobial potency against *Streptococcus mutans* and *Aggregatibacter actinomycetemcomitans* strains. In contrary, human gingival fibroblast cells were not affected. The use of silver-platinum-carbon impregnated central venous catheters as antimicrobial agents showed low rates of catheter-related bloodstream infection[168] and polyaniline/silver-platinum nanocomposites revealed an inhibition efficiency against *Staphylococcus aureus.*[169]

3. Methods

All devices used are listed in section 4.3.

3.1 Dynamic Light Scattering and Zeta Potential

Dynamic light scattering (DLS) is a method for the size determination of colloidal dispersed particles. For optimal results, the sample must be highly diluted. Monochromatic (laser) light is shone onto the sample which is scattered by the particles and detected by a photodetector. Particles move through the dispersion because of Brownian motion, so scattered light waves interfere constructively or destructively resulting in a frequency shift (Doppler Effect). The time dependent fluctuations in scattered light intensity are recorded and compared to the initial laser beam. An autocorrelation function of time and light intensity is generated which enables the determination of the diffusion coefficient *D*. The Stokes-Einstein equation[57] (Equation 1) is used to determine the hydrodynamic radius *r* of the particles with k_B the Boltzmann constant, *T* the temperature, and η the viscosity of the dispersant.

$$r = \frac{k_B \cdot T}{6\pi \cdot \eta \cdot D} \tag{1}$$

Because the hydrodynamic radius is determined, the particle size is overestimated.[170] Another factor which enables size overestimation is the higher scattering intensity of bigger than smaller particles. The polydispersity index (PDI) shows the rate of the size distribution. PDIs between 0 and 0.3 mean monodisperse systems, whereas PDIs above 0.3 indicate polydisperse colloids.

The Zeta potential is measured via the particle motion through an electric field by the same physical method as the size, where the velocity of the particle is a measure for the potential. All measurements are carried out in a double folded capillary cell.

3.2 Differential Centrifugal Sedimentation

Differential centrifugal sedimentation (DCS) is another method for particle size determination. A transparent rotating disc is filled with a density gradient of sucrose. At the edge of the disc, a laser beam is focused through it onto a detector. Before each measurement, a calibration standard with a known particle size is measured. For the size determination, the time which the

particles need to get from the inserting point to the laser beam and the detector is quantified. When particles arrive at the laser, the beam is weakened because of absorption and scattering. For the diameter *D* calculation, the Stokes equation (2) is used with η the viscosity, R_f the outer disc radius, R_0 the inner disc radius, ρ_p the particle density, ρ_f the fluid density, ω the angular velocity, and *t* the sedimentation time.

$$D = \sqrt{\frac{18 \cdot \eta \cdot \ln\left(\frac{R_f}{R_0}\right)}{(\rho_p - \rho_f) \cdot \omega^2 \cdot t}} \tag{2}$$

The rotation fastens the sedimentation and the density gradient separates the particles according to size because bigger particles sediment faster than smaller ones. The resolution of the measurement is increased with this method. The DCS slightly underestimates the particle size. Because of the ligand shell on the particle surface, they migrate slower to the laser beam/detector couple.[170] All samples are measured by inserting 0.1 mL diluted particle dispersion after calibration measurement.

3.3 UV/vis spectroscopy

UV/vis spectroscopy is a technique for measuring the absorption wavelength of compounds. Electron transitions from ground to excited states have characteristic energies which can be detected. Metallic nanoparticles exhibit surface plasmon resonance which is also measured and gives information about morphology, width of size distribution, and alloy character. The absorption intensity is proportional to the sample concentration as described by the Bouguer-Lambert-Beer law (Equation 3) with *E* the extinction, I_0 the intensity of incident light, *I* the intensity of transmitted light, ε the extinction coefficient, *c* the concentration of the sample, *d* the thickness of the cuvette/path length of light.

$$E = \log\left(\frac{I_0}{I}\right) = \varepsilon \cdot c \cdot d \tag{3}$$

All samples are measured in a Suprasil® quartz cuvette after dilution and background correction.

3.4 Fluorescence spectroscopy

Fluorescence spectroscopy is a method to determine the emission wavelength of a photon which is generated after an excited electron returns from the excited to the ground state. The emission wavelength is red-shifted compared to the absorption wavelength because of internal conversion and vibrational relaxation. They occur when the electron returns to the vibrational ground state of the excited state. Those phenomena lead to an emission-free energy loss. Relaxation from the vibrational ground state of the excited state to the absolute ground state yields the measured photon emission. The excitation wavelength is determined with UV/vis spectroscopy and the samples are measured in a Suprasil® quartz cuvette.

3.5 Atomic Absorption Spectrometry

Atomic absorption spectrometry (AAS) allows the qualitative and quantitative detection of metals from which the concentration and molar composition of bimetallic samples can be calculated. Before the sample measurement, a calibration standard with a known metal content is measured to create a calibration curve. The metallic sample is digested in an appropriate acid to transform the metals into ionic form. Those ions are atomized and brought into the analysis chamber where they are irradiated with light. The light source consists of the same material as the to-be investigated element. Electron transitions in the sample are induced which lead to absorption of the incident light that is proportional to the atom concentration according to Bouguer-Lambert-Beer law (Equation 3). Before each measurement, the bimetallic samples are digested.

Silver digestion: A defined amount of silver containing nanoparticle dispersion is added to 1 mL nitric acid and heated to 130 °C for one hour (silver-platinum) or 30 minutes (silver-gold). Then, the solution is diluted with Millipore water and filtrated with syringe filters (PTFE, 0.45 μm) to remove the undissolved platinum and gold species. Detection limit: 50 ppb.

Gold and platinum digestion: A defined amount of gold or platinum containing nanoparticle dispersion is added to 0.5 mL *aqua regia*, heated to improve the solubility and remove nitrosyl chloride and chlorine. After dissolution, the liquid is diluted with Millipore water and silver chloride can precipitate. It is removed by filtration with syringe filters (Whatman® Anotop 25, 0.02 μm). Detection limits: gold 1 ppm, platinum 24 ppm.

The measurements were performed by Kerstin Brauner and Robin Meya in the Laboratory of Microanalysis, University of Duisburg-Essen.

3.6 Energy Dispersive X-ray Spectroscopy

Energy dispersive X-ray spectroscopy (EDX) serves as an elemental analysis which allows a qualitative and quantitative determination of the elements present in a sample. An electron beam is focused on the sample where it leads to inelastic scattering. An electron from the inner shell of the sample atom is removed. The empty space is filled with an electron from an outer shell. The energy difference of this electron is emitted as an X-ray quantum which is characteristic for the certain element. The X-ray energies are compared to literature data bases and a spectrum of the containing elements is obtained. EDX maps allow the imaging of element distribution within a sample by marking the elements with different colors. Sample preparation see 3.7 Scanning Electron Microscopy or 3.8 Transmission Electron Microscopy.

3.7 Scanning Electron Microscopy

Scanning electron microscopy (SEM) is performed for visualization of samples which are smaller than the wavelength of visible light. For this purpose, electrons are used to overcome the optical Abbé limit (Equation 4) with d the resolution, λ the wavelength of the electron beam, n the refractive index of the immersion medium, α the aperture angle, and NA the numerical aperture.

$$d = \frac{\lambda}{2n \cdot \sin(\alpha)} = \frac{\lambda}{2NA} \tag{4}$$

Under vacuum, the electron beam (primary electrons, PE) is focused and scanned over the sample surface. Different types of interaction of the primary electrons with the sample occur. Elastic scattering yields back scattered electrons (BSE) with high energies which give information about the material contrast because denser elements appear brighter and less dense elements darker. Secondary electrons (SE) are produced because of inelastic scattering, where electrons are removed from inner shells of the sample atoms. Those low energy electrons give information on the topography of the sample surface. Edges and higher parts appear bright, whereas deeper parts appear dark. If the sample is not conductive, sputtering with a conductive material is necessary to prevent charging of the sample upon electron bombardment.

Before each measurement, the nanoparticle dispersion is dropped and dried on a silicon wafer (previously cleaned with acetone) which is fixed by a carbon tape on an aluminum sample holder. For better conduction, the wafer is coated with conductive silver at the edges.

3.8 Transmission Electron Microscopy

Transmission electron microscopy (TEM) is another method for visualization of small objects. The principle is similar to scanning electron microscopy with the exception that the sample must be thin enough for the electron beam to pass through. The electron beam is focused on the sample or scanned over it (scanning transmission electron microscopy, STEM) and the transmitted electrons are detected with a bright field detector. A dark field detector allows high-angle annular dark field imaging (HAADF) which is highly sensitive to atomic number contrast.[171]

Before measuring, the nanoparticle dispersion is dropped on a holey carbon-coated copper grid and dried.

All TEM/STEM/HAADF/EDX map/line scan measurements and the counts of alloyed versus core-shell silver-platinum nanoparticles were carried out by Dr. Kateryna Loza and Dr. Marc Heggen at the Ernst Ruska-Centre and Peter Grünberg Institute, Forschungszentrum Jülich GmbH, Germany.

3.9 Powder X-ray Diffraction

Powder X-ray diffraction (PXRD) enables the investigation of the crystallographic structure of a sample and the verification of phase purity. The sample is irradiated with X-rays because the wavelength lies in the range of interatomic distances of compounds. In crystalline substances, atoms form three dimensional lattices which influence the diffraction of X-rays as shown in Figure 10.

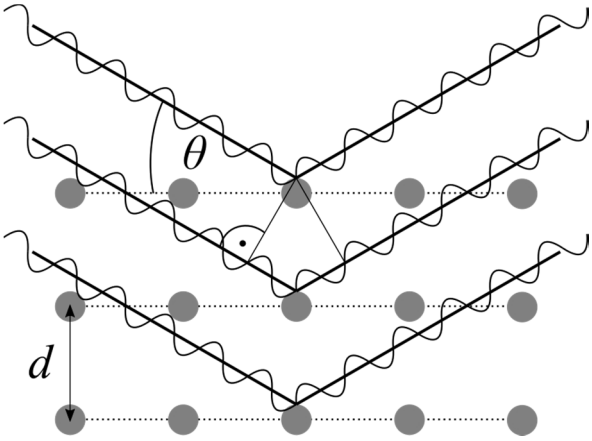

Figure 10: Scheme of constructive interference of X-rays diffracted by a lattice with θ the Bragg angle and d the distance between atomic planes.

The X-ray beam is diffracted at the electron shell of the sample atoms. The diffraction occurs at several atomic planes and results in constructive and destructive interference. The Bragg equation (5) must be fulfilled to obtain a signal (constructive interference). With n an integer, λ the X-ray wavelength, d the distance between atomic planes, and θ the Bragg angle.

$$n \cdot \lambda = 2 \cdot d \cdot \sin(\theta) \tag{5}$$

The path difference $n\lambda$ must be an integral multiple of the wavelength to yield constructive interference. Is this not the case, no sharp signal will be obtained. The width of the signal allows to calculate the crystallite size D with the Scherrer equation[172] (6) and the microstrain ε with the Stokes-Wilson equation[173] (7) where K is the Scherrer factor, λ the X-ray wavelength, β the full width at half maximum of a reflex, and θ the Bragg angle.

$$D = \frac{K \cdot \lambda}{\beta \cdot \cos(\theta)} \tag{6}$$

$$\varepsilon = \frac{\beta}{4 \cdot \tan(\theta)} \tag{7}$$

The lattice parameter a may be calculated using equation (8) for a cubic system[174] with θ the Bragg angle and *hkl* the atomic plane with the corresponding Miller indices.

$$a = \frac{\lambda}{2 \cdot \sin(\theta)} \cdot \sqrt{h^2 + k^2 + l^2} \tag{8}$$

The sample preparation is done by freeze-drying the nanoparticles and mixing them with 10-15 wt% lanthanum hexaboride as internal standard. The powder is dispersed with ethanol on a silicon wafer with a (911) surface and measured in Bragg-Brentano geometry with the Cu K_α radiation. As alternative, the nanoparticle dispersion is directly dried on the silicon wafer, mixed with LaB_6. For the measurement in Debye-Scherrer geometry, glass capillaries from Hilgenberg® with an outer diameter of 0.5 mm and a wall thickness of 0.01 mm are used. High-temperature X-ray diffraction was measured in Bragg-Brentano geometry with a tantalum plate serving as heater and sample holder under vacuum conditions.

The measurements in Debye-Scherrer geometry, the high-temperature X-ray diffraction, and the Rietveld refinement including modeling the bct defect phase were done by Dr. Oleg Prymak, Department of X-ray Diffraction, University of Duisburg-Essen.

3.10 Electrochemistry – Cyclic Voltammetry and Underpotential Deposition

Cyclic voltammetry (CV) induces oxidation and reduction processes by applying potentials on the nanoparticles (and other substances). From the shape of the oxidation and reduction peaks, information on the alloy character may be obtained. Integration of the peaks yields the molar composition of a bimetallic system. Before the measurement, the nanoparticle dispersion is drop-cast on a glassy carbon electrode (GCE), dried, and measured in a 0.1 M hydrochloric acid solution.

Underpotential deposition (UPD) describes the deposition of a suitable metal (like lead in a silver-gold system) on a nanoparticle surface (e.g. silver-gold nanoparticles) at lower potentials than on its bulk material resulting in a monolayer. Deposition on a silver or a gold surface occurs at different potentials. This method allows the determination of the facets building up the particle surface, the determination of the outer element in a bimetallic system, and the average size of the particles. The measurements are carried out in a 0.1 M sodium hydroxide and 1 mM lead nitrate solution. A glassy carbon electrode is drop-cast with the particle dispersion and dried.

All electrochemical measurements were carried out by Christian Rurainsky from the group of Electrocatalysis & Functional Materials of Jun.-Prof. Dr. Tschulik, Department of Chemistry and Biochemistry, Ruhr-University Bochum.

4. Experimental

All experiments are carried out under inert conditions with degassed Millipore water to prevent the reaction of silver ions with dissolved oxygen or carbon dioxide. Prior to use, all glass ware is cleaned with boiling *aqua regia*, flushed with distilled water and cleaned twice with boiling Millipore water to remove residual chloride. All chemicals are handled with a glass spatula to prevent metallic impurities. Only small amounts (max. 20 mL) of stock solutions are prepared. Every described synthesis is suited for upscaling (up to 6-10-fold). Before ultracentrifugation of upscaled samples, the dispersant can be removed through rotary evaporation up to a volume of 50 mL – 100 mL.

4.1 Programs/databases used

Program/database	Purpose	Reference
ChemDraw	Molecular formula design	PerkinElmer Informatics, Inc.
Crystallography open database	Crystallographic data	[175]
EndNote X7	Citation manager	Thomson Reuters
DIFFRAC.EVA	Phase analysis	Bruker
Gimp	Graphic design	Spencer Kimball, Peter Mattis
ICDD	Crystallographic data	International Centre for Diffraction Data
ImageJ	Particle size analysis	Wayne Rasband, National Institutes of Health, USA
Inkscape	Graphic design	Free Software Foundation, Inc.
OriginPro 2016	Graph plotting, fitting	OriginLab Corporation
Refractive index database	Refractive indices of metals	[176]

4.2 Chemicals used

Chemical	Producer	Purity
Ethanol	Fisher Chemicals	p.a.
Gold powder	Alfa Aesar	99.96+ %
Hexachloridoplatinic acid	Self-made from platinum bar	
Hexachloridoplatinic acid (ICP standard)	Bernd Kraft	
Hydrochloric acid	Bernd Kraft	p.a.
11-Mercaptoundecanoic acid	Sigma Aldrich	95 %
Nitric acid	Bernd Kraft	p.a.
Palladium nitrate (ICP standard)	Bernd Kraft	
Poly(ethylene glycol) methyl ether thiol (M = 2,000 g/mol)	Sigma Aldrich	
Poly(*N*-vinylpyrrolidone) (M = 40,000 g/mol)	Sigma Aldrich	p.a.
Silver foil	Goodfellow	99.95+ %
Silver-gold 70:30 pellets	Goodfellow	
Silver-gold 50:50 rod	Goodfellow	
Silver nitrate	Carl Roth	>99.9 %
Silver-palladium 70:30 foil	Goodfellow	
Sodium borohydride	Sigma Aldrich	>96 %
Sodium hydroxide	Fisher Chemicals	p.a.
Sodium tetraborate decahydrate	Sigma Aldrich	99 %
Tannic acid	Acros	95 %
Tetrachloridoauric acid	Self-made from gold powder	
Trisodium citrate dihydrate	AppliChem	p.a.

4.3 Devices used

Device	Producer
Atomic absorption spectrometer	ThermoElectron M-Series
Centrifuge	Hettich Rotofix 32A
Disc centrifuge	CPS Instruments Disc Centrifuge DC24000
Dynamic light scattering	Malvern Nano ZS
Fluorescence spectrometer	Agilent Technologies Cary Eclipse
Lyophilizer	Christ Alpha 2-4 LSC
Potentiostate	AutoLab PGStat 12
Scanning electron microscope coupled with EDX	FEI Quanta 400 FEG, EDAX
Scanning transmission electron microscope coupled with EDX and HAADF	FEI Titan 80–200 ChemiSTEM
Sonotrode	Hielscher UP50H
Ultracentrifuge	SORVALL WX Ultra Series
Ultrasonic bath	Elmasonic S10
UV/vis spectrometer	Varian Cary 300
Vortex	Scientific Industries Vortex-Genie 2
X-ray powder diffractometer	Bruker D8 Advance (Bragg-Brentano geometry) Panalytical Empyrean (Debye-Scherrer geometry and high-temperature X-ray diffraction in Bragg-Brentano geometry)

4.4 Synthesis of silver-platinum nanoparticles

The following synthesis routes are described for the silver-platinum 50:50 mol% compositions and a reaction volume of 50 mL. Through variation of the precursor amounts (Table 3), other compositions may be achieved. To obtain an appropriate amount of nanoparticles for characterization and further experiments, five to nine upscaled syntheses were performed. The batches were mixed after DCS and UV/vis characterization.

Table 3: Precursor amounts for a desired molar composition. Suited for a reaction volume of 50 mL.

Desired Composition Ag:Pt / mol%	*V* ($AgNO_3$, 10 mM) / mL	*V* (H_2PtCl_6, 10 mM) / mL
0:100	0.00	0.50
10:90	0.05	0.45
20:80	0.10	0.40
30:70	0.15	0.35
40:60	0.20	0.30
50:50	0.25	0.25
60:40	0.30	0.20
70:30	0.35	0.15
80:20	0.40	0.10
90:10	0.45	0.05
100:0	0.50	0.00

4.4.1 Reduction by trisodium citrate and tannic acid

A mixture of trisodium citrate dihydrate and tannic acid are used as the reducing agents. The nanoparticles are recapped with poly(*N*-vinylpyrrolidone) (Fig. 11). A seeded-growth method is chosen. As platinum precursor, the platinum ICP standard is taken.

0.25 mL silver nitrate (10 mM, 2.5 µmol) are added to 50 mL of degassed Millipore water which is heated to 100 °C. For reduction, 0.5 mL trisodium citrate dihydrate (132 mM, 66 µmol) are mixed with 1 mL tannic acid (4.95 mM, 4.9 µmol) and added dropwise under vigorous stirring to the reaction mixture. After one minute, 0.5 mL platinum ICP standard (5 mM, 2.5 µmol) are added. The platinum precursor must be neutralized (with 2 M sodium hydroxide)

beforehand. The reaction mixture is heated for 20 minutes, then cooled down to room temperature (RT) with an ice-bath, and refunctionalized with 1 mL poly(*N*-vinylpyrrolidone) (90 mM, 90 µmol) by stirring overnight at RT. The purification is performed by ultracentrifugation (20,000 rpm/ 29,400 g, 30 minutes, 2x) and washing with Millipore water. The possible chemical equation is depicted in Figure 12.

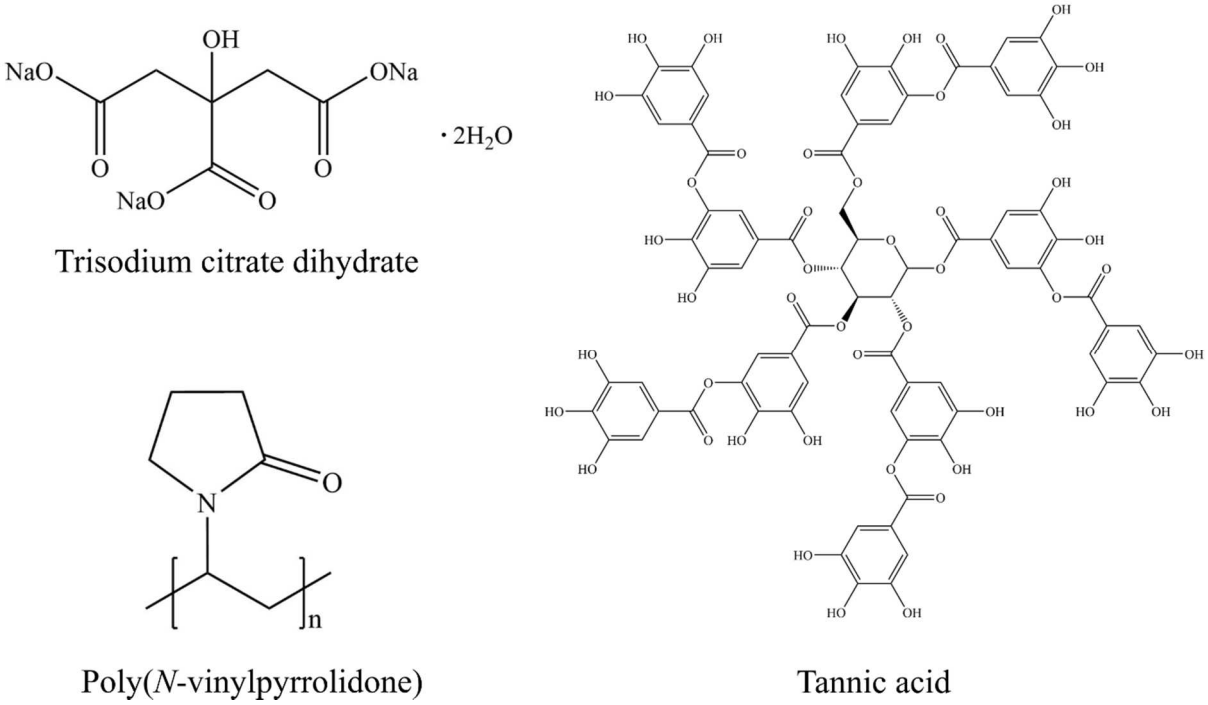

Figure 11: The reducing agents trisodium citrate dihydrate, tannic acid with its phenolic groups, and the capping agent poly(*N*-vinylpyrrolidone) with $n \cong 360$.

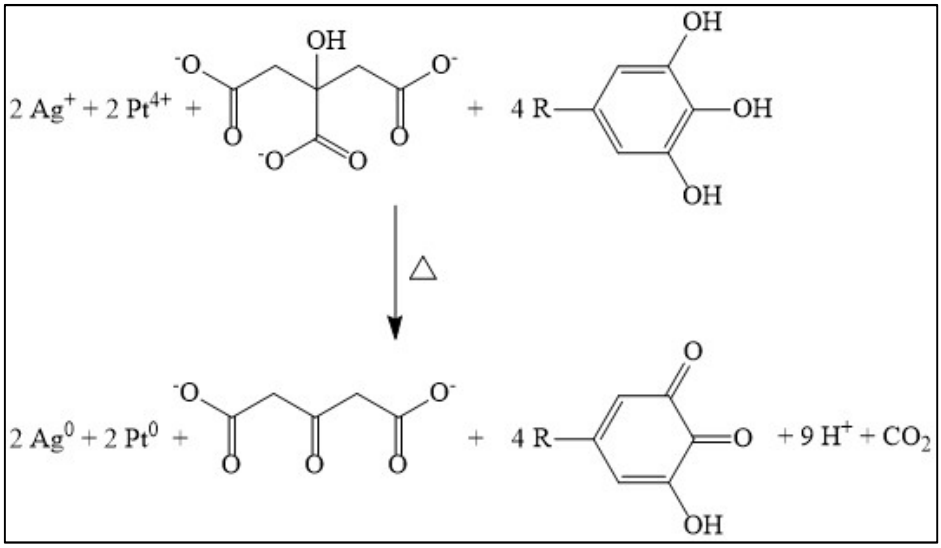

Figure 12: Chemical equation for a possible reaction pathway of a reduction with trisodium citrate and tannic acid.

4.4.2 Reduction by sodium borohydride at pH 3

Sodium borohydride is used as the reducing agent. The nanoparticles are first capped with trisodium citrate and recapped with poly(*N*-vinylpyrrolidone). A seeded-growth method is chosen. As platinum precursor, the hexachloridoplatinic acid is taken.

$$AgNO_3 + NaBH_4 + 3\ H_2O \rightarrow Ag + B(OH)_3 + NaNO_3 + 7\ H^+$$

$$H_2PtCl_6 + 6\ NaBH_4 + 18\ H_2O \rightarrow Pt + 6\ B(OH)_3 + 6\ NaCl + 44\ H^+$$

0.25 mL silver nitrate (10 mM, 2.5 µmol) and 0.5 mL trisodium citrate dihydrate (132 mM, 66 µmol) are added to 50 mL of degassed, ice-cooled Millipore water. A 10.6 mM solution of sodium borohydride in ice-cold Millipore water is prepared, of which 0.8 mL (8.5 µmol) are added rapidly to the reaction mixture under vigorous stirring and let react for two minutes. In the meantime, 0.25 mL hexachloridoplatinic acid (10 mM, 2.5 µmol) are acidified to pH 3 with 0.083 mL 2 M hydrochloric acid and added to the reaction mixture followed by further 0.8 mL (8.5 µmol) sodium borohydride. Everything is stirred for another four minutes and neutralized with 0.083 mL 2 M sodium hydroxide before refunctionalization with 1 mL poly(*N*-vinylpyrrolidone) (135 mM, 135 µmol) overnight at RT. The purification is performed by ultracentrifugation (20,000 rpm/ 29,400 g, or 30,000 rpm/ 66,000 g for platinum-rich compositions, 30 minutes, 3x) and washing with Millipore water.

4.4.3 Reduction by sodium borohydride at pH 10

Sodium borohydride is used as the reducing agent. The nanoparticles are first capped with trisodium citrate and recapped with poly(*N*-vinylpyrrolidone). A seeded-growth method is chosen. As platinum precursor, the hexachloridoplatinic acid is taken.

0.25 mL silver nitrate (10 mM, 2.5 µmol) and 0.5 mL trisodium citrate dihydrate (132 mM, 66 µmol) are added to 50 mL of degassed, ice-cooled Millipore water. A 10.6 mM solution of sodium borohydride in ice-cold Millipore water is prepared of which 0.8 mL (8.5 µmol) are added rapidly to the reaction mixture under vigorous stirring and let react for two minutes. The reaction mixture is then heated to 50 °C (oil bath 65 °C) and brought to a pH of 10 with 0.04 mL 2 M sodium hydroxide. 0.25 mL hexachloridoplatinic acid (10 mM, 2.5 µmol) are added to the reaction mixture. Further 0.8 mL (8.5 µmol) sodium borohydride are added after two minutes. Everything is stirred for 15 minutes at 50 °C and neutralized with 0.04 mL 2 M hydrochloric acid before refunctionalization with 1 mL poly(*N*-vinylpyrrolidone) (135 mM, 135 µmol)

overnight at RT. The purification is performed by ultracentrifugation (20,000 rpm/ 29,400 g, or 30,000 rpm/ 66,000 g for platinum-rich compositions, 30 minutes, 3x) and washing with Millipore water.

4.5 Synthesis of silver-platinum nanoclusters

Sodium borohydride is used as the reducing agent. The nanoparticles are capped with 11-mercaptoundecanoic acid, 11-MUA (Fig. 13). A co-reduction method is chosen. As platinum precursor, the hexachloridoplatinic acid is taken. The synthesis route for silver-platinum nanoclusters is adapted from reference[24] with slight modifications.

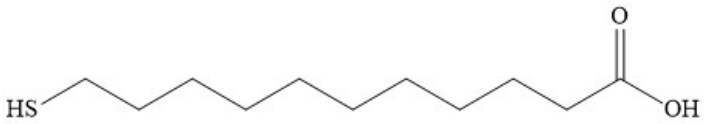

Figure 13: Structural formula of the capping agent 11-mercaptoundecanoic acid.

1 mL 11-mercaptoundecanoic acid (25 mM, 25 µmol), dissolved in ethanol, are mixed with 0.103 mL 2 M sodium hydroxide and added to 50 mL degassed Millipore water at RT. Then, 0.25 mL silver nitrate (10 mM, 2.5 µmol) and 0.25 mL hexachloridoplatinic acid (10 mM, 2.5 µmol) are added and stirred for five minutes. In the meantime, a 200 mM solution of sodium borohydride in ice-cold Millipore water is prepared of which 0.25 mL (50 µmol) are added dropwise under vigorous stirring to the reaction mixture. After ten minutes, the pH is adjusted to 3 with 2 M hydrochloric acid. The precipitate is centrifuged (3,000 rpm, 1250 g, 10 minutes, 3x) and washed with water. For storage, the nanoparticles are redispersed in 70 vol% ethanol.

4.6 Synthesis of silver-gold nanoparticles

The following synthesis routes are described for the silver-gold 50:50 mol% compositions and a reaction volume of 50 mL. Through variation of the precursor amounts (Table 4), other compositions may be achieved. All synthesis routes are already described elsewhere.[19, 23, 25, 28] Only slight modifications were done for size regulation. To obtain an appropriate amount of nanoparticles for characterization and further experiments, three to seven upscaled syntheses were performed. The batches were mixed after DCS and UV/vis characterization.

Table 4: Precursor amounts for a desired molar composition. Suited for a reaction volume of 50 mL. *Gold nanoparticle synthesis by citrate only reduction.

Desired Composition Ag:Au / mol%	*V* ($AgNO_3$, 10 mM) / mL	*V* ($HAuCl_4$, 10 mM) / mL
0:100	0.00	0.50
0:100	0.00	1.27*
10:90	0.05	0.45
20:80	0.10	0.40
30:70	0.15	0.35
40:60	0.20	0.30
50:50	0.25	0.25
60:40	0.30	0.20
70:30	0.35	0.15
80:20	0.40	0.10
90:10	0.45	0.05
100:0	0.50	0.00

4.6.1 Reduction by trisodium citrate and tannic acid

A mixture of trisodium citrate dihydrate and tannic acid are used as the reducing agents. The nanoparticles are recapped with poly(*N*-vinylpyrrolidone). A co-reduction method is chosen.

0.25 mL silver nitrate (10 mM, 2.5 µmol) and 0.25 mL tetrachloridoauric acid (10 mM, 2.5 µmol) are added to 50 mL of degassed Millipore water which is heated to 100 °C. For reduction, 0.5 mL trisodium citrate dihydrate (132 mM, 66 µmol) are mixed with 1 mL tannic acid (4.95 mM, 4.9 µmol) and added rapidly under vigorous stirring to the reaction mixture. After five minutes, the oil bath is removed and replaced by an ice-bath. The particles are refunctionalized with 1 mL poly(*N*-vinylpyrrolidone) (90 mM, 90 µmol) by stirring overnight at RT. The purification is performed by ultracentrifugation (20,000 rpm/ 29,400 g, or 30,000 rpm/ 66,000 g for gold-rich compositions, 30 minutes, 2x) and washing with Millipore water.

4.6.2 Reduction by trisodium citrate

Trisodium citrate dihydrate is used as the reducing agent. The nanoparticles are recapped with poly(*N*-vinylpyrrolidone). A co-reduction method is chosen. The synthesis is performed according to Mahl[177] with slight modifications.

0.25 mL silver nitrate (10 mM, 2.5 µmol) and 0.25 mL tetrachloridoauric acid (10 mM, 2.5 µmol) are added to 50 mL of degassed Millipore water which is heated to 100 °C. For reduction, 0.5 mL trisodium citrate dihydrate (66 mM, 33 µmol) or 2.5 mL trisodium citrate dihydrate (4.96 mM, 12.4 µmol, for pure gold nanoparticles, amount of tetrachloridoauric acid see Table 4) are added rapidly under vigorous stirring to the reaction mixture. After 60 minutes, the oil bath is removed and replaced by an ice-bath. The particles are refunctionalized with 1 mL poly(*N*-vinylpyrrolidone) (90 mM, 90 µmol) by stirring overnight at RT. The purification is performed by ultracentrifugation (20,000 rpm/ 29,400 g, 30 minutes, 2x) and washing with Millipore water.

Pure silver nanoparticles were also synthesized in the group of Electrocatalysis & Functional Materials of Jun.-Prof. Dr. Tschulik, Department of Chemistry and Biochemistry, Ruhr-University Bochum as reported in the literature[178] via a seeded-growth method. The Ag seeds are prepared by dissolving trisodium citrate (200 mg, 5.3 mmol) in 95 mL water and heating to 70 °C for 15 min. Then, silver nitrate (17 mg, 0.1 mmol, dissolved in 1.7 mL water) and sodium borohydride (2 mg, 0.053 mmol, dissolved in 2 mL water) are added under vigorous stirring. The mixture is stirred at 70 °C for 1 h and is then allowed to cool down to room temperature. For the growth of bigger particles on these Ag seeds, 10 mL of the seed solution are added to 77 mL of water, containing trisodium citrate (20 mg, 0.53 mmol) and at that point the solution is heated to 70 °C for 15 min. Then, silver nitrate (17 mg, 0.1 mmol, dissolved in 1.7 mL) and trisodium citrate (20 mg, 0.53 mmol, dissolved in 2 mL) are added and the mixture is stirred at 70 °C for 1 h. The addition of silver nitrate and citrate solutions is repeated, and the reaction mixture is allowed to cool to room temperature. The particles are isolated by ultracentrifugation (29,400 g, 30 min) and washed with ultrapure water.

4.7 Dissolution experiments

4.7.1 Dissolution of silver-gold nanoparticles

The nanoparticles are prepared as described in section 4.6.1. All nine compositions and monometallic silver particles are taken and diluted to 5 mL with a total metal concentration of 0.05 mg/mL. The particle dispersions are stirred at ambient conditions in Amicon® Ultra – 15 centrifugal filters (MWCO = 3,000 Da). The filters are immersed in 27 mL Millipore water (Fig. 14). After certain hours, 3 mL of Millipore water are taken, mixed with nitric acid (0.1 mL) and the silver amount is determined by AAS. The taken 3 mL are refilled with Millipore water to ensure that the filter is still immersed in water.

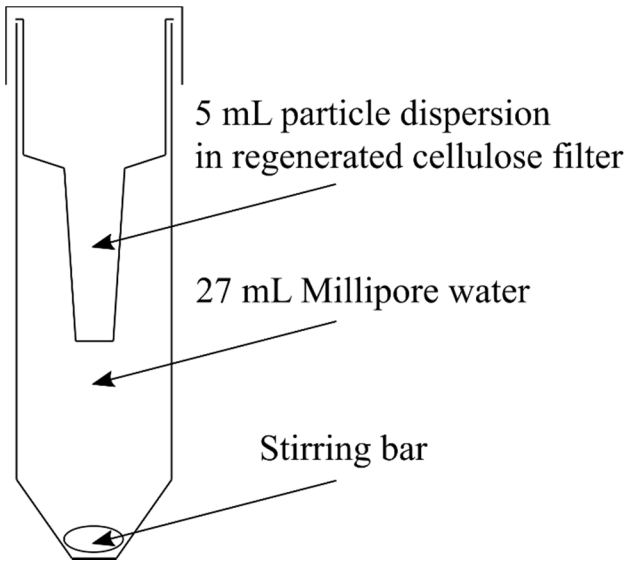

Figure 14: Amicon® Ultra – 15 centrifugal filter (MWCO = 3,000 Da) with the dissolution experiment setup. The particle dispersion is placed into the cellulose filter which is immersed in Millipore water under permanent stirring.

The same set-up is chosen for the dissolution experiments of bulk silver (Ag-foil), Ag70Au30 (pellets), Ag50Au50 (rod), and Ag70Pd30 (foil).

4.7.2 Dissolution of silver-platinum nanoparticles

The nanoparticles are prepared as described in section 4.4.2. The compositions Ag:Pt 10:90, 30:70, 50:50, 70:30, 90:10 are taken and diluted to 100 mL with a silver concentration of 0.1 mg/mL. The particle dispersions are stirred at normal conditions in PTFE bottles. After certain hours, 7 mL of particle dispersion are taken and centrifuged in Amicon® Ultra – 15

centrifugal filters (MWCO = 3,000 Da). The filtrate is taken, mixed with nitric acid (0.1 mL) and the silver amount is determined by AAS. The silver-platinum dissolution kinetics experiments were performed by Dr. Kateryna Loza with already synthesized nanoparticles.

4.8 Synthesis of monometallic nanoclusters and nanoparticles

4.8.1 Synthesis of autofluorescent palladium nanoclusters

Sodium borohydride is used as the reducing agent. The nanoparticles are capped with 11-mercaptoundecanoic acid. As palladium precursor, the palladium nitrate as ICP standard is taken. The synthesis route for palladium nanoclusters is adapted from reference[24] with slight modifications.

0.53 mL palladium ICP standard (9.4 mM, 5 µmol) are added to 50 mL degassed Millipore water at RT. 1 mL 11-mercaptoundecanoic acid (25 mM, 25 µmol), dissolved in ethanol, are mixed with 0.103 mL 2 M sodium hydroxide and added to the precursor solution. The reaction mixture is stirred for five minutes. In the meantime, a 200 mM solution of sodium borohydride in ice-cold Millipore water is prepared of which 0.25 mL (50 µmol) are added dropwise under vigorous stirring to the reaction mixture. After ten minutes, the pH is adjusted to 3 with 2 M hydrochloric acid. The precipitate is centrifuged (3,000 rpm, 1250 g, 10 minutes, 3x) and washed with water. For storage, the nanoparticles are redispersed in a borax/hydrochloric acid buffer solution at pH 9. The buffer solution is prepared by dissolving 0.4765 g (2.4 mmol) sodium tetraborate in 50 mL water. 0.83 mL concentrated hydrochloric acid is diluted to a volume of 10 mL resulting in a 0.1 M solution. 50 mL sodium tetraborate solution are combined with 4.6 mL hydrochloric acid (0.1 M) and diluted to 100 mL with water. A pH of 9 is obtained.

4.8.2 Synthesis of silver nanoparticles and ligand exchange from trisodium citrate to poly(ethylene glycol) methyl ether thiol

A mixture of trisodium citrate dihydrate and tannic acid are used as the reducing agents. The nanoparticles are recapped with poly(ethylene glycol) methyl ether thiol (mPEGthiol) (Fig. 15).

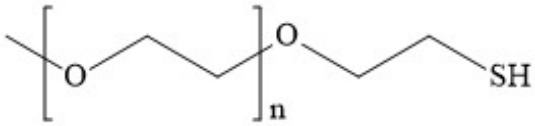

Figure 15: Structural formula of the capping agent poly(ethylene glycol) methyl ether thiol with $n \cong 14$.

0.5 mL silver nitrate (10 mM, 5 µmol) are added to 50 mL of degassed Millipore water which is heated to 100 °C. For reduction, 0.5 mL trisodium citrate dihydrate (132 mM, 66 µmol) are mixed with 1 mL tannic acid (4.95 mM, 4.9 µmol) and added rapidly under vigorous stirring to the reaction mixture. After five minutes, the oil bath is removed and replaced by an ice-bath. The particles are refunctionalized with 1 mL poly(ethylene glycol) methyl ether thiol (36.7 mM, 36.7 µmol) by stirring overnight at RT. The purification is performed by ultracentrifugation (20,000 rpm/ 29,400 g, 30 minutes, 2x) and washing with Millipore water.

5. Results and discussion

5.1 Characterization of silver-platinum nanoparticles

Within the scope of a collaboration project, the aim was to synthesize and characterize bimetallic silver-platinum nanoparticles in the size range of around 10 nm which is a relevant size for biological experiments (performed at the Bergmannsheil University Medical Centre, not further mentioned in this work). Nanoparticles in this size range are small enough to enter a cell, but still big enough not to get to the nucleus.

5.1.1 Synthesis by trisodium citrate and tannic acid reduction

From previous works of Mahl et al.[28] and Ristig et al.[23, 25] on alloyed silver-gold nanoparticles, sizes of 7 nm to 10 nm were obtained by a trisodium citrate and tannic acid mixture as reducing agent. Therefore, the silver-platinum synthesis route is adapted from the already described routes. At first, monometallic platinum particles are prepared and characterized as a proof of principle. Figure 16 shows the size distribution obtained by a DCS measurement with a size of (7 ± 3) nm. A signal at smaller sizes (around 2 nm) might originate from carrying over smaller nanoparticles during the purification process by ultracentrifugation. Also, a slight shoulder at 10 nm is visible. Nevertheless, the size distribution is narrow which is indicated by the standard deviation of 3 nm.

The dispersed platinum nanoparticles have a light brown color. After centrifugation, the supernatant appears greenish. The UV/vis spectrum (Fig. 17) shows two absorption maxima in the UV region at 270 nm and 211 nm which is also described in the literature.[179-181] A broad tail is observable which results from an absorption of the whole visible spectrum leading to the brown color of the nanoparticle dispersion. The Zeta potential at pH 7 is (-28 ± 7) mV which indicates a good electrostatic stabilization of the nanoparticles. Since the particles are initially capped with trisodium citrate and tannic acid and further functionalized with PVP, a neutral Zeta potential is expected. The negative value may be attributed to only a partial removal of trisodium citrate (and tannic acid) from the particle surface.

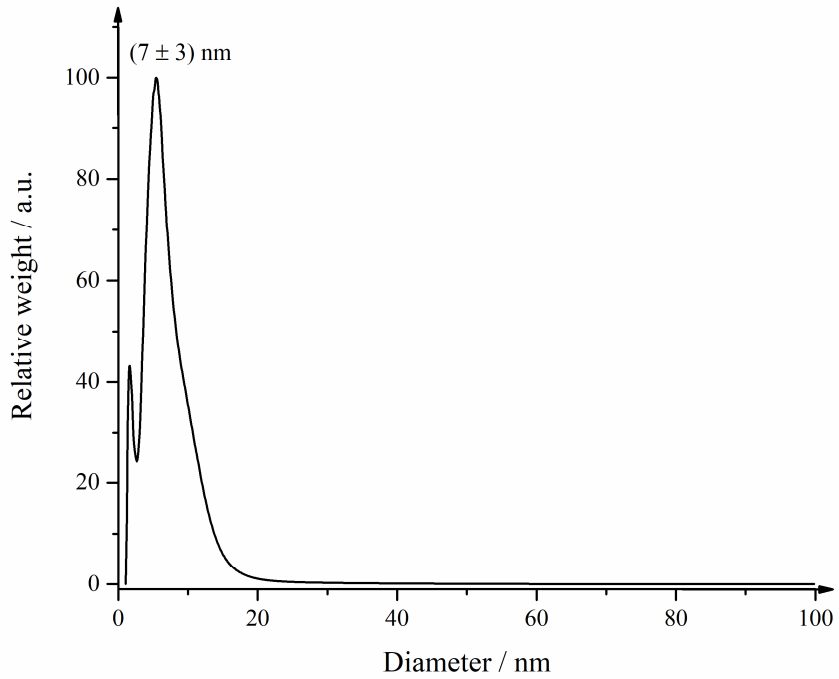

Figure 16: Size distribution of platinum nanoparticles prepared by trisodium citrate and tannic acid reduction according to DCS.

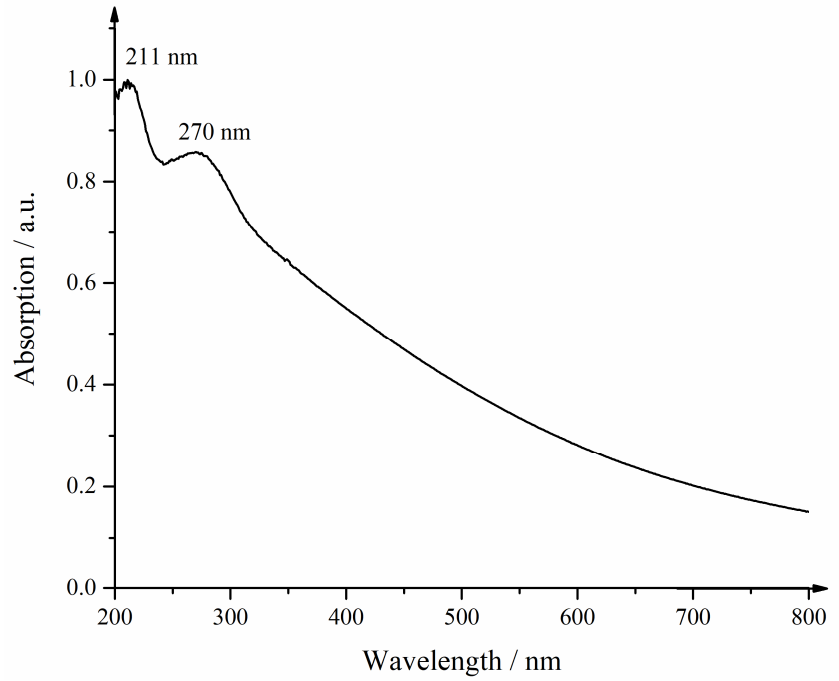

Figure 17: UV/vis spectrum of platinum nanoparticles prepared by trisodium citrate and tannic acid reduction.

The synthesis of bimetallic silver-platinum nanoparticles is performed by a seeded-growth method because a co-reduction of both precursors, silver nitrate and hexachloridoplatinic acid, leads to the formation of the insoluble silver hexachloridoplatinate. At first, the seeded-growth method for the synthesis of alloyed silver-platinum nanoparticles appears not intuitional.

Considering the redox potentials of both precursors ($Pt^0/[PtCl_4]^{2-}$: +0.758 V; $[PtCl_4]^{2-}/[PtCl_6]^{4-}$: +0.726 V; Pt^0/Pt^{2+}: +1.188 V and Ag^0/Ag^+: +0.799 V), the chloridoplatinum complexes are slightly less noble, but platinum is nobler than silver. However, if preparing silver seeds first and adding hexachloridoplatinic acid, a galvanic replacement reaction occurs which leads to the oxidation of the silver seeds and reduction of Pt^{4+} via Pt^{2+} to Pt^0. Silver ions are reduced again because of excess reducing agent leading to alloyed nanoparticles as described by Chen et al.[182] and Fu et al.[48] (Fig. 18).

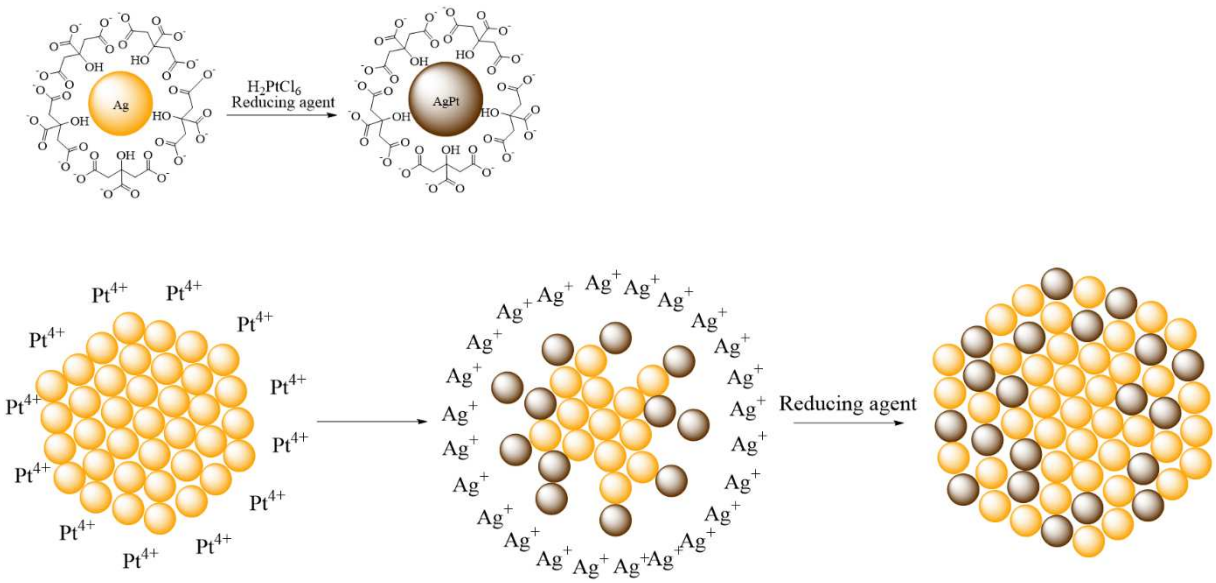

Figure 18: Schematic galvanic replacement reaction during the synthesis of silver-platinum nanoparticles. Yellow spheres depict silver atoms and brown spheres depict platinum atoms in the lower part of the image.

Figure 19 shows the size distribution of silver-platinum 50:50 nanoparticles obtained by a DCS measurement with a bimodal size of (35 ± 5) nm and (3 ± 1) nm in diameter. The weight of each fraction is determined by the corresponding peak integral. The integral of the bigger fraction is 2.5 times higher than the integral of the smaller fraction. Therefore, the significant amount of sample is built up of 35 nm sized nanoparticles. The particles are bigger than expected. The reason might lie in the firstly synthesized silver seeds which have a size of around 30 nm as also described by Ristig et al.[25] for the same synthesis route. This core is the size dependent parameter which determines the diameter of the alloyed nanoparticles. The 3 nm sized nanoparticles were probably carried over during the centrifugation.

The DLS curve (Fig. 20) also shows a multimodal size distribution with sizes by intensity of (73 ± 33) nm, (7 ± 2) nm, and (2 ± 0.4) nm. The sizes measured by DLS are bigger than the sizes obtained from DCS and result from the hydrodynamic diameters of the nanoparticles.

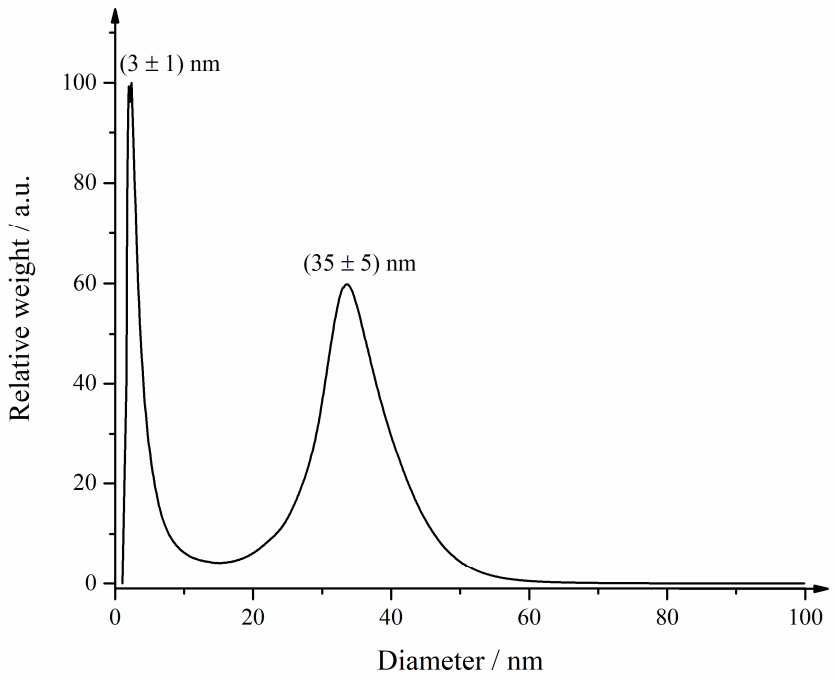

Figure 19: Size distribution of silver-platinum 50:50 nanoparticles prepared by trisodium citrate and tannic acid reduction according to DCS.

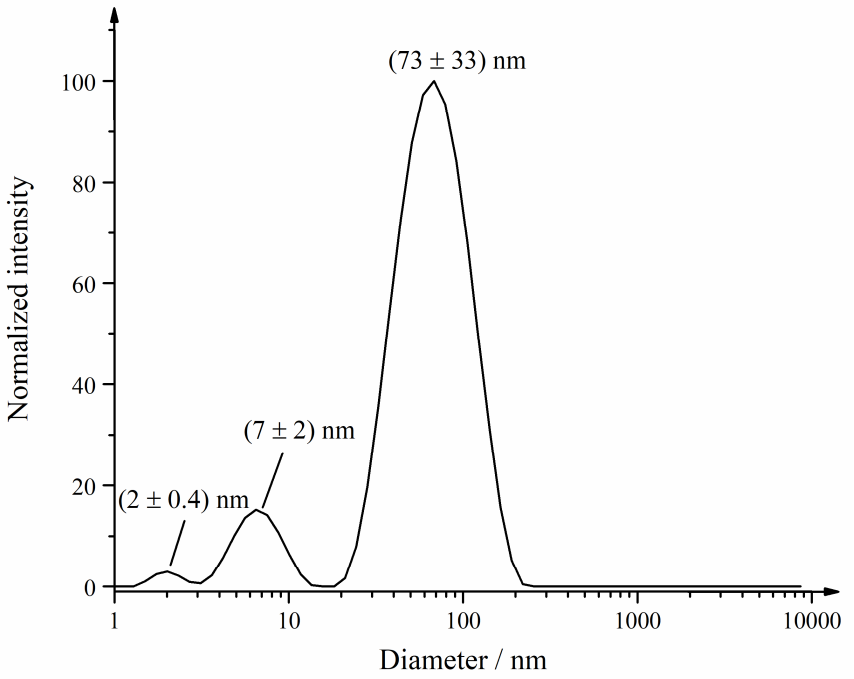

Figure 20: Size distribution of silver-platinum 50:50 nanoparticles prepared by trisodium citrate and tannic acid reduction according to DLS.

Dynamic light scattering uses scattered light to determine the diffusion coefficient and with that the particle diameter. Because bigger particles scatter more light than smaller ones ($I \sim r^6$), the intensity-weighted measurement shows increased sizes. However, the 7 nm and 2 nm sized nanoparticles are less significant because their amount is not large enough to yield the same

scatter intensities as the big particles. The PDI is 0.491 which corresponds to a polydisperse system because three size distribution peaks are obtained. The Zeta potential at pH 7 lies at (-43 ± 11) mV indicating a good electrostatic stabilization of the nanoparticles.

Scanning electron micrographs show spherical nanoparticles which appear as agglomerates probably because of drying effects (Fig. 21). The analysis of individual particles is depicted as a histogram and shows a size distribution of (21 ± 7) nm (Fig. 22). Overall, 200 not agglomerated particles were measured. The deviation of the sizes obtained from DLS and SEM originates from the measurement characteristics. In the DLS, the nanoparticles are dispersed in water and have a polymer-capped surface. This polymer slows the Brownian motion and the particle size is overestimated. In SEM, only the metallic core is depicted because the polymer shell collapses in the high vacuum. Also, the silver-platinum particles are not ideally spherical and agglomerated. The particles might agglomerate upon drying. If the particles are already agglomerated in dispersion, the DLS would show increased sizes. Since the DCS does not show particles with diameters above 60 nm, an agglomeration in dispersion is excluded.

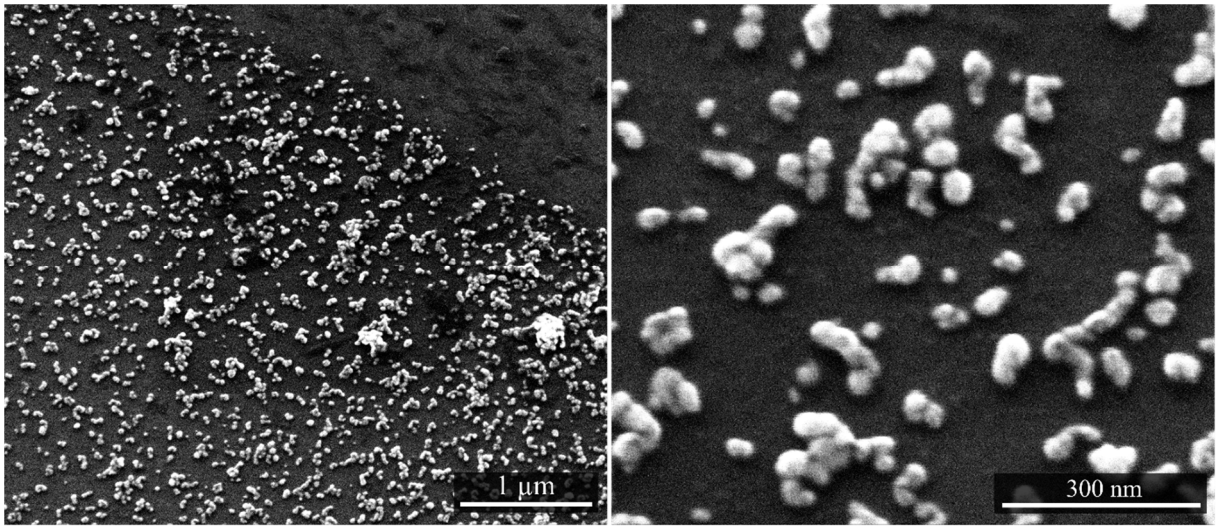

Figure 21: Scanning electron micrographs of different magnifications of silver-platinum 50:50 nanoparticles synthesized by trisodium citrate and tannic acid reduction.

The EDX spectrum (Fig. 23) shows the elements which are present in the sample. The dominating silicon peak originates from the silicon wafer serving as sample substrate. Carbon and oxygen are found in the capping agents PVP, trisodium citrate, and tannic acid. Sodium originates from trisodium citrate. Signals for platinum are found at 2.07 keV (M_α), 9.45 keV (L_α), and 11.1 keV (L_β). Silver peaks are positioned at 3.0 keV (L_α) and 3.17 keV (L_β). Quantitative elemental analysis yields a composition of 67 at% silver and 33 at% platinum.

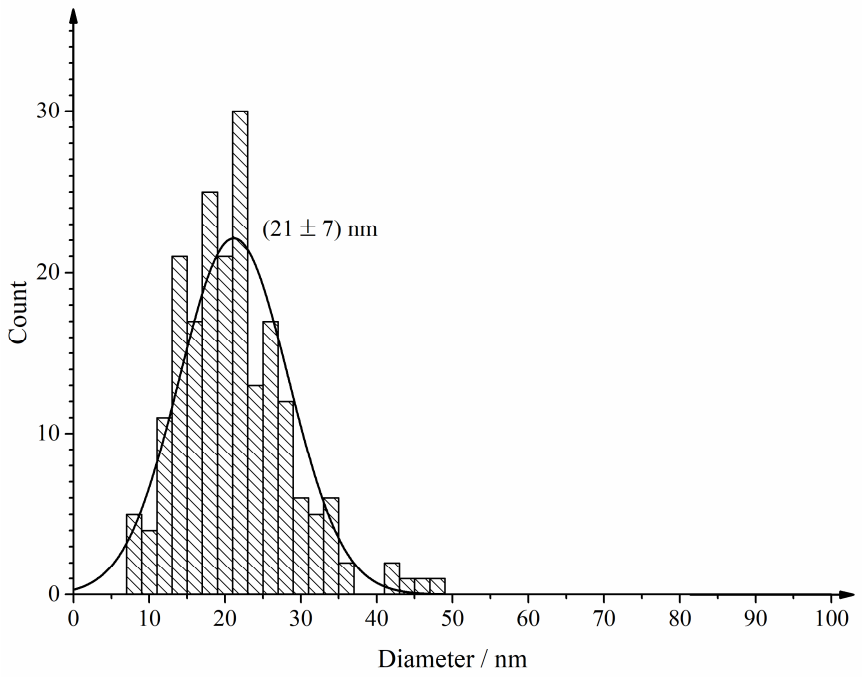

Figure 22: Particle size distribution of silver-platinum 50:50 nanoparticles synthesized by trisodium citrate and tannic acid reduction as measured by scanning electron microscopy.

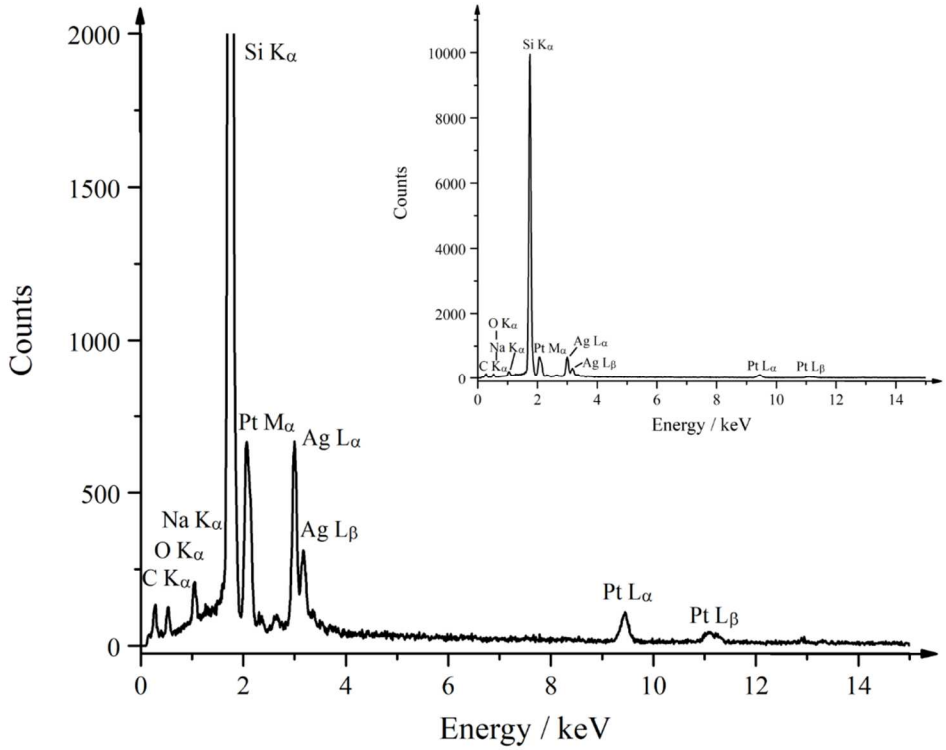

Figure 23: EDX spectrum of silver-platinum 50:50 nanoparticles synthesized by trisodium citrate and tannic acid reduction. The insert shows the same sample with the whole measured count range.

The UV/vis spectroscopy of silver-platinum 50:50 nanoparticles reveals one absorption band at 375 nm which is located between the absorption bands of pure platinum (270 nm) and pure

silver nanoparticles (421 nm) synthesized by trisodium citrate and tannic acid reduction (Fig. 24). The absorption band shape of silver-platinum is broader than the absorption band of silver nanoparticles. Therefore, the presence of a physical mixture of silver particles and platinum particles is excluded. It is known from literature,[46, 102, 104-105, 149] that alloyed nanoparticles exhibit absorption bands which lie between the maxima of the pure metals. That means it is possible to estimate the molar composition by UV/vis spectroscopy. The theoretical absorption for a silver-platinum 50:50 mol% composition, calculated from the measured values for silver and platinum, lies at 346 nm. A redshift to 375 nm means a silver amount of 70 mol% which is also observable in the quantitative analysis from EDX. In bimetallic systems, the shift of the absorption band is affected heavier by the composition than the nanoparticle size.

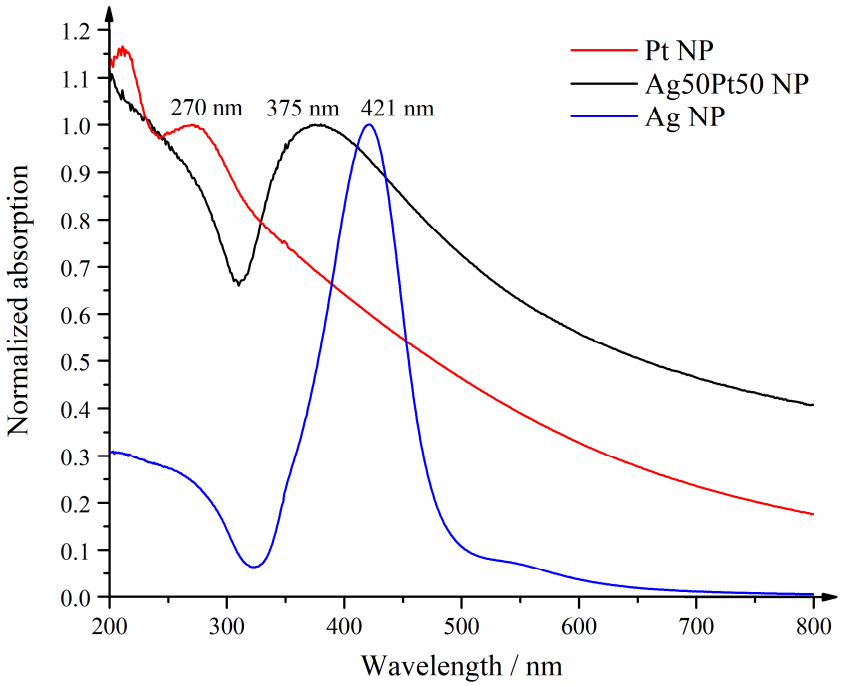

Figure 24: UV/vis spectrum of 35 nm sized silver-platinum 50:50 nanoparticles in comparison to silver (35 nm diameter) and platinum (7 nm diameter) particles synthesized by trisodium citrate and tannic acid reduction.

In summary, the synthesis by trisodium citrate and tannic acid reduction yields platinum nanoparticles with sizes of around 7 nm. In a seeded-growth synthesis pathway, where silver nanoparticles serve as seeds, particles with sizes of 35 nm according to DCS and 21 nm according to SEM are obtained. Those show spherical morphologies which appear to agglomerate upon drying. UV/vis spectroscopy shows an alloy character of the nanoparticles because the absorption maximum of the bimetallic nanoparticles lies between the monometallic particles. Quantitative analysis by EDX shows a composition of 67 at% silver and 33 at% platinum.

5.1.2 Synthesis by sodium borohydride reduction at pH 3

Sodium borohydride is chosen as a reducing agent because of its strong reducing ability. The aim is to synthesize silver seeds between 7 nm and 10 nm diameter as the seed size determines the bimetallic particle size. Sodium borohydride undergoes a hydrolysis in an aqueous solution. Its rate is pH and temperature dependent as reported by Kreevoy et al.[183] The half-life $t_{1/2}$ in minutes of sodium borohydride can be calculated by Equation 9 with T the temperature in Kelvin.

$$\log(t_{1/2}) = \mathrm{pH} - (0.034 \cdot T - 1.92) \quad (9)$$

Table 5 shows half-lives of sodium borohydride for the three during the syntheses relevant pH values of 3, 7, and 10 as well as the three used temperatures, 277 K (4 °C), 298 K (25 °C), and 338 K (65 °C). The choice of the reaction conditions is influenced by the hydrolysis half-life of sodium borohydride. Note that the pH of the reaction solution itself is adjusted, not the pH of the sodium borohydride solution.

Table 5: Half-lives of sodium borohydride at different pH values and temperatures.

pH	Temperature / K	Half-life / min
3	298	$6.14 \cdot 10^{-6}$
3	277	$3.2 \cdot 10^{-5}$
7	298	0.0614
7	277	0.32
10	298	61.4
10	338	2.68

The hexachloridoplatinate complex, which is used as the platinum precursor, also undergoes hydrolysis if diluted in water as shown in the following equation:[184]

$$[PtCl_6]^{2-} + H_2O \rightarrow [PtCl_5(H_2O)]^- + Cl^-$$

Because of excess water, the reaction follows pseudo first order kinetics (Equation 10) with $[A]_t$ the concentration at a certain time t, $[A]_0$ the concentration at $t = 0$, e Euler's number, and k the reaction constant.

$$[A]_t = [A]_0 \mathrm{e}^{-kt} \quad (10)$$

$$t_{1/2} = \frac{\ln(2)}{k} \tag{11}$$

The half-life of the hydrolysis can be determined with Equation 11 to obtain a value of 230 min at RT and a pH of 7 as shown by Nachtigall et al.[184] In their experiments, Nachtigall et al. analyzed the diluted hexachloridoplatinate complex after certain times by ion chromatography. The peak area corresponding to the hexachloridoplatinate complex was fitted as a function of time to obtain a first-order kinetics curve and the reaction constant *k*. The hydrolysis equilibrium is reached after 30 hours. This hydrolysis alters the redox potential of the platinum precursor. To ensure equal reaction conditions, the hydrolysis equilibrium should be reached after diluting the hexachloridoplatinic acid in water.

Since the seeded-growth method is chosen, the prepared silver seeds are characterized at first. The characterization of the unpurified silver seeds destined for the synthesis of silver-platinum nanoparticles in the composition of 50:50 is performed by DCS, DLS, and UV/vis spectroscopy. The size distribution obtained from DCS (Fig. 25) shows a bimodal particle size distribution at (4 ± 0.3) nm and (8 ± 2) nm. The smaller particles can be removed by ultracentrifugation (20,000 rpm/ 29,400 g, 30 minutes, 2x) because they do not sediment. The sedimentation time can be calculated by Equation 12 which lies at 4 hours for particles of 4 nm diameter at a centrifugation velocity of 20,000 rpm. Since the ultracentrifugation is performed for 30 minutes, the 4 nm sized nanoparticles should be removed with the supernatant. The 8 nm sized particles lie in the desired size range of 7 nm to 10 nm, and therefore are suited for further bimetallic nanoparticle syntheses.

$$t = \frac{k_{adj}}{s} = k \cdot \left(\frac{70000}{v}\right)^2 \cdot \left(d \cdot \left(\frac{\rho_P - \rho_M}{\eta}\right)\right)^{-1} \tag{12}$$

t = Sedimentation velocity

k_{adj} = k-factor for the rotor velocity v

s = Svedberg-factor

k = k-factor for the maximal rotor velocity

v = Rotor velocity

d = Particle diameter

ρ_P = Density of the particles

ρ_M = Density of the medium

η = Viscosity of the medium

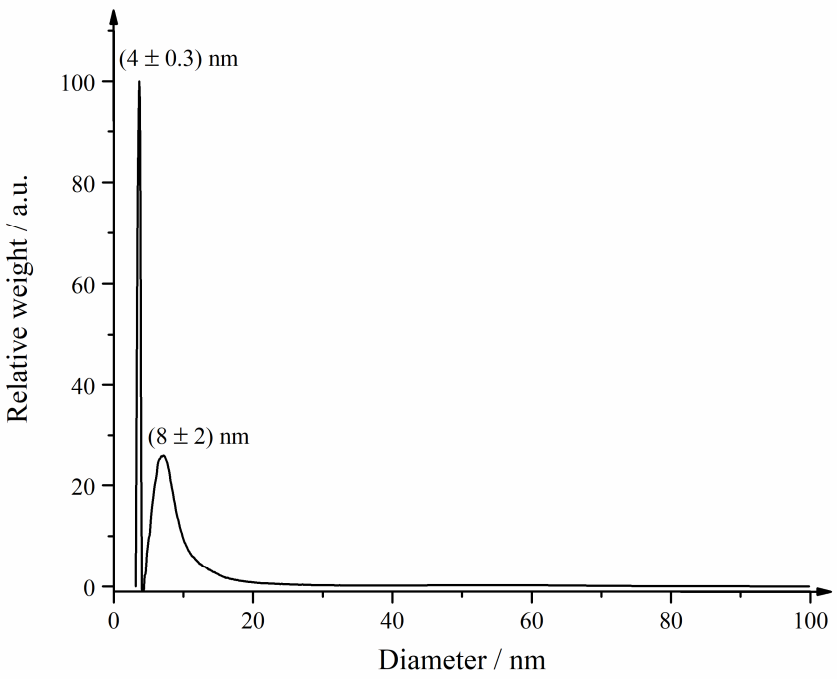

Figure 25: Size distribution of unpurified silver seeds by reduction with sodium borohydride as obtained by DCS.

Dynamic light scattering (Fig. 26) yields a bimodal size distribution as well, but shows much bigger sizes. Because the scattering intensity of bigger particles is higher than the scattering intensity of small particles, the size can be overestimated if just a few big particles or agglomerates are present. The obtained hydrodynamic diameters are (186 ± 184) nm and (13 ± 3) nm with a PDI of 0.439 speaking for a broad size distribution. Regarding the intensity weighted size distribution, the 13 nm sized particles are less significant. The hydrodynamic diameter of 186 nm probably originates from agglomerates and has a high standard deviation of 184 nm which makes it necessary to use other techniques for the size determination, like the already described differential centrifugal sedimentation. A general observation from DLS measurements of nanoparticles around 10 nm in diameter is that the obtained sizes do not always match the diameters obtained from DCS or SEM.

The UV/vis spectrum of silver seeds (Fig. 27) shows an absorption band at 406 nm that is characteristic for spherical silver nanoparticles with sizes of around 10 nm which lies in the range of 400 nm.[74] The broad peak indicates the presence of agglomerates and underlines the findings from DLS.

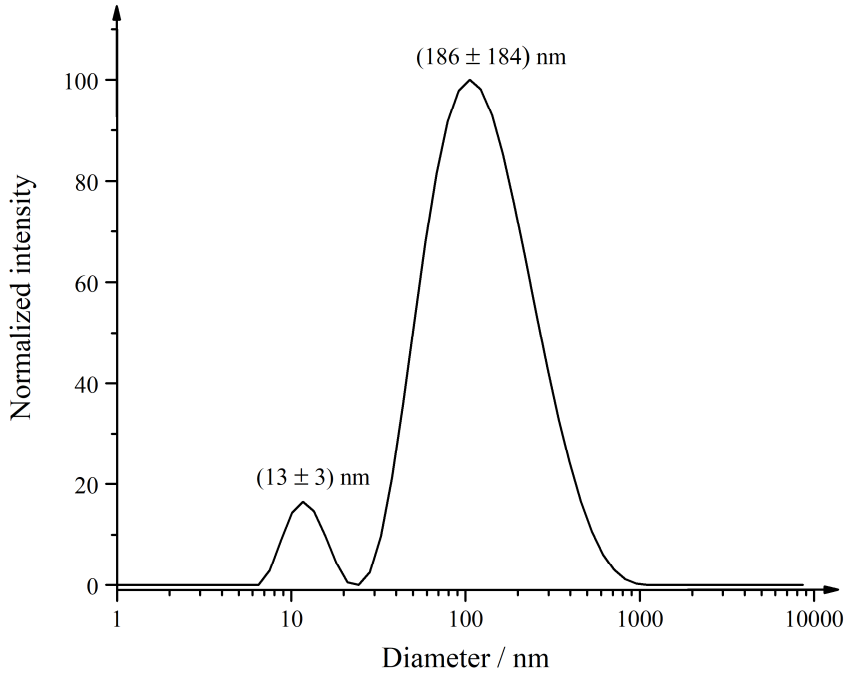

Figure 26: Size distribution of unpurified silver seeds by reduction with sodium borohydride as obtained by DLS.

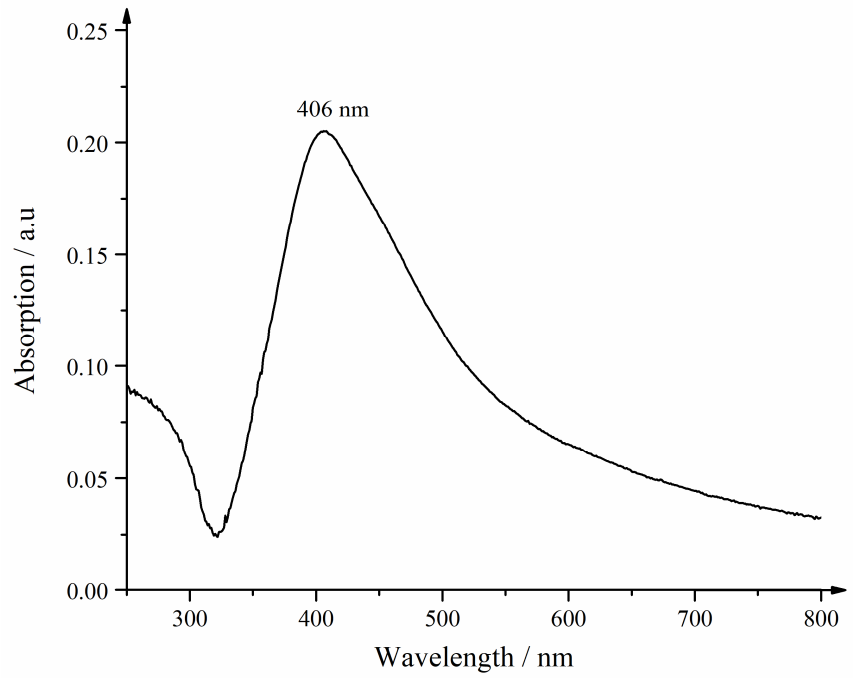

Figure 27: UV/vis spectrum of unpurified silver seeds by reduction with sodium borohydride.

Bimetallic silver-platinum nanoparticles were synthesized in all compositions between 10:90 and 90:10 in steps of 10 mol%. The hydrodynamic radii of silver-platinum 50:50 particles are compared to the silver seeds to determine a growth in size which is expected after addition of hexachloridoplatinic acid (Fig. 28).

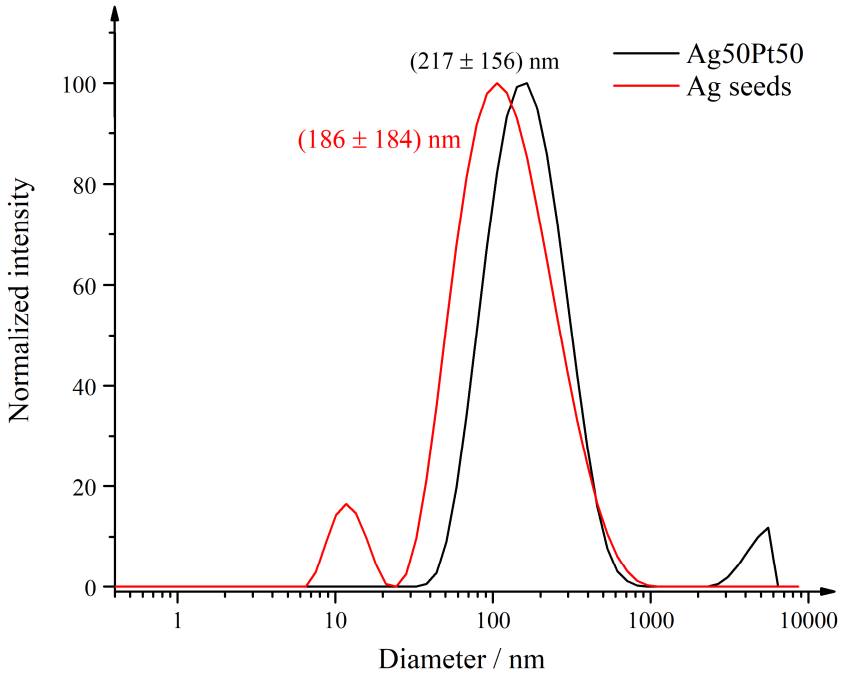

Figure 28: Size distribution of unpurified silver seeds by reduction with sodium borohydride (red) and the size distribution of silver-platinum 50:50 nanoparticles (black) as obtained by DLS.

The size of the nanoparticles grows from 186 nm to 217 nm indicating either a successful synthesis of bimetallic particles or the presence of even bigger agglomerates. Nevertheless, a systematic shift to bigger sizes is obtained. The PDI is 0.187 which indicates a narrow size distribution. The Zeta potential at pH 7 is (-19 ± 5) mV resulting in a weak electrostatic stabilization. After re-functionalization with PVP, a neutral Zeta potential is expected. The negative value implies still present citrate molecules which were not completely exchanged by PVP. Because the size obtained by DLS is overestimated, DCS measurements are performed. Figure 29 shows the size distributions of all compositions from silver-platinum 10:90 to 90:10 in steps of 10 mol%. The diagram on the right depicts the whole measured range from 3 nm to 100 nm, whereas the diagram on the left shows the section from 3 nm to 40 nm for a better overview. The diameters lie between 6 nm and 9 nm and show narrow size distributions. In contrary to the DLS measurements, no signals between 100 nm and 40 nm are visible that show the occurrence of big particles or agglomerates. Table 6 contains an overview of the representative diameters and their standard deviations.

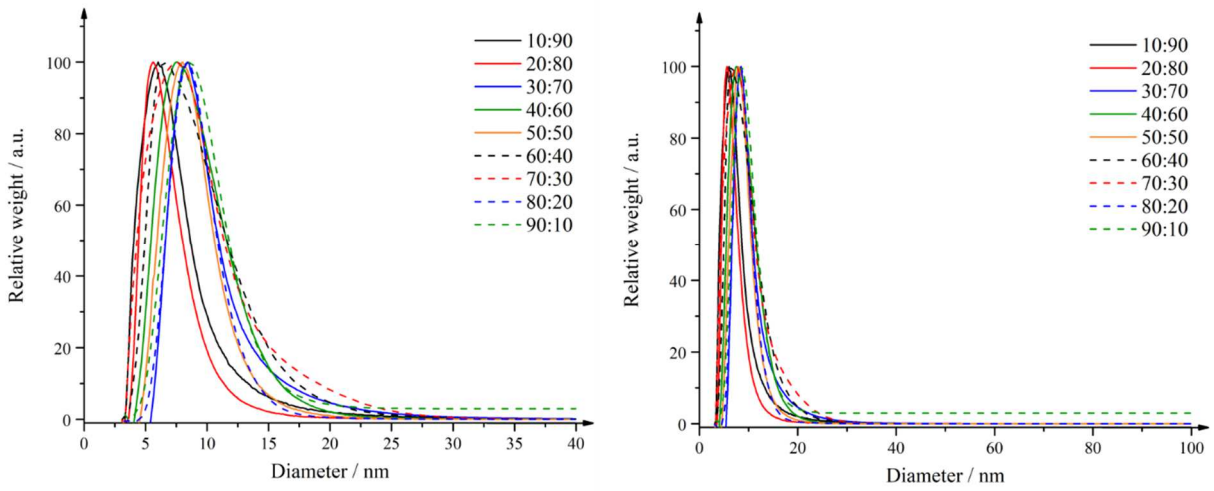

Figure 29: Representative size distributions of silver-platinum nanoparticles by reduction with sodium borohydride at pH 3 in the compositions of 10:90 to 90:10 in steps of 10 mol% as obtained by DCS.

Table 6: Representative sizes of silver-platinum nanoparticles by reduction with sodium borohydride in the compositions of 10:90 to 90:10 in steps of 10 mol% as obtained by DCS and their corresponding standard deviations.

Composition Ag:Pt	Size as obtained by DCS / nm
10:90	7 ± 2
20:80	6 ± 2
30:70	9 ± 2
40:60	9 ± 3
50:50	9 ± 2
60:40	9 ± 4
70:30	9 ± 4
80:20	9 ± 2
90:10	9 ± 3

Transmission electron micrographs (Fig. 30) show spherical and branched particles. Some spherical nanoparticles, especially in silver-rich samples, appear to have a hollow structure. Those hollow structures correspondingly grow with the silver composition. Usually, hollow structures appear after galvanic replacement reactions, where the less noble metal is oxidized by the nobler metal and reduced again because of excess reducing agent. Those structures are reported in the literature.[48-49, 182]

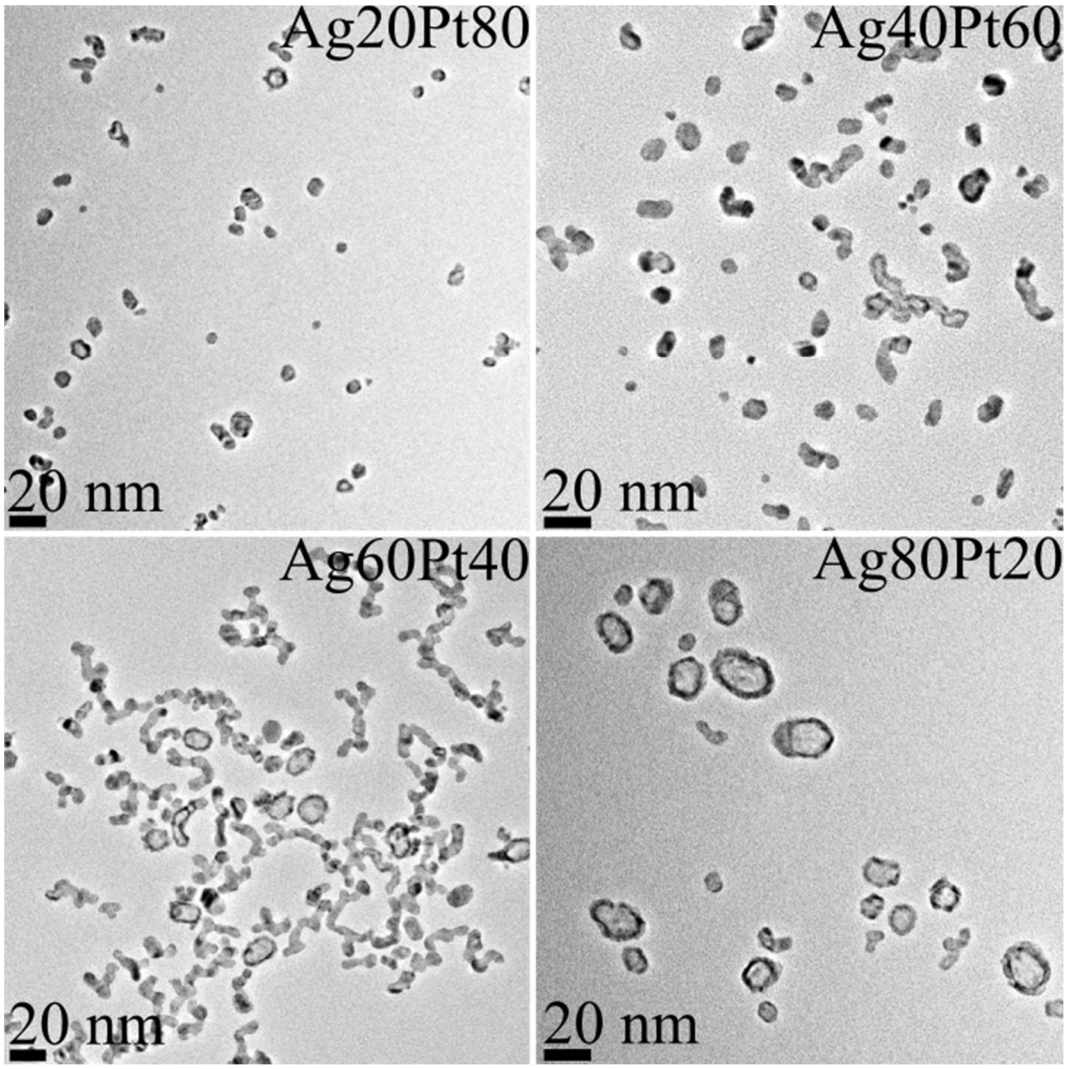

Figure 30: Transmission electron micrographs of silver-platinum nanoparticles in the compositions 20:80, 40:60, 60:40, and 80:20 prepared by reduction with sodium borohydride at pH 3.

Histograms obtained from transmission electron micrographs (Fig. 31) show narrow size distributions of (8 ± 2) nm and (7 ± 3) nm for the platinum-rich compositions 20:80 and 40:60. With increasing silver amount, the nanoparticles become bigger and show a broader size distribution with (8 ± 4) nm for 60:40 and (11 ± 5) nm for 80:20. Again, no particles with sizes around 180 nm are observed, indicating some agglomeration in dispersion.

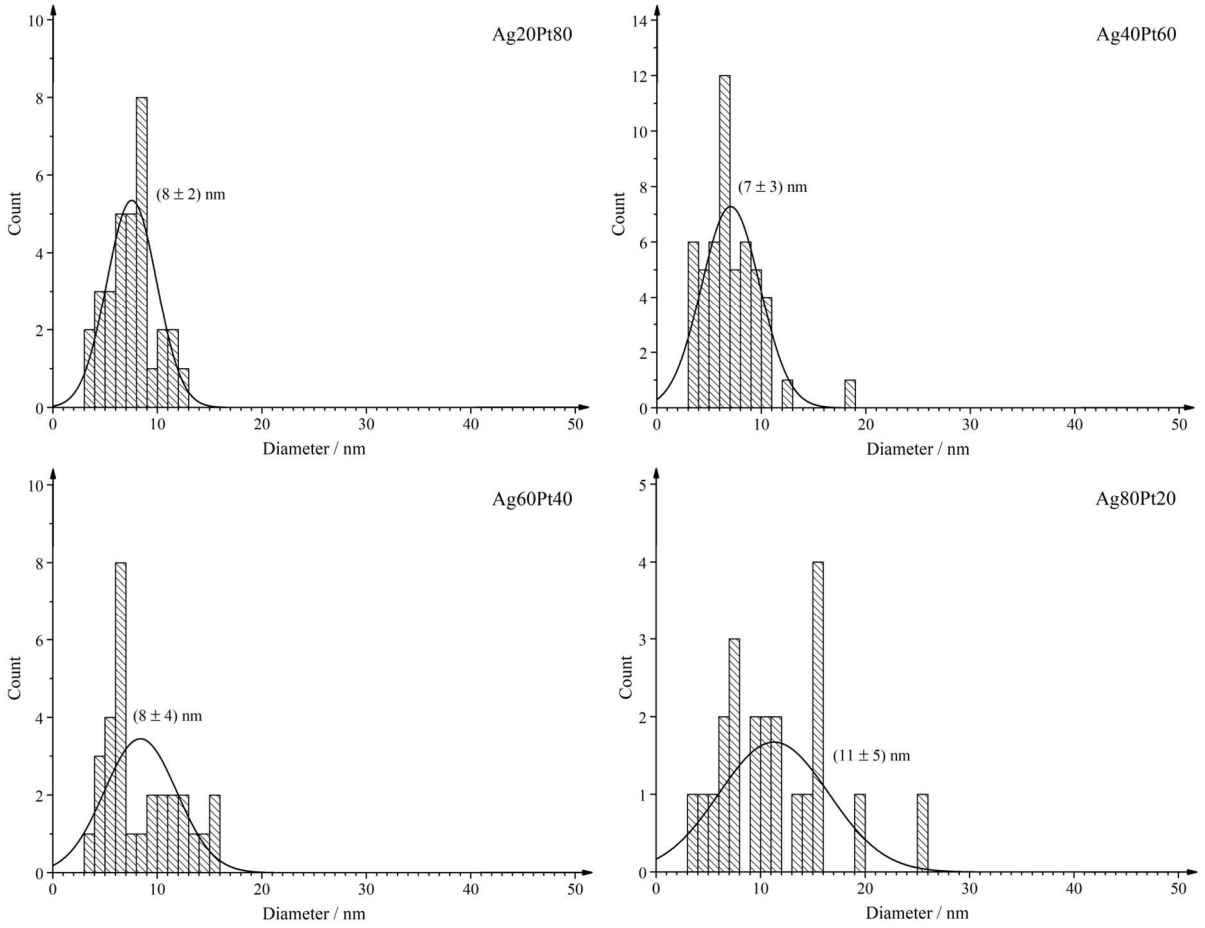

Figure 31: Particle size distribution of silver-platinum nanoparticles in the compositions of 20:80, 40:60, 60:40, and 80:20 prepared by reduction with sodium borohydride at pH 3 as measured by transmission electron microscopy.

To investigate the crystallinity and element distribution within the nanoparticles, high-angle annular dark field STEM images and energy dispersive X-ray spectroscopy maps are recorded. Figure 32 shows the HAADF-STEM image of a spherical nanoparticle with a nominal composition of 30 mol% silver and 70 mol% platinum with a high contrast at the outer parameter of the particle indicating a hollow structure. Several crystalline domains are visible, which are oriented in different directions suggesting polycrystallinity. The EDX map depicts a uniform distribution of both elements, silver and platinum, within the nanoparticle speaking for the appearance of a nanoalloy. The elemental composition for this particle according to EDX quantitative analysis is found to be 37 at% silver and 63 at% platinum. Besides hollow alloyed particles, core-shell particles with a silver core and a platinum shell of about 1 nm are found (representative image in Fig. 33 bottom).

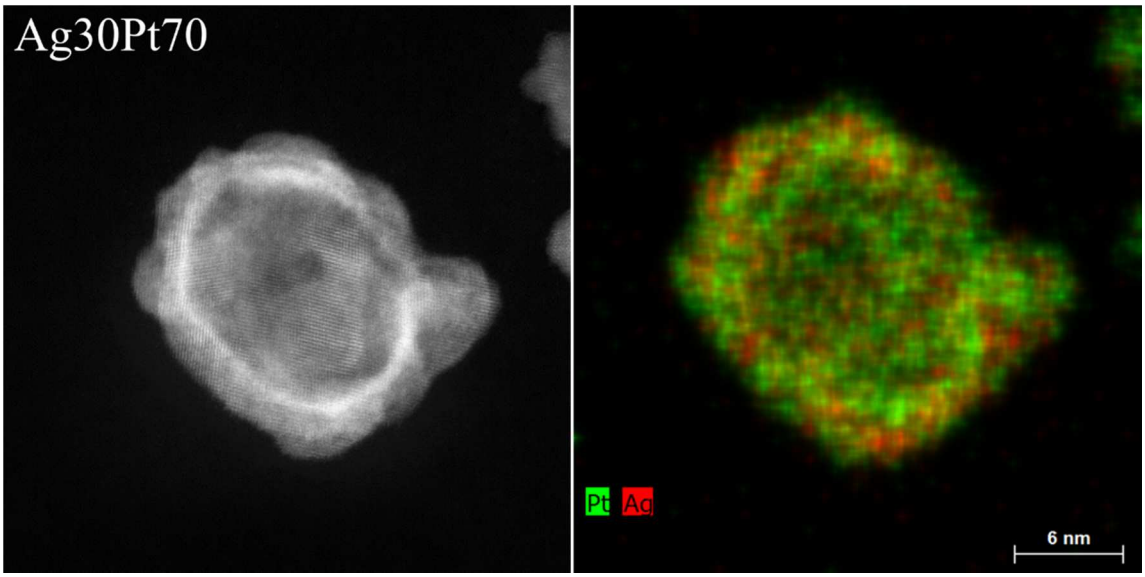

Figure 32: High-angle annular dark field STEM image (left) and EDX map (right) of silver-platinum 30:70 nanoparticles prepared by reduction with sodium borohydride at pH 3.

HAADF-STEM images of the composition silver-platinum 50:50 also reveal two kinds of particles present in one sample (Fig. 33). There is a certain amount of hollow alloyed nanoparticles mixed with dense core-shell nanoparticles. The dense core-shell particles show pronounced crystalline domains without twinning, whereas the hollow alloyed particles present crystallites with different orientations indicating polycrystallinity. The Z-contrast allows the differentiation between the core and the shell (Fig. 33 lower HAADF-STEM image). The lighter element silver appears dark in the core of the nanoparticles, the heavier element platinum appears brighter in the particle shell.

EDX line scans thorough the two nanoparticle species (indicated by the yellow arrows in Fig. 34) show the counts of characteristic X-rays versus the scanned distance. The alloyed character is confirmed because the amount of signal for both elements is equal and the hollow structure is observed through the signal decrease in the center of the scanned path in comparison to the beginning and the end. The core-shell nature of the nanoparticles is observed through the increased signal for platinum in the beginning and the end of the scan path, whereas the center is dominated by the silver signal. The composition of the particles according to quantitative EDX analysis is 54 at% silver and 46 at% platinum. Remarkably, the alloyed particles are overall bigger than the core-shell particles. Also, the amount of hollow alloyed nanoparticles increases with increasing silver amount (Fig. 35). Both findings may have their reason in the size of the silver seeds. Because the amount of the silver precursor is varied, and the amount of the reducing agent remains constant, bigger silver seeds are created with a higher silver amount. This leads to bigger alloyed particles. The higher number of alloyed nanoparticles proportional

to the silver composition is attributed to the amount of reducing agent left for reduction of platinum ions. With a decreasing silver precursor concentration, more sodium borohydride is accessible for the platinum ions which do not attack the silver seeds, but grow on their surface. The other way around, with a higher concentration of the silver precursor, less reducing agent is left for the platinum precursor reduction. Therefore, the silver seeds are oxidized via a galvanic replacement reaction leading to a partial dissolution of the silver core.

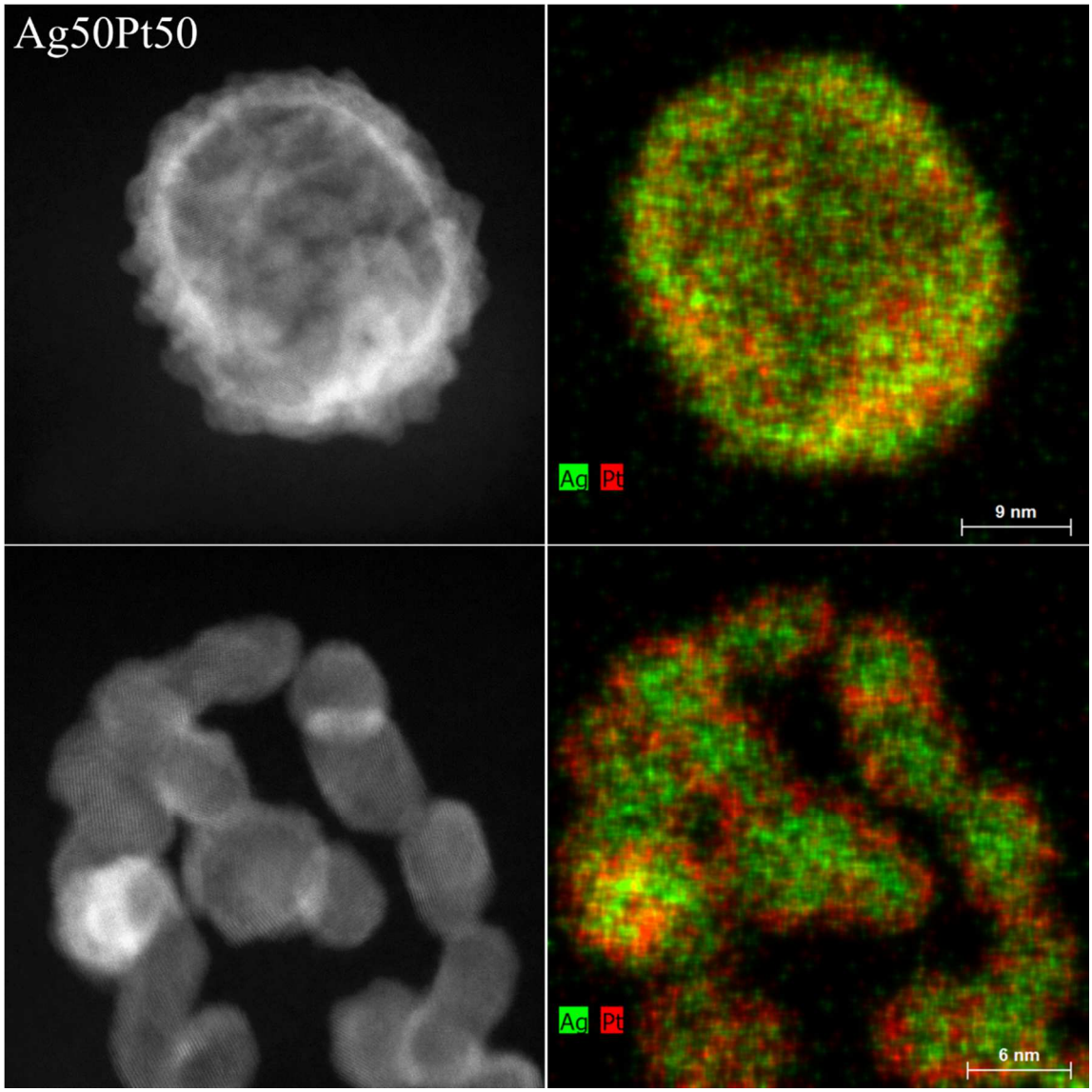

Figure 33: High-angle annular dark field STEM images (left) and EDX maps (right) of silver-platinum 50:50 nanoparticles prepared by reduction with sodium borohydride at pH 3.

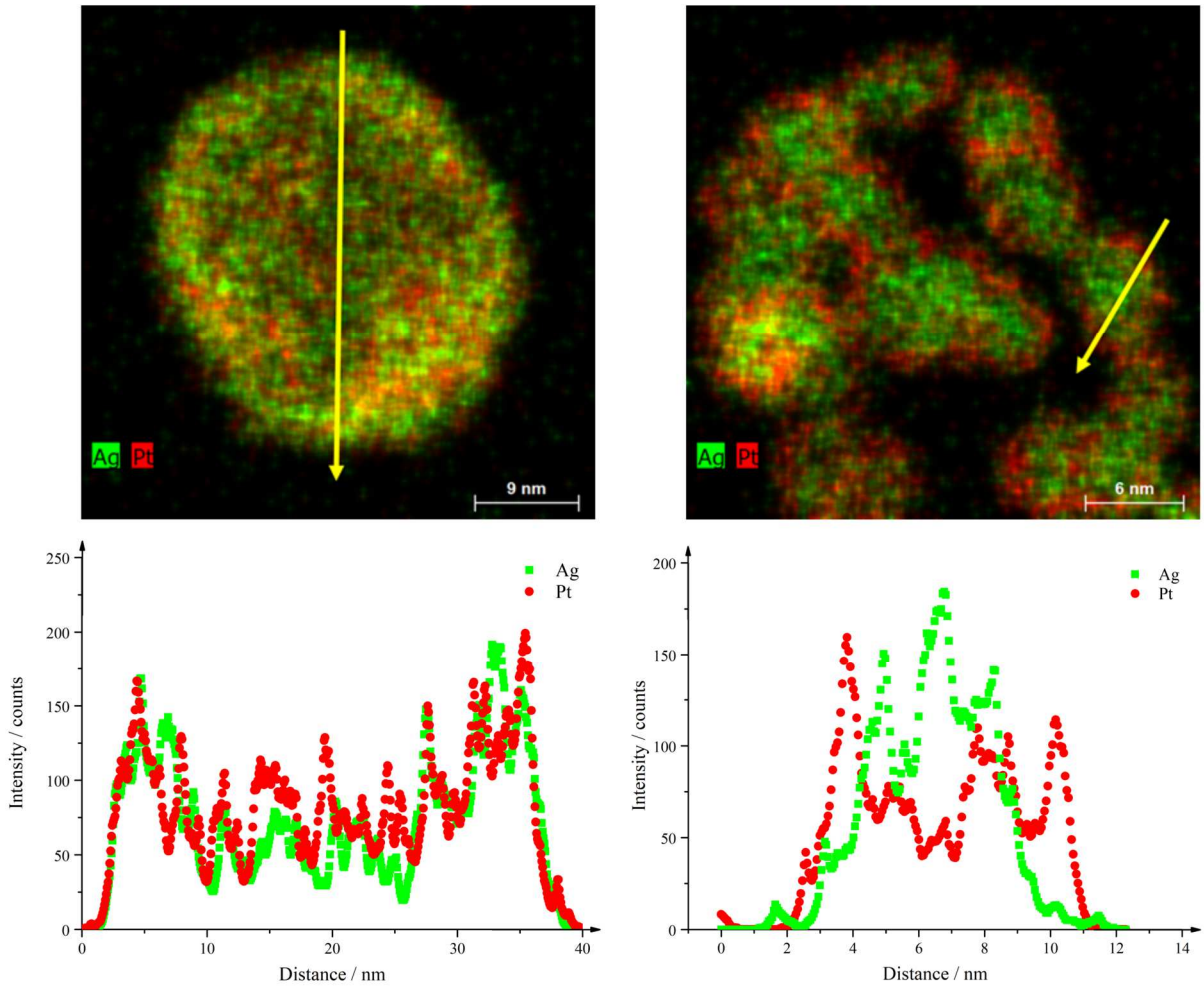

Figure 34: Line scans through the alloyed and core-shell silver-platinum 50:50 nanoparticles prepared by reduction with sodium borohydride at pH 3. The yellow arrows in the EDX maps indicate the scan direction.

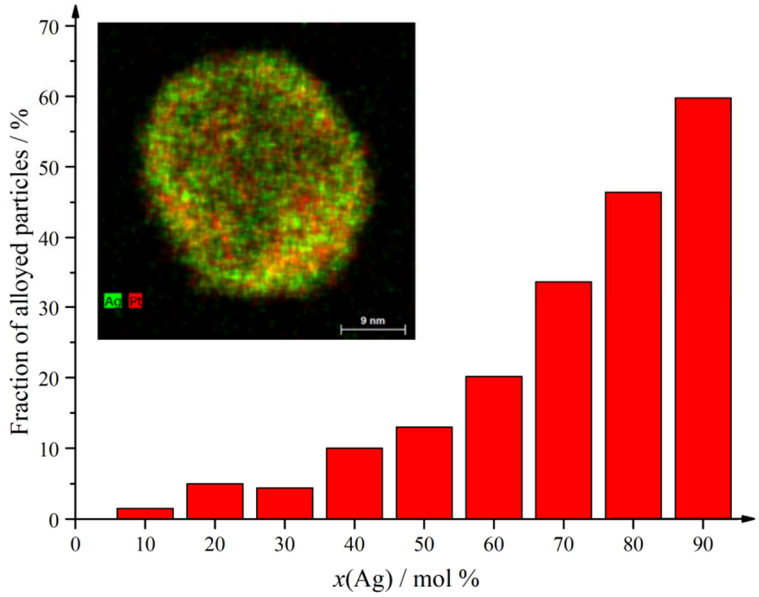

Figure 35: Fraction of alloyed nanoparticles versus the silver content.

The synthesis is fully reproducible and yields comparable nanoparticles as shown in Figure 36 for the silver-platinum composition of 70:30. Several batches were prepared and analyzed. In every sample, alloyed and core-shell nanoparticles are found.

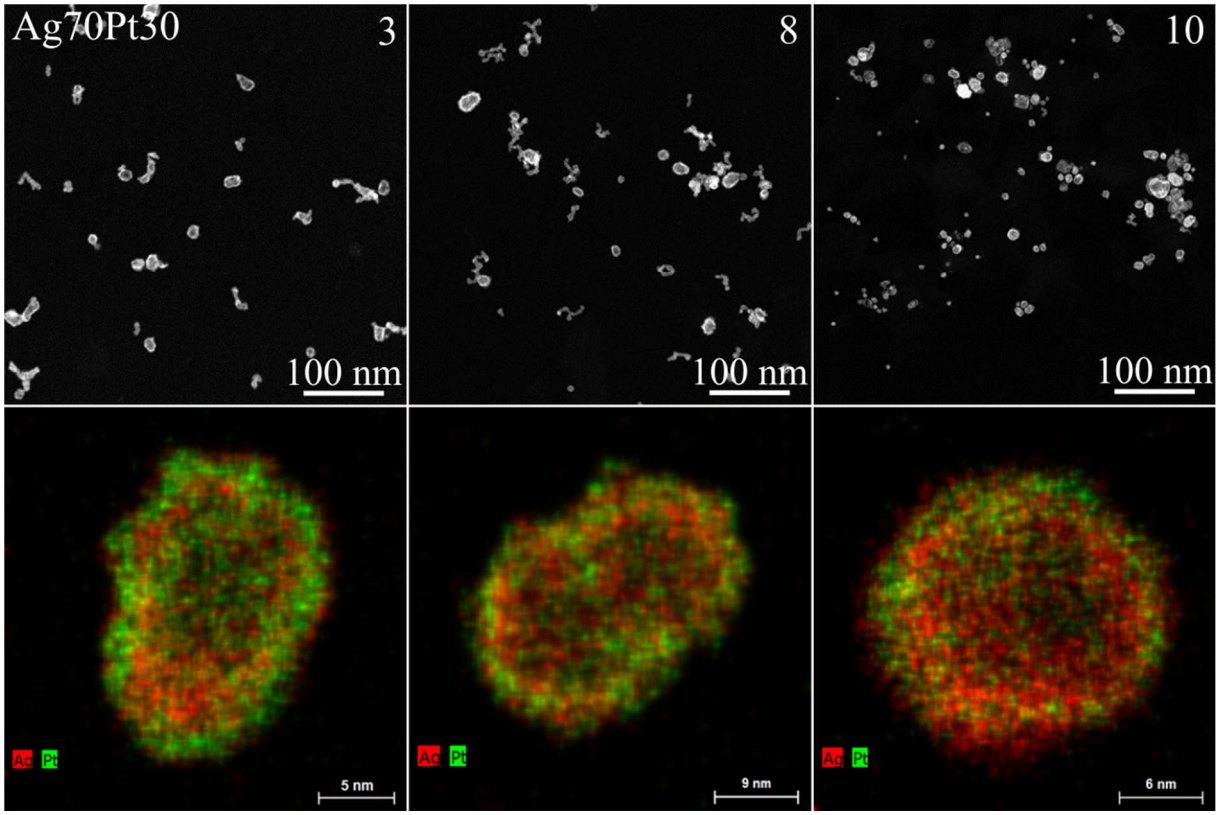

Figure 36: HAADF-STEM images and EDX maps of silver-platinum 70:30 nanoparticles prepared by reduction with sodium borohydride at pH 3. Numbers 3, 8, and 10 depict the batch number.

Atomic absorption spectrometry yields nanoparticles with overall compositions which fit the nominal compositions (Table 7). The stated compositions are averaged over up to five composition determinations. The digest of platinum is performed with *aqua regia* which perturbs the determination and increases the detection limit of platinum to 24 mg/L (24 ppm). The detection limit for silver lies at 0.05 mg/L (50 ppb) in nitric acid.

Table 7: Average compositions of the silver-platinum nanoparticles prepared at pH 3 as obtained by atomic absorption spectrometry.

Nominal composition Ag:Pt	Composition according to AAS / mol%
10:90	11:89
20:80	31:69
30:70	32:68
40:60	47:53
50:50	49:51
60:40	53:47
70:30	64:36
80:20	71:29
90:10	89:11

UV/vis spectroscopy is performed to investigate the surface plasmon resonance of the silver-platinum nanoparticles. In alloyed systems, the absorption maxima lie between the pure metal absorption maxima and show a linear dependence. Therefore, the molar composition of the system can be estimated. The UV/vis spectra in Figure 37 show the SPR of the alloyed silver-platinum particles. A redshift in absorption with higher silver compositions is obtained indicating an alloy character of the nanoparticles. Absorption maxima plotted against the silver composition show a nearly linear dependency. The slight deviation can be attributed to the complexity of the nanoparticles because alloyed and core-shell particles are present. The nanoparticles with a platinum shell show no absorption in the visible, and therefore are difficult to detect and qualify in the UV/vis spectrum in the presence of alloys. On the other hand, if the platinum shell is too thin (< 4 nm), only the silver absorption band should be observable at around 400 nm. The absence of an absorption band at 400 nm underlines the complexity of the system.

Silver-rich compositions show a pronounced absorption band because the number of alloyed particles increases as shown in Figure 35. The absorption at 250 nm decreases and correlates well with the decreasing platinum composition. The colors of the diluted nanoparticle dispersions vary from brown-grey for the platinum-rich compositions to brown-yellow for the silver-rich compositions as shown in Figure 38. The concentrated dispersions are black and not translucent.

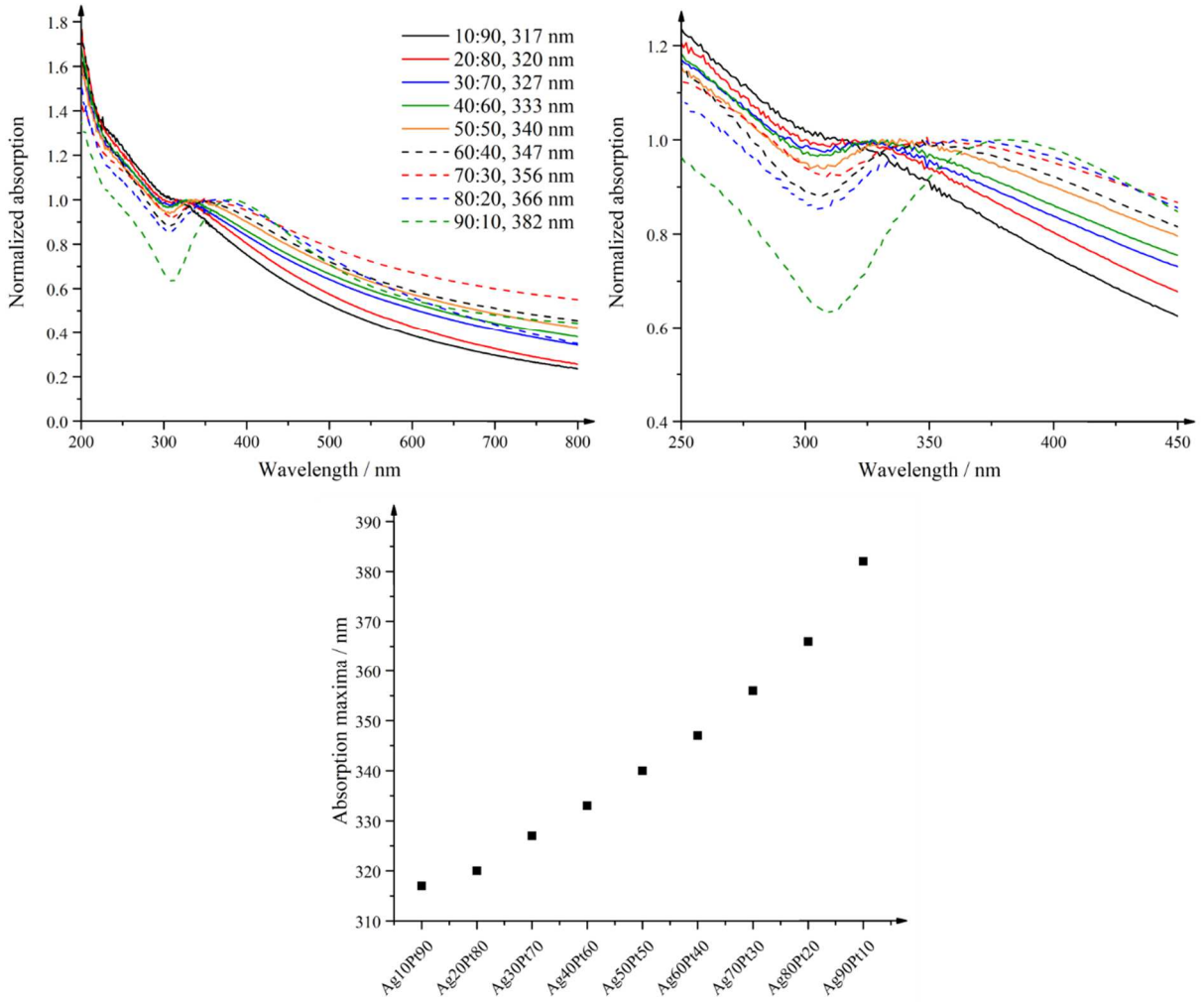

Figure 37: UV/vis spectra of silver-platinum nanoparticles in the composition from 10:90 to 90:10 in 10 mol% steps from reduction by sodium borohydride at pH 3 in comparison (upper left image). The upper right image shows the shift of absorption maxima in a close-up. The lower image depicts the absorption maxima dependent on the composition. Monometallic platinum nanoparticles synthesized by sodium borohydride reduction do not show an absorption maximum above 200 nm. Monometallic silver nanoparticles exhibit an absorption maximum at 406 nm.

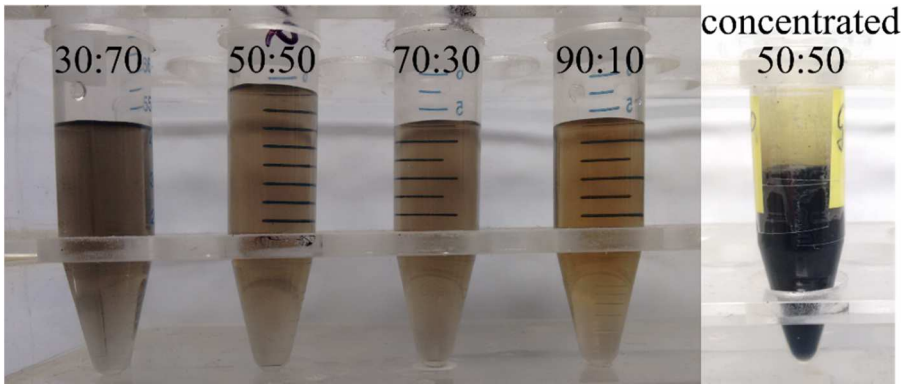

Figure 38: Photographs of diluted and concentrated silver-platinum nanoparticles in the compositions 30:70, 50:50, 70:30, and 90:10.

To exclude the presence of a physical mixture of pure silver and pure platinum nanoparticles, UV/vis measurements are performed with a physical mixture of silver and platinum particles in different molar ratios from 10 mol% silver, 90 mol% platinum to 90 mol% silver, 10 mol% platinum. The compositions are prepared by diluting the concentrated silver and platinum nanoparticle dispersions to a metal concentration of 1 mmol/L. Then, certain amounts of the silver and platinum dispersions are taken to obtain the desired molar ratios (shown in Table 8) and diluted with 1.8 mL Millipore water to a volume of 2 mL.

Table 8: Volumes taken from the monometallic silver and platinum nanoparticle dispersions (c = 1 mmol/L) to obtain the desired molar ratios as a physical mixture.

Molar ratio Ag:Pt	V(Ag) / µL	V(Pt) / µL
0:100	0	200
10:90	20	180
20:80	40	160
30:70	60	140
40:60	80	120
50:50	100	100
60:40	120	80
70:30	140	60
80:20	160	40
90:10	180	20
100:0	200	0

The UV/vis spectra (Fig. 39) show an evolution of the silver surface plasmon absorption band with increasing silver molar ratios. At first, the absorption band is broadened as seen for the ratios 20:80 or 30:70, but becomes narrow and pronounced with higher silver molar ratios. The absorption maximum lies always at 386 nm and does not shift with varying molar ratios. The jump of the absorption curve at 350 nm results from the switching from the tungsten-halogen lamp (visible light) to the deuterium lamp (UV light) which was not subtracted properly after the background measurement. Remarkably, the absorption spectrum of pure platinum nanoparticles prepared by sodium borohydride synthesis differs from the absorption spectrum of platinum nanoparticles prepared by trisodium citrate and tannic acid reduction (Fig. 17). This shape is also described in the literature.[185-186] The reason might be the different reduction and capping species present. In the trisodium citrate and tannic acid synthesis, both reductants also serve as capping agents and partly remain on the nanoparticle surface even after

refunctionalization with PVP. In the sodium borohydride synthesis, trisodium citrate is used as the first reductant and mostly replaced by PVP in a refunctionalization. It is known from literature[108] that capping agents change the electronic environment of nanoparticles, and therefore affect the surface plasmon resonance by influencing the oscillation frequency of conduction band electrons on the nanoparticle surface. Another reason might be the size difference due to different synthesis methods which also affects the SPR. Larger particles show absorptions which are redshifted compared to smaller particles of the same element. Particles obtained from the trisodium citrate and tannic acid synthesis are around 30 nm in diameter, whereas the particles synthesized by sodium borohydride reduction have diameters of 10 nm average.

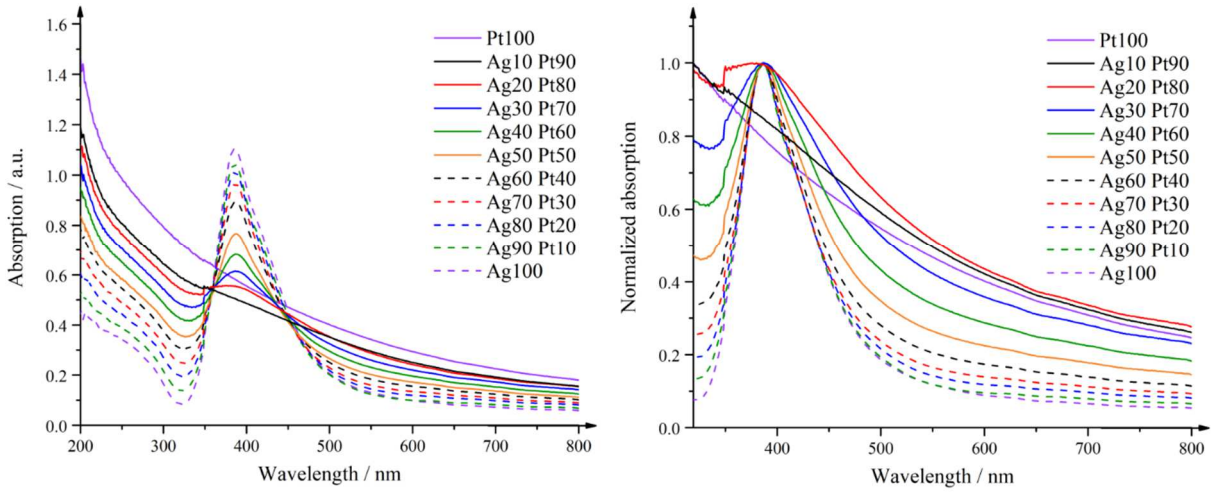

Figure 39: UV/vis spectra of physical mixtures of silver and platinum nanoparticles in different composition from 10:90 to 90:10 in 10 mol% steps. Left: not normalized, right: normalized to the absorption maximum.

The colors of the physical mixtures are depicted in Figure 40. They differ from those of the alloyed nanoparticles as observable from the 90:10 composition of the alloyed particles where the color has a brown-yellow appearance, whereas the physical mixture of the molar composition 90:10 shows a yellow color.

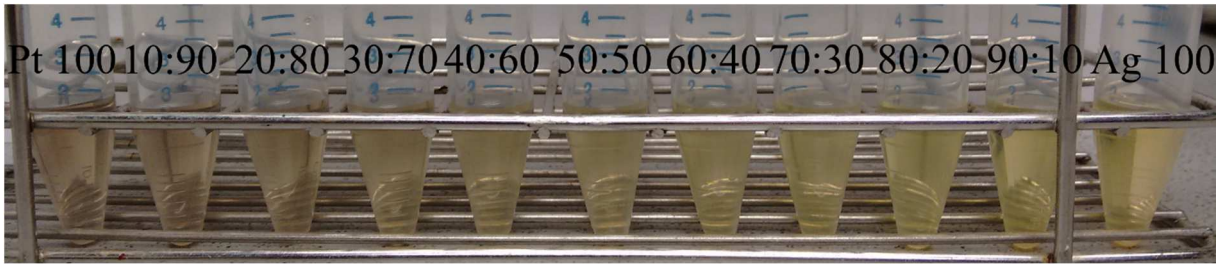

Figure 40: Photographs of diluted silver and platinum nanoparticles as physical mixtures in the molar ratios of 10:90 to 90:10 in steps of 10 mol% together with pure silver and pure platinum nanoparticles.

For the characterization of the crystallographic properties, powder X-ray diffraction is used. All nine compositions of the bimetallic silver-platinum nanoparticles are measured in the presence of lanthanum hexaboride as an internal standard for the determination of lattice parameters, microstrains and crystallite sizes. Prior to every measurement, the samples are lyophilized (Fig. 41 left). The powder shows electrostatic charging, and therefore is handled with an antistatic wrist strap. For each measurement, the powder is dispersed on a silicon sample holder with ethanol for immobilization and to prevent sample displacement (Fig. 41 right). The silicon sample holder is polished to have the (911) facet on the surface to eliminate diffraction of X-rays in the measured angle range.

Figure 41: Lyophilized silver-platinum nanoparticles (left) and ethanol-dispersed silver-platinum powder on a silicon sample holder (right). Scale bar unit in centimeters.

The powder diffraction patterns (Fig. 42) are characteristic for a face-centered cubic (fcc) phase and show no formation of other phases. The sharp reflexes marked with an asterisk originate from lanthanum hexaboride which was mixed with the sample powder. Both, silver and platinum crystallize in the same crystal structure with the space group $Fm\bar{3}m$. A shift in the reflex position to smaller angles with increasing silver composition means an expansion in the lattice parameters because silver has larger lattice parameters (a = 4.0862 Å) than platinum (a = 3.923 Å). This shift indicates the presence of alloys. Figure 43 depicts the reflex position of the silver-platinum 50:50 composition which lies directly in between the literature reflexes of silver (PDF 00-004-0783[132]) and platinum (PDF 00-001-1194[131]) indicating an alloy character.[33,138-140] The reflexes show broadening because of nano crystallinity. Small crystallites of just a few nanometers lead to broader diffraction reflexes because of natural lattice defects. These defects affect the reflex shape through the limited statistical probability of extinction of not exactly constructive interfering waves because of the small number of lattice planes.[187] EDX maps show the presence of core-shell particles. Those are not detected by

X-ray diffraction because the platinum shell is roughly 1 nm thick and lies under the detection limit of powder X-ray diffraction.[188] The reflex broadening complicates the distinguishing of silver cores as well. Those are small with approximate sizes of 4 nm and can be overlapping with the reflexes for the nanoalloys.

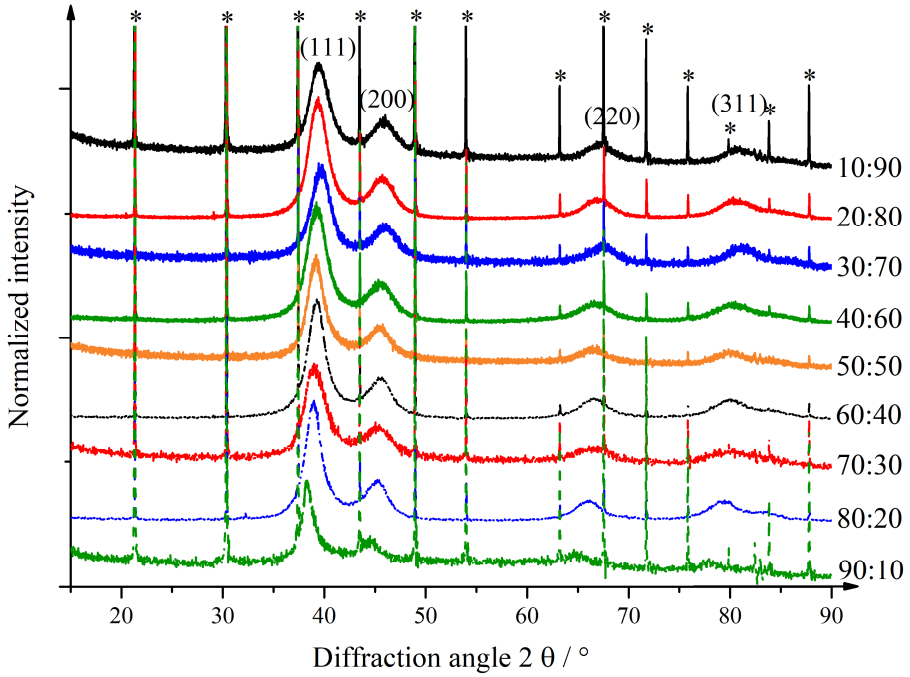

Figure 42: Powder diffraction patterns of the silver-platinum nanoparticles synthesizes by sodium borohydride reduction at pH 3 in the compositions Ag:Pt 10:90 to 90:10 in 10 mol% steps. The asterisks mark the lanthanum hexaboride reflexes (PDF 00-034-0427[189]).

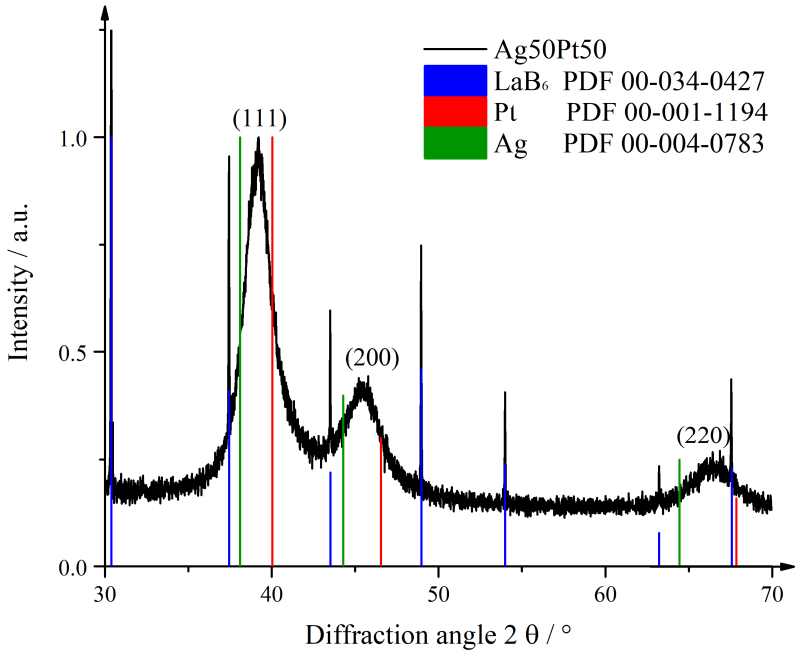

Figure 43: Diffraction pattern of the silver-platinum 50:50 composition compared to the patterns of pure silver (PDF 00-004-0783[132]) and pure platinum (PDF 00-001-1194[131]).

Table 9 summarizes the crystallographic properties of the bimetallic silver-platinum samples. Because PXRD measurements were performed with only one sample per composition, the compositions according to AAS measurements are stated. The actual molar composition affects the crystallographic properties. From the values of the lattice parameter *a* as well as from the diffraction patterns itself is observable that the unit cell expands with the increasing silver composition indicating the existence of alloys in the whole composition range. Consequently, the cell volume *V* increases as well. The crystallize size *D* varies from 5.4 nm to 8.5 nm and underlines the assumption of nano crystallinity because of reflex broadening. No trend is observable which would indicate bigger crystallites with an increasing silver composition. Comparing crystallite sizes and nanoparticle diameters (Fig. 44) it is visible that the crystallite sizes are smaller than the diameters obtained by differential centrifugal sedimentation. This means that the particles are polycrystalline which is also observable from HAADF-STEM images. The microstrain ε slightly increases from 0.85 % for silver-platinum 05:95 to 1.03 % for silver-platinum 47:53 and overall decreases to 0.22 % for the composition 82:18. An outlier with 1.24 % for the composition 60:40 is observed. In general, the microstrain within a unit cell increases after the incorporation of foreign atoms because of the slightly different atomic radii.

Table 9: Crystallographic properties obtained from Rietveld refinement of silver-platinum nanoparticles in different compositions prepared by reduction with sodium borohydride at pH 3. The values in parenthesis indicate the error for the last digit.

Composition according to AAS Ag:Pt / mol%	Lattice parameter *a* / Å	Cell volume *V* / Å^3	Crystallite size *D* / nm	Microstrain ε / %
05:95	3.9437(2)	61.33(1)	5.4(1)	0.85(2)
23:77	3.9323(2)	60.80(1)	5.5(1)	0.87(2)
31:69	3.9583(1)	62.02(1)	6.2(1)	0.93(2)
43:57	3.9793(2)	63.01(1)	7.3(3)	0.84(2)
47:53	3.9706(2)	62.60(1)	6.6(1)	1.03(1)
53:47	3.9757(1)	62.84(1)	6.4(1)	0.82(1)
60:40	3.9876(3)	63.41(2)	8.5(6)	1.24(3)
71:29	4.0048(1)	64.23(2)	6.3(1)	0.73(1)
82:18	4.0571(4)	66.78(2)	6.7(2)	0.22(4)

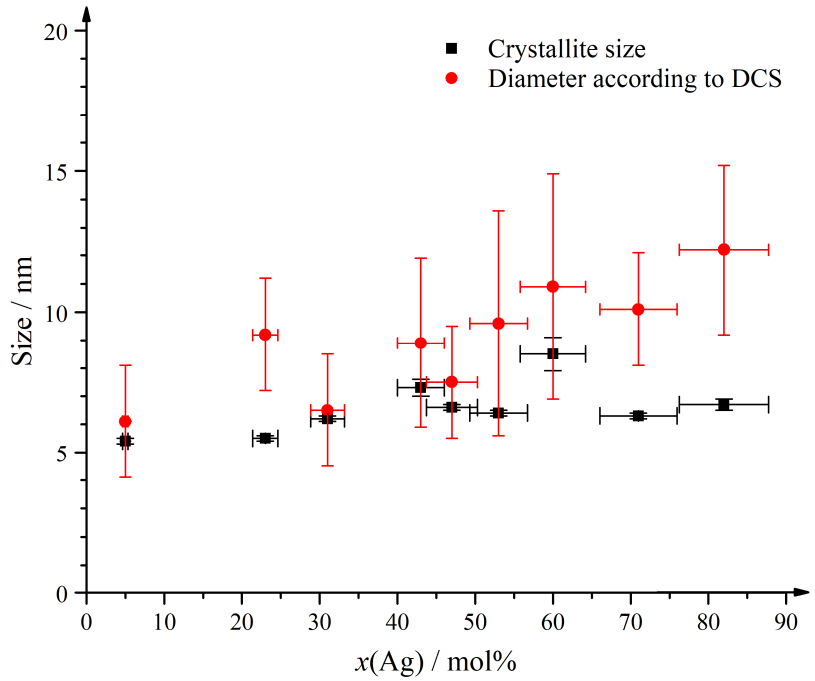

Figure 44: Crystallite size versus nanoparticle diameter of the silver-platinum particles in different compositions obtained by reduction with sodium borohydride at pH 3.

As mentioned before, the lattice parameter *a* increases with the silver composition. Vegard's law[142-143] describes the lattice parameter variation as a function of composition for alloyed systems. Equation 13 depicts the calculation of the theoretical lattice parameter a_M for a mixed crystal with the molar compositions *x* for the two species A and B and their corresponding lattice parameters *a*. In an ideal system, a linear dependency is obtained.

$$a_M = x_A a_A + x_B a_B \tag{13}$$

Figure 45 shows the theoretical versus the real values for the lattice parameters obtained from powder X-ray diffraction. The theoretical values are obtained from calculations using lattice parameters of bulk silver and bulk platinum. A linear dependency is received which lies overall slightly beneath the theoretical values. Similar results were also reported by Peng et al.[50] Reports in the literature[163-166] show that metallic nanoparticles of silver, gold, and platinum with sizes of 6 nm may have lattice parameters which deviate from the bulk parameters up to 0.5 %. The silver-platinum system overall follows Vegard' law, but shows contraction of lattice parameters compared to the bulk. This may be caused by the size of the nanoparticles. Small crystallites lead to a unit cell contraction. The lattice parameter deviation of the silver-platinum nanoparticles compared to Vegard's law is between 0.03 % and 0.9 % which lies in the reported deviation range of 0.5 %.

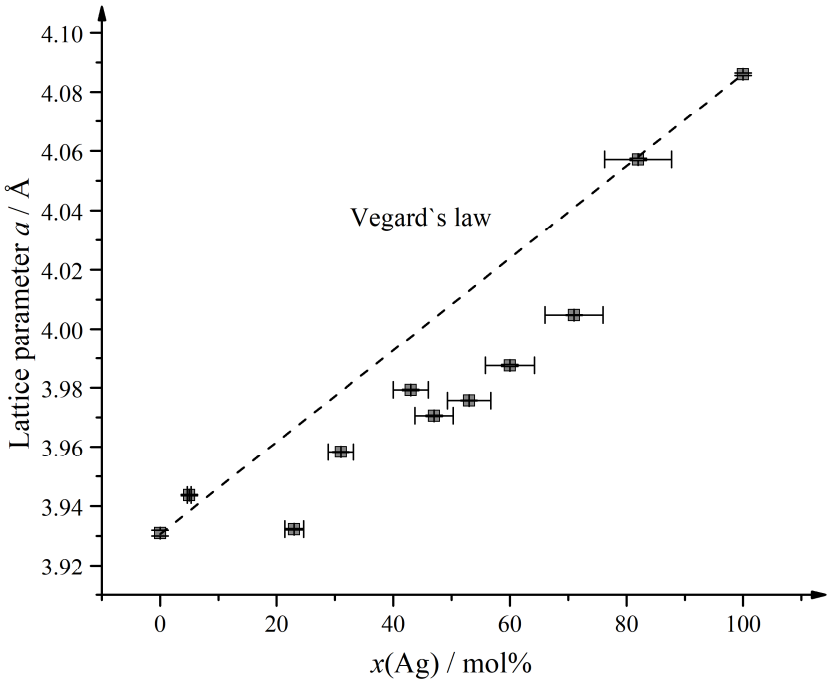

Figure 45: Lattice parameters calculated for the silver-platinum nanoparticles as a function of composition compared to Vegard's law and the reference values for bulk silver[132] and platinum.[131] Please note that the errors of the lattice parameters are very small.

In summary, the synthesis by sodium borohydride reduction at pH 3 yields spherical nanoparticles with diameters between 6 nm and 9 nm. The goal of synthesizing nanoparticles in the size of 10 nm is, consequently, reached. EDX maps show two kinds of nanoparticles that can be obtained: hollow alloyed particles and dense core-shell particles with a silver core and a platinum shell. The hollow alloyed nanoparticles are the product of a galvanic replacement reaction. Their amount increases with the silver composition. The average composition according to AAS matches the nominal composition. The UV/vis shows a redshift in surface plasmon resonance with the increasing silver content underlining the alloy character of the nanoparticles. The occurrence of a physical mixture of silver and platinum nanoparticles is excluded by UV/vis spectroscopy. Powder X-ray diffraction shows an increase in the lattice parameters with higher silver contents which follows Vegard's law. The actual values for the lattice parameters are lying slightly underneath the theoretical values. These findings corroborate the presence of a silver-platinum nanoalloy. The platinum shell of the core-shell nanoparticles is too thin to be detected by X-ray diffraction. Because the crystallite sizes of the nanoparticles are smaller than the diameters, polycrystallinity of the alloys is concluded.

5.1.3 Synthesis by sodium borohydride reduction at pH 10

The variation of the pH from 3 to 10 is to destabilize the hexachloridoplatinate by a partly exchange of chloride ions by hydroxide ions:

$$[PtCl_6]^{2-} + OH^- \rightarrow [PtCl_5(OH)]^{2-} + Cl^-$$

The idea of the destabilization of the platinum precursor is to enhance its reduction rate and prevent the galvanic exchange reaction to obtain core-shell nanoparticles. The same mechanism was recently reported for a silver-gold, silver-platinum, and silver-palladium core-shell system with a nano prismatic morphology.[54] The disadvantage of working at high pH values is the increased stability of the applied reducing agent sodium borohydride. Table 5 in section 5.1.2 shows the half-life of sodium borohydride depending on the pH and the temperature. At pH 10 and at room temperature, the half-life is above 60 minutes which drastically increases the reaction time of the synthesis. To avoid the high reaction time, the reaction mixture is heated to 65 °C which decreases the half-life of sodium borohydride to 3 minutes. The compositions Ag:Pt of 10:90, 30:70, 50:50, 70:30, and 90:10 are prepared and characterized by DCS, UV/vis, HAADF-STEM, and EDX. The size distributions obtained from differential centrifugal sedimentation are shown in Figure 46. The graphs on the right depict the whole measured range from 3 nm to 100 nm. The graphs on the left show the size range from 3 nm to 40 nm for a better overview. The size distributions are narrow and exhibit only one signal indicating monodispersity. The sizes lie between 8 nm and 12 nm as can be found in Table 10.

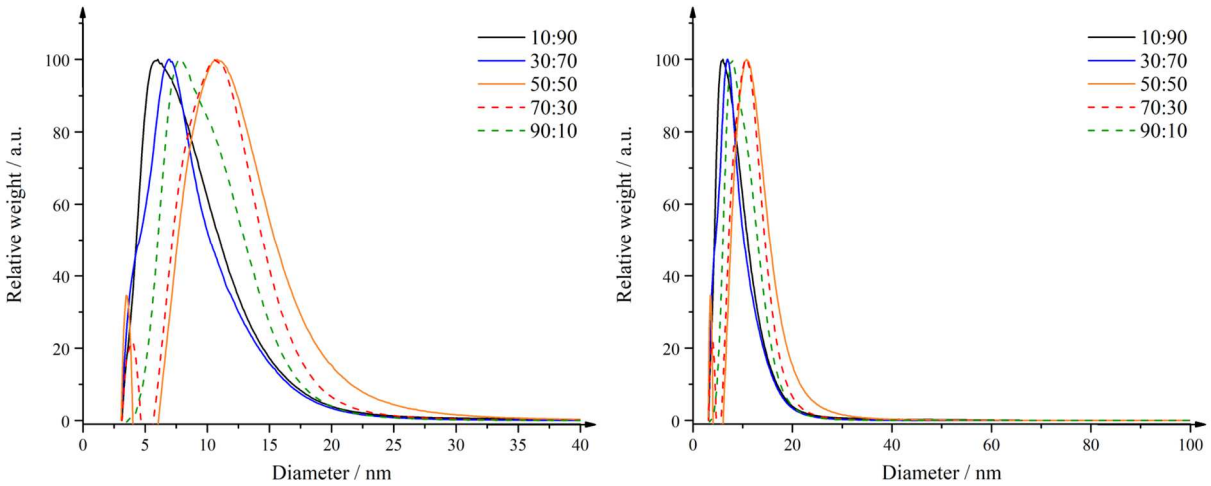

Figure 46: Representative size distributions of silver-platinum nanoparticles by reduction with sodium borohydride at pH 10 in the compositions of 10:90 to 90:10 in steps of 20 mol% as obtained by DCS.

Histograms obtained from HAADF-STEM micrographs reveal sizes between 6 nm and 11 nm with a monodisperse size distribution (Fig. 47). The width of the size distribution decreases with increasing silver content. The high numbers of 3 nm particles in the silver-platinum 10:90 and 30:70 compositions are attributed to platinum-rich particles as is seen in Figures 48 and 49.

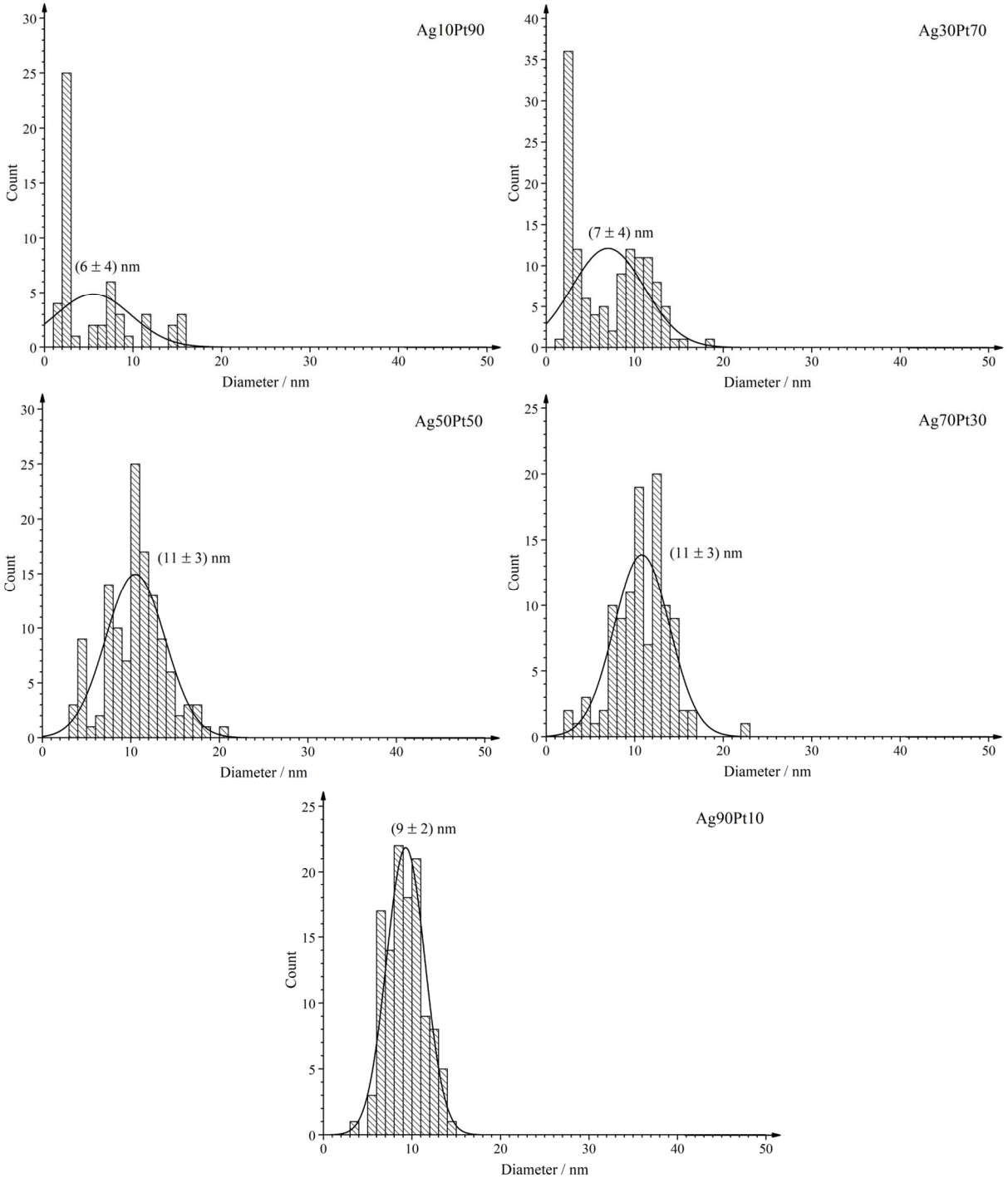

Figure 47: Particle size distributions of silver-platinum nanoparticles in the compositions of 10:90, 30:70, 50:50, 70:30, and 90:10 prepared by reduction with sodium borohydride at pH 10 as measured by HAADF-STEM.

Sizes obtained from DCS are comparable to the sizes obtained from HAADF-STEM (Table 10). Both methods show a high monodispersity with particles in the range of approximately 10 nm which is a relevant size for biological studies as they can be taken up by cells or bacteria.[190]

Table 10: Representative size distributions of silver-platinum nanoparticles by reduction with sodium borohydride at pH 10 in the compositions of 10:90 to 90:10 in steps of 20 mol% as obtained by DCS and HAADF-STEM and their corresponding standard deviations.

Composition Ag:Pt	Size as obtained by DCS / nm	Size as obtained by HAADF-STEM / nm
10:90	8 ± 4	6 ± 4
30:70	8 ± 4	7 ± 4
50:50	12 ± 4	11 ± 3
70:30	11 ± 3	11 ± 3
90:10	10 ± 4	9 ± 2

High-angle annular dark field STEM images show spherical nanoparticles (Fig. 48). In the compositions silver-platinum 10:90 and 30:70, a high number of particles with sizes of 3 nm is observed. Those particles consist mostly of platinum as is visible from EDX maps. Lots of publications report the formation of 3 nm small platinum nanoparticles beside bigger particles obtained by various synthesis pathways like sonochemical reduction,[191] standard wet chemical reduction[192] or laser ablation.[193] With the decreasing platinum amount, the nanoparticle size distributions become narrower with less particles of 3 nm diameter. Throughout the samples, a small number of still hollow particles is observed. The nanoparticles in the silver-platinum 70:30 composition show half-moon shaped particles beside spherical ones. EDX maps (Fig. 49) reveal the element distribution within the nanoparticles. For the Ag:Pt 10:90 composition a hollow particle is depicted which shows randomly distributed silver and platinum atoms speaking for an alloy. The HAADF-STEM image shows a particle that appears to be single crystalline. The 30:70 composition shows a single twinned core-shell particle with branched, small, single crystalline platinum particles. The compositions 50:50 and 70:30 imply the presence of aggregated, poly crystalline silver-core platinum-shell particles or alloys with a gradient element distribution, whereas the 90:10 sample exhibits a perfect core-shell structure which appears single crystalline. The platinum shell thickness lies between 1 nm and 2 nm.

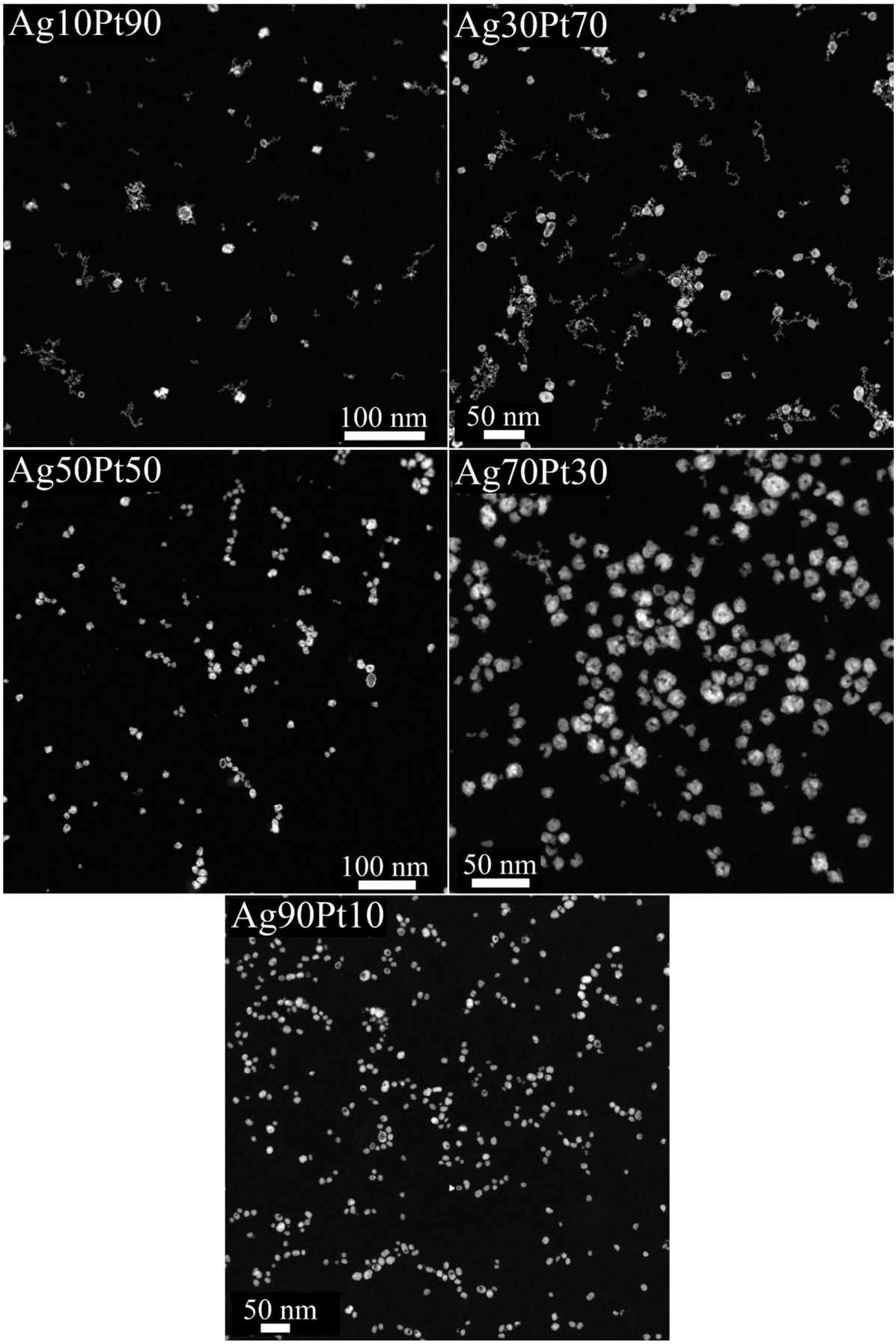

Figure 48: HAADF-STEM images of silver-platinum nanoparticles by reduction with sodium borohydride at pH 10 in the compositions of 10:90 to 90:10 in steps of 20 mol%.

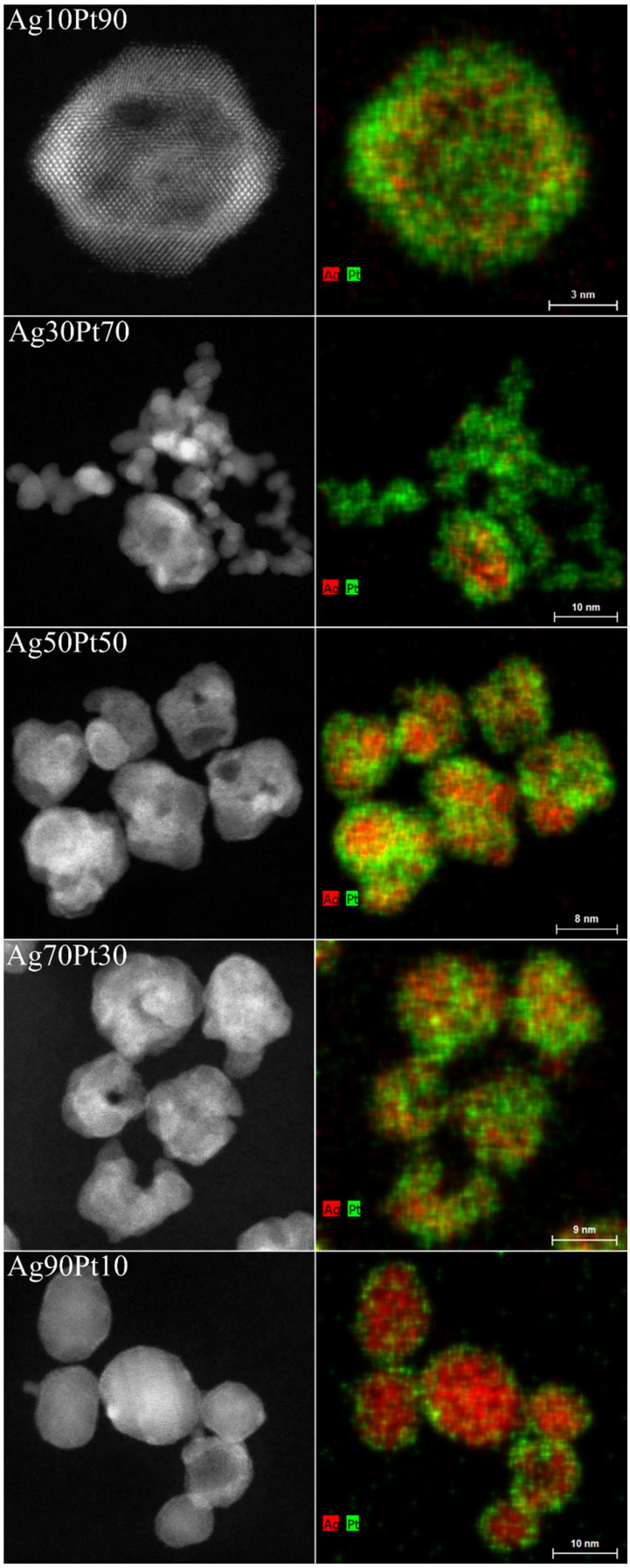

Figure 49: High-angle annular dark field STEM images (left) and EDX maps (right) of silver-platinum nanoparticles prepared by reduction with sodium borohydride at pH 10.

The quantitative EDX analysis (Table 11) shows the compositions in atom percent. The nominal compositions Ag:Pt 30:70 and 70:30 show major deviations in their actual compositions from the intended ones. The reason is that only the depicted area is analyzed quantitatively and sample inhomogeneities have a high impact on the results. The Ag:Pt 30:70 sample shows silver-platinum and pure platinum particles. Therefore, the platinum amount dominated the outcome.

Table 11: Quantitative EDX analysis of silver-platinum nanoparticles prepared by reduction with sodium borohydride at pH 10.

Composition Ag:Pt	Atomic ratio according to EDX analysis / at%
10:90	05:95
30:70	16:84
50:50	48:52
70:30	58:42
90:10	89:11

The UV/vis spectra (Fig. 50) show an evolution of a shoulder with increasing silver content which results in a pronounced absorption band for the silver-platinum 90:10 composition. The platinum-rich composition Ag:Pt 10:90 has no shoulder. The absorption spectrum resembles the UV/vis spectrum of pure platinum nanoparticles as discussed in section 5.1.2, Figure 39. The samples 30:70, 50;50, and 70:30 exhibit nearly the same absorption maxima which implies the presence of alloyed particles with similar compositions. The silver-platinum 90:10 sample shows an absorption at 387 nm which corresponds to the absorption of silver nanoparticles with a size of approximately 7 nm. This is already described in section 5.1.2, Figure 39. The absorption band shows a slight broadening which can be attributed to the formation of a certain number of alloyed particles. No absorption of the platinum shell is observed because the shell is rather thin, and the platinum absorption occurs under 200 nm which lies beyond the possible measuring range of the used UV/vis spectrophotometer. Comparing the UV/vis spectra of alloyed silver-platinum nanoparticles with a composition of 90:10 to core-shell particles of the same composition, a difference is observed. The absorption band of the core-shell particles is more pronounced than the absorption band of the nanoalloys. Photographs of the freshly prepared nanoparticle dispersions (Fig. 51) show different colors that appear brown in platinum-rich compositions shifting to dark yellow in silver-rich compositions.

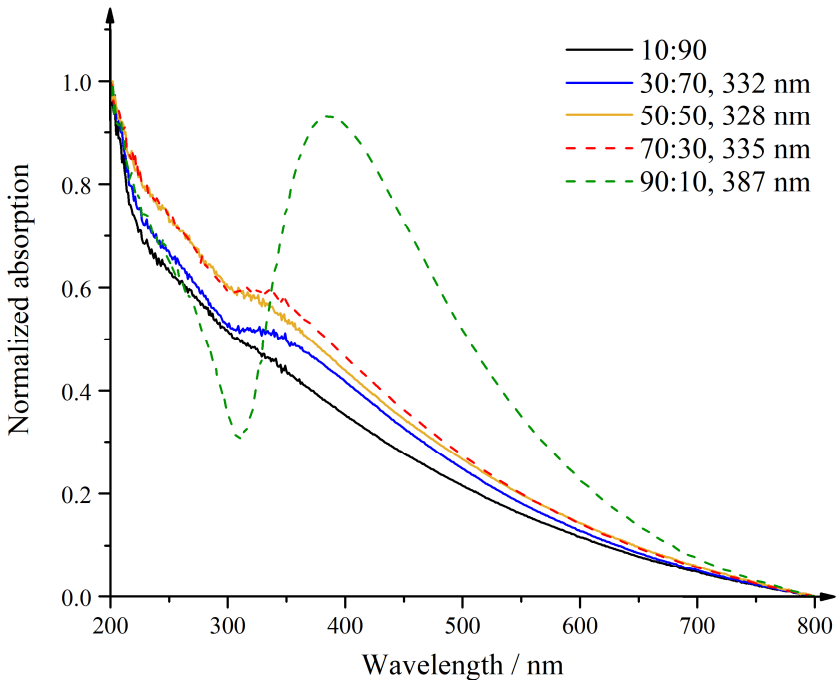

Figure 50: UV/vis spectra of silver-platinum nanoparticles in the composition from 10:90 to 90:10 in 20 mol% steps obtained from reduction by sodium borohydride at pH 10. An increase in absorption intensity and an overall redshift with increasing silver composition is observed.

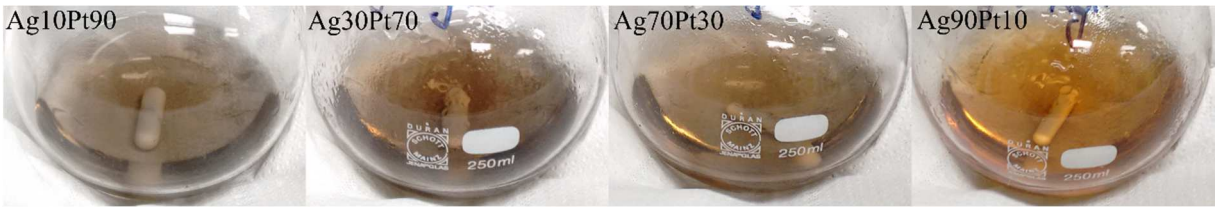

Figure 51: Photographs of silver-platinum nanoparticles in the compositions Ag:Pt 10:90, 30:70, 70:30, and 90:10 directly after synthesis by reduction with sodium borohydride at pH 10.

In summary, the synthesis by sodium borohydride reduction at pH 10 yields spherical nanoparticles with diameters between 8 nm and 12 nm according to DCS and 6 nm to 11 nm according to HAADF-STEM. The goal of synthesizing nanoparticles in the size of 10 nm is, consequently, reached. Platinum-rich samples show the presence of pure platinum nanoparticles. Overall, core-shell particles are obtained between which occasionally a few single hollow alloyed particles appear. While the Ag:Pt 50:50 and 70:30 compositions appear to consist of aggregated core-shell particles or alloyed particles with a gradient structure, the 90:10 sample is well dispersed and exhibits clearly visible boundaries between the silver core and the platinum shell. The UV/vis spectroscopy shows a characteristic silver absorption band at 387 nm for the 90:10 sample indicating core-shell particles with a silver core which is underlined by the EDX maps.

5.1.4 Conclusion on silver-platinum nanoparticles

Some questions were posed in the beginning which can be answered now. The first one was whether it is possible to synthesize alloyed silver-platinum nanoparticles in the compositions from 10:90 to 90:10 in steps of 10 mol% despite their large miscibility gap. The answer is yes, it is possible. Even the variation of reducing agents like a mixture of trisodium citrate and tannic acid or sodium borohydride, and the pH change from 3 to 10 yield alloyed silver-platinum nanoparticles. Another question was raised about the structure of the nanoparticles. Two different nanoparticles species can be obtained by the adjustment of reaction conditions like pH or temperature. Hollow alloyed silver-platinum nanoparticles are received at pH 3 and at 4 °C together with dense silver-core, platinum-shell particles. The number of hollow alloyed nanoparticles increases with the silver composition, whereas the number of the core-shell particles increases with the platinum composition. At pH 10 and at 65 °C, the element distribution depends on the composition. This time, only a few stray hollow particles are obtained. Silver-poor compositions 10:90 and 30:70 contain a mixture of bimetallic silver-platinum and pure platinum particles. The silver-platinum 50:50 and 70:30 compositions are dense particles with a rough surface which show a gradient element distribution or aggregated core-shell nanoparticles. The silver-platinum 90:10 composition particles have a smooth surface and a core-shell structure with a silver core and a platinum shell. The element distribution within the nanoparticles is tunable by the reaction conditions.

5.2 Characterization of silver-platinum nanoclusters

For the synthesis of silver-platinum nanoclusters capped with 11-mercaptoundecanoic acid (11-MUA), the work of Ristig et al.[24] is used with slight modifications. The nanoclusters are prepared in the compositions silver-platinum 10:90 to 90:10 in steps of 10 mol%. As comparison, pure silver and pure platinum nanoclusters are synthesized with the same method. In this case, 11-mercaptoundecanoic acid may serve not only as capping agent, but as reductant as well.[194] The characterization is performed with differential centrifugal sedimentation, UV/vis spectroscopy, transmission electron microscopy, fluorescence spectroscopy, and Zeta potential measurement. Size distributions obtained from DCS measurements show one peak with a diameter of (1.7 ± 0.4) nm for platinum nanoclusters and two peaks with sizes of (4.3 ± 1.1) nm and (22 ± 9) nm for silver nanoclusters (Fig. 52). The peak at 22 nm can be attributed to agglomerates because the dispersion is colorless. If 22 nm big silver nanoparticles were present, the dispersion would be yellow which is not the case. The platinum nanoclusters show an overall narrow size distribution and smaller diameters than the silver nanoclusters. This can be explained by the reduction velocities of silver and platinum. The reduction takes place under basic conditions which destabilize the hexachloridoplatinate complex and allow a fast reduction of platinum. This leads to a formation of a great amount of platinum seeds that result in smaller particles. On the other hand, silver is reduced slower which leads to less seeds and bigger particles. Silver-platinum clusters in different compositions also show a formation of agglomerates which is more distinct in silver-rich clusters (Fig. 53). The diameters of the bimetallic nanoclusters lie between (2.1 ± 0.7) nm and (3.2 ± 0.8) nm as summarized in Table 12. The size increases with the silver composition.

The exact compositions could not be determined using AAS. The reason is that although the clusters are purified from excess reductant, excess capping agent (11-MUA) cannot be removed completely from the dispersion. The purification is performed by precipitation of 11-MUA with hydrochloric acid and subsequent centrifugation which does not remove redundant 11-MUA. After the centrifugation and redispersion of the clusters in ethanol, excess capping agent remains in the samples. During sample preparation for AAS using *aqua regia*, a yellow precipitate is observed which does not dissolve after addition of further *aqua regia*. This precipitate might be silver hexachloridoplatinate.[113]

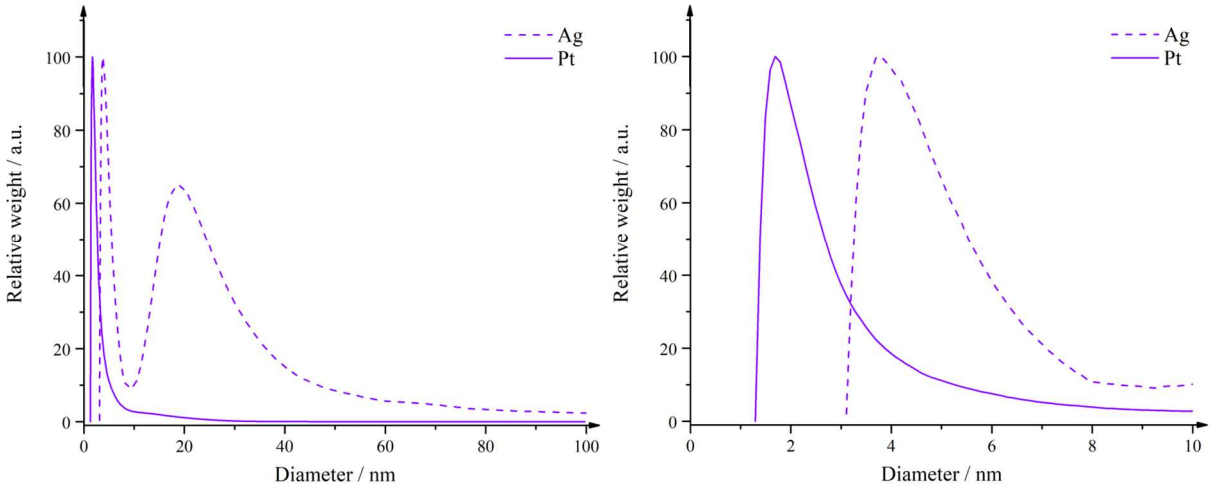

Figure 52: Size distribution of silver and platinum nanoclusters as obtained by DCS. The left side shows the whole measured range, the right side depicts the enlargement of the size distribution of cluster sized particles.

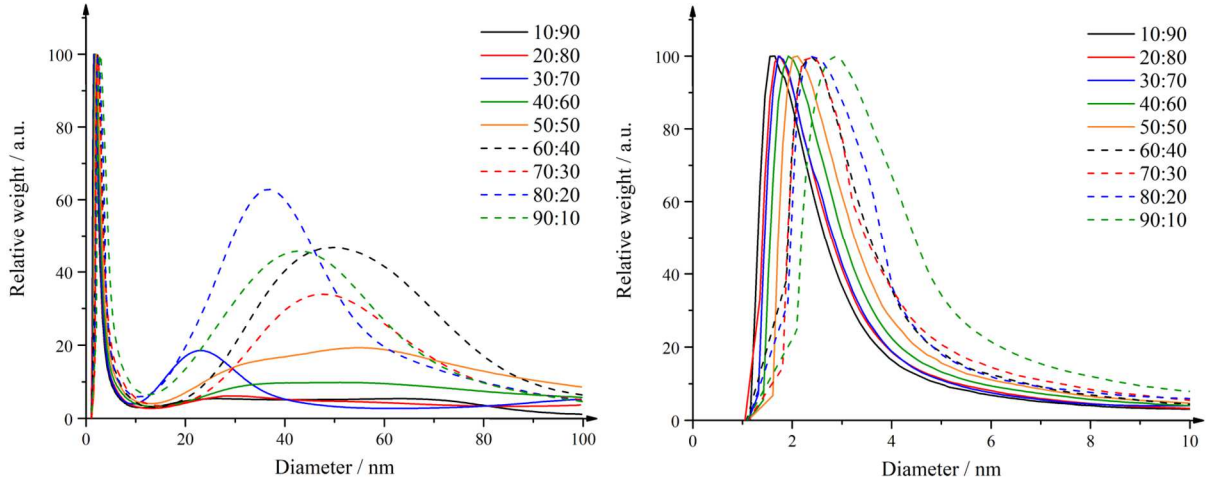

Figure 53: Size distribution of silver-platinum nanoclusters as obtained by DCS. The left side shows the whole measured range, the right side depicts the enlargement of the size distribution of cluster sized particles.

Table 12: Size distributions of silver, platinum, and silver-platinum nanoclusters in the compositions of 10:90 to 90:10 in steps of 10 mol% as obtained by DCS and their corresponding standard deviations. The sizes of the agglomerates are not stated.

Composition Ag:Pt	Size as obtained by DCS / nm
0:100	1.7 ± 0.4
10:90	2.1 ± 0.7
20:80	2.2 ± 0.8
30:70	2.2 ± 0.7
40:60	2.3 ± 0.7
50:50	2.5 ± 0.7
60:40	2.6 ± 0.6
70:30	2.7 ± 0.7
80:20	2.8 ± 0.8
90:10	3.2 ± 0.8
100:0	4.3 ± 1.1

The Zeta potential measured in ethanol at pH 8 lies between (4 ± 17) mV and (11 ± 12) mV. Under basic conditions, the carboxyl group of 11-MUA is deprotonated and a negative Zeta potential is expected. In ethanol, no deprotonation takes place and the Zeta potential is expected to be neutral. A sterical stabilization is concluded (Fig. 54 a). Because of the excess application of 11-MUA to the reaction mixture, a depletion flocculation might occur which would lead to the formation of agglomerates as observed in DCS measurements. Furthermore, carboxylic acids tend to form intermolecular hydrogen bonds which might decrease the colloidal stability and enable agglomeration. Those hydrogen bonds can be dimers or catemers[195] (Fig. 54 b).

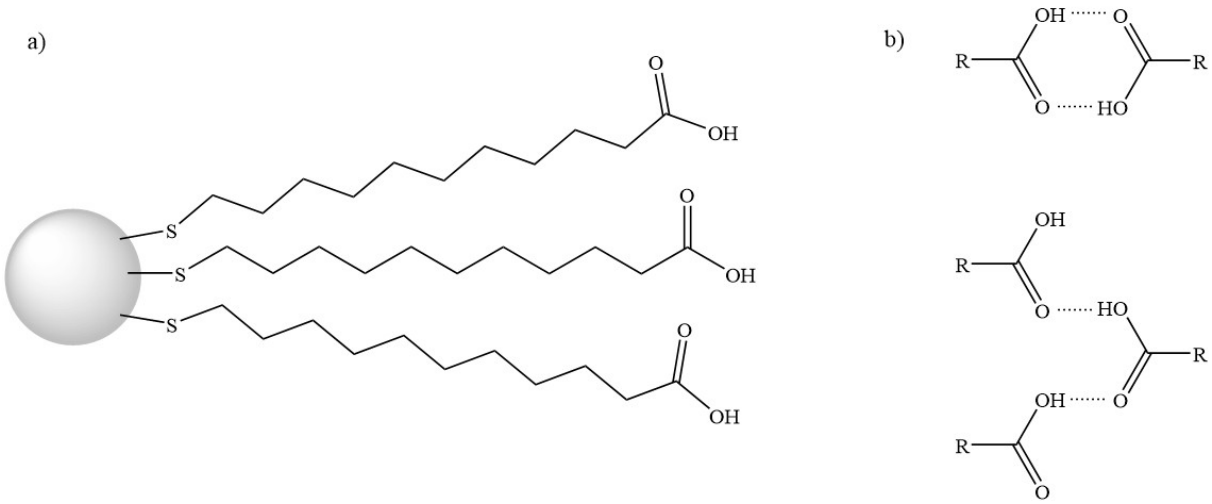

Figure 54: a) Covalently bound 11-mercaptoundecanoic acid to the nanocluster resulting in a steric stabilization. b) Possible synthons in hydrogen bond formation of carboxyl acids: dimer (upper part) and catemer (lower part). R depicts the residual part of 11-MUA covalently bound to the cluster.

Directly after the synthesis, silver-containing nanoclusters appear light brown. This coloration disappears after 24 hours (Fig. 55) and occurs in all silver-containing samples regardless of the composition. Pure platinum clusters do not appear brown. It is possible that silver ions react with hydroxide ions to silver hydroxide which further reacts to insoluble silver oxide that has a brown color.[113] Under light illumination as well as at room temperature, silver oxide decomposes to silver and oxygen leading to the discoloration of the dispersion. Because of excess 11-MUA, which is not completely removed from the reaction mixture, the formed silver particles are stabilized and stay cluster-sized.

$$2\ Ag^{+} + 2\ OH^{-} \rightarrow 2\ AgOH \rightleftharpoons Ag_2O + H_2O$$

$$2\ Ag_2O \xrightarrow{h\nu} 4\ Ag + O_2$$

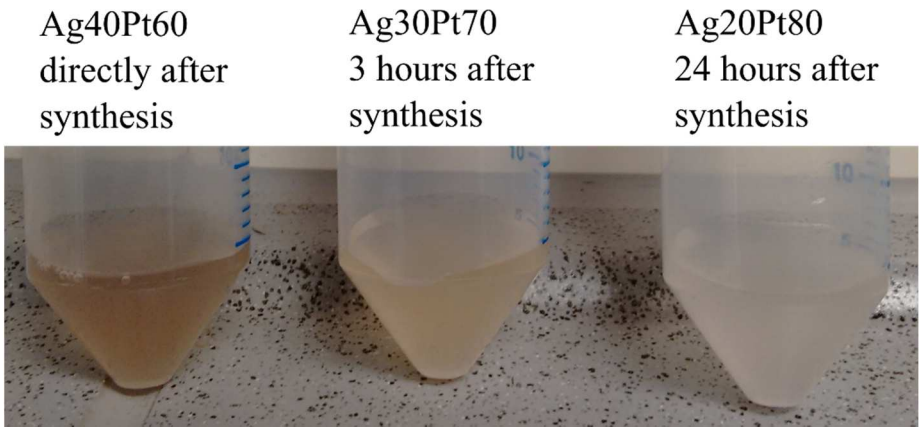

Figure 55: Photographs of silver-platinum nanoclusters in different compositions directly after the synthesis, after 3 hours, and after 24 hours. The discoloration behavior is the same for all compositions.

The transmission electron micrographs in Figure 56 show spherical clusters with sizes of around 2 nm. A few particles with sizes of 5 nm to 6 nm are visible as well. The clusters exhibit only a small number of crystallographic planes. They appear amorphous in powder X-ray diffractograms. The bigger particles are polycrystalline. Because the silver-platinum clusters are small, they are hard to distinguish from the sample substrate and no EDX mapping is possible to gain the element distribution of silver and platinum within a single cluster.

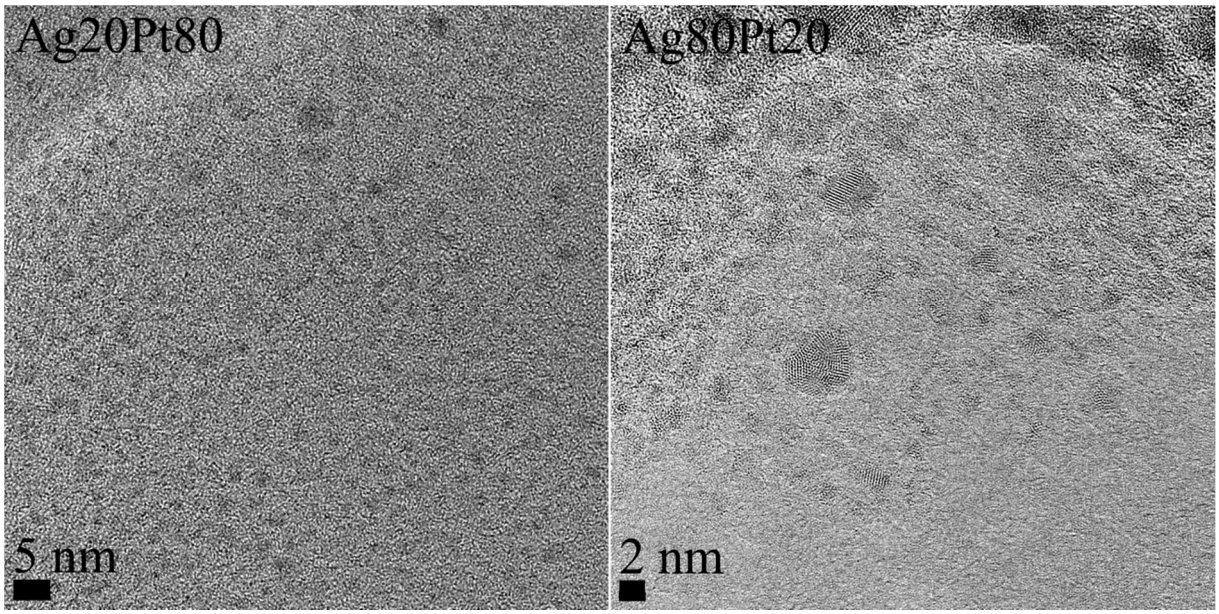

Figure 56: Transmission electron micrographs of silver-platinum 20:80 and 80:20 nanoclusters in different magnifications.

The UV/vis spectra in Figure 57 show the absorption bands of pure silver and pure platinum as well as silver-platinum nanoclusters in different compositions. Platinum nanoclusters do not show any absorption above 200 nm as is also the case for platinum nanoparticles and already described in the literature.[196] Silver nanoclusters exhibit one absorption maximum at 250 nm with two shoulders at 290 nm and 346 nm. A similar absorption spectrum is described by Calvo Fuentes et al.[58] with absorption maxima for an unprotected silver nanocluster of 220 nm and a shoulder at 235 nm. Those defined absorption bands show the molecular-like behavior of silver clusters. Bimetallic silver-platinum nanoclusters show absorption bands comparable to the silver cluster absorption. With increasing silver amount in the clusters, the absorption bands become more pronounced and silver-like. Time dependent density functional theory (TDDFT) calculations for silver-platinum nanoclusters[196] predict absorptions at 248 nm (5 eV) corresponding to a Ag 4d → Ag 5s transition, at 270 nm (4.6 eV) indicating a Pt 5d → Ag 5p transition, and 344 nm (3.6 eV) corresponding to a Pt 5d → Pt 6s transition. Those absorptions are in good agreement with the measured spectra, although the silver absorption is rather similar

as well. Therefore, a physical mixture of silver and platinum nanoclusters cannot be excluded completely.

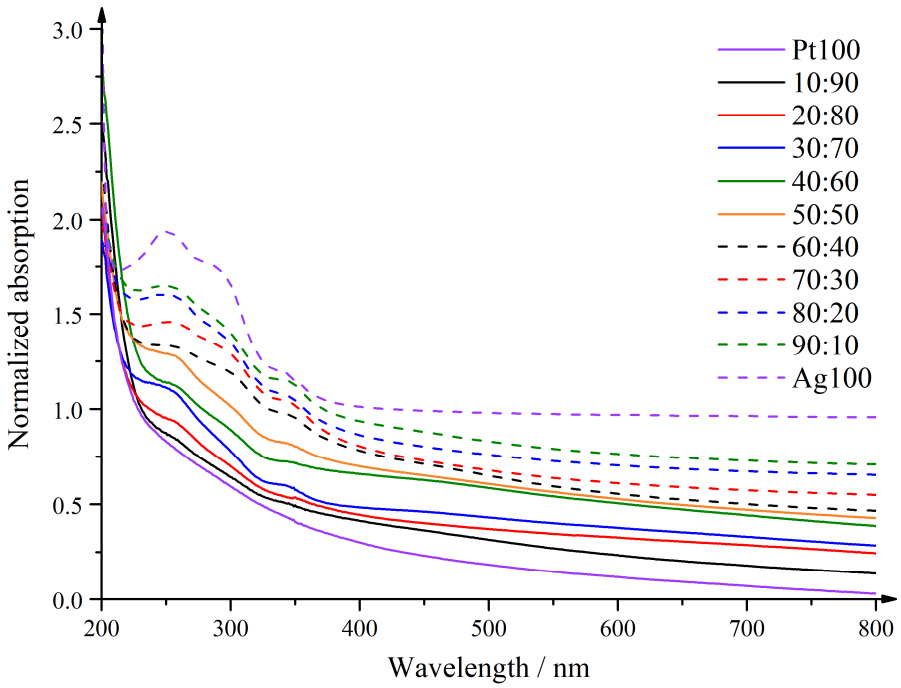

Figure 57: UV/vis spectra of silver, platinum, and silver-platinum nanoclusters in the compositions 10:90 to 90:10 in 10 mol% steps. The spectra are stacked for a better overview.

Clusters of different sizes show divergent fluorescence. Au_n with n = 13, 23, 31 exhibit fluorescence at 510 nm, 760 nm, and 866 nm, respectively.[197] The emission wavelength correlates directly with the gap between HOMO and LUMO. With increasing cluster sizes, the HOMO – LUMO gap decreases which results in a lower gap energy. A smaller gap energy means a bigger wavelength that is emitted. Like gold, silver and platinum nanoclusters also show fluorescence. Pt_5 clusters can be excited by a wavelength of 365 nm and emit at 440 nm and 470 nm.[198] Depending on the dispersion medium and cluster environment, Ag_6 clusters are excited at 280 nm and emit at 495 nm and 670 nm.[199] Overall, silver clusters under 2 nm in diameter show a tunable fluorescence. [200-201] Figure 58 depicts the fluorescence spectra of the silver-platinum nanoclusters in different compositions. Table 13 shows the corresponding excitation and emission wavelengths. Remarkably, all compositions have a strong emission at approximately 424 nm, independent of the excitation wavelength. A second, weaker emission at 360 nm to 370 nm redshifts and disappears into a shoulder with increasing silver compositions. The clusters also exhibit fluorescence in the near infrared region. Here, the emission is not as uniform and patterned as in the visible region. The emission in the near infrared region can be assigned to bigger clusters, whereas the emission in the visible range is attributed to smaller clusters with wider HOMO – LUMO gaps.

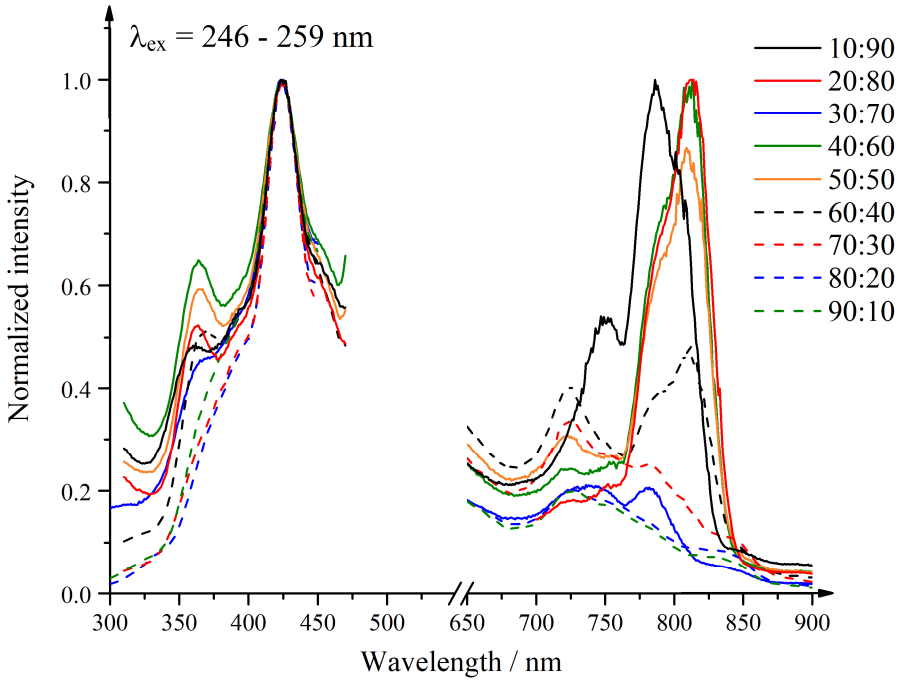

Figure 58: Fluorescence spectra of silver-platinum nanoclusters excited with wavelengths between 246 nm and 259 nm. The gap is due to second-order scattering.

Table 13: Absorption and emission maxima of silver-platinum nanoclusters of different compositions. λ_{ex}: excitation wavelength, λ_{em}: emission wavelength.

Composition Ag:Pt	λ_{ex} / nm	λ_{em} / nm
10:90	254	360, 423, 747, 786
20:80	259	364, 424, - , 812
30:70	250	365, 425, 736, 782
40:60	258	364, 423, 724, 813
50:50	258	367, 424, 722, 809
60:40	258	370, 424, 724, 812
70:30	253	- , 423, 723, 779
80:20	246	- , 425, 726, -
90:10	248	- , 425, 726, -

Compared to the silver-gold nanocluster system described by Ristig et al.,[24] the silver-platinum system yields clusters in the same size range. Also, an autofluorescence is observed as well, although the emission is too weak to be noticed with the naked eye.

In summary, pure silver nanoclusters show a size of 4 nm, whereas platinum clusters are 2 nm big. Bimetallic silver-platinum nanoclusters show a spherical morphology and have sizes between 2.1 nm and 3.2 nm increasing with the silver amount. A slight positive Zeta potential

indicates there is no deprotonation of 11-MUA in ethanol which leads to a sterical stabilization that can be disrupted by intermolecular hydrogen bonds of the carboxyl group of 11-MUA. The clusters show an absorption in the UV region and fluorescence in the visible and near infrared range.

5.2.1 Conclusion on silver-platinum nanoclusters

The synthesis of bimetallic nanoclusters reported by Ristig et al.[24] is applicable to the silver-platinum system. UV/vis spectra indicate the presence of alloys, but a physical mixture cannot be excluded completely since the silver absorption bands appear at similar positions. Because of the small nanocluster sizes, EDX maps of single clusters are difficult to obtain. Fluorescence spectroscopy shows an autofluorescent behavior of the nanoclusters.

5.3 Characterization of silver-gold nanoparticles

5.3.1 Synthesis by trisodium citrate and tannic acid reduction

The silver-gold nanoparticles prepared by trisodium citrate and tannic acid reduction are already established in our workgroup and characterized by Dr. Simon Ristig in his work.[25-26] Therefore, the characterization by differential centrifugal sedimentation, UV/vis spectroscopy, atomic absorption spectrometry, transmission and scanning electron microscopy as well as energy dispersive X-ray spectroscopy will be kept short. The powder X-ray diffraction, containing high-temperature powder diffraction as the supplementary and newly investigated part, will be focused on. To confirm the particles have the same properties as already described by Ristig et al., they are characterized by DCS, UV/vis, AAS, TEM, SEM, and EDX. Figure 59 shows the size distributions of the silver, gold, and silver-gold nanoparticles as obtained by DCS. The gold and silver-gold particles lie in the same size range around 7 nm with small standard deviations around 0.6 nm, whereas the silver nanoparticles have sizes of 35 nm and a bigger standard deviation of 4 nm. This is also described by Ristig et al.[23, 25-26] Gold is nobler than silver and is reduced faster generating a high concentration of crystallization seeds which leads to smaller particle sizes. As soon as no gold as crystallization seed is present, the size of the particles increases.

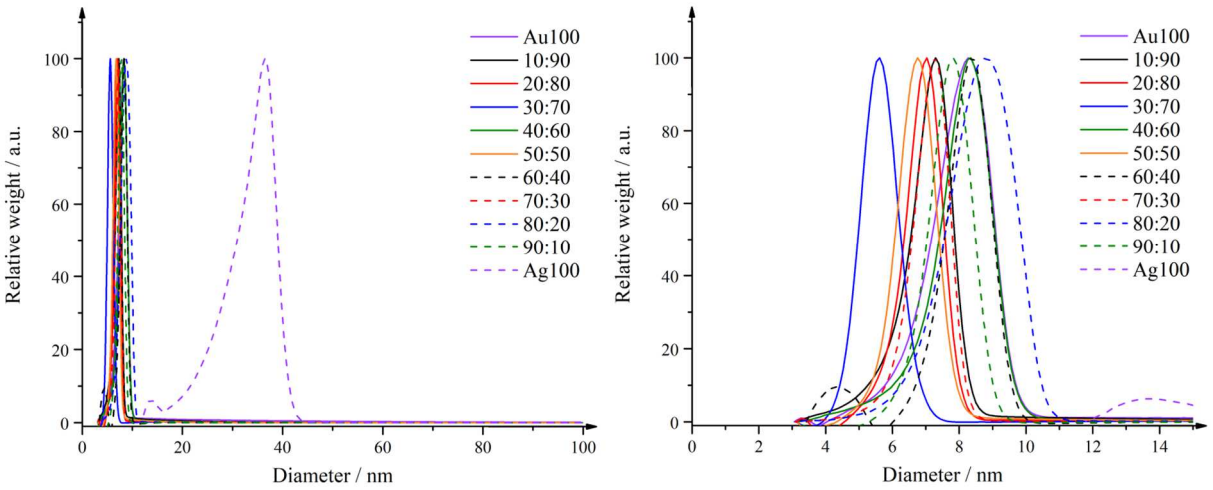

Figure 59: Size distributions of silver-gold nanoparticles prepared by trisodium citrate and tannic acid reduction as obtained by DCS. The graphic on the left depicts the whole measured range from 3 nm to 100 nm. The graphic on the right shows the range between 3 nm and 15 nm for a better overview.

The UV/vis spectra in Figure 60 show narrow absorption bands with no shoulders indicating monodisperse systems with no agglomerates which is already observed from DCS

measurements. The absorption maxima of the bimetallic silver-gold particles lie between the absorption of silver and gold particles pointing to the presence of nanoalloys.

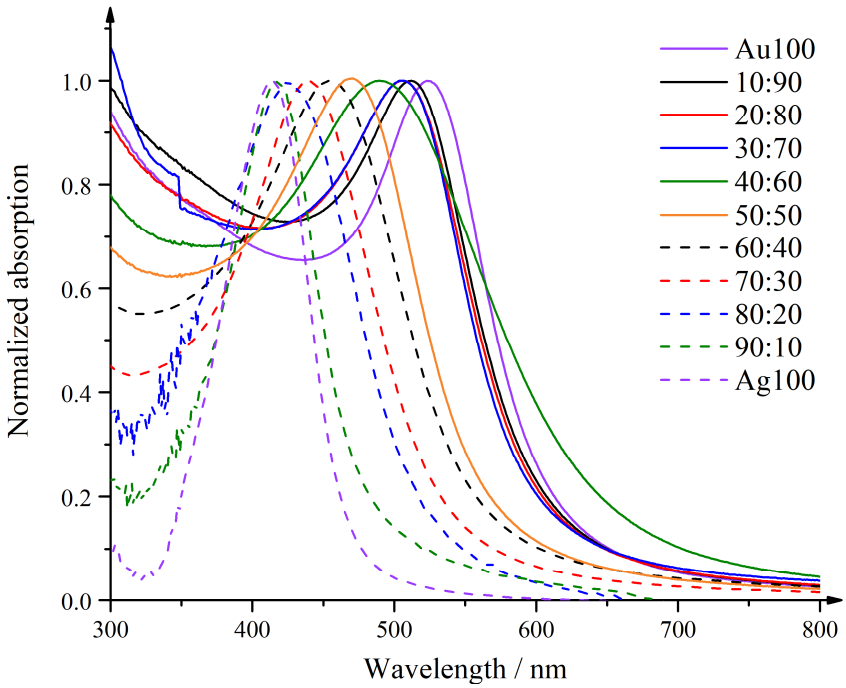

Figure 60: UV/vis spectra of silver, gold, and silver-gold nanoparticles prepared by trisodium citrate and tannic acid reduction.

Table 14 shows the sizes, absorption maxima and the actual composition of the silver-gold nanoparticles. All results are comparable to previous results of Ristig et al.

The obtained nanoparticles have a spherical morphology and are polycrystalline showing several domains. The element distribution obtained by EDX mapping depicts a gold-rich core and a silver-rich shell, but an overall alloy character because no strict boundary between silver and gold is observed (Fig. 61). The theoretical and experimental yield is determined from three to five batches of freeze-dried nanoparticles which are weighed (Table 15). The yield varies from 31 % for silver-gold 10:90 to 68 % for silver-gold 30:70. A great part of rather small nanoparticles is lost during the purification process by ultracentrifugation because they do not sediment. This is observed by a still colorful supernatant after centrifugation.

Table 14: Diameters, absorption maxima, and actual compositions of the silver-gold nanoparticles prepared by trisodium citrate and tannic acid reduction.

Nominal composition Ag:Au	Diameter by DCS / nm	UV/vis absorption maximum / nm	Composition according to AAS / mol%
0:100	8.2 ± 0.8	523	0:100
10:90	7.2 ± 0.6	512	12:88
20:80	7.0 ± 0.6	505	25:75
30:70	5.6 ± 0.6	505	34:66
40:60	8.3 ± 0.7	490	45:55
50:50	6.7 ± 0.6	474	62:38
60:40	8.3 ± 0.6	454	64:36
70:30	7.2 ± 0.5	439	74:26
80:20	8.7 ± 1.0	424	83:17
90:10	7.8 ± 0.6	418	90:10
100:0	35.0 ± 4.0	414	100:0

Table 15: Theoretical and experimental yield of silver-gold nanoparticles prepared by trisodium citrate and tannic acid reduction.

Nominal composition Ag:Au	Theoretical yield out of three to five synthesis / mg	Experimental yield out of three to five synthesis / mg	Yield / %
0:100	35.4	17.1	48
10:90	33.4	10.5	31
20:80	31.4	17.4	55
30:70	29.4	19.9	68
40:60	27.4	15.7	57
50:50	25.4	12.9	51
60:40	23.3	12.8	55
70:30	21.3	12.2	57
80:20	19.3	12.6	65
90:10	17.3	11.5	67
100:0	25.5	17.0	67

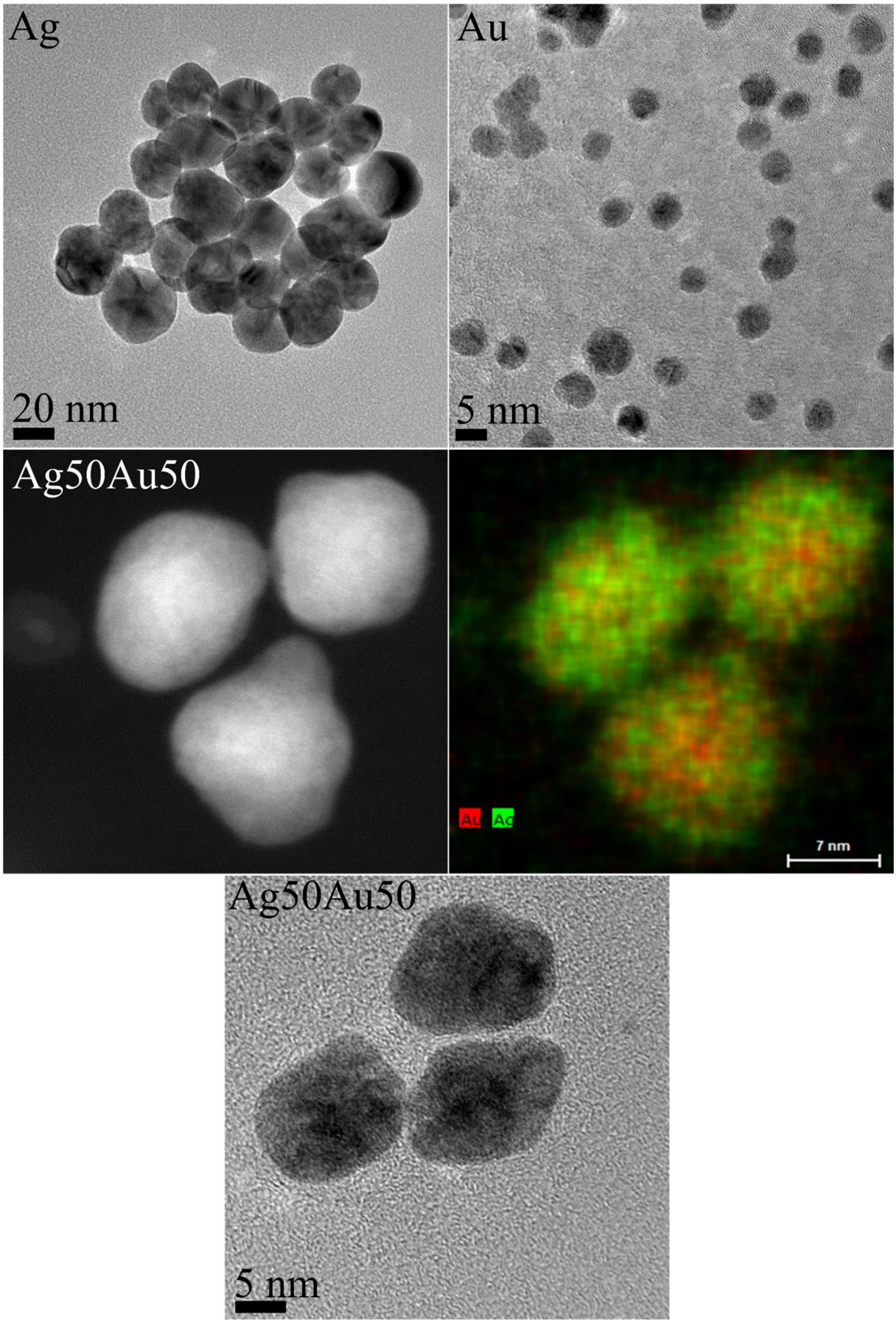

Figure 61: TEM images of silver, gold, and silver-gold 50:50 nanoparticles together with a HAADF-STEM image, and EDX map of silver-gold 50:50 nanoparticles.

Supplementary to the previous work of Ristig et al., powder X-ray diffraction experiments are performed in transmission geometry to obtain a better resolution of the diffraction patterns than in reflexion geometry. The silver-gold system forms unlimited solid solutions in all compositions.[141] That is why it is deeply characterized. Remarkably, this system shows a negative deviation of lattice parameters from Vegard's law as described by Ristig et al.[25], Petkov et al.[145], Girao et al.[202], and Bozzolo et al.[203] which has its maximum for the silver-gold 50:50 mol% composition. The lattice parameter deviation takes higher values for smaller than for bigger nanoparticles.[163, 166] The diffraction patterns of silver, gold, and silver-gold nanoparticles are shown in Figure 62. They correspond to the diffraction pattern of silver (PDF 00-004-0783[132]) and gold (PDF 00-004-0784[133]). The broad reflexes indicate the nanocrystalline character of the particles. Lanthanum hexaboride is used as a standard, the reflexes are marked with an asterisk.

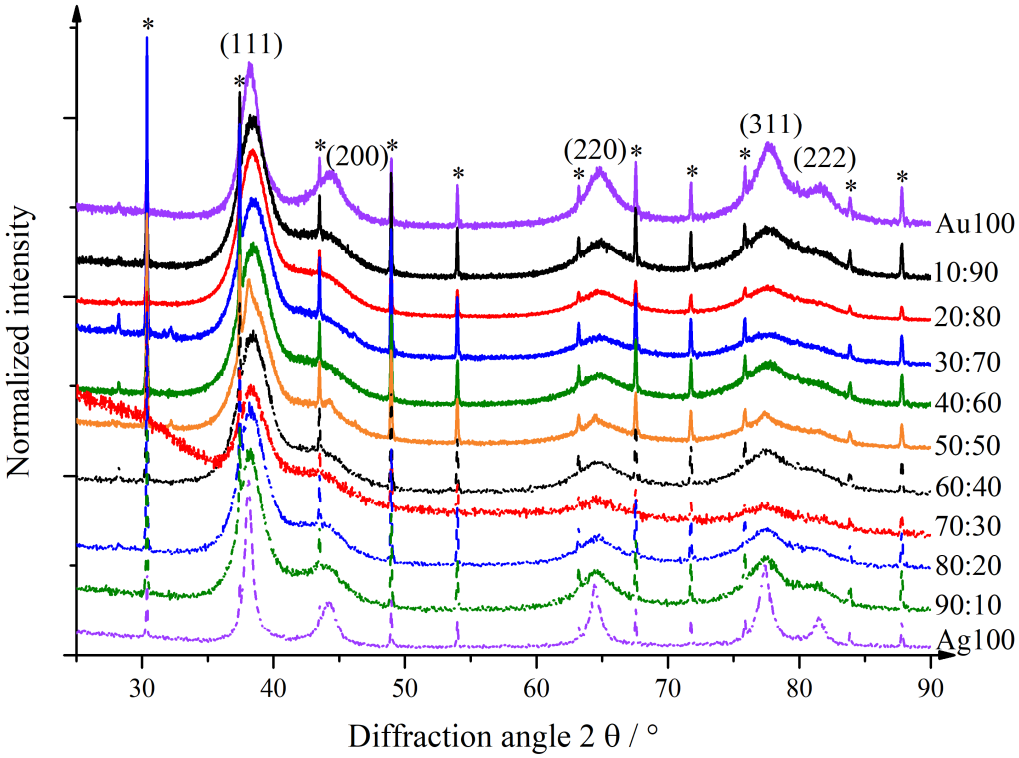

Figure 62: Powder diffraction patterns of the silver-gold nanoparticles synthesizes by sodium citrate and tannic acid reduction in the compositions 10:90 to 90:10 in 10 mol% steps measured in Debye-Scherrer geometry. The asterisks mark the lanthanum hexaboride reflexes (PDF 00-034-0427[189]). The reflexes of the alloys are compared with the powder diffraction files 00-004-0783 for silver[132] and 00-004-0784 for gold.[133]

For the determination of crystallographic constants like lattice parameters, cell volumes, and crystallite sizes, the Rietveld refinement is used. All Rietveld refinements and interpretations of the body-centered tetragonal phase described in the following were performed by Dr. Oleg

Prymak, University of Duisburg-Essen. Rietveld refinement is a method which applies mathematic models like the Gaussian function or the Lorentzian function as well as crystallographic geometries of the unit cells to describe the reflex profile of a powder sample.[204] The Rietveld method enables the characterization of nanocrystalline materials where reflex broadening plays a significant role and leads to information loss because of reflex overlapping. Like silver and gold, silver-gold particles crystallize in the face-centered cubic (fcc) system with the $Fm\bar{3}m$ space group. The Rietveld refinement plot for the silver-gold 50:50 composition is shown in Figure 63. An overlapping of the (111) and (200) reflexes is observable. The measured data is depicted in blue, the red line shows the fit function for the fcc model, and the grey line displays the difference plot. It is visible that the fit function does not fit the measured data completely. The modeled reflex profile differs from the measured one as indicated by the arrows in Figure 63.

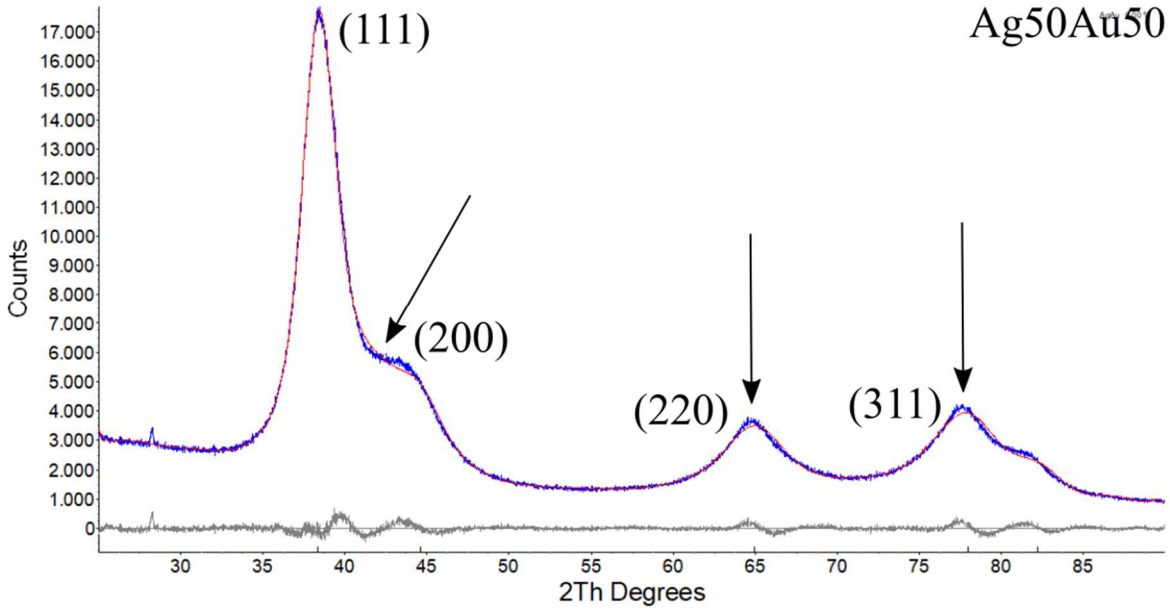

Figure 63: Reflex fitting according to the Rietveld method with the fcc lattice as model. The blue line depicts the measurement, the red line shows the fit function, and the grey line displays the difference plot which gives an idea about the quality factor of the fit. The arrows indicate the positions where the fit function does not fit the measurement. The graph is plotted by the program TOPAS.

Usually, nanoparticles are not exactly spherical, but decahedral or icosahedral structures.[32, 135, 205-206] They show a penta-twinning which leads to defects between the crystallite boundaries because of stress (Fig. 64). Those defects have a high impact on the diffractogram because the nanoparticles, and consequently the crystallites, are small. Also, those defects may have a different crystal structure than the crystallites themselves. Sun et al.[135] describe the occurrence of a body-centered tetragonal (bct) phase with the space group *I4/mmm* in silver nanorods at

ambient conditions because of distortion of the cubic unit cell. It alters the reflex profiles in the powder diffractogram by reflex splitting because the fcc and bct phases show similar diffraction patterns where the diffraction angles and the reflex intensities are slightly shifted. The $(200)_{fcc}$ reflex is split into two $(002)_{bct}$ and $(200)_{bct}$ reflexes, just as the $(220)_{fcc}$ reflex is split in two $(202)_{bct}$ and $(220)_{bct}$ reflexes. Bain et al.[207] reported the distortion of the crystal structure in the transition from austenite to martensite. They suggested the transition from the fcc to the bct phase because of the expansion of one a_{fcc} axis to one c_{bct} axis. The other two a_{fcc} axes contract by the factor of $a_{fcc}/\sqrt{2}$ to yield the a_{bct} axes (Fig.65). Hahn et al.[208] also reported the occurrence of a bct phase in copper thin films deposited on palladium (100) which transforms to fcc upon annealing. For the gold-palladium system which, like the silver-gold system, is completely miscible, three intermetallic phases are described. Two of them show a cubic crystal structure (Au_3Pd and $AuPd_3$), whereas the third (AuPd) exhibits a tetragonal phase.[209-210]

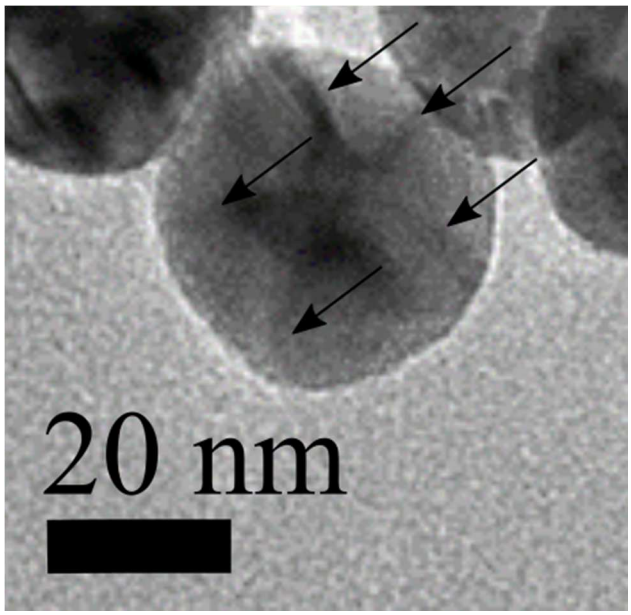

Figure 64: Transmission electron micrograph of a silver nanoparticle. The arrows indicate crystallite boundaries which show lattice defects. Close-up of Figure 61.

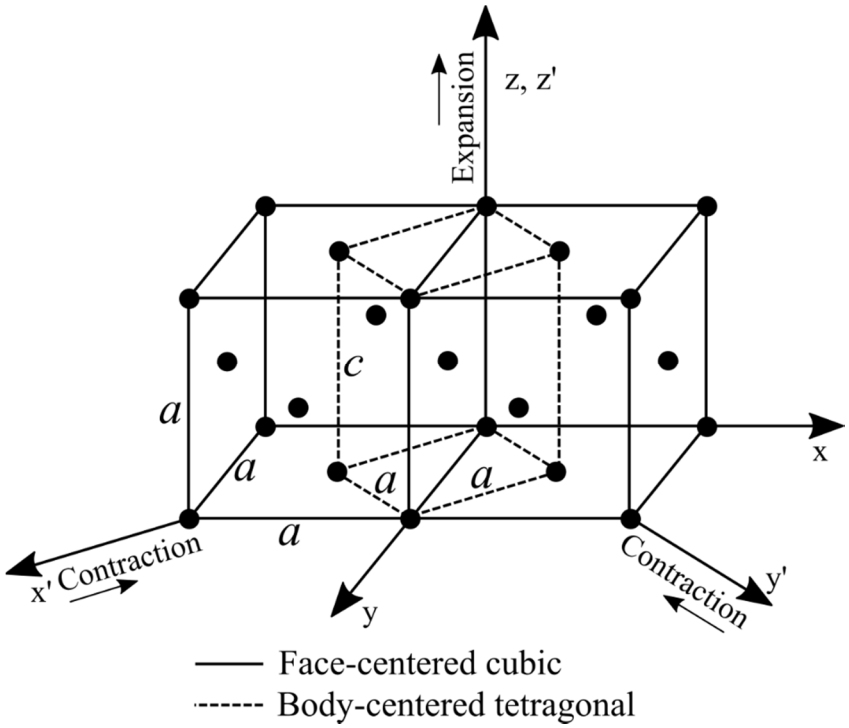

Figure 65: Face-centered cubic unit cell with the transformation to the body-centered tetragonal structure upon contraction of the x' and y' axes, and expansion of the z' axis.

As a trial for a better fitting, the occurrence of the bct phase is considered to describe the defects. No certain evidence is found which can confirm the presence of the bct phase, it is just used as a model. Figure 66 shows the reflex fitting using the fcc and the bct model.

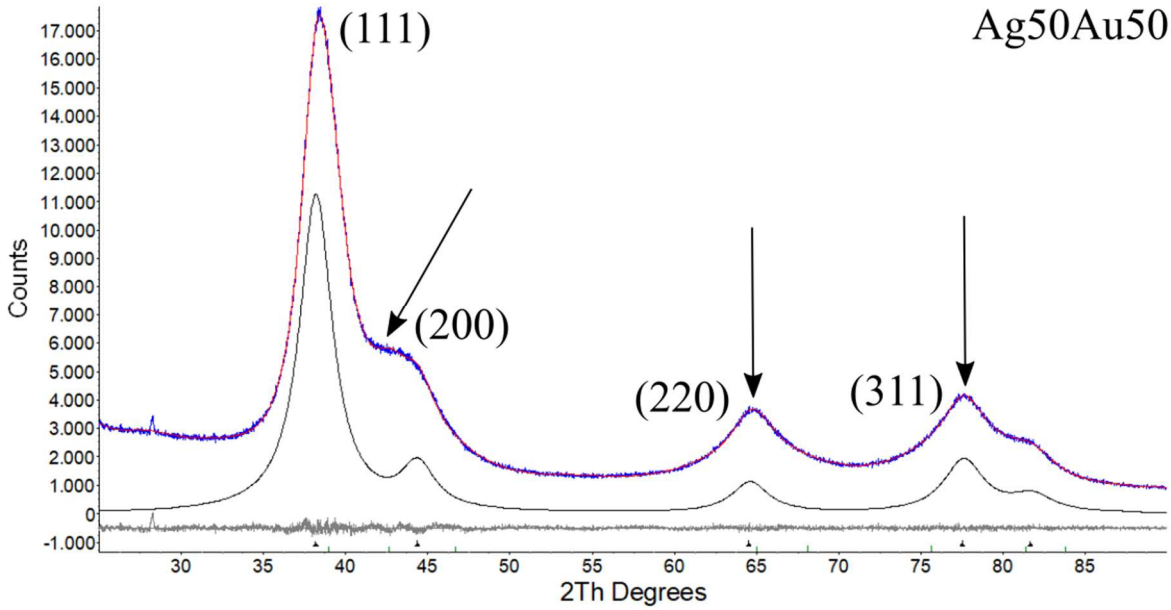

Figure 66: Reflex fitting according to the Rietveld method with the fcc and bct lattice as model. The blue line depicts the measurement, the red line shows the fit function, the black line shows the pattern for the fcc phase, and the grey line displays the difference plot which gives an idea about the quality factor of the fit. The arrows indicate the improved fit. The graph is plotted by the program TOPAS.

Taking the bct defect phase and the fcc phase into account, the fit function describes the diffraction pattern much better because no difference between fitted and measured graph is observed. The arrows in Figure 66 indicate the positions of the improved fit as compared to only fcc modeling shown in Figure 63. Regarding the lattice parameters of the different compositions of silver and gold in the nanoparticles, it is observed that if only the fcc phase is considered, a negative deviation from Vegard's law is obtained. When the bct defect phase and the fcc phase are refined, the lattice parameters for the fcc lattice match Vegard's law (Fig. 67). It is possible that the nanoparticles with a high composition of either silver or gold, like 12:88, 25:75, 34:66, 74:26, 83:17, and 90:10, have less defects than the nanoparticles with a nearly equal composition of 45:55, 62:38, and 64:36 mol%. The lattice constants of silver with 4.0862 Å and gold with 4.0786 Å are slightly different. Therefore, the most defects should be present in the silver-gold 45:55 followed by the 62:38 and the 64:36 composition. These compositions have the highest amounts of both metals which increases the microstrain within the unit cell as described by Ristig et al.[25] This leads to a higher deviation from Vegard's law if only the fcc phase is refined. Upon bct defect phase refinement, the lattice parameters show no deviation from Vegard's law.

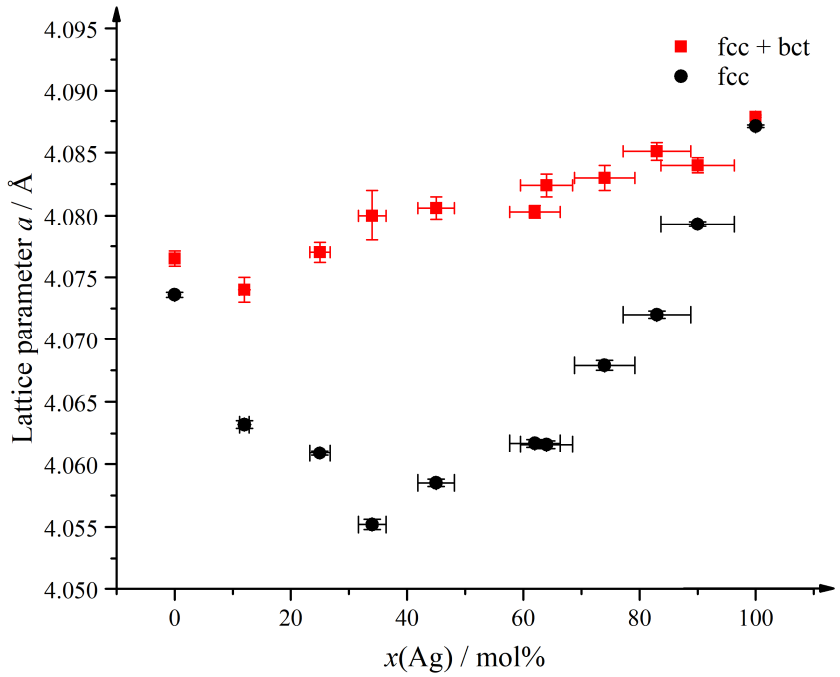

Figure 67: Lattice parameters calculated for the silver-gold nanoparticles as a function of composition. The red squares depict the lattice parameters for the fcc lattice calculated by taking the bct defect phase into account, whereas the black dots show the lattice parameters from the fcc only model.

Table 16 depicts the crystallographic properties of the silver-gold nanoparticles refined with the fcc structure only and the bct defect phase plus the fcc structure (fcc + bct). As already

displayed in Figure 67, the lattice constants do not increase linearly with the silver composition for the fcc only model, whereas they do in the fcc + bct model. The crystallite sizes lie between 3 nm and 5 nm for the alloys which indicates the presence of polycrystallinity. The silver and gold nanoparticles are also polycrystalline because the crystallite size is smaller than the nanoparticle diameter obtained from differential centrifugal sedimentation. Comparing the crystallite sizes obtained from the fcc only model with the fcc + bct model, the values are slightly bigger after fcc + bct refinement. The reason for the increase is the reflex broadening by the presence of a defect phase and not because of the crystallite size.

Table 16: Crystallographic properties of silver, gold, and silver-gold nanoparticles in different compositions prepared by reduction with trisodium citrate and tannic acid. The lattice parameter stated refer to the fcc lattice.

Composition	Fcc only model			Fcc + bct defect phase model		
Ag:Au according to AAS / mol%	Lattice parameter *a* / Å	Cell volume *V* / Å^3	Crystallite size *D* / nm	Lattice parameter *a* / Å	Cell volume *V* / Å^3	Crystallite size *D* / nm
0:100	4.0736(2)	67.60(1)	4.8(1)	4.0765(6)	67.74(3)	5.7(2)
12:88	4.0632(3)	67.08(1)	3.3(1)	4.074(1)	67.62(7)	3.6(1)
25:75	4.0609(2)	66.97(1)	3.3(1)	4.0770(8)	67.77(4)	3.4(1)
34:66	4.0552(4)	66.08(2)	2.8(1)	4.080(2)	67.9(1)	2.7(1)
45:55	4.0585(3)	66.85(2)	3.1(1)	4.0806(9)	67.93(4)	3.2(1)
62:38	4.0617(3)	67.00(2)	3.2(1)	4.0803(5)	67.93(5)	3.4(1)
64:36	4.0616(3)	67.00(2)	3.1(1)	4.0824(9)	68.04(5)	3.4(1)
74:26	4.0679(4)	67.32(2)	3.3(1)	4.083(1)	68.09(6)	3.7(1)
83:17	4.0720(3)	67.52(1)	3.5(1)	4.0851(7)	68.17(3)	3.9(5)
90:10	4.0793(2)	67.88(1)	4.0(1)	4.0840(6)	68.12(3)	4.4(1)
100:0	4.0871(1)	68.27(1)	11(1)	4.0879(1)	68.31(1)	15(1)

The crystallographic properties of the bct defect phase are shown in Table 17. The lattice parameter *a* decreases from pure gold with the increasing silver amount until it reaches its minimum of 2.752 Å for the 62:38 composition. With a further increase of the silver amount, no remarkable increase of *a* is observed. The *a* lattice parameter of the defect phase in pure silver particles is highest with a value of 2.879 Å. On the other hand, the *c* lattice parameter is smallest for the silver nanoparticles with 4.112 Å and greatest for the 34:66 composition with a value of 4.260 Å. Overall, the alloyed samples show higher *c* constants than the pure metal

particles. Sun et al.[135] reported values of a = 2.899 Å and c = 4.058 Å for silver nanorods (bct phase). It corresponds to a c/a ratio of 1.400. The c/a ratio describes the tetragonality of the lattice.[211] If c/a = 1, the bct lattice turns into a body-centered cubic (bcc) lattice. If $c/a = \sqrt{2}$ = 1.414, the bct lattice corresponds to an fcc lattice.

Table 17: Crystallographic properties of the bct defect phase of silver-gold nanoparticles in different compositions.

Composition Ag:Au according to AAS / mol%	Lattice parameter a / Å	Lattice parameter c / Å	Cell volume V / Å^3
0:100	2.849(1)	4.152(3)	33.70(4)
12:88	2.792(3)	4.198(4)	32.72(7)
25:75	2.762(2)	4.241(2)	32.34(6)
34:66	2.760(5)	4.260(3)	32.45(11)
45:55	2.758(3)	4.258(3)	32.40(7)
62:38	2.752(2)	4.238(2)	32.09(6)
64:36	2.755(5)	4.249(6)	32.25(11)
74:26	2.756(5)	4.232(6)	32.15(10)
83:17	2.755(5)	4.237(4)	32.15(10)
90:10	2.753(4)	4.206(3)	31.88(9)
100:0	2.879(1)	4.112(2)	34.08(3)

The alterations upon transition from the fcc to the bct lattice parameters are depicted in Table 18. The c axis in the bct lattice is elongated in comparison to the fcc lattice, whereas the a axis is compressed upon transformation from fcc to bcc. The cell volume decreases as well. The c/a ratios of the monometallic nanoparticles are 1.457 for gold and 1.428 for silver. Both values lie near 1.414 where the bct lattice turns into the fcc lattice. Therefore, the lattice distortion for the monometallic particles caused by defects is considered rather small. In contrary, the alloyed nanoparticles show c/a ratios of 1.504 to 1.544 indicating a bigger distortion and deviation from the fcc lattice. These findings are in good agreement with the results described in Figure 67. The monometallic particles show smaller lattice parameter deviations of fcc to fcc + bct compared to the bimetallic nanoparticles. This means there is a greater number of defects in alloyed nanoparticles than in monometallic ones which is underlined by the crystallite sizes in Table 16. The crystallites are smaller in the bimetallic than in the monometallic systems.

Table 18: Alteration of the lattice parameters upon transformation from face-centered cubic to body-centered tetragonal unit cells.

Composition Ag:Au according to AAS / mol%	$c_{bct}/a_{fcc} = \Delta_c$ / %	$\sqrt{2} \cdot a_{bct}/a_{fcc} = \Delta_a$ / %	$2 \cdot V_{bct}/V_{fcc} = \Delta_V$ / %	c_{bct}/a_{bct}
0:100	+ 1.9	- 1.2	- 0.5	1.457
12:88	+ 3.0	- 3.1	- 3.2	1.504
25:75	+ 4.0	- 4.2	- 4.6	1.536
34:66	+ 4.4	- 4.3	- 4.4	1.544
45:55	+ 4.4	- 4.4	- 4.6	1.544
62:38	+ 3.9	- 4.6	- 5.5	1.540
64:36	+ 4.1	- 4.6	- 5.2	1.542
74:26	+ 3.7	- 4.6	- 5.6	1.536
83:17	+ 3.7	- 4.6	- 5.7	1.538
90:10	+ 3.0	- 4.7	- 6.4	1.528
100:0	+ 0.6	- 0.4	- 0.2	1.428

To determine the thermal behavior of the silver-gold nanoparticles, high-temperature X-ray diffraction experiments are performed. The experiments take place in a vacuum chamber on a heatable tantalum sample holder in Bragg-Brentano geometry. It is expected that the crystallinity of the nanoparticles increases with the temperature because of the transition from smaller to bigger crystallites (recrystallization). Hence, the number of defects and the microstrain shall decrease with the temperature. The aim is to investigate the linear thermal expansion coefficient α, the changes of the lattice parameter a, the crystallite size D, and the microstrain ε.

Figures 68-72 depict the diffraction patterns of gold, silver-gold, and silver nanoparticles at different temperatures. The marked reflexes correspond to lanthanum hexaboride and tantalum, the unmarked arise from the nanoparticle samples. The reflexes collected at room temperature have a broad character indicating nanocrystallinity. The (111) reflex of the nanoparticles overlays with the (110) reflex of tantalum at 38°. Upon temperature increase, a slight shift to lower diffraction angles is observed. This is attributed to the unit cell and consequently the d-spacing expansion. The Bragg-equation (5) shows the relationship between the d-spacing and the diffraction angle. When the angle decreases, d must increase to fulfill the equation. Another consequence of the temperature increase is the change of the reflex shape. It becomes narrower

and more pronounced indicating a recrystallization, and therefore crystallite growth and microstrain decrease as described by Equations (6) and (7). None of the samples shows a (111) reflex splitting at elevated temperatures which would be the case if a segregation of the elements silver and gold took place.

At 700 °C, for the gold nanoparticles (Fig. 68), a shoulder at a diffraction angle of 38° is observable which evolves into a reflex at 850 °C. At room temperature after annealing, this reflex shifts to higher angles (contraction of the unit cell), but is still visible. It depicts a crystallite size growth. Table 19 summarizes the crystallographic results obtained by Rietveld refinement and by calculations using Equation (8). For those calculations, the $K\alpha_2$ stripped diffractogram is used and the (220) reflex is taken and fitted using a Voigt function with the program Origin®. The (220) reflex is considered because its location does not overlap with the reflexes of neither lanthanum hexaboride nor tantalum. The Voigt function is a convolution of the Gaussian and the Lorentzian functions and describes the reflex profiles appropriately.[212-213] The obtained values are summarized in the appendix. Both methods, Rietveld refinement and standard calculations, are compared to show that same results are obtained. Standard calculations could be applied if a Rietveld refinement is not accessible.

The lattice parameters obtained by refinement and calculations are very similar. They only differ by 0.2 % to 0.03 %. The calculated results are slightly lower than the refined numbers. At room temperature before annealing, the lattice parameter *a* of gold is 4.0760 Å or 4.0673 Å non-refined. The literature value is 4.0786 Å. After annealing, 4.0790 Å or 4.0780 Å non-refined are obtained for *a*. With increasing temperature, the lattice parameter increases up to 1.41 % as already expected from observations of the diffraction patterns. The crystallite size *D* grows from 7 nm to 12 nm with the temperature, whereas the microstrain ε decreases from 0.56 % to 0.03 %. The microstrain, caused by a displacement of the unit cells about their regular positions, is not only produced by dislocations, but also by domain boundaries. Tables 14 and 16 depict the particle sizes and the crystallite sizes of the samples. The nanoparticles appear polycrystalline. The polycrystallinity and the presence of a possible defect phase, as described earlier, increase the microstrain. Both factors, the crystallite size *D* and the microstrain ε, influence the reflex broadness. The reflex shape narrows with the increasing temperature.

The crystallite size and microstrain are not as easy obtained by simple calculations as the lattice parameter. This is because the degree of contribution from the crystallite size and the microstrain to the reflex broadening is uncertain. A further reason is the instrumental reflex broadening which is influenced by the instrumental setup and the X-ray beam optics. Therefore, only the lattice parameters are calculated using the Voigt fit.

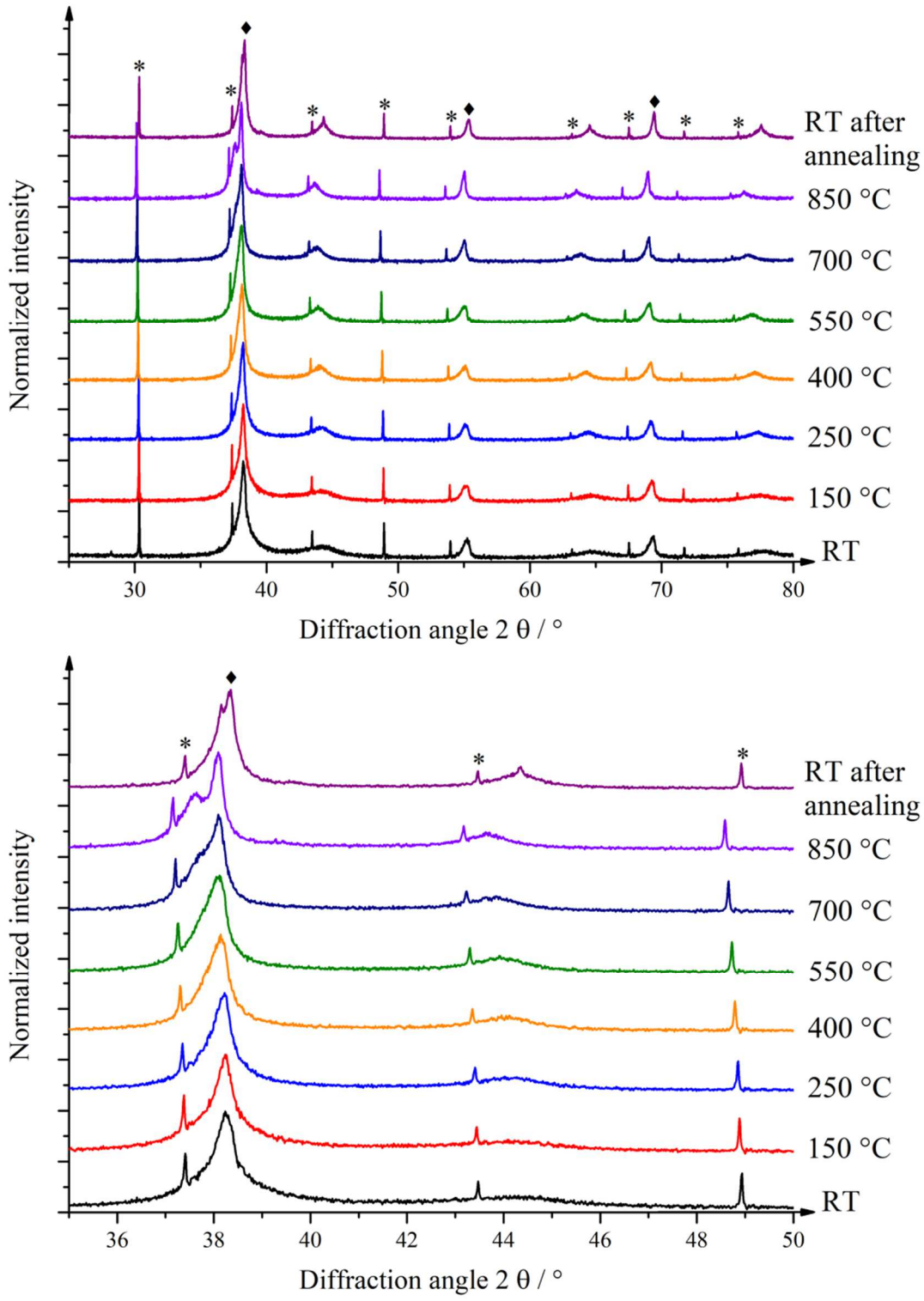

Figure 68: Diffraction patterns of gold nanoparticles at different temperatures and after annealing to 850 °C. The upper part shows the whole diffractogram collected, the lower part depicts the range from 35° to 50°. The asterisks mark the lanthanum hexaboride reflexes,[189] the diamonds denote the tantalum reflexes.[214]

Table 19: Crystallographic properties of the gold nanoparticles prepared by reduction with trisodium citrate and tannic acid during high-temperature X-ray diffraction.

Temperature / °C	Lattice parameter *a* / Å		Cell volume *V* / Å^3	Crystallite size *D* / nm	Microstrain *ε* / %
	Rietveld refined	Non-refined			
25	4.0760(5)	4.0673	67.72(2)	7(1)	0.56(3)
150	4.0831(5)	4.0741	68.07(2)	7(1)	0.60(3)
250	4.0906(4)	4.0859	68.45(2)	7(1)	0.23(2)
400	4.1002(3)	4.0967	68.93(2)	9(1)	0.23(2)
550	4.1104(3)	4.1076	69.45(1)	10(1)	0.21(2)
700	4.1218(3)	4.1202	70.03(1)	12(1)	0.23(1)
850	4.1343(2)	4.1335	70.66(1)	12(1)	0.05(4)
25 after 850	4.0790(2)	4.0780	67.87(1)	12(1)	0.03(2)

Figure 69 shows the diffraction patterns of the silver-gold 30:70 nanoparticles at different temperatures. Because of a low amount of sample, the reflexes are weak. Nevertheless, a reflex evolution is observable at 37.5° at 850 °C and at 44.8° at room temperature after annealing. This is attributed to the crystallite growth. Table 20 summarizes the crystallographic properties of the sample. The lattice parameter *a* increases with the temperature. At room temperature, *a* is 4.042 Å and 4.0673 Å non-refined. At 850 °C, the unit cell expands to a length of 4.1373 Å and 4.1347 Å non-refined just to shrink again upon cooling to 4.0789 Å and 4.0769 Å non-refined. The overall unit cell expansion lies at 2.30 %. The deviation from the refined to the non-refined values varies from 0.6 % to 0.05 %. The crystallite size grows with the temperature because of recrystallization processes. The microstrain is not determined because of the lack of, or too weak reflexes at higher angles. Those are usually regarded during a microstrain determination because the statistical influence of the *d*-spacing is more significant. At higher angles, the *d*-spacing between the atomic planes decreases and every deviation affects the reflex width more than at lower angles.

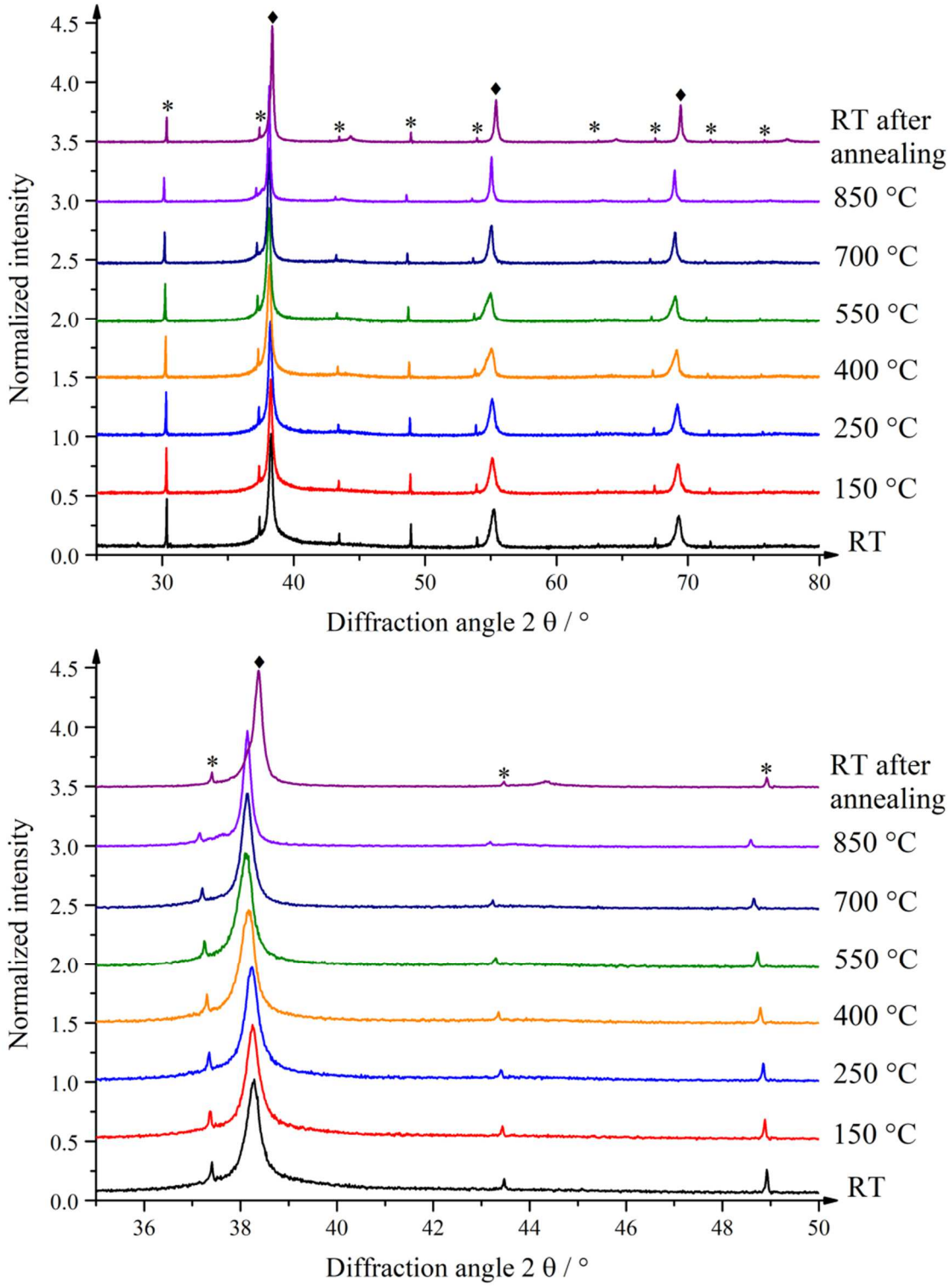

Figure 69: Diffraction patterns of silver-gold 30:70 nanoparticles at different temperatures and after annealing to 850 °C. The upper part shows the whole diffractogram collected, the lower part depicts the range from 35° to 50°. The asterisks mark the lanthanum hexaboride reflexes,[189] the diamonds denote the tantalum reflexes.[214]

Table 20: Crystallographic properties of the silver-gold 30:70 nanoparticles prepared by reduction with trisodium citrate and tannic acid during high-temperature X-ray diffraction.

Temperature / °C	Lattice parameter *a* / Å		Cell volume *V* / Å^3	Crystallite size *D* / nm	Microstrain ε / %
	Rietveld refined	Non-refined			
25	4.042(2)	4.0673	66.0(1)	3(1)	-
150	4.045(1)	4.0735	66.2(1)	3(1)	-
250	4.078(2)	4.0853	67.8(1)	3(1)	-
400	4.100(2)	4.0956	69.0(1)	3(1)	-
550	4.121(3)	4.1030	70.0(1)	4(1)	-
700	4.137(2)	4.1168	70.78(9)	5(1)	-
850	4.1373(6)	4.1347	70.82(3)	9(1)	0.04(1)
25 after 850	4.0789(3)	4.0769	67.86(1)	14(1)	0.004(10)

Figure 70 depicts the diffraction patterns of the silver-gold 50:50 nanoparticles at different temperatures. As already observed in the previous samples, a reflex evolution and a shift to lower angles takes place. The (111) reflex at 38° appears first as a shoulder at 215 °C and is distinguishable at 550 °C. A summary of the crystallographic properties can be found in Table 21. An increase of the lattice parameters with the temperature from 4.057 Å and 4.0590 Å non-refined to 4.1361 Å and 4.1341 Å non-refined is observable. It corresponds to an expansion of 1.91 %. After cooling down to room temperature, the unit cell constant is 4.0780 Å and 4.0763 Å non-refined. The deviation from Rietveld refined to non-refined is 0.04 % to 0.05 %. The crystallites grow from 4 nm at room temperature to 17 nm at 800 °C. Since the particle size lies at 7 nm, the particles seem to sinter upon annealing around a temperature of 250 °C.

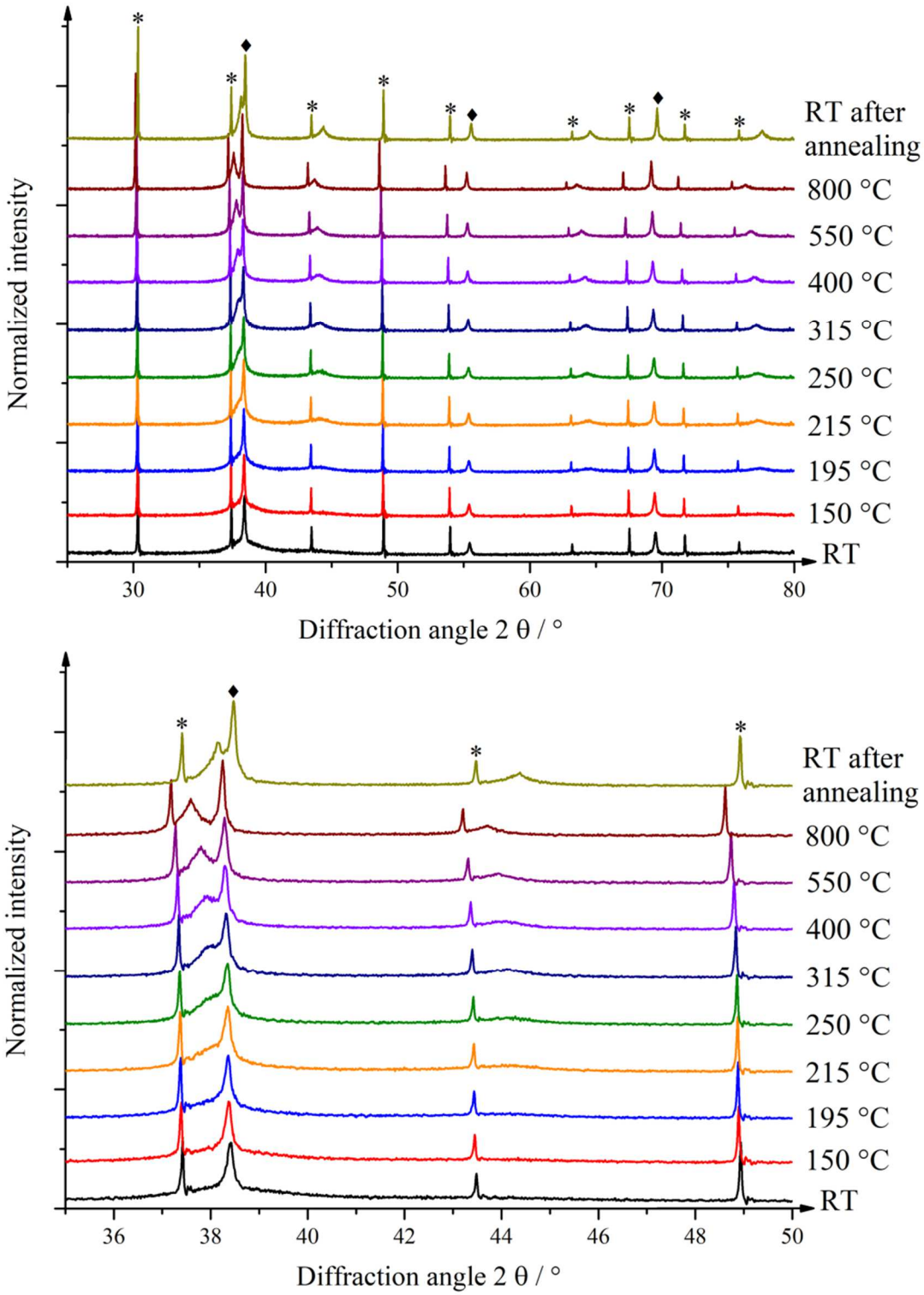

Figure 70: Diffraction patterns of silver-gold 50:50 nanoparticles at different temperatures and after annealing to 850 °C. The upper part shows the whole diffractogram collected, the lower part depicts the range from 35° to 50°. The asterisks mark the lanthanum hexaboride reflexes,[189] the diamonds denote the tantalum reflexes.[214]

Table 21: Crystallographic properties of the silver-gold 50:50 nanoparticles prepared by reduction with trisodium citrate and tannic acid during high-temperature X-ray diffraction.

Temperature / °C	Lattice parameter *a* / Å		Cell volume *V* / Å^3	Crystallite size *D* / nm	Microstrain *ε* / %
	Rietveld refined	Non-refined			
25	4.057(1)	4.0590	66.77(5)	4(1)	-
150	4.072(1)	4.0786	67.50(4)	4(1)	-
195	4.0857(5)	4.0836	68.20(2)	6(1)	0.01(1)
215	4.0893(3)	4.0865	68.38(2)	8(1)	0.06(7)
250	4.0922(3)	4.0899	68.53(1)	10(1)	0.05(5)
315	4.0965(2)	4.0956	68.74(1)	12(1)	0.04(4)
400	4.1031(2)	4.1018	69.08(1)	13(1)	0.05(3)
550	4.1152(2)	4.1144	69.69(1)	14(1)	0.02(6)
800	4.1361(2)	4.1341	70.76(1)	17(1)	0.01(8)
25 after 850	4.0780(1)	4.0763	67.82(1)	17(1)	0.02(4)

The diffractograms of the silver-gold 80:20 nanoparticles at different temperatures are shown in Figure 71. A reflex evolution at approximately 38° is observable. It begins with a shoulder at 250 °C which results in a pronounced reflex at 550 °C. At 850 °C, the reflex intensity decreases that indicates loss of sample material because of possible sublimation owing to the annealing of the material under vacuum conditions. At room temperature after annealing, no distinguishable reflex is visible for the (111) plane as is the case in gold and silver-gold 50:50 nanoparticles. As observed in the other samples before, a reflex shift to lower angles occurs. The crystallographic properties are summarized in Table 22. The initial lattice parameter *a* at room temperature is 4.067 Å and 4.0803 Å non-refined. It expands to 4.1427 Å and 4.1405 Å non-refined by 1.83 %. At room temperature after annealing, the cell constants are 4.0794 Å and 4.0786 Å non-refined. The deviation from Rietveld refined to non-refined *a* values is 0.3 % to 0.02 %. The crystallite size grows with the temperature from 4 nm to 18 nm. At 250 °C, the particles appear single crystalline because the nanoparticle diameter of 9 nm corresponds to the crystallite size. At 550 °C, the crystallite size increases to 16 nm indicating sintering of the particles.

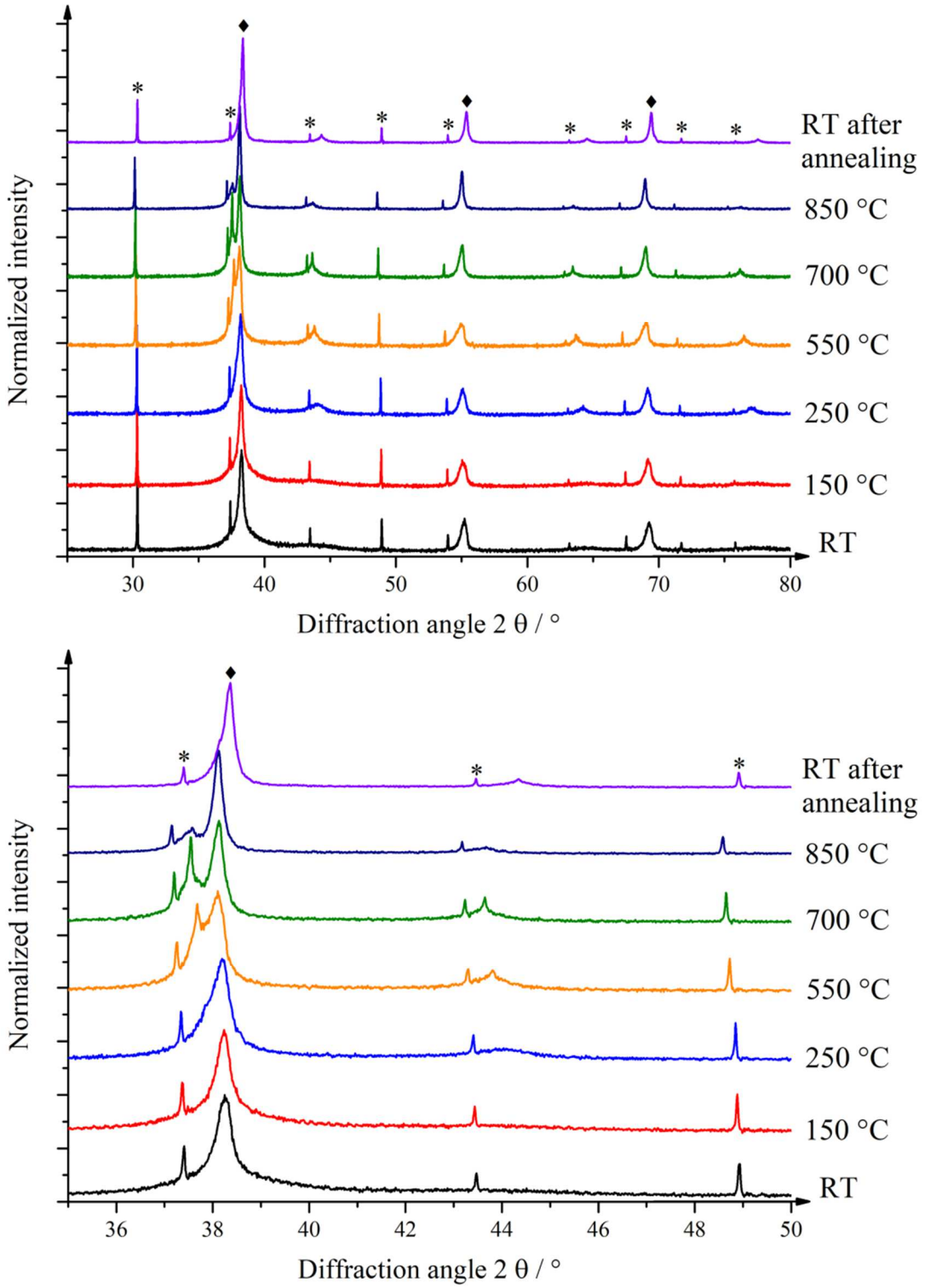

Figure 71: Diffraction patterns of silver-gold 80:20 nanoparticles at different temperatures and after annealing to 850 °C. The upper part shows the whole diffractogram collected, the lower part depicts the range from 35° to 50°. The asterisks mark the lanthanum hexaboride reflexes,[189] the diamonds denote the tantalum reflexes.[214]

Table 22: Crystallographic properties of the silver-gold 80:20 nanoparticles prepared by reduction with trisodium citrate and tannic acid during high-temperature X-ray diffraction.

Temperature / °C	Lattice parameter *a* / Å		Cell volume *V* / Å^3	Crystallite size *D* / nm	Microstrain *ε* / %
	Rietveld refined	Non-refined			
25	4.067(1)	4.0803	67.26(5)	4(1)	-
150	4.078(1)	4.0820	67.82(6)	3(1)	-
250	4.1004(4)	4.0990	68.94(2)	9(1)	0.01(9)
550	4.1262(2)	4.1248	70.25(1)	16(1)	0.01(5)
700	4.1410(2)	4.1394	71.01(1)	20(1)	0.001(10)
850	4.1427(2)	4.1405	71.09(1)	16(1)	0.02(10)
25 after 850	4.0794(1)	4.0786	67.89(1)	18(1)	0.06(2)

The diffractograms of the silver nanoparticles at different temperatures are given in Figure 72. The reflex evolution takes place, as expected, with increasing temperature. Especially at 38° and at 44°, the increase in reflex intensity is pronounced. At 400 °C, the silver (111) reflex evolves as a shoulder out of the (110) reflex of tantalum and is sharp at 700 °C. The silver (200) reflex at 44° is also pronounced at 700 °C. The diffractogram recorded at 850 °C shows small, nearly invisible reflexes which disappear completely in the diffraction pattern at room temperature after annealing. There are two possible explanations for this observation. The first is that the silver nanoparticles melt at 850 °C, and therefore show weak reflexes. The second is sublimation. Melting can be excluded since after cooling down to room temperature and because of recrystallization, the reflexes should be visible again. As no reflexes are present, sublimation of the nanoparticles is a plausible reason because the measurements take place under vacuum conditions. Asoro et al.[215] showed by *in situ* TEM measurements that 20 nm silver particles sublimate at 720 °C. Smaller nanoparticles sublimate at lower temperatures. Ding et al.[216] also described the sublimation of silver nanocubes with sizes of 100 nm and temperatures of 874 °C using *in situ* TEM.

Table 23 resumes the crystallographic properties of the silver nanoparticles. The lattice parameter *a* has values of 4.0884 Å and 4.0837 Å non-refined at room temperature. The unit cell expands by 1.43 % to 4.1477 Å and 4.1482 Å non-refined at 700 °C. The deviation of the Rietveld refined and non-refined values is between 0.1 % and 0.01 % depending on the temperature, and therefore the diffraction pattern resolution. The crystallite size grows from 11 nm to 99 nm because of recrystallization and sintering. Through sublimation of the silver

nanoparticles, no crystallographic data is obtained at 850 °C and at room temperature after annealing and subsequent cooling down to room temperature.

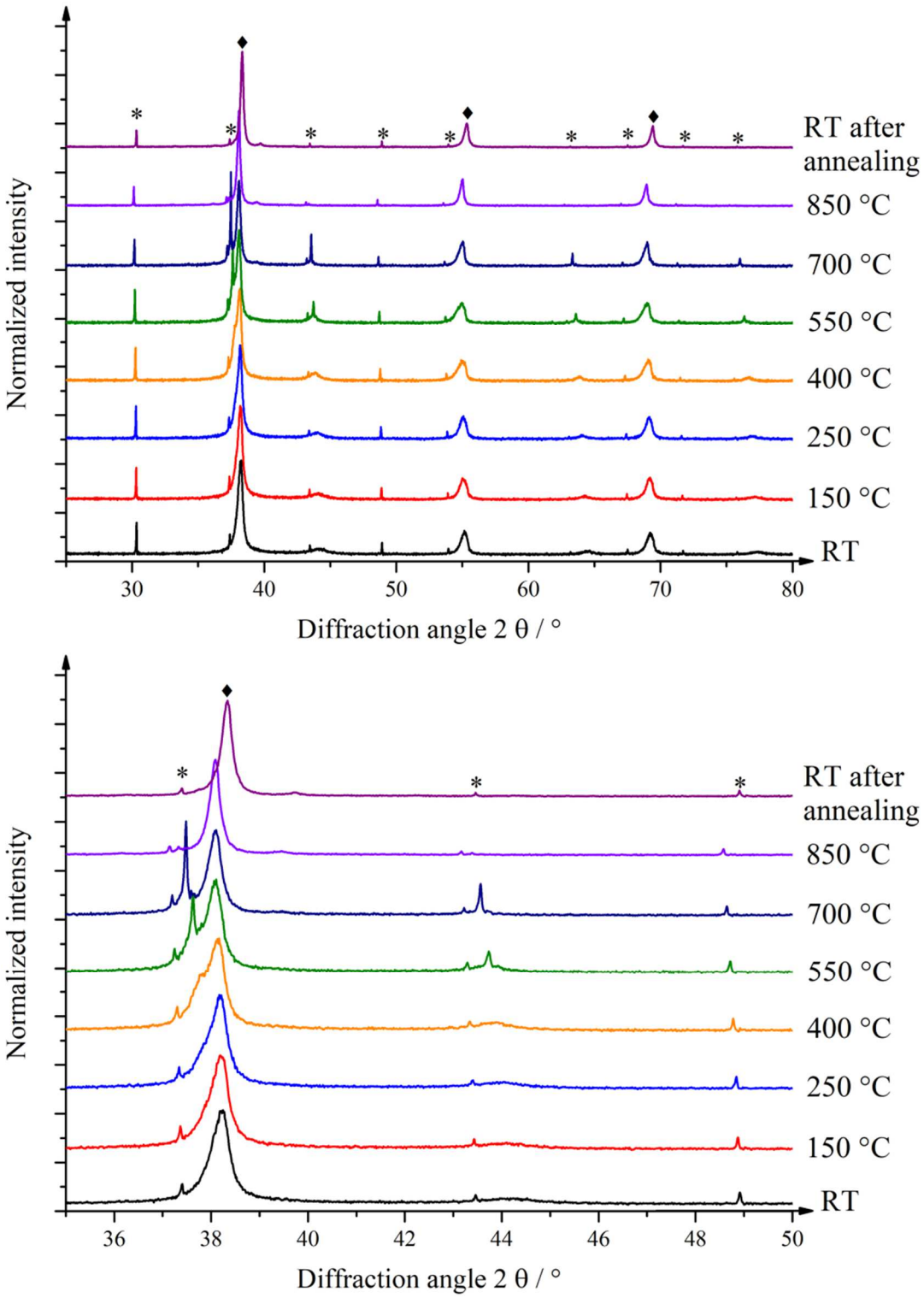

Figure 72: Diffraction patterns of silver nanoparticles at different temperatures and after annealing to 850 °C. The upper part shows the whole diffractogram collected, the lower part depicts the range from 35° to 50°. The asterisks mark the lanthanum hexaboride reflexes,[189] the diamonds denote the tantalum reflexes.[214]

Table 23: Crystallographic properties of the silver nanoparticles prepared by reduction with trisodium citrate and tannic acid during high-temperature X-ray diffraction. Because of sublimation of the nanoparticles, no diffraction signals and consequently no lattice parameters were obtained at 850 °C and at RT after annealing.

Temperature / °C	Lattice parameter *a* / Å		Cell volume *V* / Å^3	Crystallite size *D* / nm	Microstrain *ε* / %
	Rietveld refined	Non-refined			
25	4.0884(5)	4.0837	68.34(2)	11(1)	0.17(3)
150	4.0988(5)	4.0950	68.86(3)	12(1)	0.20(3)
250	4.1063(5)	4.1041	69.24(2)	13(1)	0.18(2)
400	4.1201(3)	4.1185	69.94(2)	17(1)	0.04(5)
550	4.1328(2)	4.1330	70.59(1)	33(1)	0.001(10)
700	4.1477(1)	4.1482	71.35(1)	99(5)	0.001(12)

As shown in Figure 67, a negative deviation from Vegard's law is observed if the fcc only model is applied for Rietveld refinement. Upon heating, a unit cell expansion takes place and the negative deviation decreases as depicted in Figure 73. At room temperature, the composition with the minimal lattice parameter is silver-gold 30:70 if Rietveld refined. The smallest lattice parameter in the non-refined calculation has the 50:50 composition. During the temperature increase to 550 °C, the highest deviation from Vegard's law is observed for the silver-gold 30:70 system in the non-refined calculation, whereas the Rietveld refined values show a nearly linear behavior. The comparison between the lattice parameters before and after annealing shows a strong negative deviation from Vegard's law before annealing and only a slight negative deviation after annealing and cooling down to room temperature (Fig. 73). Both models, Rietveld refined and non-refined, yield the same results. The curve shape is similar to the results obtained by Lubarda et al.[144] for bulk silver-gold alloys as well as to the lattice parameters obtained by Naidu et al.[217] for bulk gold and bulk silver-gold 50:50, and by Venudhar et al.[218] for bulk silver-gold 50:50. The results mean that annealing leads to recrystallization (crystallite growth) and the minimization of microstrain within the nanoparticles because of defect disappearing. The lattice constants become bulk-like. The comparison between Rietveld refined and non-refined cell parameters shows only small deviations. Thus, the non-refined calculation is perfectly suitable for first determinations of the lattice constants when Rietveld refinement is not accessible. For this purpose, the diffraction pattern must have a good resolution which allows a reliable calculation.

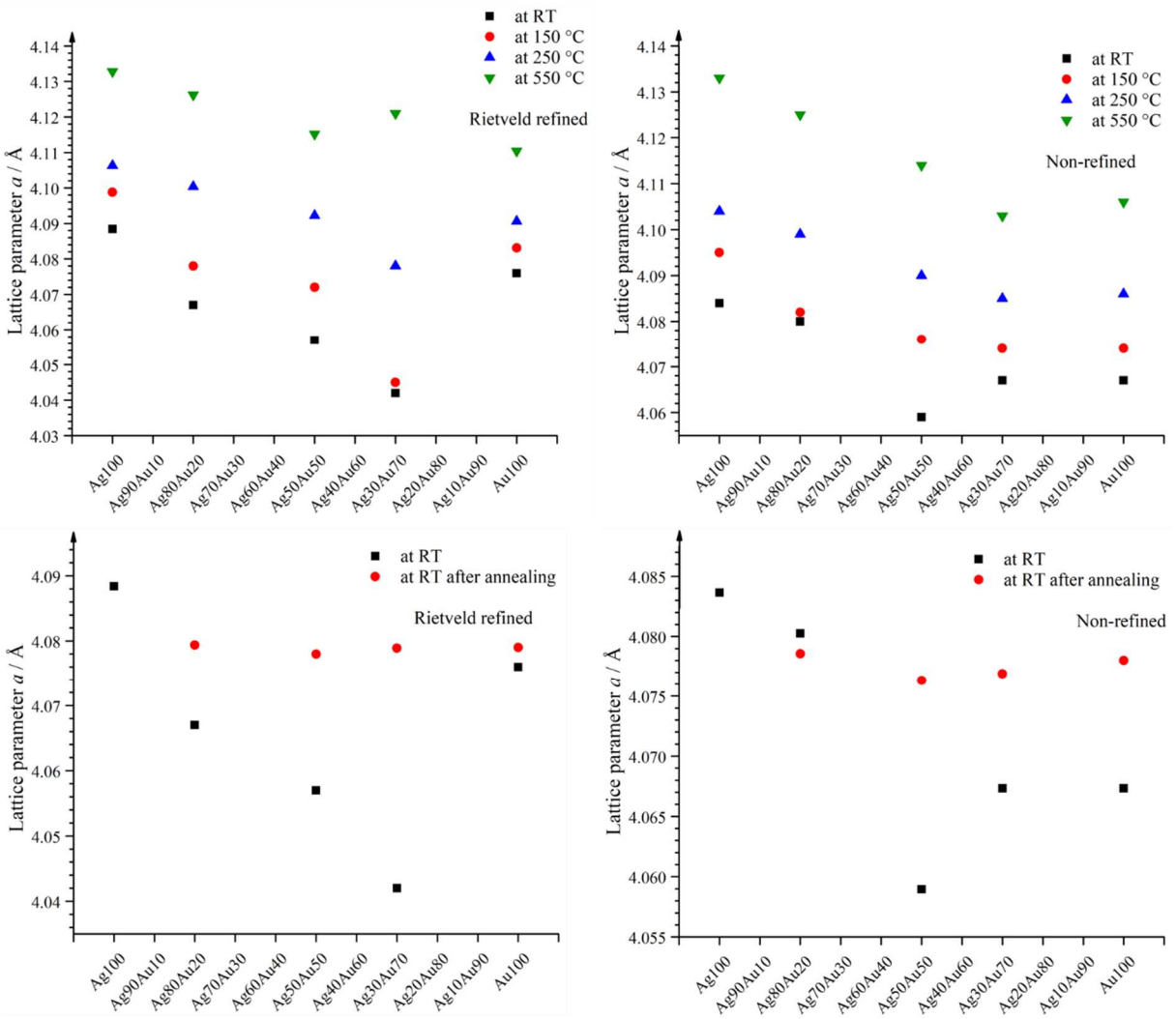

Figure 73: Vegard's law at different temperatures (upper graphs) and before and after annealing (lower graphs) of Rietveld refined (left) and non-refined (right) lattice parameters of the silver, gold, and silver-gold nanoparticles. Because of sublimation of the silver nanoparticles, no diffraction signals and consequently no lattice parameters were obtained at RT after annealing.

The obtained lattice parameters (refined and non-refined) are used to determine the linear thermal expansion coefficient α of silver, gold, and silver-gold nanoparticles. All samples are mixed with lanthanum hexaboride (LaB_6) as a stress-free, microcrystalline standard. To determine the suitability of the method, the linear thermal expansion coefficient of lanthanum hexaboride is calculated and compared to the literature. Figure 74 depicts the dependence of the lattice parameter on the temperature (left) and the linear thermal expansion coefficient versus the temperature (right).

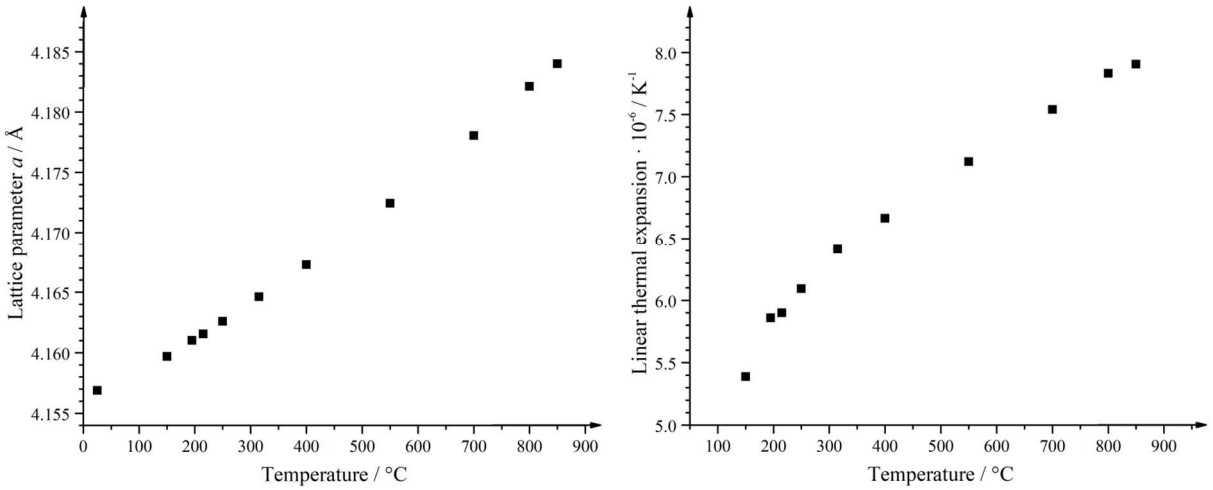

Figure 74: The lattice parameter versus temperature (left) and the linear thermal expansion coefficient versus temperature (right) graphs of lanthanum hexaboride.

The unit cell expansion of lanthanum hexaboride is not perfectly linear. At room temperature, the lattice parameter is 4.1569 Å which expands by 0.65 % to 4.1840 Å at 850 °C as shown in Table 24. The linear thermal expansion coefficient α from room temperature to a certain temperature (RT → T, integral determination) is calculated using the following formula with ΔL the length difference of the unit cells at different temperatures, L the initial unit cell length, and ΔT the temperature difference in Kelvin.

$$\alpha = \frac{\Delta L}{L \cdot \Delta T} \tag{14}$$

As seen in Figure 74, the expansion coefficient is not a constant value, but varies from $5.39 \cdot 10^{-6}$ K^{-1} at 150 °C to $7.91 \cdot 10^{-6}$ K^{-1} at 850 °C. Craciun et al.[219] found a value of $6.0 \cdot 10^{-6}$ K^{-1} at 27 °C and Sirota et al.[220] reported a value of $5.24 \cdot 10^{-6}$ K^{-1} at 47 °C. Xu et al.[221] calculated the volume thermal expansion coefficient $\alpha_V = 3\alpha$ of lanthanum hexaboride from 0 K to 1500 K and found a non-constant thermal expansion coefficient which fits the calculated values and the curve shape in this work. At 27 °C, the reported linear thermal expansion coefficient is $7.03 \cdot 10^{-6}$ K^{-1}. Linear thermal expansion coefficients from RT → T_1, T_1 → T_2 and so on (differential calculation) can be found in the appendix. All calculated values are in good agreement with the literature reported ones. Therefore, the determination of the linear thermal expansion coefficient leads to reliable results and can be applied to the silver-gold system.

Table 24: Lattice parameters *a* and the linear thermal expansion coefficients α (integral calculation) of LaB_6 at different temperatures as obtained from X-ray diffraction after Rietveld refinement.

Temperature / °C	Lattice parameter *a* / Å	Thermal expansion coefficient $\alpha \cdot 10^{-6}$ / K^{-1}
25	4.1569	-
150	4.1597	5.39
195	4.1610	5.86
215	4.1616	5.90
250	4.1626	6.09
315	4.1646	6.41
400	4.1673	6.67
550	4.1724	7.12
700	4.1781	7.54
800	4.1821	7.83
850	4.1840	7.91

The comparison of the unit cell expansion as a function of the temperature for the silver, gold, and silver-gold nanoparticles is given in Figure 75. The lattice constants of the silver and gold particles expand linearly in both, Rietveld refined and non-refined, systems, whereas the lattice constants of the alloyed particles do not. Especially the Rietveld refined values show a change of the slope between 150 °C and 250 °C. Therefore, the expansion appears not identical at every temperature.

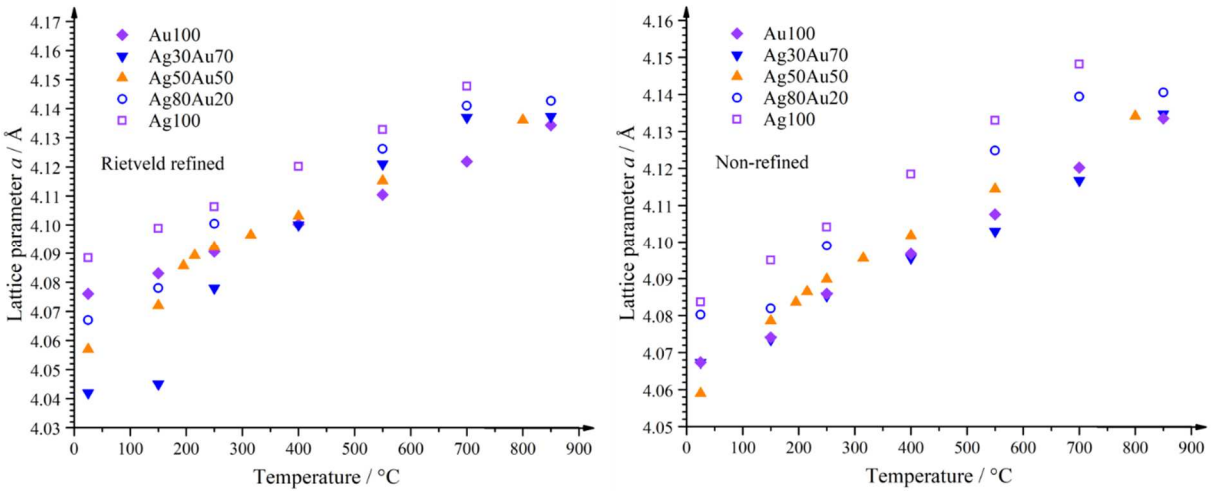

Figure 75: Lattice parameters of the silver, gold, and silver-gold nanoparticles versus temperature showing the unit cell expansion with temperature increase. On the left side: Rietveld refined values, on the right side: non-refined values.

The theoretical unit cell expansion of the silver, gold, and silver-gold nanoparticles is calculated from the lattice parameters at room temperature using the thermal expansion coefficients shown in Table 25, ref.[129] It is assumed that the expansion of silver and gold occurs linearly which is supported by the literature.[222-223] The obtained calculated values for the lattice parameters are plotted against the temperature (Fig. 76). In the same graphic, the X-ray-diffraction-measured lattice parameters are plotted as a function of the temperature and compared to each other. Also, Rietveld refined and non-refined values are compared. The expansion of gold nanoparticles is linear, but shows a steeper slope than predicted by the calculated values. It means that the nanoparticle lattice constants expand faster than the lattice constants of bulk gold. The silver-gold 30:70 alloy exhibits a non-linear expansion of the unit cell parameters. Up to 150 °C, the slope of the expansion is lower than predicted. Between 150 °C and 250 °C, the ascendance rate increases and is higher than expected. According to the values obtained by Rietveld refinement, there is no slope between 700 °C and 850 °C. The silver-gold 50:50 nanoparticles expand up to 250 °C much faster than predicted and show a linear dilatation after 250 °C. The silver-gold 80:20 nanoparticles behave like the silver-gold 30:70 particles if considering the Rietveld refined values. They show no linear expansion. Pure silver nanoparticles expand linearly, but have a steeper slope than predicted. The steeper than expected dilatation slope of the monometallic nanoparticles might originate from a lattice contraction which is found in nanoparticles. Upon heating, the lattice relaxes and the parameters approach the bulk lattice constants. From the obtained data for the lattice parameter expansion of the alloyed samples, it is assumed that the thermal expansion coefficient varies from temperature to temperature. The non-refined values correspond to the Rietveld refined numbers. Only a small discrepancy between the values is found in the silver-gold 30:70 sample where the curve shape of the Rietveld refined and non-refined results is not similar. The non-linear dilatation of the alloyed nanoparticles might be caused by the defects at the grain boundaries. With increasing temperature, the defects disappear. At around 250 °C, all nanoparticles show crystallite sizes which correspond to the particle sizes pointing to single crystalline particles. With by this means obtained values, the calculation of the linear thermal expansion coefficients of the monometallic and bimetallic samples is possible using Equation 14.

Table 25: Linear thermal expansion coefficients of bulk silver, gold, and silver-gold as found in the literature and theoretical calculated values for the silver-gold nanoalloys for comparison.

System	Temperature range / K	Thermal expansion coefficient $\alpha \cdot 10^{-6}$ / K^{-1}	Reference and comments
Gold	80 → 298	13.1	[217]
	100 → 600	12.4 – 14.6	[166] **nanoparticles**, from scanning high-energy electron diffraction
	283 → 338	13.4	[224]
	RT	14.2	[129]
	RT	14.0	[222] measured with a dilatometer
	RT	14.4	[31] **nanoparticles**, measured with X-ray scattering
	293 → 1100	13.6	[223] measured with a dilatometer
	293 → 1325	12.7	[223] obtained from XRD
	1000	17.5	[222] measured with a dilatometer
	Near 1336	19.8	[30] **nanoparticles** in Al_2O_3 matrix, calculations
Silver	80 → 298	17.9	[217]
	283 → 338	18.7	[224]
	RT	18.9	[129]
	293 → 1000	17.7	[223] measured with a dilatometer
	293 → 1228	18.1	[223] obtained from XRD
	Near 1234	29.5	[30] **nanoparticles** in Al_2O_3 matrix, calculations
Silver-gold 50:50 at%	80 → 298	13.8	[217]
Silver-gold 30:70 mol%	RT	15.8	Theoretical, calculated from ref.[129] ($x(Ag)\cdot\alpha(Ag) + x(Au)\cdot\alpha(Au) = \alpha_{calc.}$)
Silver-gold 50:50 mol%	RT	17.1	Theoretical, calculated from ref.[129]
Silver-gold 80:20 mol%	RT	18.1	Theoretical, calculated from ref.[129]

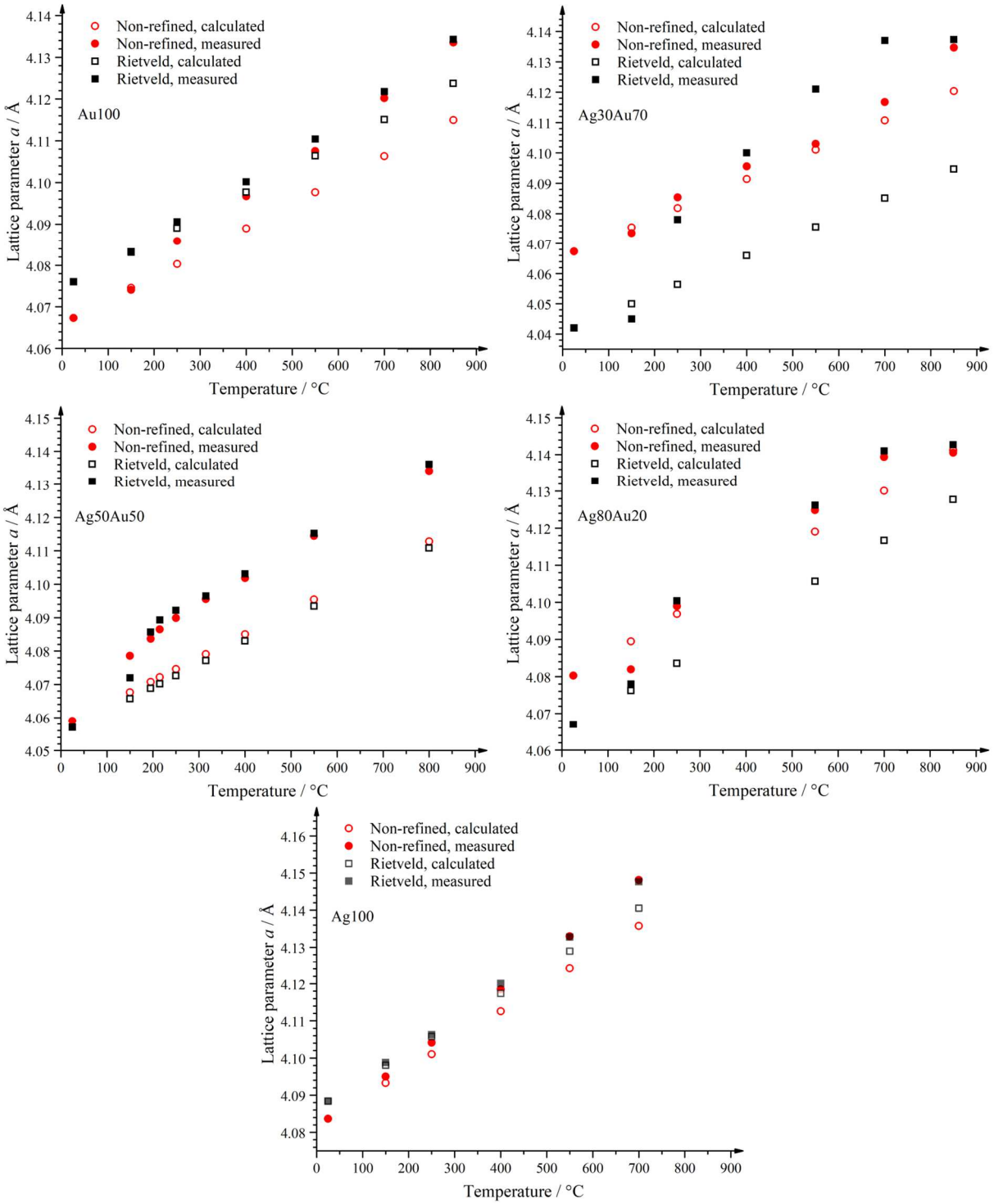

Figure 76: Theoretical and experimental unit cell expansions of the silver, gold, and silver-gold nanoparticles as a function of temperature. Rietveld refined and non-refined results are compared. Calculated means calculated from the lattice parameter at RT and Equation 14 with the corresponding linear thermal expansion coefficients of the pure metals. Measured means obtained from diffraction patterns at different temperatures.

The linear thermal expansion coefficients of silver, gold, and silver-gold nanoparticles are depicted in Figure 77. They are determined in two different ways: The first determination considers the expansion from room temperature to a certain temperature T_y and is denoted with RT → T_y (integral calculation). The second determination studies the lattice parameter dilatation from T_x to T_y, where T_y is the next higher temperature measured, and is indicated with $T_x \rightarrow T_y$ (differential calculation). Over the temperature range from room temperature to 850 °C, the thermal expansion coefficients of silver and gold are nearly constant. The values vary from $13.9 \cdot 10^{-6}$ K^{-1} to $17.3 \cdot 10^{-6}$ K^{-1} (Rietveld refined), alternatively from $13.2 \cdot 10^{-6}$ K^{-1} to $20.3 \cdot 10^{-6}$ K^{-1} (non-refined) for gold and from $20.4 \cdot 10^{-6}$ K^{-1} to $21.5 \cdot 10^{-6}$ K^{-1} (Rietveld refined), and alternatively from $22.2 \cdot 10^{-6}$ K^{-1} to $23.4 \cdot 10^{-6}$ K^{-1} (non-refined) for silver. This constancy correlates with the linearity of the unit cell expansion which is observed in Figure 76. The calculated numbers for the linear thermal expansion coefficients are summarized in Table 26. Compared to the values reported in the literature for bulk materials (Table 25), the results obtained in these experiments are slightly higher than for the bulk metals. This can be explained by the small size of the crystallites and the size of the nanoparticles. Gamarnik et al.[163] and Solliard et al.[166] showed that the unit cell contraction increases with decreasing particle size. This means that nanoparticles around 3 nm have smaller lattice parameters than particles with sizes of 40 nm of the same metal. Upon annealing, the nanoparticles recrystallize and show bulk-like lattice parameters. It is possible that the transition from small to bigger crystallites influences the unit cell constants resulting in higher thermal expansion coefficients.

The thermal expansion coefficients of the alloyed particles from room temperature to 850 °C (RT → T_y) are not constant, but vary with the temperature. Usually, the coefficients decrease with increasing temperature as shown by the graphs in Figure 77 (upper part) with the Rietveld refined and non-refined numbers. Comparing the obtained values for the silver-gold 50:50 composition with the literature value for the bulk alloy of $13.8 \cdot 10^{-6}$ K^{-1},[217] the experimental thermal expansion coefficient is at least two to three times larger for the nanoparticles. The explanation is the same as for the monometallic particles. Because of small crystallite sizes, the expansion is large in the beginning and decreases at higher temperatures owing to recrystallization. Yang et al.[225] reported an increase of the volume thermal expansion coefficient with a decreasing crystallite size for selenium and lead. Zhu et al.[226] also showed an increase of the linear thermal expansion coefficient with a decreasing grain or particle size for iron and copper. These results suggest a recrystallization of the nanoparticles with ascending temperatures and a crystallite size dependency of the thermal expansion coefficient. Another and additional explanation might be the alloy effect. The incorporation of foreign atoms into

the silver lattice leads to a contraction of the unit cell and a decrease of the lattice parameters. Upon heating, this contraction is relaxed after 250 °C resulting in a higher thermal expansion coefficient at lower temperatures and a smaller thermal expansion coefficient at higher temperatures.

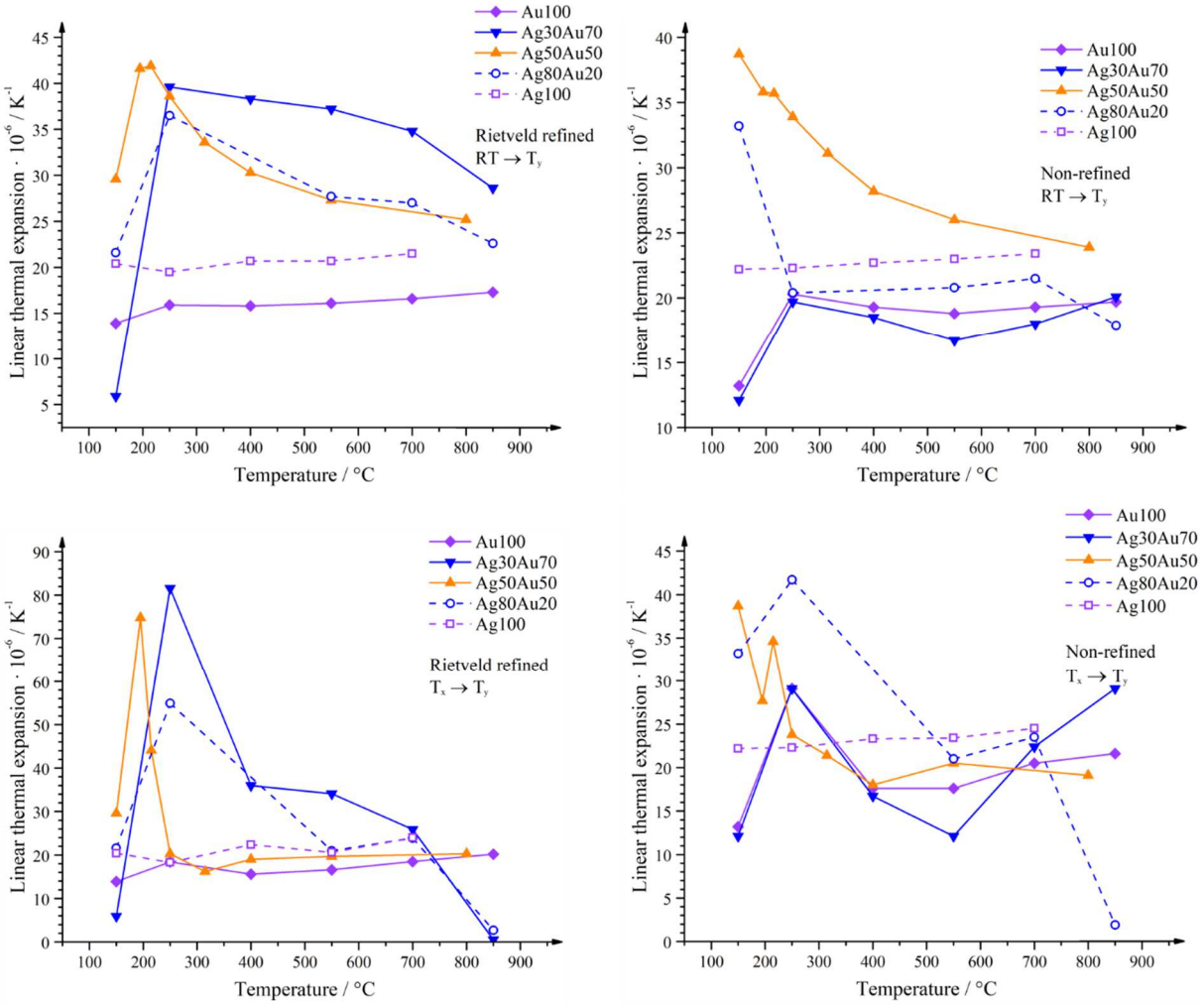

Figure 77: Linear thermal expansion coefficients of silver, gold, and silver-gold nanoparticles as a function of temperature. Left: Rietveld refined values, right: non-refined values. Upper part: values considered from room temperature to a certain temperature (integral calculation), lower part: values considered from T_x to T_y where T_y is the next higher temperature (differential calculation).

Over the temperature range from T_x to T_y, the linear thermal expansion coefficients of monometallic silver and gold are nearly constant as well. Only the non-refined calculation for Au100 shows two outliers at 150 °C and at 250 °C. The alloyed particles show a non-linear behavior of the thermal expansion coefficients. Like in the RT → T_y consideration, the highest thermal expansion coefficients are found in the region below 250 °C. The explanation is the same as mentioned above. The results are summarized in Table 26.

Table 26: Linear thermal expansion coefficients calculated from X-ray diffraction data with Rietveld refinement and without. The table continues on page 115.

Rietveld refined	Thermal expansion coefficient $\alpha \cdot 10^{-6} / K^{-1}$				
Temperature range / °C	Gold	Ag30Au70	Ag50Au50	Ag80Au20	Silver
25 → 150	13.9	5.9	29.6	21.6	20.4
25 → 195			41.6		
25 → 215			41.9		
25 → 250	15.9	39.6	38.6	36.5	19.5
25 → 315			33.6		
25 → 400	15.8	38.3	30.3		20.7
25 → 550	16.1	37.2	27.3	27.7	20.7
25 → 700	16.6	34.8		27.0	21.5
25 → 800			25.2		
25 → 850	17.3	28.6		22.6	
150 → 250	18.4	81.6		54.9	18.3
150 → 195			74.8		
195 → 215			44.1		
215 → 250			20.3		
250 → 315			16.2		
250 → 400	15.7	36.0			22.4
250 → 550				21.0	
315 → 400			19.0		
400 → 550	16.6	34.1	19.7		20.6
550 → 700	18.5	25.9		23.9	24.0
550 → 800			20.3		
700 → 850	20.2	0.5		2.7	

Table 26: Continued.

Non-refined Temperature range / °C	Thermal expansion coefficient $\alpha \cdot 10^{-6}$ / K^{-1}				
	Gold	Ag30Au70	Ag50Au50	Ag80Au20	Silver
25 → 150	13.2	12.1	38.7	33.2	22.2
25 → 195			35.8		
25 → 215			35.7		
25 → 250	20.3	19.7	33.9	20.4	22.3
25 → 315			31.1		
25 → 400	19.3	18.5	28.2		22.7
25 → 550	18.8	16.7	26.0	20.8	23.0
25 → 700	19.3	18.0		21.5	23.4
25 → 800			23.9		
25 → 850	19.7	20.1		17.9	
150 → 250	29.1	29.1		41.7	22.3
150 → 195			27.7		
195 → 215			34.6		
215 → 250			23.8		
250 → 315			21.4		
250 → 400	17.6	16.7			23.3
250 → 550				21.0	
315 → 400			18.0		
400 → 550	17.7	12.1	20.5		23.4
550 → 700	20.5	22.4		23.5	24.5
550 → 800			19.1		
700 → 850	21.6	29.1		1.9	

To summarize, the silver-gold nanoparticles are spherical and monodisperse with sizes of around 7 nm. The pure silver particles are 35 nm in diameter as already described by Ristig et al.[25-26] TEM images show twinned structures and EDX maps exhibit a gold-rich core with a silver-rich shell, but an overall alloy character with a gradient structure. The UV/vis and AAS confirm the presence of alloys with the desired compositions from silver-gold 10:90 to 90:10 mol%. The yield lies between 31 % and 68 %. Powder X-ray diffraction measurements in Debye-Scherrer geometry reveal that the fcc only modeling during Rietveld refinement does

not describe the reflex profiles properly. The defects existing between the crystallites are modeled as a bct phase. This results in a better description of the line profile. Regarding the lattice parameters as a function of composition using the fcc only model, a negative deviation from Vegard's law is obtained. When applying the fcc + bct model, the lattice parameters follow Vegard's law. Upon annealing, an expansion of the unit cell is observed on the one hand. On the other hand, the crystallite size and the microstrain decrease. The lattice parameters obtained after Rietveld refinement and non-refined are nearly identical showing a well-suited method of calculating the unit cell constants without Rietveld refinement if first considerations of a system are needed and the Rietveld method is not accessible. Silver nanoparticles sublimate in vacuum if heated to 850 °C. Before annealing, the lattice parameter deviation from Vegard's law is bigger than after annealing and cooling down to room temperature. This shows the elimination of defects because of recrystallization of the particles and sintering after 250 °C. The expansion of the unit cells of silver and gold nanoparticles is constant and linear, whereas the expansion of the alloys is not. The calculated thermal expansion coefficients of silver and gold agree well with so far reported values. For the silver-gold 50:50 composition, the obtained thermal expansion coefficient is larger than reported in the literature. This is the case because in this work, nanoparticles with small crystallites are considered. The value reported in the literature refers to the bulk alloy. No values for the 30:70 and 80:20 compositions are found which could be compared to the values obtained in this work.

5.3.2 Synthesis by trisodium citrate reduction

Silver-gold nanoparticles described in chapter 5.3.1 are prepared by trisodium citrate and tannic acid reduction and yield nanoparticles with sizes of around 7 nm in diameter which show a gradient structure with a gold-rich core and a silver-rich shell. To increase the size of the particles, trisodium citrate only is applied as the reducing agent since a weaker reductant is desired to enlarge the size. The aim is to synthesize particles with diameters between 30 nm and 40 nm to investigate the element distribution within the particles. The question is whether there is a difference between small and bigger particles concerning the element distribution of silver and gold. The nanoparticles are synthesized according to Mahl[177] with slight modifications and characterized by UV/vis spectroscopy, AAS, EDX, SEM, TEM, powder X-ray diffraction, DCS, DLS, measuring the Zeta potential, cyclic voltammetry (CV), and underpotential deposition (UPD). Cyclic voltammetry allows the differentiation between core-shell and alloyed particles. If core-shell particles are present, it is possible to determine whether

the shell is closed or broken if the core material can be oxidized at lower potentials than the shell material.[227] In alloys, the oxidation potential of the less noble metal is shifted to higher potentials because the less noble metal is partially enclosed by the nobler metal. It requires a higher potential to be oxidized. The resulting broad signal is due to the less noble metal leaching out of the particle. Furthermore, the molar composition can be calculated from the oxidation and reduction peaks after integration.[83, 146] The UPD of lead on the silver-gold nanoparticles is a method of depositing a monolayer of lead on the nanoparticle surface to investigate its composition and crystal facets.[228-230] Lead is used in this case because it crystallizes, like silver and gold, in the fcc structure with similar lattice constants. It is called underpotential deposition because lead, as a monolayer, is deposited at less negative potentials on foreign atoms than on bulk lead. The UPD also allows the size determination of particles if they are spherical and monodisperse.

The size distributions by DCS of the synthesized nanoparticles are depicted in Figure 78 with sizes between (27 ± 5) nm for silver-gold 70:30 to (34 ± 3) nm for the pure gold particles which have narrow distributions. Only the silver-gold 50:50 nanoparticles show a broad size distribution and diameters of (43 ± 15) nm. The high noise in the measurements of the samples silver-gold 50:50 and silver-gold 30:70 results from a low amount of sample during the measurements. The size distributions by DLS are shown in Figure 79. The DLS overestimates the sizes of the particles because of the hydrodynamic diameter, so the particles appear larger than they really are. The sizes vary from 30 nm for the pure gold particles to 74 nm for the silver-gold 50:50 particles if considering the Z-average (Table 27). The Z-average is an average value which is determined from the whole size distribution curve, even if the distribution is bimodal. That is the case for the silver, gold, and silver-gold 30:70 nanoparticles. Although the PDIs of those samples lie over 0.3, the Z-average appears small because of the presence of small (10 nm and below) particles. The hydrodynamic diameter of the particles regarding the main peak shows sizes of (54 ± 19) nm for silver-gold 70:30 to (98 ± 49) nm for silver-gold 50:50, both with a monomodal size distribution. It is assumed that the bimodal distributions result from uncertainties during the measurements because no particles with sizes of 10 nm and smaller are observed during scanning and transmission electron microscopy. The Zeta potentials of the samples at pH 7 are negative because the silver particles are capped with trisodium citrate and gold as well as the alloyed particles are recapped with PVP, but are still containing a certain amount of trisodium citrate on their surface.

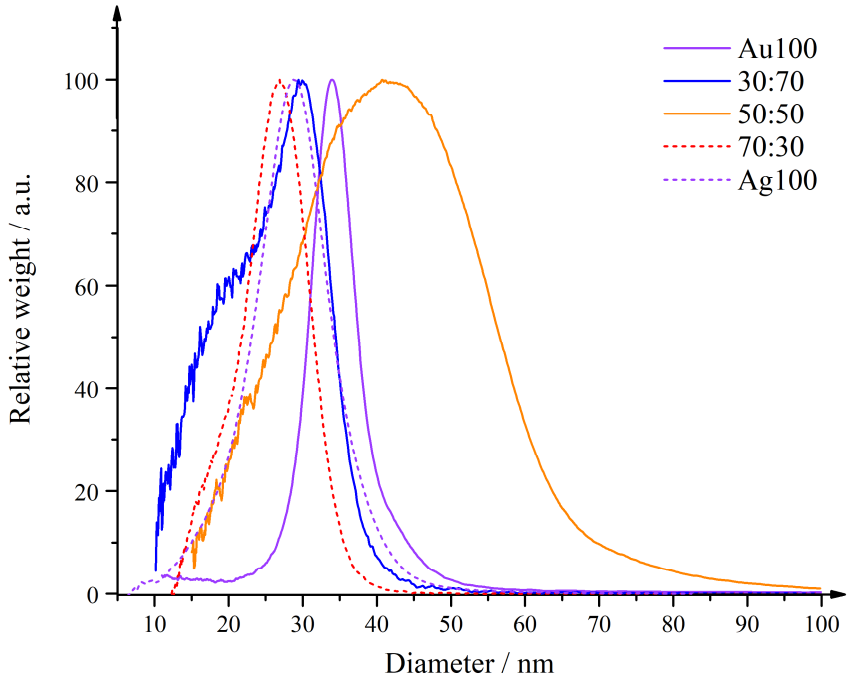

Figure 78: Size distribution of the silver, gold, and silver-gold nanoparticles reduced by trisodium citrate as obtained by differential centrifugal sedimentation. The noise in the Ag:Au 30:70 and 50:50 measurements results from low sample amounts.

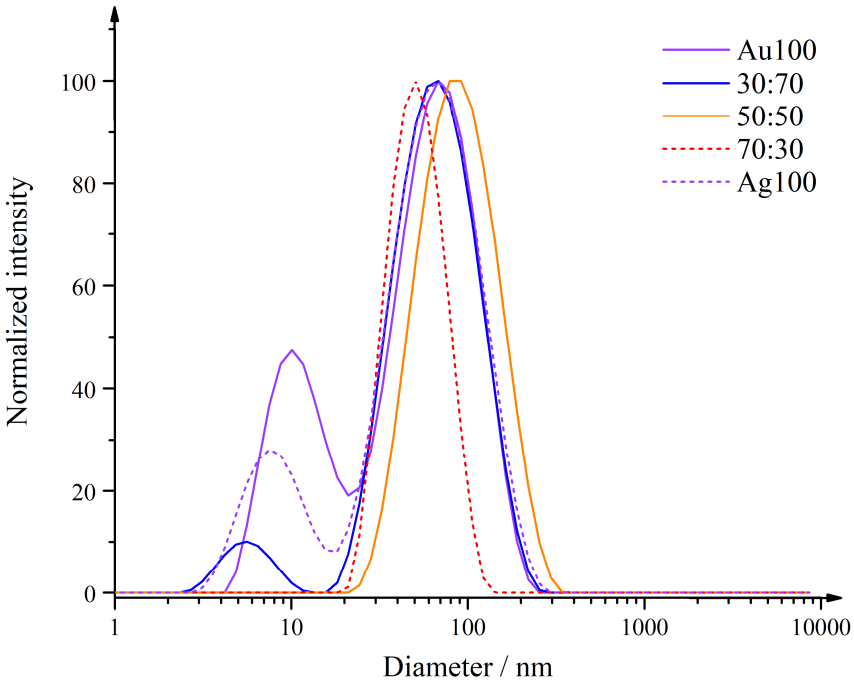

Figure 79: Size distribution of the silver, gold, and silver-gold nanoparticles reduced by trisodium citrate as obtained by dynamic light scattering.

Table 27: Summarized size distributions of the silver, gold, and silver-gold nanoparticles as obtained by DCS and DLS (by intensity) with their corresponding PDIs, Zeta potentials at pH 7, and standard deviations.

Nominal composition Ag:Au	Diameter / nm by DCS	Z-average / nm by DLS	Peak size / nm by DLS	PDI	Zeta potential / mV
0:100	34 ± 3	30	74 ± 37	0.512	-18 ± 10
30:70	27 ± 10	49	74 ± 38	0.312	-27 ± 11
50:50	43 ± 15	74	98 ± 49	0.229	-32 ± 12
70:30	27 ± 5	47	54 ± 19	0.145	-31 ± 25
100:0	29 ± 5	33	75 ± 41	0.565	-40 ± 17

The histograms obtained from measuring 80 to 90 particles out of scanning electron micrographs are shown in Figure 80. The corresponding values are summarized in Table 28. The sizes lie, as desired, between 30 nm and 40 nm. The only exception are the gold particles with a size of (47 ± 6) nm. The diameters obtained from DCS are slightly underestimated which is the reason why they appear smaller than the sizes obtained from SEM.

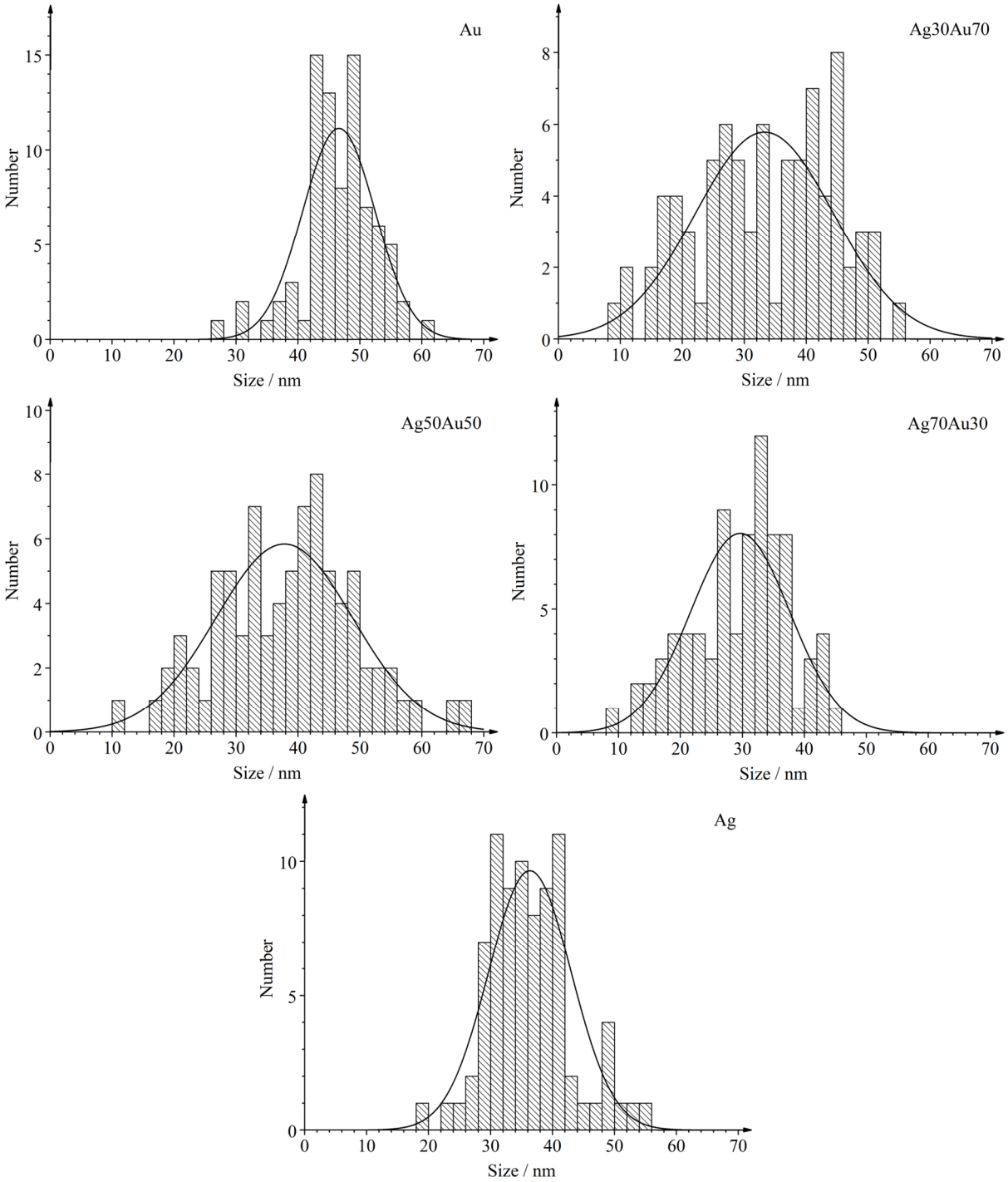

Figure 80: Particle size distribution of silver-gold nanoparticles in the compositions of 0:100, 30:70, 50:50, 70:30, and 100:0 prepared by reduction with trisodium citrate as measured by SEM.

Table 28: Size distributions of the silver-gold nanoparticles in the compositions of 0:100, 30:70, 50:50, 70:30, and 100:0 prepared by reduction with trisodium citrate as obtained by scanning electron microscopy and their corresponding standard deviations.

Nominal composition Ag:Au	Diameter / nm
0:100	47 ± 6
30:70	33 ± 11
50:50	38 ± 11
70:30	30 ± 8
100:0	36 ± 7

The nanoparticles have a mostly spherical morphology, although some platelets, rods and elongated platelets (especially in the gold sample) are also present (Figure 81, 82). The particles show several domains which indicate polycrystallinity. This is in good agreement with previous studies on silver nanoparticles[21] and gold particles.[28] There are also monocrystalline particles (Figure 82, gold) and particles with stacking faults (Figure 82, silver) present.

TEM images show no particles with sizes of 10 nm and smaller. Figures 83 to 85 depict high-angle annular dark field (HAADF) images, their corresponding individual particle EDX maps, and HRTEM images of the silver-gold nanoparticles. The EDX maps show silver-rich patches on the surface of the nanoparticles. In the HAADF-STEM images, those patches appear as low-contrast features because of the specific Z-contrast conditions. The number of the silver-rich patches increases with the silver molar fraction. Aside from the silver segregation on the surface, the EDX maps show an overall alloy character of the particles. Wei et al.[231] and Guisbers et al.[27] reported such a silver segregation on the surface of alloyed nanoparticles. As opposed to the investigation of gold-coated silver nanocubes by HAADF-STEM, reported by Yang et al.,[232] where the Z-contrast showed a clear border between the silver-core and the gold-shell, no distinct border is observed in the spherical particles because of their less regular surface.

The characteristics of the element distribution are ascribed to the reduction process. During the nanoparticle synthesis, both precursors (silver nitrate and tetrachloridoauric acid) are simultaneously reduced by trisodium citrate. Because of the nobler character of gold and its higher redox potential, Au^{3+} ions are reduced faster to gold atoms than Ag^{+} ions to silver atoms (redox potentials at pH = 0: Au^{3+}/Au +1.498 V and Ag^{+}/Ag +0.7991 V).[113] Consequently, gold seeds are formed first which is discernible by the red color of the dispersion. With proceeding reaction, a color change to orange is visible after 20 minutes that indicates the beginning of Ag^{+}

reduction. The remaining Au^{3+}/Ag^{+} ions are reduced within the next 40 minutes. The late Ag^{+} reduction leads to the silver patches on the particle surface as observed in the EDX maps. Because of signal superposition and a limited resolution, it is not easy to derive from EDX maps whether the surface layer consists of silver only or is alloyed. Therefore, underpotential deposition is applied which will be explained later.

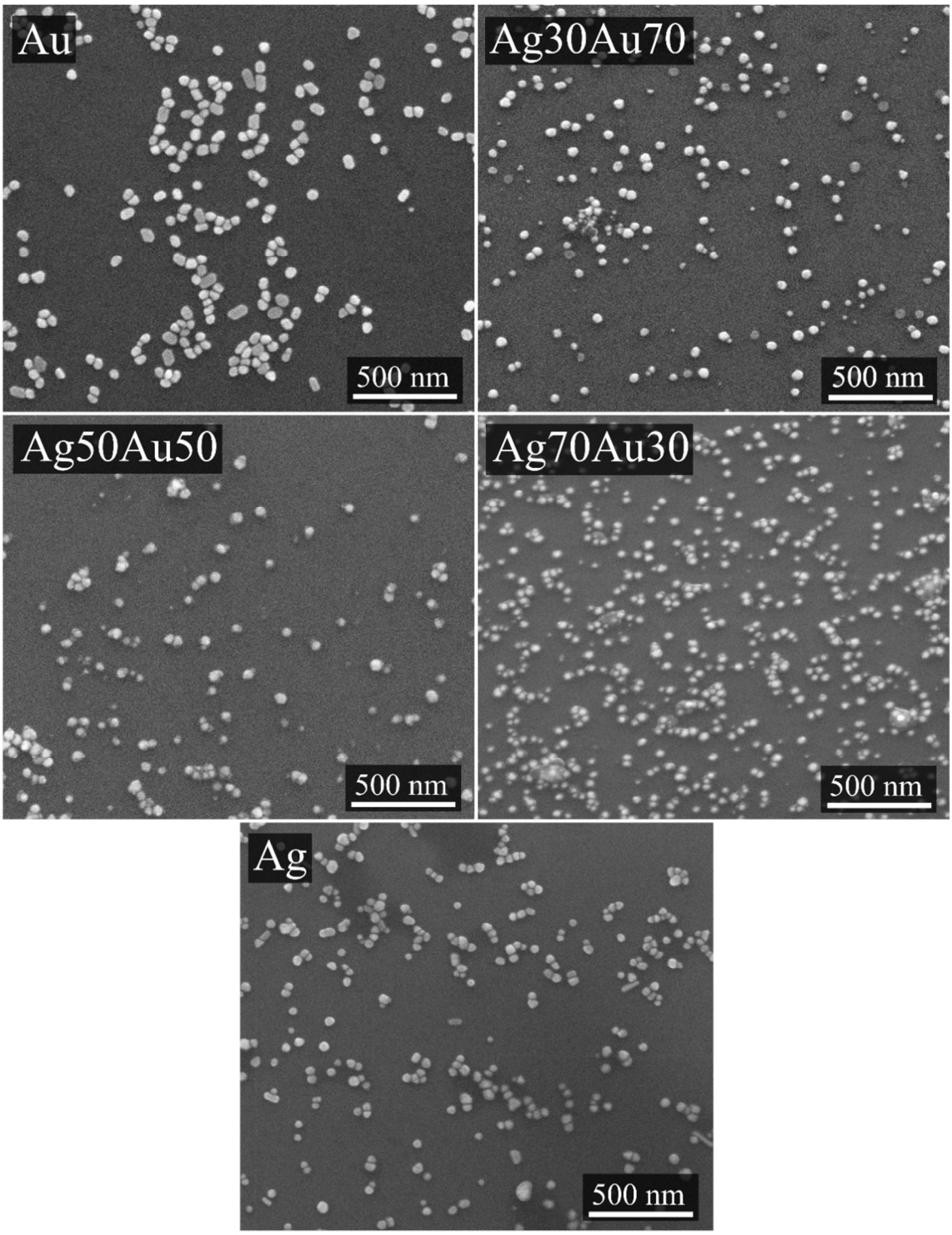

Figure 81: Scanning electron micrographs of the silver-gold nanoparticles in the compositions of 0:100, 30:70, 50:50, 70:30, and 100:0 prepared by reduction with trisodium citrate.

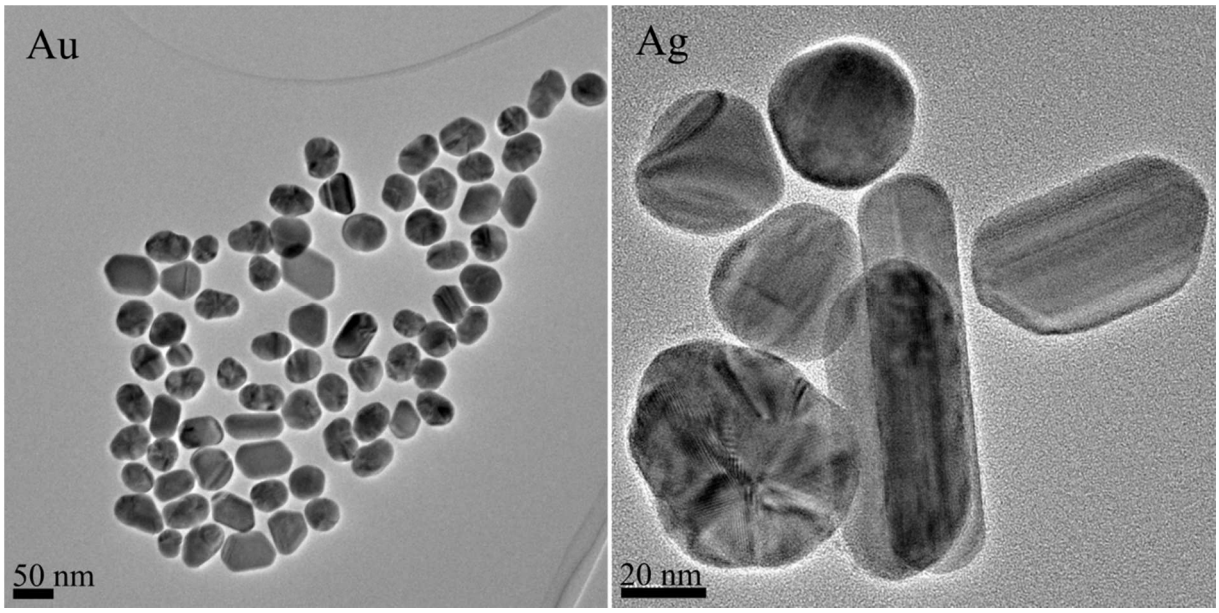

Figure 82: Transmission electron micrographs of gold (left) and silver (right) nanoparticles prepared by trisodium citrate reduction.

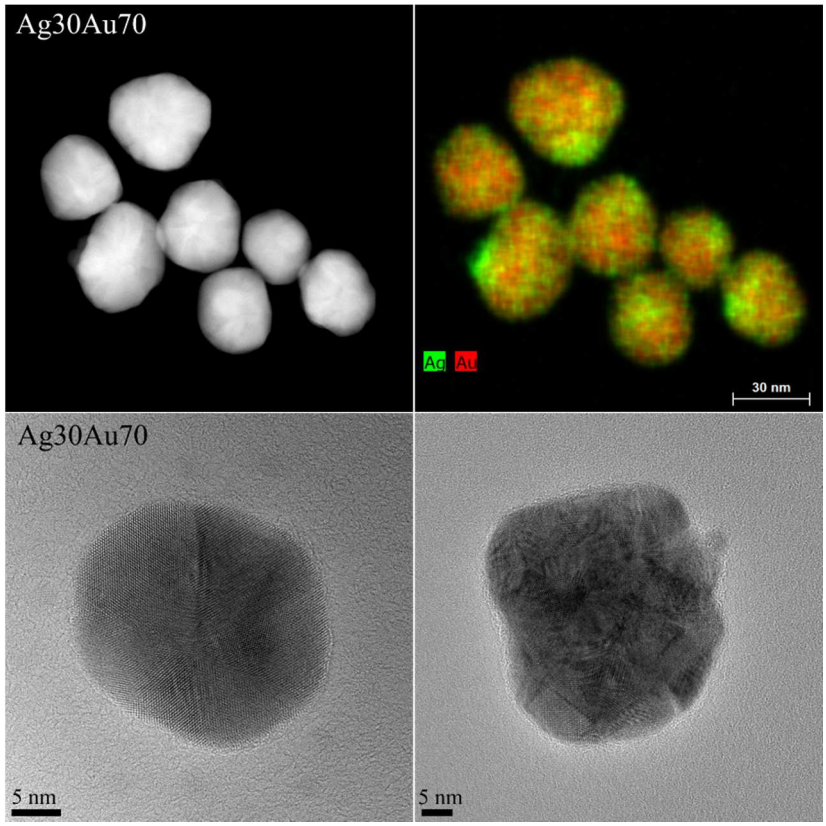

Figure 83: HAADF-STEM image, corresponding EDX map, and HRTEM images of representative Ag30Au70 nanoparticles.

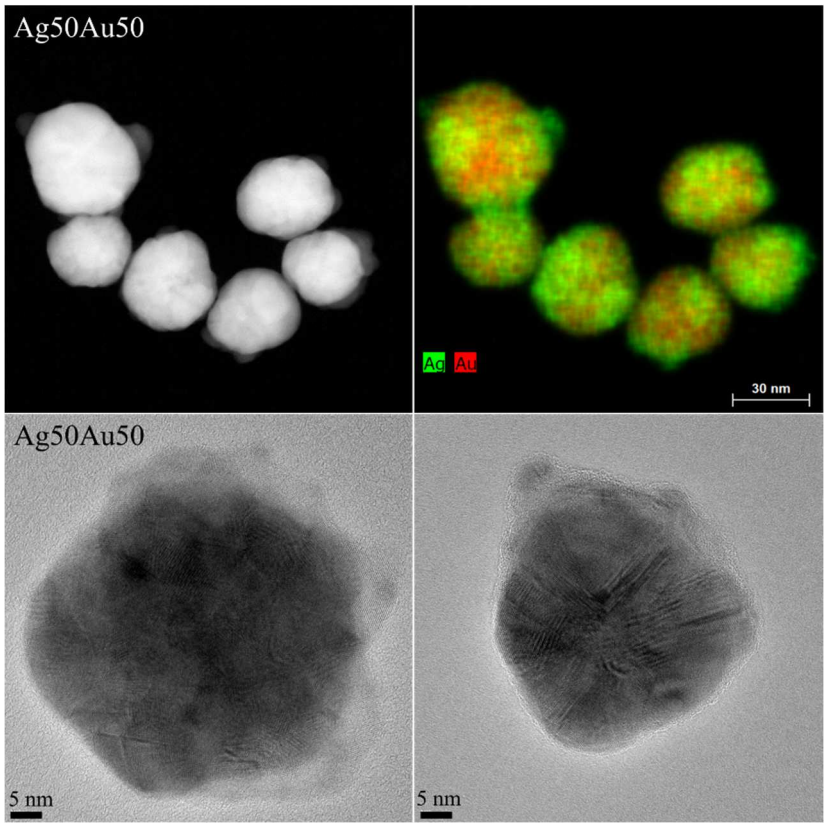

Figure 84: HAADF-STEM image, corresponding EDX map, and HRTEM images of representative Ag50Au50 nanoparticles.

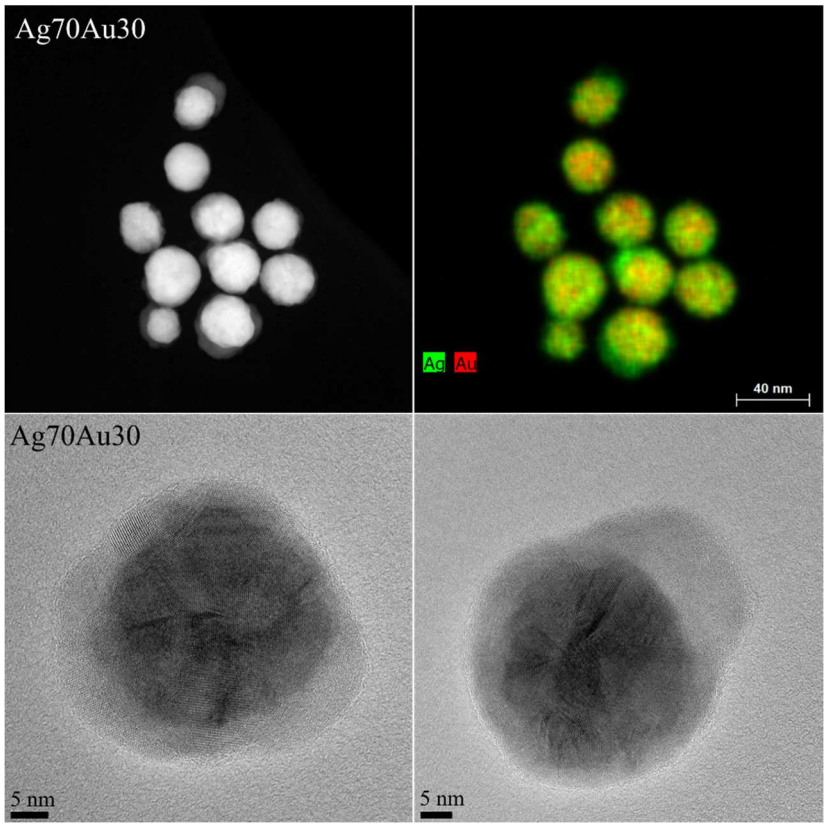

Figure 85: HAADF-STEM image, corresponding EDX map, and HRTEM images of representative Ag70Au30 nanoparticles.

UV/vis spectroscopy gives information about the element distribution in bimetallic nanoparticles. The location of the absorption maximum and the absorption band shape allow predictions on the presence of alloys or core-shell particles. If only one absorption band is obtained which lies between the maxima of the pure metals, then, an alloy is present. The location of the absorption maximum indicates the molar composition of the system and shows a linear dependence if plotted against the composition as depicted in Figure 86. The absorption maxima of the bimetallic systems lie nearly perfectly on the regression line made by connecting the absorption maxima of pure silver and pure gold particles which assumes the presence of the desired compositions. The UV/vis spectra of the silver-gold nanoparticles indicate an alloy character. In a core-shell system, two absorption bands should be visible, one for the gold absorption at 520 nm and one for the silver absorption around 400 nm. If the shell is thick enough, only the absorption characteristic for the shell material should be visible. In this instance, it should be the silver absorption at 400 nm. Since this is not the case, the presence of a core-shell system is excluded. The obtained spectra have narrow shapes which correlates with the mostly narrow size distributions obtained from DCS and SEM.

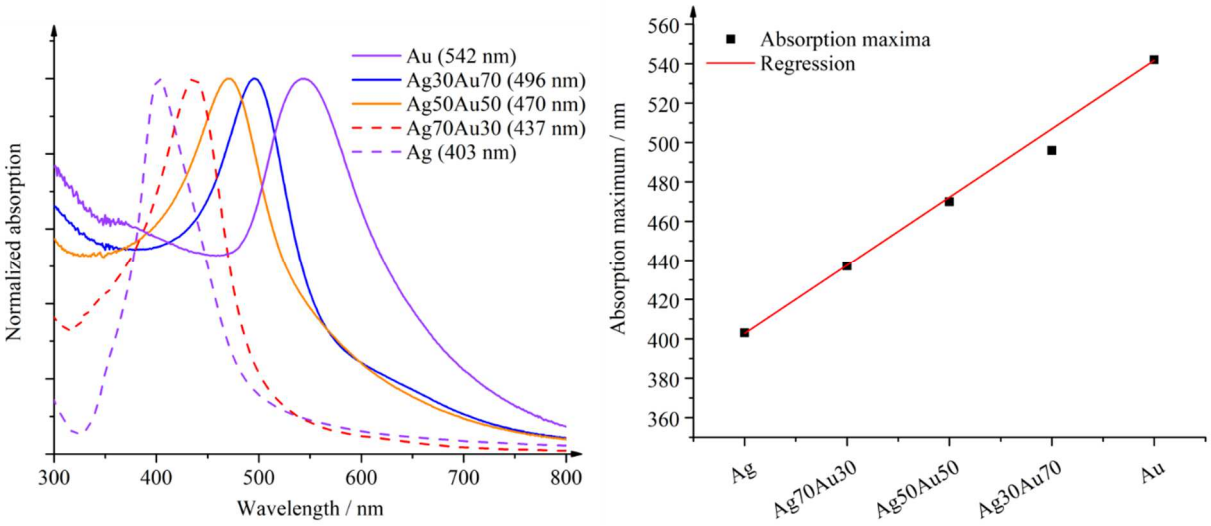

Figure 86: UV/vis spectra (left) and absorption maxima dependence on composition (right) of silver, gold, and silver-gold nanoparticles prepared by trisodium citrate.

The colors of the nanoparticle dispersions are shown in Figure 87. Pure silver particles appear yellow and pure gold particles have a red to rose color. The bimetallic nanoparticles show a yellow (70:30), an orange (50:50), and a dark orange (30:70) color depending on their composition.

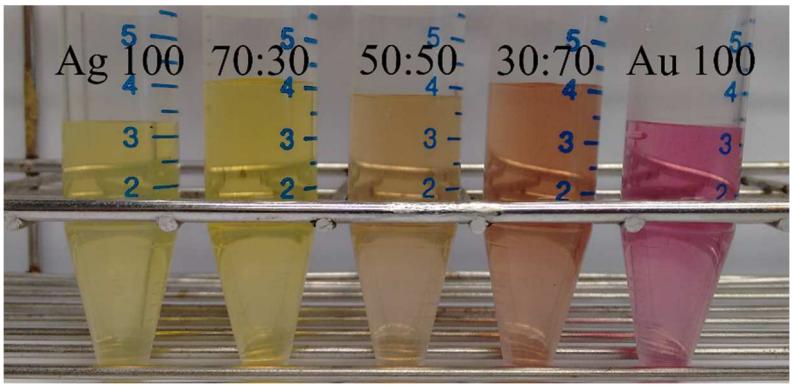

Figure 87: Photograph of the silver, gold, and silver-gold nanoparticles in the compositions 30:70, 50:50, 70:30 prepared by trisodium citrate reduction.

The exact molar compositions are determined by AAS, EDX, and cyclic voltammetry and given in Table 29. All electrochemical measurements and calculations were carried out by Christian Rurainsky from the group of Electrocatalysis & Functional Materials of Jun.-Prof. Dr. Tschulik, Department of Chemistry and Biochemistry, Ruhr-University Bochum. The values obtained from AAS, EDX, and CV are comparable and lie in the intended composition range. They confirm the assumption made from the UV/vis measurement that the particles have the desired compositions. The composition determination from CV is performed by integration of the oxidation (cathodic) peaks and obtaining the total charge by using the following equation with Q the total charge, I the current, E the applied potential and v the scan rate.

$$Q = \frac{\int I dE}{v} \tag{15}$$

For the determination of the silver content, the silver reduction peak is integrated and the resulting charge is divided by $z \cdot F$, where $z = 1$ is the number of transferred electrons per atom and F the Faraday constant. This yields the amount of substance for silver in mole. The charge obtained from the silver reduction peak is subtracted from the total charge (obtained from the silver and gold oxidation peaks). The remaining charge is used to calculate the amount of substance for gold by, again, dividing the charge by $z \cdot F$ with $z = 1.9$ (see below).

Table 29: Molar composition of the alloyed nanoparticles by AAS, EDX, and cyclic voltammetry (CV).

Sample	AAS Ag:Au / mol%	EDX (TEM) Ag:Au / at%	CV Ag:Au / mol%
Ag30Au70	20:80	31:69	19:81
Ag50Au50	47:53	49:51	48:52
Ag70Au30	69:31	70:30	76:24

The cyclic voltammograms are shown in Figure 88. For a better comparison, the graphs of silver and gold are normalized to their oxidation peaks, and the graphs of the silver-gold 30:70, 50:50, and 70:30 are normalized to their silver reduction peak, respectively. The oxidation peak in the pure silver sample is found at about +0.12 V and is associated with the formation of slightly soluble silver chloride[83] (Equation 16). In the reverse cycle, the reduction to silver occurs at +0.01 V.

$$Ag + Cl^- \rightleftharpoons AgCl + e^- \quad (16)$$

Upon oxidation of gold, two soluble species (Au^+ and Au^{3+})[233-234] are generated at +1.05 V as shown in Equations 17 and 18. The oxidation releases 1.9 electrons per gold atom on average. The ions are reduced at +0.39 V in the reverse cycle.

$$Au + 2\,Cl^- \rightleftharpoons [AuCl_2]^- + e^- \quad (17)$$

$$Au + 4\,Cl^- \rightleftharpoons [AuCl_4]^- + 3\,e^- \quad (18)$$

The silver oxidation peak in the bimetallic samples is shifted to higher potentials compared to the pure silver sample, indicating an alloy character of the particles.[83] The peak shape of the silver oxidation peak broadens with decreasing silver content through the leaching of enclosed silver atoms out of the particle because of the alloyed structure. A silver oxidation pre-peak is observed in the silver-rich Ag70Au30 sample which is attributed to the silver atom aggregates on the nanoparticle surface, also observed from EDX maps. Earlier studies by Saw et al.[83] on smaller alloyed nanoparticles (14 nm) did not show this effect. The explanation lies in the different sizes of the investigated particles and the application of distinct reducing agents (trisodium citrate and tannic acid for the smaller, and only trisodium citrate for the bigger particles) which results in differing element distributions within the nanoparticles. The slope of the gold oxidation peak in the bimetallic nanoparticles is steeper than in the pure gold sample because the former enclosed silver atoms are abruptly oxidized as soon as the gold atoms are oxidized through an overpotential in comparison to the equilibrium potential.

Figure 89 depicts the cyclic voltammograms recorded during underpotential deposition of lead on the nanoparticles. The left diagram depicts the UPD on pure silver and pure gold nanoparticles with their corresponding stripping peaks. UPD experiments on gold single crystals showed that gold (111), (100), and (110) facets exhibit deposition and stripping peaks at different potentials.[235] The sharp stripping peak at -0.97 V is assigned to the gold (111) facet and the broad peak at -0.81 V to the (110) facet.[230] No peak for the gold (100) facet is observed.

With this method, the surface area and the different surface sites of nanoparticles can be investigated. Lead deposition on silver nanoparticles shows just one peak in the experiments in this work which cannot be attributed to a specific facet. The UPD on the bimetallic particles gives one deposition peak lying at the same position as the lead deposition peak on a silver surface which indicates that the surface consists of silver atoms only. Similar behavior was reported by Kamundi et al.[228] for spherical alloyed silver-gold nanoparticles. These results show that the surface of the particles is not alloyed, but monometallic silver.

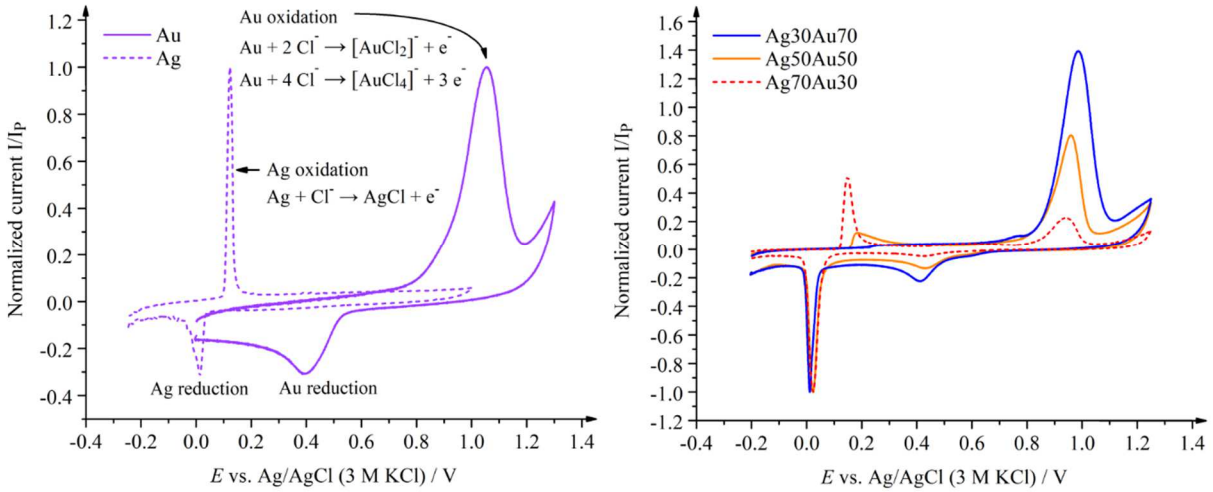

Figure 88: Cyclic voltammograms of the pure silver and gold nanoparticles (left) and of the alloyed nanoparticles Ag30Au70, Ag50Au50, and Ag70Au30 (right).

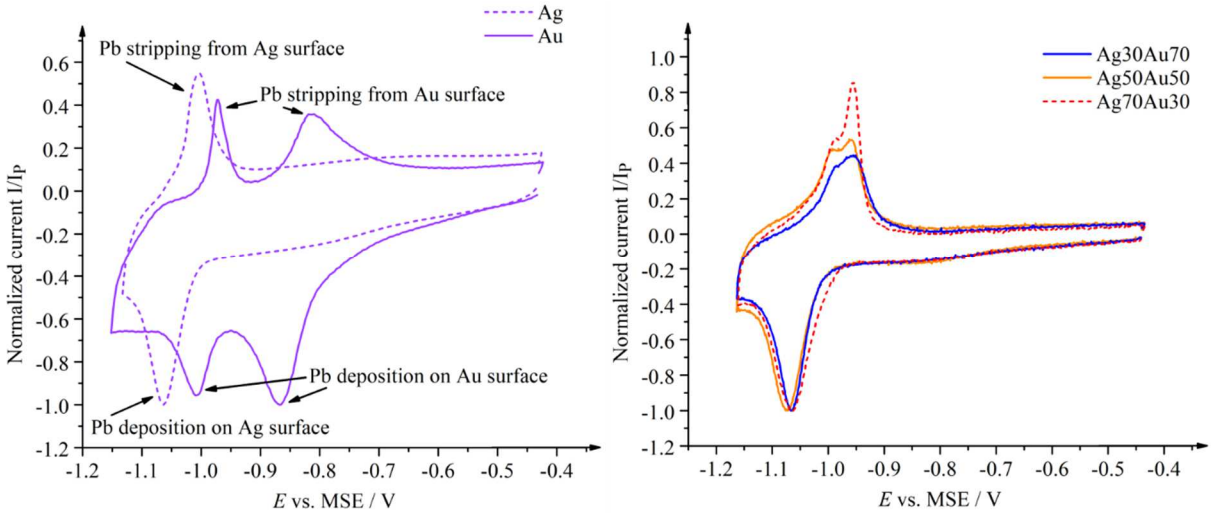

Figure 89: Underpotential deposition (UPD; Pb) voltammograms of the pure silver and gold particles (left) and of the samples Ag30Au70, Ag50Au50, and Ag70Au30 (right).

To obtain the nanoparticle size, the lead deposition peak is integrated to calculate the total transferred charge *Q* during the lead monolayer formation. For the silver and gold surfaces *S*, a charge to surface ratio of 330 µC/cm^2 is assumed for the lead monolayer.[236] The nanoparticles

are anodically stripped from lead in hydrochloric acid to determine the particle volume *V*. The particle diameter *d* is calculated by Equation 19. The particles are assumed as ideal spheres and are averaged over the whole sample. The obtained sizes are: (38 ± 3) nm for silver-gold 30:70, (37 ± 2) nm for silver-gold 50:50, and (26 ± 2) nm for silver-gold 70:30. They match the sizes by DCS, DLS, and SEM very well. The sizes for the monometallic silver and gold nanoparticles were not determined because of their not ideal spherical morphology observed from TEM and SEM.

$$d = 6 \cdot \frac{V}{S} \tag{19}$$

The powder diffraction patterns of the silver, gold, and silver-gold nanoparticles are depicted in Figure 90. All samples show reflex broadening indicating nanocrystallinity. In contrast to the smaller silver-gold particles reduced by trisodium citrate and tannic acid (Fig. 62), the reflexes appear slightly narrower. This means a bigger crystallite size and a smaller microstrain. Reflex broadening is not only caused by the crystallite size, but also by the microstrain within a particle and consequently the number of defects.

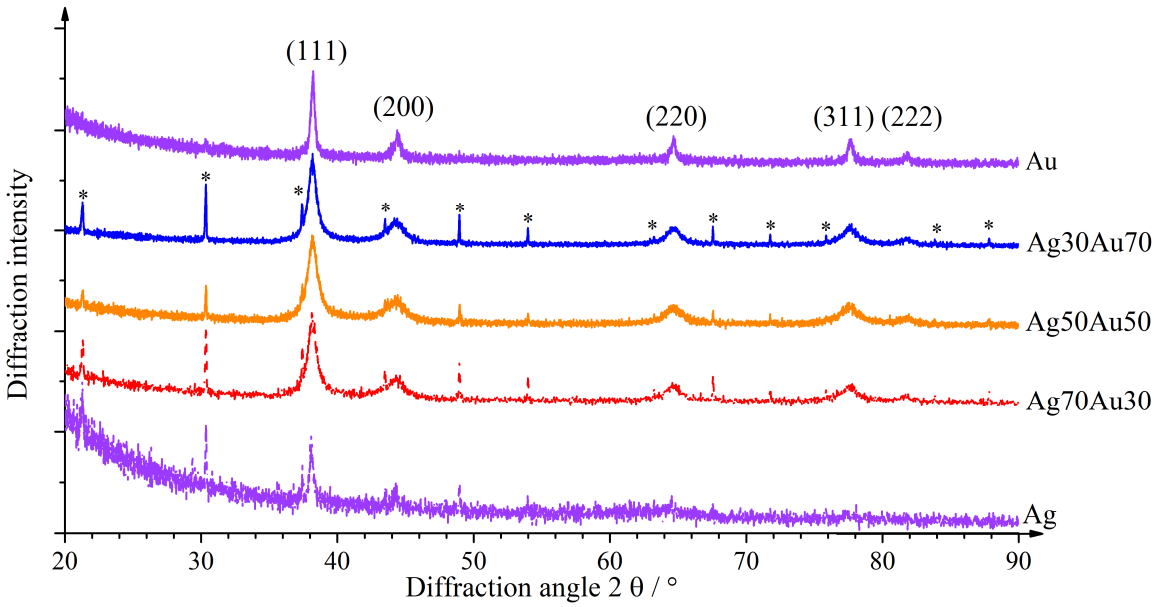

Figure 90: Diffraction patterns of the silver, gold, and silver-gold nanoparticles prepared by trisodium citrate reduction. The asterisks mark lanthanum hexaboride reflexes (PDF 00-034-0427).[189]

Table 30 summarizes the crystallographic properties of the samples. Notably, the crystallite sizes of the pure particles are twice as big as the crystallite sizes of the alloyed particles. The smallest crystallites are found in the silver-gold 50:50 composition with a value of 11 nm. Compared to the nanoparticle sizes, all particles are polycrystalline because the crystallite sizes are smaller than the particle sizes as shown in Tables 27 and 28. Contrary to the crystallite size,

the microstrain is smallest in the pure silver and gold nanoparticles and highest in the silver-gold 50:50 sample. This is because the microstrain within a unit cell increases upon incorporation of foreign atoms with slightly differing atomic radii. The atomic radius of silver with a value of 1.445 Å is marginally larger than the radius of gold with 1.442 Å.[113] With the incorporation of silver atoms into the gold lattice, electronic interactions of the outer electron shells of the silver atoms with the surrounding gold atoms occur which lead to a contraction of the silver atoms. Those become smaller than the gold atoms.[144] Thus, the distortion of the unit cell is highest in the silver-gold 50:50 composition resulting in a smaller unit cell volume and smaller lattice parameters which increase the microstrain as reported by Lubarda et al.[144] and Ristig et al.[25]

Table 30: Crystallographic properties of the silver, gold, and silver-gold nanoparticles prepared by trisodium citrate reduction.

Nominal composition Ag:Au	Lattice parameter a / Å	Cell volume V / Å^3	Crystallite size D / nm	Microstrain ε / %
0:100	4.0747(5)	67.65(3)	28(3)	0.05(1)
30:70	4.0778(2)	67.81(1)	13(1)	0.28(1)
50:50	4.0771(2)	67.77(1)	11(1)	0.31(1)
70:30	4.0788(2)	67.86(1)	12(1)	0.24(1)
100:0	4.0860(4)	68.22(2)	28(1)	0.02(1)

The lattice parameters for the silver, gold, and silver-gold nanoparticles as a function of composition compared to Vegard's law and bulk silver and gold are given in Figure 91. A negative deviation from Vegard's law is received. The lattice parameters denoted with 'literature' refer to bulk materials. As mentioned earlier, Solliard et al.[166] and Gamarnik et al.[163] reported a decrease of lattice parameters of gold particles with the particle size compared to the bulk material. The authors explain this observation by the occurrence of surface stress and lower repulsive forces between the atoms in smaller nanoparticles. The contraction of the unit cell is more pronounced for gold nanoparticles than for silver particles.[163]

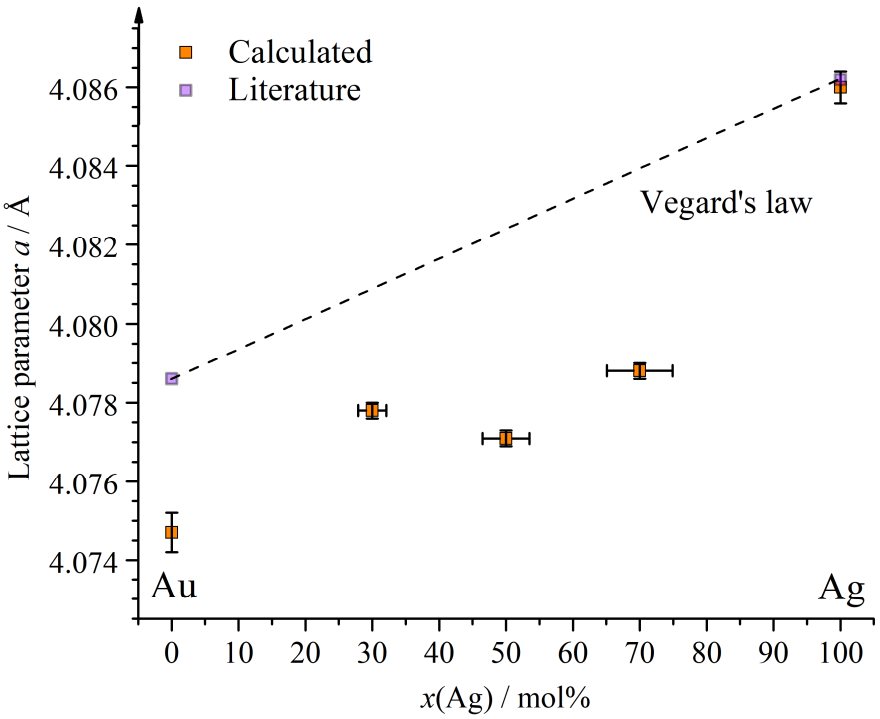

Figure 91: Lattice parameters *a* calculated for gold, silver, and silver-gold particles as a function of composition compared to the Vegard's law and the reference values for gold[133] and silver.[132]

The negative deviation from Vegard's law was reported earlier[25, 145, 202-203] for bulk as well as for nano-sized silver-gold alloys. As showed in the previous chapter of this work, the negative deviation decreases if the particles are annealed to 850 °C. The lattice parameters as a function of composition exhibit a bulk like behavior (Fig.73). Also, the modeling of a bct defect phase removes the negative deviation completely (Fig 67). Both methods eliminate the defects, like grain boundaries or stacking faults which can be found in particles and cause the lattice distortion.

In summary, the desired sizes of 30 nm to 40 nm are achieved by the reduction with trisodium citrate only (Table 31). The nanoparticles are mostly spherical with occasional appearances of rods or platelets and show polycrystallinity. UV/vis spectra show an alloy character of the bimetallic particles which is confirmed by the cyclic voltammetry. EDX maps show silver-rich patches or a silver skin on the particle surface which is also observable from CV by a silver oxidation pre-peak. This was not found for smaller (14 nm) particles. Underpotential deposition of lead on the nanoparticle surface reveals a silver outermost layer on the particle surface. Powder X-ray diffraction shows the nanocrystalline character of the samples because of reflex broadening and a negative deviation from Vegard's law.

Table 31: Sizes of the silver, gold, and silver-gold nanoparticles as obtained by DCS, DLS, SEM, and UPD and the corresponding crystallite sizes in comparison.

Nominal composition Ag:Au	Diameter / nm by DCS	Z-average / nm by DLS	Peak size / nm by DLS	Diameter / nm by SEM	Diameter / nm by UPD	Crystallite size by PXRD / nm
0:100	34 ± 3	30	74 ± 37	47 ± 6	-	28 ± 3
30:70	27 ± 10	49	74 ± 38	33 ± 11	38 ± 3	13 ± 1
50:50	43 ± 15	74	98 ± 49	38 ± 11	37 ± 2	11 ± 1
70:30	27 ± 5	47	54 ± 19	30 ± 8	26 ± 2	12 ± 1
100:0	29 ± 5	33	75 ± 41	36 ± 7	-	28 ± 1

5.3.3 Conclusion on silver-gold nanoparticles

The posed questions were whether alloyed silver-gold nanoparticles synthesized with different reducing agents show distinct element distributions within a particle and whether there are any differences between those particles. Both questions are answered with yes, there is a difference in the element distribution and yes, the nanoparticles differ in their size. The case of using trisodium citrate and tannic acid as the reductants yields particles with sizes of 7 nm which exhibit a gradient structure regarding the element distribution. A gold-rich core and a silver-rich shell are obtained. The nanoparticles are considered as alloys. Using trisodium citrate only as the reducing agent yields nanoparticles with sizes of around 35 nm. Those particles are alloys as well, but exhibit a silver segregation on the surface which is not observed in the small particles. Underpotential deposition experiments reveal that the outermost nanoparticle surface consists of silver atoms only. Upon annealing of the silver-gold nanoparticles prepared by trisodium citrate and tannic acid reduction, a unit cell expansion and a crystallite growth as well as a decrease in the microstrain are observed. The deviation from Vegard's law after annealing and cooling down is less negative due to recrystallization processes, sintering, and the removing of defects. The linear thermal expansion coefficients of the alloyed nanoparticles are at least twice the size as the linear thermal expansion coefficients of the monometallic particles and show a non-linear behavior.

5.4 Evaluation of dissolution experiments

The dissolution kinetics of silver nanoparticles is a current topic in the literature.[120-121, 237-241] It is found that the presence of oxidizing species, like oxygen or hydrogen peroxide, fastens the dissolution of silver. Also, the temperature, the pH, and the surface functionalization influence the silver release. The silver dissolution out of bimetallic alloyed particles is not studied as much. Several publications exist[23, 242] which show an increasing toxicity of silver-gold nanoparticles on cells or bacteria with silver amounts above 50 mol%. This toxicity is ascribed to the dissolution of silver and the generation of the toxic Ag^+ species. Ristig et al.[23] showed that the composition of Ag 80 mol% and Au 20 mol% had the highest influence on hMSC and HeLa cells. Other publications[29, 153-154] described a toxicity decrease of silver nanoparticles alloyed with gold compared to pure silver nanoparticles. The question is whether the alloying of silver with gold has an influence on the dissolution behavior of silver. The same question arises for the silver-platinum nanoparticles. Only few publications can be found on the dissolution of silver or of platinum out of silver-platinum particles. The platinum dissolution could be achieved by oxidation with tetrachloridoauric acid and investigation with *in situ* TEM by Wu et al.[243] The silver dissolution out of silver-platinum particles was investigated by Ma[244] with cyclic voltammetry. The results were that higher potentials had to be applied for the dissolution of silver with the increasing platinum composition. Now, the aim is to perform dissolution kinetics experiments in aqueous solutions.

5.4.1 Dissolution of silver-gold nanoparticles

The silver-gold nanoparticles are characterized by AAS and DCS prior to the experiments (Table 32). The total metal concentration is determined to prepare dispersions with a total metal concentration of 0.05 mg/mL. The nanoparticle sizes are comparable to the sizes obtained by Ristig et al.[23] The acquired values from AAS during the dissolution kinetics experiments are took to gain the weight of the silver ions which are found in solution because a dilution factor must be considered (see experimental section). Figure 92 shows the weight of the silver ions found in solution as a function of time during the dissolution kinetics experiments of silver-gold nanoparticles. After 24 hours and 48 hours, no silver ions are detected because the diffusion of the ions through the cellulose membrane takes some time and is considered as the limiting factor.

Table 32: Compositions, total metal concentrations, and diameters of the silver-gold nanoparticles prepared by trisodium citrate and tannic acid reduction for the dissolution experiments.

Nominal composition / mol% Ag:Au	Actual composition / mol% Ag:Au	Total metal concentration / mg/mL	Diameter by DCS / nm
10:90	15:85	2.56	7.8 ± 2.1
20:80	35:65	5.23	5.4 ± 1.0
30:70	31:69	2.62	4.5 ± 0.8
40:60	45:55	2.82	4.7 ± 0.9
50:50	43:57	6.06	6.4 ± 0.9
60:40	61:39	2.39	4.5 ± 0.8
70:30	71:29	2.31	4.9 ± 0.9
80:20	87:13	2.23	6.3 ± 0.6
90:10	87:13	2.47	5.5 ± 0.8
100:0	100:0	1.80	33.1 ± 5.1

Up to 2784 hours, less silver ions are released from the pure silver nanoparticles than from the bimetallic nanoparticles. The reason lies in the size of the silver nanoparticles compared to the size of the silver-gold particles which is up to 5 times higher. Smaller particles are dissolved faster than bigger particles because of their higher surface area to volume ratio.[241] At 384 hours and at 576 hours, the highest amount of silver in solution is found from the composition Ag90Au10, followed by Ag70Au30, Ag80Au20, Ag60Au40, and Ag100. Up to 840 hours, silver ions only from the compositions Ag100, Ag90Au10, Ag80Au20, Ag70Au30, and Ag60Au40 are released. The dissolution of the pure silver nanoparticles and Ag80Au20 increases after 1584 hours and surpasses the dissolution of Ag70Au30. Contrary to the other samples, Ag60Au40 does not show a strong increase in silver ion release during the time. The release seems to be nearly constant. Remarkably, after 1584 hours, Ag50Au50 and even Ag20Au80 show the presence of silver ions. After 2784 hours, the most silver is released from the monometallic silver nanoparticles. The silver amount dissolved from sample Ag80Au20 decreases which can be explained by a dilution effect. Every time, 3 mL of the solution, in which the cellulose filter is immersed, are taken and replaced with 3 mL ultrapure water. If no further silver ions are released, but aliquots still taken, the detected silver amount will decrease.

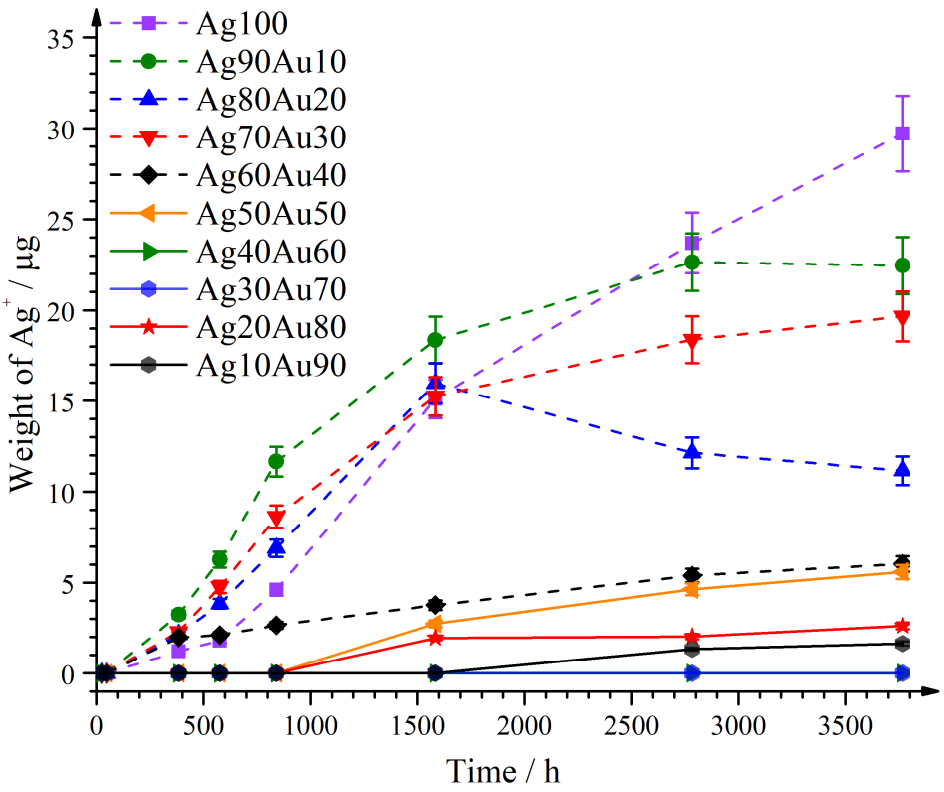

Figure 92: Weight of the silver ions found in solution as a function of time during dissolution kinetics experiments of silver-gold nanoparticles. Note that the data points of samples Ag40Au60 and Ag30Au70 overlap.

The graphs in Figure 92 are used to determine the silver ion dissolution rate out of the silver-gold nanoparticles. For this purpose, the sigmoidal curves are fitted with a Gompertz function (Equation 20) and linear graphs are fitted with a linear regression which corresponds to zero order kinetics. Both models are used in the literature to describe dissolution profiles.[245]

$$f(x) = a\mathrm{e}^{-\mathrm{e}^{-k(x-x_c)}} \tag{20}$$

With a the asymptote, e Euler's Number, k the dissolution rate, x the time, and x_c the time at the inflection point. In the case of rate determination by linear regression, the slope of the linear regression gives the dissolution rate. All fits, the corresponding equations, and the values can be found in the appendix. The dissolution rates of silver are summarized in Table 33. To obtain the average dissolution rate $k_{average}$ before reaching maximum dissolution, the maximum dissolved silver amount at a time t is divided by t (Equation 21).

$$k_{average} = \frac{maximum\ dissolved\ silver(t)}{t} \tag{21}$$

Table 33: Silver ion dissolution rates out of silver-gold nanoparticles of different compositions. If not noted otherwise, the dissolution rate is determined using the Gompertz function. *Linear regression.

Sample	Dissolution rate *k* of silver / ng/h	Asymptote *a* / µg	Time at inflection point x_c / h	Average dissolution rate $k_{average}$ of silver / ng/h
Ag100	1.2 ± 0.2	30.5 ± 1.5	1365.7 ± 84.4	7.9
Ag90Au10	2.1 ± 0.2	22.4 ± 0.5	685.0 ± 27.1	8.1
Ag80Au20	3.5 ± 1.7	13.0 ± 1.2	633.7 ± 88.0	10.1
Ag70Au30	1.9 ± 0.2	19.2 ± 0.4	753.4 ± 26.3	5.2
Ag60Au40	1.2 ± 0.4	5.9 ± 0.6	714.6 ± 149.4	1.6
Ag50Au50	2.0 ± 0.5	5.3 ± 0.2	1423.6 ± 67.1	1.5
Ag40Au60	0	0	0	0
Ag30Au70	0	0	0	0
Ag20Au80	4.6 ± 6.1	2.3 ± 0.2	1203.8 ± 509.4	0.7
Ag10Au90	0.8 ± 0.2*	0*	0*	0.4

The highest dissolution rate with an acceptable error is found for Ag80Au20 followed by Ag90Au10, and Ag70Au30 which are all silver-rich samples with the same sizes. Pure silver nanoparticles exhibit a lower dissolution rate because of the bigger size as mentioned above. Ag60Au40 has the same dissolution rate of silver with a value of 1.2 ng/h as Ag100. Although the dissolution rate of Ag50Au50 lies in the range of Ag90Au10, the dissolution starts not until after 1584 hours. The silver ion release out of Ag20Au80 happens with a rate of 4.6 ng/h, but also shows a great standard deviation and does not take the late beginning of dissolution into account (inflection point x_c at 1204 hours). Because Ag10Au90 only shows silver dissolution after 2784 hours and 3768 hours, a linear dependency is assumed for the data points taken. The dissolution rate of 0.8 ng/h is obtained which is rather low. On the contrary, the average dissolution rates consider the late beginning of silver dissolution. The $k_{average}$ values for the silver-rich compositions are in good agreement with the *k* values obtained from Gompertz function showing the fastest rate for Ag80Au20 followed by Ag90Au10 and Ag70Au30. For the silver-poor compositions, low average dissolution rates are obtained because the silver release starts after 1584 hours.

The dissolution curve in Figure 92 depends on the initial amount of silver in the sample. This means that silver-rich samples have the potential to release more ions than silver-poor samples,

even if the dissolution velocity is the same.[239] Therefore, the percentage of the released ions versus the initial amount of silver is regarded (Fig. 93). Notably, the most silver relatively to the initial amount after 384 hours is released from the Ag90Au10, Ag80Au20, Ag70Au30, and Ag60Au40 samples. After 576 and 840 hours, only Ag90Au10, Ag80Au20, and Ag70Au30 show the highest silver release. The samples Ag80Au20 and Ag90Au10 reach their silver dissolution maxima after 1584 hours and 2784 hours, respectively. With nearly 14 % after 3768 hours, Ag70Au30 exhibits the strongest silver dissolution. Even Ag50Au50 with Ag20Au80, and Ag10Au90 show silver ion release after 1584 hours and 2784 hours, respectively. Sotiriou et al.[246] also showed in their dissolution kinetics experiments with silver-gold nanoparticles of Ag:Au compositions 95:5, 90:10, 80:20, 70:30, 50:50, and 25:75 a silver ion release of 3 % for the Ag:Au 25:75 composition which is similar to the obtained value of 3.5 % after 1584 h in this work. Those findings also underline the experiments with hMSC and HeLa cells described by Ristig et al.[23] where the Ag80Au20 composition showed the uppermost toxicity. This toxicity is explained by an augmented silver release which could be confirmed by the determination of dissolution rates. The average dissolution rate of Ag80Au20 shows the highest value of 10.1 ng/h. An explanation might be the surface constitution of the nanoparticles. EDX maps and EDX line scans[25] as well as cyclic voltammetry experiments[83] on nanoparticles prepared by the same method showed an alloyed silver-rich surface of the nanoparticles. The water, in which the dissolution experiments are performed, contains oxygen which oxidizes the silver in the nanoparticles to silver ions. The same cyclic voltammetry experiments, as mentioned before,[83] reveal a shift of the oxidation potential of silver to higher potentials upon alloying with gold. Silver gets nobler and is oxidized, that means dissolved, slower. That might be the reason for the slow and late silver release of the samples with a silver amount below 50 mol%. The dissolution kinetics experiments of alloyed silver-gold nanoparticles in the whole composition range from 90 mol% silver to 10 mol% silver in steps of 10 mol% show a late silver dissolution for silver-poor samples correlating with results obtained from biological experiments and dissolution kinetics experiments in the literature.[23, 28-29, 153-154, 246]

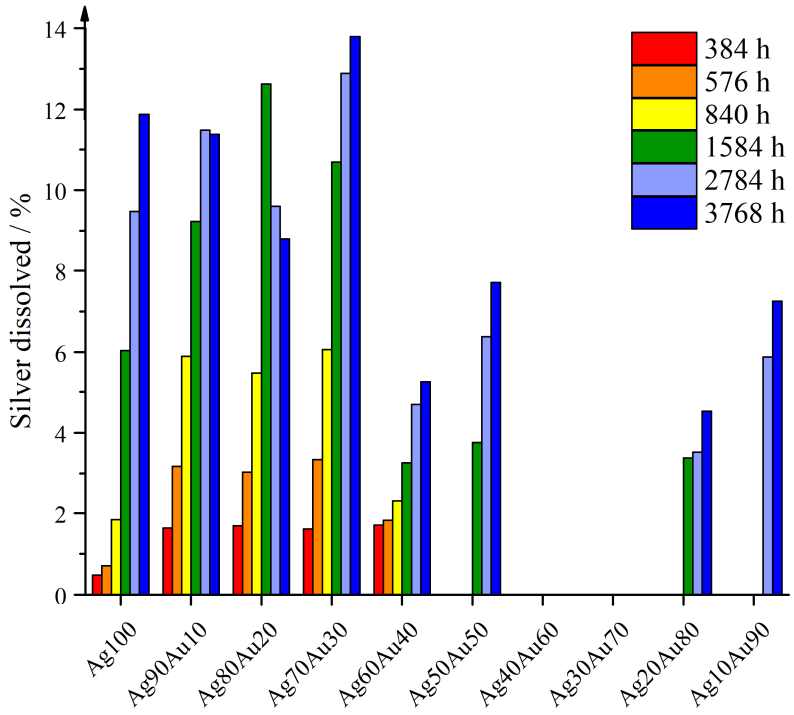

Figure 93: Silver dissolved from silver-gold nanoparticles, in percent, as a function of the composition after several hours.

To compare the dissolution behavior of bulk materials with nanomaterials, dissolution experiments with alloyed bulk metals are performed. The same set-up as for the nanoparticle dissolution is chosen. Table 34 summarizes the applied metals and their properties. Aliquots are taken after 96 hours, 432 hours, and 1080 hours. None of the aliquots contains silver ions. In theory, the dissolution of bulk materials is slower than the dissolution of nanoparticulate materials because of the lower surface area to volume ratio.[241] On the other hand, a silver release should be visible, as showed by Liu et al.[241] A possible explanation for the results is an unsuitable experimental set-up. Probably, the silver release is rather slow and the diffusion of the silver ions through the cellulose membrane even slower. For future experiments, the cellulose membrane should be omitted.

Table 34: Applied bulk metals and their properties.

Ag100 foil	Ag70Au30 pellets	Ag50Au50 rod	Ag70Pd30 foil
Purity: 99.95 + %			
Thickness: 0.15 mm	Max. pellet size:	Diameter: 3 mm	Thickness: 0.15 mm
Size: (25 x 25) mm	4 mm	Length: 10 mm	Size: (25 x 25) mm
Weight: 1.02 g	Weight: 1.05 g	Weight: 1.06 g	Weight: 1.03 g

5.4.2 Dissolution evaluation of silver-platinum nanoparticles

The silver-platinum dissolution experiments were performed by Dr. Kateryna Loza with already synthesized nanoparticles. The silver-platinum nanoparticles are characterized by AAS and DCS prior to the experiments (Table 35). The silver concentration is determined to prepare dispersions with a silver concentration of 0.1 mg/mL. The nanoparticle sizes lie in the range of 5 nm to 9 nm, so the size effect on the dissolution is neglected.

The trend for the silver ion release from silver-platinum nanoparticles is comparable to the silver-gold particles (Fig. 94). Please note that the experimental set-ups are not identical. The dissolution experiments with silver-gold were performed in Amicon® spin-filters, whereas the silver-platinum dissolution was performed in PTFE bottles with a subsequent centrifugal filtration. After 24 hours, silver ions from the compositions silver-platinum 90:10 and 70:30 are found in the filtrate. After 48 hours, the concentration in those samples increases and the 50:50 sample releases silver ions as well. After 72 hours, the detected silver ion concentration does not increase anymore and a saturation is observable.

Table 35: Compositions, total metal concentrations, and diameters of the silver-platinum nanoparticles prepared by sodium borohydride reduction for the dissolution kinetics experiments.

Nominal composition / mol% Ag:Pt	Actual composition / mol% Ag:Pt	Total metal concentration / mg/mL	Diameter by DCS / nm
10:90	13:87	4.0	5.4 ± 1.2
30:70	30:70	8.0	6.7 ± 2.1
50:50	52:48	7.5	8.1 ± 1.9
70:30	60:40	9.6	8.5 ± 3.9
90:10	92:08	4.2	8.9 ± 3.2

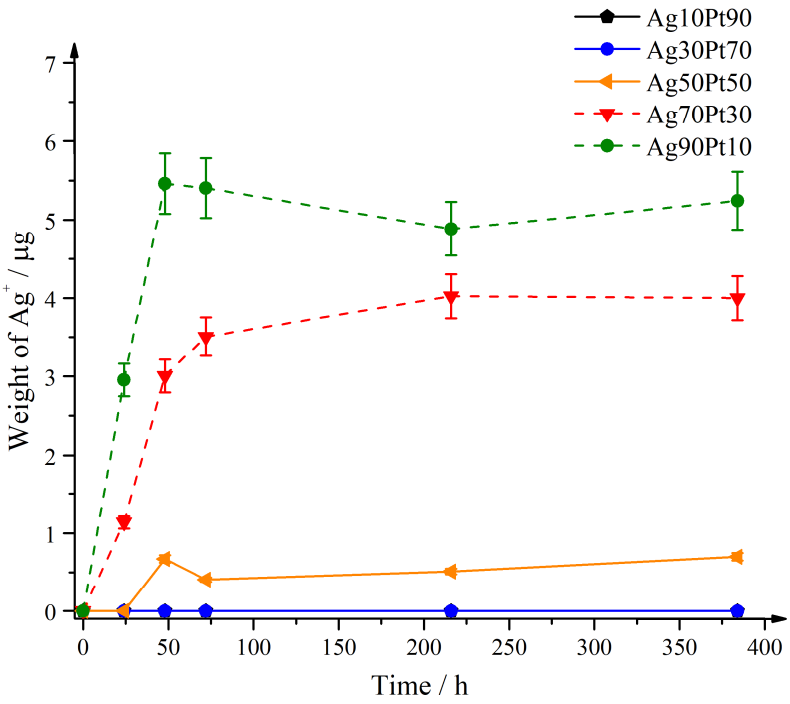

Figure 94: Silver ion concentration as a function of time during dissolution kinetics experiments of silver-platinum nanoparticles. Please note that the data points of Ag10Pt90 lie directly under the data points of Ag30Pt70.

The samples with the highest platinum molar fractions, Ag30Pt70 and Ag10Pt90, do not show silver dissolution at all. The silver dissolution rate is determined by using the Gompertz fit function (Equation 20) and linear regression.[245] All fits, the corresponding equations, and the values can be found in the appendix. Table 36 summarizes the obtained dissolution rates of silver ions out of silver-platinum nanoparticles of different compositions. The dissolution rates decrease proportionally with the silver molar fraction in the sample. For Ag90Pt10, a linear regression is chosen to determine the dissolution rate because the silver amount found in solution does not increase after 48 hours any more. The dissolution rate is 114 ng/h. The data points of Ag70Pt30 are fitted with the Gompertz fit function because of a sigmoidal curve shape to yield a dissolution rate value of 57 ng/h. A linear regression for Ag50Pt50 is chosen which is divided in two sections because of a slope change. In section one, between 24 hours and 72 hours, the silver dissolution is rather fast with a value of 8.5 ng/h. Section two, between 72 hours and 384 hours, shows a dissolution rate of 1.0 ng/h. This means a fast dissolution at first and a coming saturation afterwards. The silver dissolution rates of the silver-platinum nanoparticles are greater than the dissolution rates of silver-gold nanoparticles because the initial concentration of silver in the silver-platinum samples is higher.[239]

Table 36: Silver ion dissolution rates out of silver-platinum nanoparticles of different compositions. The comments give the applied fit model.

Sample	Silver dissolution rate / ng/h	Comment
Ag90Pt10	113.8 ± 5.4	Linear regression: 0 h – 48 h
Ag70Pt30	57.0 ± 5.9	Gompertz function
Ag50Pt50	8.5 ± 11.3	Linear regression:
	1.0 ± 0.1	24 h – 72 h and 72 h – 384 h
Ag30Pt70	0	
Ag10Pt90	0	

The dissolution behavior depends on the initial silver amount which is equal in all silver-platinum samples. The highest silver amount relative to the initial silver amount in the sample is released from the silver-platinum 90:10 composition followed by the 70:30 composition and then the 50:50 composition (Fig. 95). A non-linear dissolution behavior is observed. For the Ag90Pt10 sample, the saturation is reached after 48 hours, whereas for Ag70Pt30 the saturation occurs after 216 hours. The dissolution kinetics of silver may be influenced by the element distribution within the particles. In section 5.1.2 is described that two nanoparticle species occur in one sample. Those are hollow alloyed particles and dense core-shell particles with a silver core. The silver-platinum 90:10 composition contains 60 % alloyed particles compared to the 50:50 composition which contains roughly 10 %. The silver ion release is easier from alloyed particles than from core-shell particles with a silver core and a platinum shell. Nevertheless, the silver ion release is dependent on the molar silver amount in the sample. The higher the silver molar fraction in the nanoparticles, the more silver is released. Vice versa, the nanoparticles are more stable against silver dissolution with higher platinum molar fractions. The same was observed by Ma[244] during cyclic voltammetry measurements of alloyed silver-platinum films. Like for the silver-gold nanoparticles, the silver release can be slowed by alloying silver particles with a nobler metal – platinum.

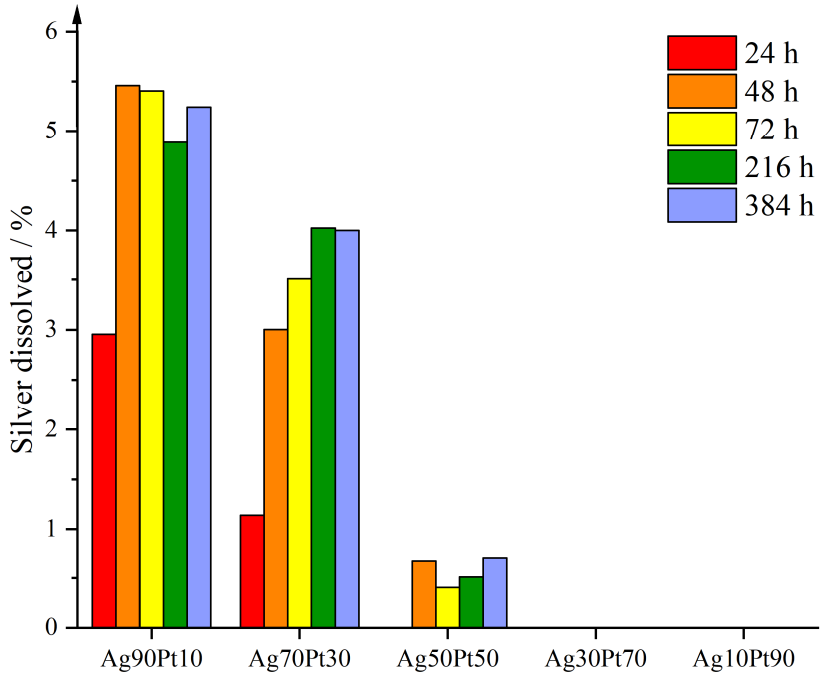

Figure 95: Silver dissolved from silver-platinum nanoparticles in percent as a function of the composition after several hours.

5.4.3 Conclusion on the dissolution experiments

The questions that should be answered were whether the composition of silver-gold and silver-platinum nanoparticles influences the dissolution rate of silver. In the case of silver-gold, the composition indeed seems to play a crucial role. The silver-gold 80:20 composition releases the most silver ions after 1584 hours and shows the greatest dissolution rate followed by the 70:30 and the 90:10 compositions. After 2784 hours, silver-gold 70:30 releases the most silver. The samples 40:60 and 30:70 show no dissolution at all and the 60:40 composition exhibits a constant silver ion release. A non-linear dissolution behavior is observed. A rule of thumb that can be formulated is: Alloying of silver with gold increases the oxidation potential of silver and inhibits the silver release. The silver-platinum system also shows a non-linear dissolution behavior. The most silver is released from the silver-rich sample 90:10 followed by 70:30 and 50:50. No silver ions are detected in the 30:70 and 10:90 samples. In this case as well as above, the same rule of thumb can be formulated: Alloying of silver with platinum increases the oxidation potential of silver and inhibits the silver release.

5.5 Characterization of monometallic nanoclusters and nanoparticles

5.5.1 Characterization of autofluorescent palladium nanoclusters

The synthesis of palladium nanoclusters capped with 11-mercaptoundecanoic acid is based on the work of Ristig et al.[24] The characterization is performed with differential centrifugal sedimentation, UV/vis and fluorescence spectroscopy as well as by measuring the Zeta potential. The size distribution obtained from DCS is shown in Figure 96. A peak at 3 nm with a narrow distribution of ± 0.7 nm is observed. A second peak at (19 ± 14) nm is found which is attributed to agglomerates rather than to such sized particles because the color of the dispersion appears not brown, but yellow (Fig.97). Palladium nanoparticles with sizes of 8 nm and larger appear brown.[99] Hyotanishi et al.[247] report a yellow color for 1 nm to 1.5 nm palladium clusters. The coloration during the synthesis appears already after addition of 11-mercaptoundecanoic acid and does not change after sodium borohydride addition. Probably, the 11-MUA serves as the reducing agent as described by Sun et al.[194] No discoloration occurs even after months which is also the case for silver-platinum nanoclusters. The Zeta potential at pH 9 lies at -33 mV. It shows a good electrostatic stabilization because the carboxylic groups of 11-MUA are deprotonated.

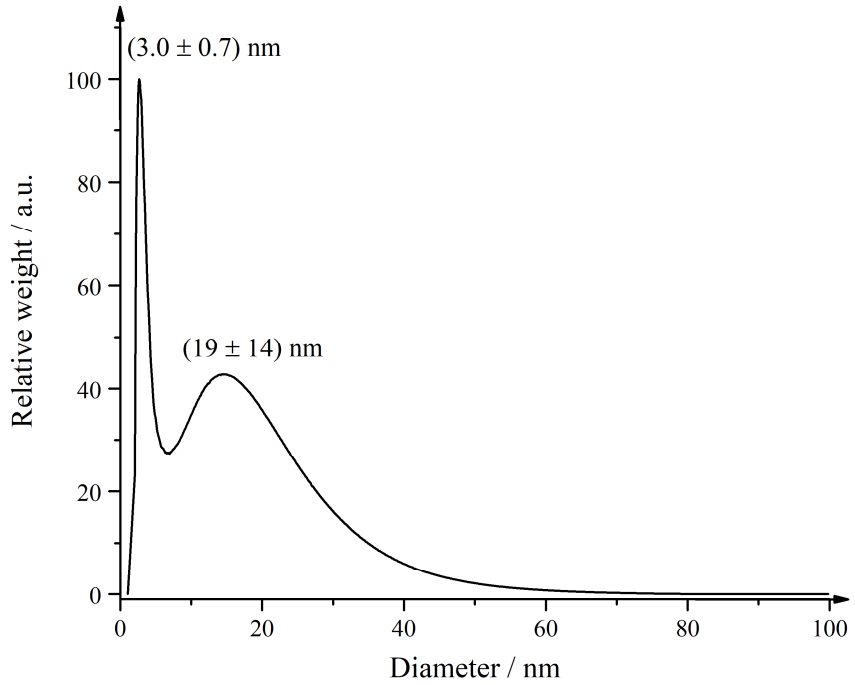

Figure 96: Representative size distribution of 11-MUA capped palladium nanoclusters.

Figure 97: Coloring of the 11-MUA capped palladium nanoclusters.

The absorption and emission spectra are depicted in Figures 98 and 99. The palladium nanoclusters absorb at 278 nm and 389 nm. After excitation with 389 nm, the emission occurs at 532 nm with a shoulder at 496 nm. Excitation with 278 nm yields an emission at 495 nm. Hyotanishi et al.[247] report an emission at 460 nm after excitation with 350 nm for 1.5 nm sized clusters. Because the clusters obtained in this work are twice the size, a redshift in absorption and emission is observed. The gap between HOMO and LUMO shrinks[248-249] resulting in an energy decrease for the absorption and emission. Low energies are characterized by large wavelengths. Another reason is the different capping agent, 11-MUA, in this work versus dimethylformamide in ref[247] which influences the electronical structure on the cluster surface, and therefore affects the optical properties of the clusters.

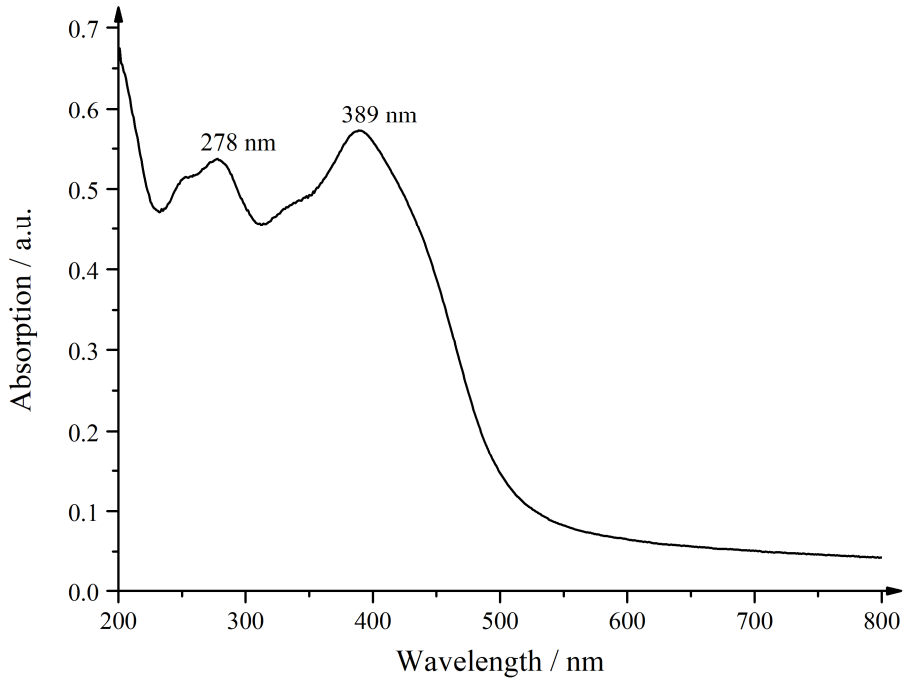

Figure 98: Representative UV/vis absorption spectrum of 11-MUA capped palladium nanoclusters.

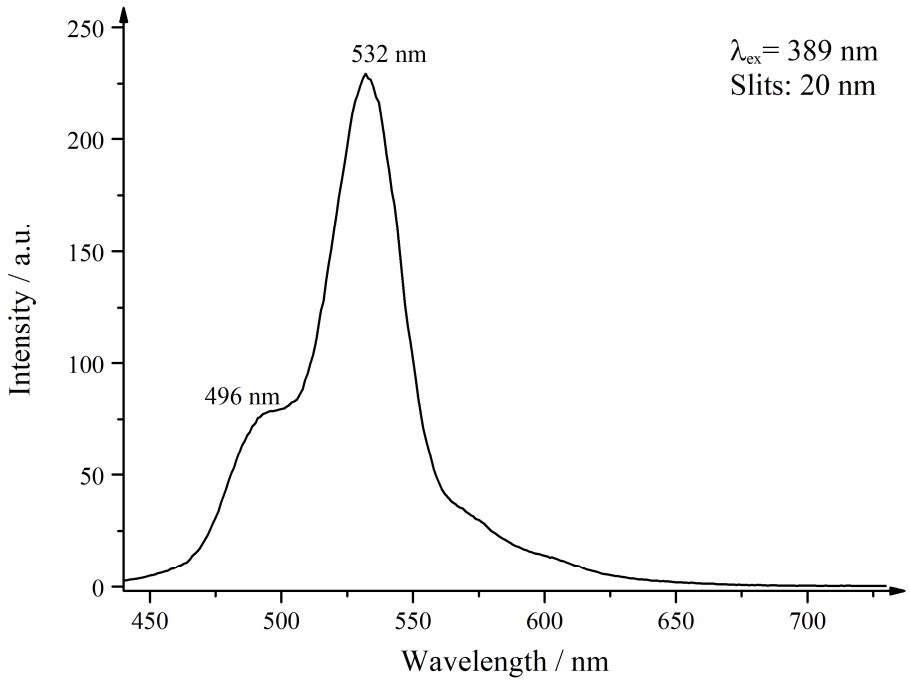

Figure 99: Representative fluorescence emission spectrum of 11-MUA capped palladium nanoclusters.

5.5.2 Characterization of silver nanoparticles after refunctionalization with poly(ethylene glycol) methyl ether thiol

The aim is to refunctionalize trisodium citrate capped silver nanoparticles with poly(ethylene glycol) methyl ether thiol (mPEGthiol) and characterize them with straightforward methods like Zeta potential, differential centrifugal sedimentation, and UV/vis spectroscopy. The silver nanoparticles are prepared by trisodium citrate and tannic acid reduction. Before refunctionalization with mPEGthiol, some aliquots are taken, and characterized by measuring the Zeta potential, DCS, and UV/vis. The same is done after refunctionalization. All obtained data are compared. The idea is to utilize the distinct physical properties of differently capped particles. The polymer mPEGthiol is a steric stabilizer with a higher molecular weight than the electrostatic stabilizer trisodium citrate with its lower molecular weight. When measuring the nanoparticles with the DCS, the density of the trisodium citrate capped particles is higher than the density of the mPEGthiol capped particles. Therefore, the trisodium citrate functionalized nanoparticles will sediment faster than the mPEGthiol capped particles and be considered larger.[170] A decrease in the particle size obtained by DCS shall show a successful refunctionalization. The Zeta potential of the trisodium citrate capped nanoparticles should be larger than of the mPEGthiol functionalized ones because more trisodium citrate ought to be found on the nanoparticle surface. Upon refunctionalization, a certain amount would be

removed from the particle. The UV/vis spectroscopy uses the conduction band electron oscillation to detect the surface plasmon resonance. A change of the electron density, caused by different surfactants, should induce a peak shift in the absorption spectrum.[108] The bulky mPEGthiol will decrease the eigenfrequency of the electron gas which will cause a redshift of the absorption. The results of trisodium citrate functionalized and mPEGthiol refunctionalized particles are summarized in Table 37. A decrease of the particle size from (46 ± 3) nm to (40 ± 3) nm is obtained after recapping. The Zeta potential also decreases from -43.5 mV to -40.6 mV and an absorption redshift of the trisodium citrate capped to the mPEGthiol capped nanoparticles is observed in the UV/vis spectroscopy (Fig. 100). All data obtained confirm the predictions made beforehand. Therefore, a successful refunctionalization with mPEGthiol is assumed. The analysis with standard laboratory equipment such as DCS, DLS, UV/vis, and Zeta potential measurement shows straightforward methods of characterization to determine a successful refunctionalization.

Table 37: Comparison of trisodium citrate and mPEGthiol capped silver nanoparticles according to DCS, Zeta potential and UV/vis.

	Trisodium citrate capped	mPEGthiol capped
Diameter by DCS / nm	46 ± 3	40 ± 3
Zeta potential at pH 7 / mV	-43.5	-40.6
UV/vis absorption max. / nm	430	438

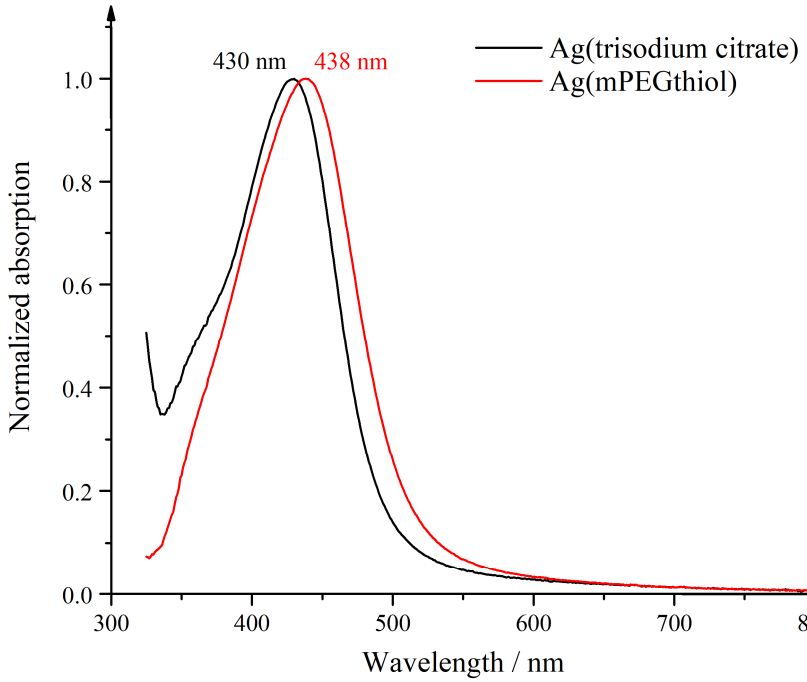

Figure 100: UV/vis spectra of trisodium citrate and mPEGthiol capped silver nanoparticles.

5.5.3 Conclusion on the monometallic nanoclusters and nanoparticles

The synthesis of bimetallic nanoclusters reported by Ristig et al.[24] is applicable to the monometallic palladium system. The obtained palladium nanoclusters are 11-mercapto-undecanoic acid capped and show autofluorescent properties.

The refunctionalization of silver nanoparticles with poly(ethylene glycol) methyl ether thiol is successful as the results from differential centrifugal sedimentation, Zeta potential, and UV/vis spectroscopy show.

6. Conclusion

The results in this work show that the synthesis of bimetallic silver-platinum nanoparticles in different compositions from Ag10Pt90 to Ag90Pt10 in 10 mol% steps is possible through variation of the reductants and the reaction conditions. A seeded-growth method was applied which uses the galvanic exchange reaction. The size of the silver seeds affected the resulting nanoparticle size. With trisodium citrate and tannic acid as reductants, particles with diameters of 35 nm were obtained. Using sodium borohydride, 10 nm sized nanoparticles were achieved. At a pH of 3 during the reaction, two species could be found in one sample of which one was the hollow alloyed particle and the other a core-shell nanoparticle species. The core-shell particles show a silver core and a platinum shell. The number of alloyed particles in the samples increases with the silver composition. The alloy character was confirmed by UV/vis spectroscopy, EDX maps on single particles, and powder X-ray diffraction. A physical mixture was excluded by measuring physical mixtures of silver and platinum nanoparticles in different ratios by UV/vis spectroscopy. Powder X-ray diffraction showed a reflex shift to smaller angles with increasing silver composition. The nanoparticles are polycrystalline which was shown by HAADF-STEM and PXRD. The lattice constants of the different compositions follow Vegard's law, although the lattice parameters are slightly contracted. At pH 10, 8 nm to 12 nm sized nanoparticles were obtained. Platinum rich samples showed pure platinum nanoparticles together with core-shell particles, whereas the compositions with moderate platinum amounts exhibited aggregated core-shell particles or alloys with a gradient structure. Particles with low platinum molar fractions revealed core-shell particles with a silver core and a platinum shell.

The silver-platinum nanoclusters could be synthesized by sodium borohydride reduction and were capped with 11-mercaptoundecanoic acid. They were spherical with sizes of around 3 nm in diameter and showed an absorption in the UV range and an emission at 425 nm and in the near infrared region.

Silver-gold nanoparticles with sizes of 7 nm were investigated by powder X-ray diffraction. The line profile in the Rietveld refinement could be improved by the addition of the body-centered tetragonal phase to describe the defects in the nanoparticles. The lattice parameters of the different compositions from Ag10Au90 to Ag90Au10 in 10 mol% steps showed a negative deviation from Vegard's if only the face-centered cubic phase was modeled. Upon refinement of the fcc and the bct phases, the lattice parameters follow the Vegard's law. During annealing of the nanoparticles to 850 °C, a recrystallization and a unit cell expansion were observed. After cooling down, the lattice parameters showed a smaller deviation from Vegard's law than before

annealing. The lattice parameters obtained after Rietveld refinement and non-refined parameters were compared and showed only a deviation of maximum 0.6 %. The linear thermal expansion coefficients were calculated from the unit cell parameters. Pure silver and pure gold nanoparticles showed a linear expansion, whereas the alloyed samples showed a non-linear expansion with a jump of slope in the range between 150 °C and 250 °C. The silver-gold nanoparticles synthesized by the trisodium citrate reduction only had sizes around 35 nm. They were spherical and polycrystalline. On the nanoparticle surface, silver rich patches could be found. The silver segregation to the surface of the particles is more pronounced in bigger than in smaller nanoparticles. Cyclic voltammetry and underpotential deposition revealed that the outermost layer of the nanoparticles consists of silver atoms only.

Dissolution experiments of silver-gold and silver-platinum nanoparticles with sizes of 7 nm to 10 nm showed a composition dependent dissolution behavior for the silver-gold particles. The nanoparticles from the silver-gold 80:20 composition released the most silver ions relative to the initial silver amount after 1584 hours. In general, silver-rich samples showed the most silver ion release. The composition silver-gold 60:40 showed a constant, but slow silver dissolution. After 1584 hours (66 days), the compositions silver-gold 40:60 and 30:70 still did not show the presence of silver ions. For the silver-platinum nanoparticles, no outliers for the silver dissolution could be observed. The silver-rich composition 90:10 showed the highest silver ion release, followed by the compositions 70:30, and 50:50. No silver ions were detected after 384 hours in the silver-platinum 30:70, and 10:90 samples. A non-linear dissolution behavior of silver out of bimetallic silver-gold and silver-platinum particles was observed. Particles with silver molar fractions below 50 mol% showed silver release either after long periods of time or no release at all.

The palladium nanoclusters could be synthesized by sodium borohydride reduction and were capped with 11-mercaptoundecanoic acid. They had sizes of around 3 nm in diameter and showed an absorption in the UV and visible range and an emission at 532 nm. The color of the cluster dispersion was yellow. The refunctionalization of 40 nm sized silver nanoparticles with poly(ethylene glycol) methyl ether thiol was possible as characterization by differential centrifugal sedimentation, the Zeta potential determination, and UV/vis measurements showed.

7. References

[1] *Nanoscience and nanotechnologies: opportunities and uncertainties*, The Royal Society, London, **2004**.

[2] S. Iijima, *Nature* **1991**, *354*, 56.

[3] J. P. Rao, K. E. Geckeler, *Prog. Polym. Sci.* **2011**, *36*, 887.

[4] B. Song, Y. Zhang, J. Liu, X. Feng, T. Zhou, L. Shao, *Beilstein J. Nanotechnol.* **2016**, *7*, 645.

[5] J. A. Darr, J. Zhang, N. M. Makwana, X. Weng, *Chem. Rev.* **2017**, *117*, 11125.

[6] W. J. E. Beek, M. M. Wienk, R. A. J. Janssen, *Adv. Mater.* **2004**, *16*, 1009.

[7] W. Habraken, P. Habibovic, M. Epple, M. Bohner, *Mater. Today* **2016**, *19*, 69.

[8] C. Hadjicharalambous, D. Kozlova, V. Sokolova, M. Epple, M. Chatzinikolaidou, *J. Biomed. Mater. Res., Part A* **2015**, *103*, 3834.

[9] R. Dastjerdi, M. Montazer, *Colloids Surf. B* **2010**, *79*, 5.

[10] M. Auffan, J. Rose, M. R. Wiesner, J.-Y. Bottero, *Environ. Pollut.* **2009**, *157*, 1127.

[11] T. J. Antosiewicz, S. P. Apell, *RSC Adv.* **2015**, *5*, 6378.

[12] C. T. Campbell, J. C. Sharp, Y. X. Yao, E. M. Karp, T. L. Silbaugh, *Faraday Discuss.* **2011**, *152*, 227.

[13] C. Cui, L. Gan, M. Heggen, S. Rudi, P. Strasser, *Nat. Mater.* **2013**, *12*, 765.

[14] A. Wittstock, A. Wichmann, J. Biener, M. Baumer, *Faraday Discuss.* **2011**, *152*, 87.

[15] R. Narayanan, M. A. El-Sayed, *Nano Lett.* **2004**, *4*, 1343.

[16] C. Wang, H. Daimon, T. Onodera, T. Koda, S. Sun, *Angew. Chem. Int. Ed.* **2008**, *47*, 3588.

[17] J. Turkevich, *Gold Bull.* **1985**, *18*, 125.

[18] J. Turkevich, *Gold Bull.* **1985**, *18*, 86.

[19] J. Turkevich, P. C. Stevenson, J. Hillier, *Faraday Discuss.* **1951**, *11*, 55.

[20] J. Helmlinger, M. Heise, M. Heggen, M. Ruck, M. Epple, *RSC Adv.* **2015**, *5*, 92144.

[21] J. Helmlinger, O. Prymak, K. Loza, M. Gocyla, M. Heggen, M. Epple, *Cryst. Growth Des.* **2016**, *16*, 3677.

[22] J. Helmlinger, C. Sengstock, C. Gross-Heitfeld, C. Mayer, T. A. Schildhauer, M. Koeller, M. Epple, *RSC Adv.* **2016**, *6*, 18490.

[23] S. Ristig, S. Chernousova, W. Meyer-Zaika, M. Epple, *Beilstein J. Nanotechnol.* **2015**, *6*, 1212.

[24] S. Ristig, D. Kozlova, W. Meyer-Zaika, M. Epple, *J. Mater. Chem. B* **2014**, *2*, 7887.

[25] S. Ristig, O. Prymak, K. Loza, M. Gocyla, W. Meyer-Zaika, M. Heggen, D. Raabe, M. Epple, *J. Mater. Chem. B* **2015**, *3*, 4654.

[26] S. Ristig, *Bimetallische Silber-Gold-Nanopartikel - Synthese, Charakterisierung und zellbiologische Untersuchungen*, Thesis, University of Duisburg-Essen, **2014**.

[27] G. Guisbiers, R. Mendoza-Cruz, L. Bazan-Diaz, J. J. Velazquez-Salazar, R. Mendoza-Perez, J. A. Robledo-Torres, J.-L. Rodriguez-Lopez, J. M. Montejano-Carrizales, R. L. Whetten, M. Jose-Yacaman, *ACS Nano* **2016**, *10*, 188.

[28] D. Mahl, J. Diendorf, S. Ristig, C. Greulich, Z.-A. Li, M. Farle, M. Koeller, M. Epple, *J. Nanopart. Res.* **2012**, *14*, 1.

[29] T. Li, B. Albee, M. Alemayehu, R. Diaz, L. Ingham, S. Kamal, M. Rodriguez, S. Whaley Bishnoi, *Anal. Bioanal. Chem.* **2010**, *398*, 689.

[30] V. V. Bardushkin, D. A. Kirillov, Y. I. Shilyaeva, S. A. Gavrilov, V. B. Yakovlev, M. V. Silibin, *Russ. J. Phys. Chem. A* **2017**, *91*, 1099.

[31] A. Plech, V. Kotaidis, S. Grésillon, C. Dahmen, G. von Plessen, *Phys. Rev. B* **2004**, *70*, 195423.

[32] J. R. Morones, J. L. Elechiguerra, A. Camacho, K. Holt, J. B. Kouri, J. T. Ramirez, M. J. Yacaman, *Nanotechnology* **2005**, *16*, 2346.

[33] M. Rai, A. Yadav, A. Gade, *Biotechnol. Adv.* **2009**, *27*, 76.

[34] A. Lemelle, B. Veksler, I. S. Kozhevnikov, G. G. Akchurin, S. A. Piletsky, I. Meglinski, *Laser Phys. Lett.* **2009**, *6*, 71.

[35] N. J. Durr, T. Larson, D. K. Smith, B. A. Korgel, K. Sokolov, A. Ben-Yakar, *Nano Lett.* **2007**, *7*, 941.

[36] I. H. El-Sayed, X. Huang, M. A. El-Sayed, *Nano Lett.* **2005**, *5*, 829.

[37] I. H. El-Sayed, X. Huang, M. A. El-Sayed, *Cancer Lett.* **2006**, *239*, 129.

[38] L. R. Hirsch, R. J. Stafford, J. A. Bankson, S. R. Sershen, B. Rivera, R. E. Price, J. D. Hazle, N. J. Halas, J. L. West, *Proc. Natl. Acad. Sci. U. S. A.* **2003**, *100*, 13549.

[39] X. Huang, I. H. El-Sayed, W. Qian, M. A. El-Sayed, *J. Am. Chem. Soc.* **2006**, *128*, 2115.

[40] C. Loo, A. Lowery, N. Halas, J. West, R. Drezek, *Nano Lett.* **2005**, *5*, 709.

[41] V. P. Zharov, K. E. Mercer, E. N. Galitovskaya, M. S. Smeltzer, *Biophys. J.* **2006**, *90*, 619.

[42] P. Ghosh, G. Han, M. De, C. K. Kim, V. M. Rotello, *Adv. Drug Del. Rev.* **2008**, *60*, 1307.

[43] P. Durussel, P. Feschotte, *J. Alloys Compd.* **1996**, *239*, 226.

[44] I. Karakaya, W. T. Thompson, *Bull. Alloy Phase Diagr.* **1987**, *8*, 334.

[45] D. Lahiri, B. Bunker, B. Mishra, Z. Zhang, D. Meisel, C. M. Doudna, M. F. Bertino, F. D. Blum, A. T. Tokuhiro, S. Chattopadhyay, T. Shibata, J. Terry, *J. Appl. Phys.* **2005**, *97*, 094304.

[46] L. M. Liz-Marzan, A. P. Philipse, *J. Phys. Chem.* **1995**, *99*, 15120.

[47] F. Papa, C. Negrila, A. Miyazaki, I. Balint, *J. Nanopart. Res.* **2011**, *13*, 5057.

[48] T. Fu, J. Fang, C. Wang, J. Zhao, *J. Mater. Chem. A* **2016**, *4*, 8803.

[49] J. Gao, X. Ren, D. Chen, F. Tang, J. Ren, *Scr. Mater.* **2007**, *57*, 687.

[50] Z. Peng, H. Yang, *J. Solid State Chem.* **2008**, *181*, 1546.

[51] K. Torigoe, Y. Nakajima, K. Esumi, *J. Phys. Chem.* **1993**, *97*, 8304.

[52] M.-L. Wu, L.-B. Lai, *Colloids Surf. A* **2004**, *244*, 149.

[53] S. Chen, S. Thota, X. Wang, J. Zhao, *J. Mater. Chem. A* **2016**, *4*, 9038.

[54] S. Krishnan, M. Estevez-González, R. Perez, R. Esparza, M. Meyyappan, *RSC Adv.* **2017**, *7*, 27170.

[55] C. Bock, C. Paquet, M. Couillard, G. A. Botton, B. R. MacDougall, *J. Am. Chem. Soc.* **2004**, *126*, 8028.

[56] T. Cosgrove, *Colloid Science: Principles, methods and applications*, 2 ed., John Wiley & Sons Ltd, **2010**.

[57] H.-D. Dörfler, *Grenzflächen und kolloid-disperse Systeme*, Springer, **2002**.

[58] J. Calvo Fuentes, J. Rivas, M. López-Quintela, in *Encyclopedia of Nanotechnology* (Ed.: B. Bhushkan), Springer, Dordrecht, New York, **2012**, pp. 2639.

[59] G. Schmid, *Nanoparticles: From Theory to Application*, Wiley-VCH, **2005**.

[60] S. Horikoshi, N. Serpone, *Microwaves in Nanoparticle Synthesis: Fundamentals and Application*, Wiley-VCH Verlag GmbH & Co. KGaA, Weinheim, **2013**.

[61] B. Derjagin, L. Landau, *Acta Physicochim. URSS* **1941**, *14*, 633.

[62] E. J. W. Verwey, J. T. G. Overbeek, *Theory of the Stability of Lyophobic Colloids*, Elsevier, Amsterdam, **1948**.

[63] H. Schulze, *J. Prakt. Chem.* **1882**, *25*, 431.

[64] H. Schulze, *J. Prakt. Chem.* **1883**, *27*, 320.

[65] W. B. Hardy, *Proc. Royal Soc. London* **1900**, *66*, 110.

[66] W. B. Hardy, *Z. physik. Ch.* **1900**, *33*, 385.

[67] J. Thorne, G. J. Vine, M. Snowden, *Colloid Polym. Sci.* **2011**, *289*, 625.

[68] N. Barsch, J. Jakobi, S. Weiler, S. Barcikowski, *Nanotechnology* **2009**, *20*, 445603.

[69] C. L. Sajti, R. Sattari, B. N. Chichkov, S. Barcikowski, *J. Phys. Chem. C* **2010**, *114*, 2421.

[70] P. Wagener, S. Ibrahimkutty, A. Menzel, A. Plech, S. Barcikowski, *Phys. Chem. Chem. Phys.* **2013**, *15*, 3068.

[71] V. K. La Mer, R. H. Dinegar, *J. Am. Chem. Soc.* **1950**, *72*, 4847.

[72] E. M. Zaiser, V. K. La Mer, *J. Colloid Sci.* **1948**, *3*, 571.

[73] W. O. Ostwald, *An Introduction to Theoretical and Applied Colloid Chemistry*, John Wiley & Sons, New York, **1917**.

[74] S. Agnihotri, S. Mukherji, S. Mukherji, *RSC Adv.* **2014**, *4*, 3974.

[75] M.-L. Wu, D.-H. Chen, T.-C. Huang, *Chem. Mater.* **2001**, *13*, 599.

[76] T. Ahmad, *J. Nanotechnol.* **2014**, *2014*, 1.

[77] S. K. Sivaraman, S. Kumar, V. Santhanam, *Gold Bull.* **2010**, *43*, 275.

[78] S. Banerjee, K. Loza, W. Meyer-Zaika, O. Prymak, M. Epple, *Chem. Mater.* **2014**, *26*, 951.

[79] H. Wang, X. Qiao, J. Chen, S. Ding, *Colloids Surf. A* **2005**, *256*, 111.

[80] S. Komarneni, D. Li, B. Newalkar, H. Katsuki, A. S. Bhalla, *Langmuir* **2002**, *18*, 5959.

[81] Y. Sun, B. Mayers, T. Herricks, Y. Xia, *Nano Lett.* **2003**, *3*, 955.

[82] X. Ji, X. Song, J. Li, Y. Bai, W. Yang, X. Peng, *J. Am. Chem. Soc.* **2007**, *129*, 13939.

[83] E. N. Saw, V. Grasmik, C. Rurainsky, M. Epple, K. Tschulik, *Faraday Discuss.* **2016**, *193*, 327.

[84] L. M. Liz-Marzan, M. Giersig, P. Mulvaney, *Langmuir* **1996**, *12*, 4329.

[85] C. Casagrande, P. Fabre, E. Raphael, M. Veyssie, *Europhys. Lett.* **1989**, *9*, 251.

[86] A. Perro, S. Reculusa, S. Ravaine, E. Bourgeat-Lami, E. Duguet, *J. Mater. Chem.* **2005**, *15*, 3745.

[87] T. Darmanin, P. Nativo, D. Gilliland, G. Ceccone, C. Pascual, B. De Berardis, F. Guittard, F. Rossi, *Colloids Surf. A* **2012**, *395*, 145.

[88] A. X. Yin, W. C. Liu, J. Ke, W. Zhu, J. Gu, Y. W. Zhang, C. H. Yan, *J. Am. Chem. Soc.* **2012**, *134*, 20479.

[89] J. E. Millstone, S. J. Hurst, G. S. Metraux, J. I. Cutler, C. A. Mirkin, *Small* **2009**, *5*, 646.

[90] W. M. Schuette, W. E. Buhro, *ACS Nano* **2013**, *7*, 3844.

[91] S. H. Im, Y. T. Lee, B. Wiley, Y. Xia, *Angew. Chem. Int. Ed.* **2005**, *44*, 2154.

[92] J. Liu, Z. Lin, X. Wang, Z. Zeng, Z. Hu, *EPL* **2014**, *108*, 37004.

[93] N. Zettsu, J. M. McLellan, B. Wiley, Y. Yin, Z. Y. Li, Y. Xia, *Angew. Chem. Int. Ed.* **2006**, *45*, 1288.

[94] Y. Gao, L. Song, P. Jiang, L. F. Liu, X. Q. Yan, Z. P. Zhou, D. F. Liu, J. X. Wang, H. J. Yuan, Z. X. Zhang, X. W. Zhao, X. Y. Dou, W. Y. Zhou, G. Wang, S. S. Xie, H. Y. Chen, J. Q. Li, *J. Cryst. Growth* **2005**, *276*, 606.

[95] H. Wang, X. Qiao, J. Chen, X. Wang, S. Ding, *Mater. Chem. Phys.* **2005**, *94*, 449.

[96] X. Xia, J. Zeng, Q. Zhang, C. H. Moran, Y. Xia, *J. Phys. Chem. C* **2012**, *116*, 21647.

[97] D. Yu, V. W.-W. Yam, *J. Am. Chem. Soc.* **2004**, *126*, 13200.

[98] D. Yu, V. W.-W. Yam, *J. Phys. Chem. B* **2005**, *109*, 5497.

[99] R. A. Ganeev, G. S. Boltaev, R. I. Tugushev, T. Usmanov, *Appl. Phys. B* **2010**, *100*, 571.

[100] G. Mie, *Ann. Phys.* **1908**, *25*, 377.

[101] H. Chen, X. Kou, Z. Yang, W. Ni, J. Wang, *Langmuir* **2008**, *24*, 5233.

[102] M. R. Jones, K. D. Osberg, R. J. Macfarlane, M. R. Langille, C. A. Mirkin, *Chem. Rev.* **2011**, *111*, 3736.

[103] S. Link, M. B. Mohamed, M. A. El-Sayed, *J. Phys. Chem. B* **1999**, *103*, 3073.

[104] C. Mirkin, R. Letsinger, R. Mucic, J. Storhoff, *Nature* **1996**, *382*, 607.

[105] S. Underwood, P. Mulvaney, *Langmuir* **1994**, *10*, 3427.

[106] R. Kubo, *J. Phys. Soc. Jpn.* **1962**, *17*, 975.

[107] S. K. Gosh, T. Pal, *Chem. Rev.* **2007**, *107*, 4797.

[108] X. Qu, Y. Li, L. Li, Y. Wang, J. Liang, J. Liang, *J. Nanomater.* **2015**, *2015*, 23.

[109] J. Zheng, P. R. Nicovich, R. M. Dickson, *Annu. Rev. Phys. Chem.* **2007**, *58*, 409.

[110] S. Wang, X. Meng, A. Das, T. Li, Y. Song, T. Cao, X. Zhu, M. Zhu, R. Jin, *Angew. Chem. Int. Ed.* **2014**, *53*, 2376.

[111] K. L. Kelly, E. Coronado, L. L. Zhao, G. C. Schatz, *J. Phys. Chem. B* **2003**, *107*, 668.

[112] L. D. Rampino, F. F. Nord, *J. Am. Chem. Soc.* **1941**, *63*, 2745.

[113] A. F. Holleman, E. Wiberg, N. Wiberg, *Lehrbuch der Anorganischen Chemie*, de Gruyter, Berlin, **2007**.

[114] C. P. Adams, K. A. Walker, S. O. Obare, K. M. Docherty, *PLoS ONE* **2014**, *9*, e85981.

[115] C. Petrarca, E. Clemente, L. Di Giampaolo, R. Mariani-Costantini, K. Leopold, R. Schindl, L. V. Lotti, R. Mangifesta, E. Sabbioni, Q. Niu, G. Bernardini, M. Di Gioacchino, *J. Immunol. Res.* **2014**, *2014*, 8.

[116] S. Dasari, P. B. Tchounwou, *Eur. J. Pharmacol.* **2014**, *0*, 364.

[117] H. Gehrke, J. Pelka, C. G. Hartinger, H. Blank, F. Bleimund, R. Schneider, D. Gerthsen, S. Bräse, M. Crone, M. Türk, D. Marko, *Arch. Toxicol.* **2011**, *85*, 799.

[118] C. Beer, R. Foldbjerg, Y. Hayashi, D. S. Sutherland, H. Autrup, *Toxicol. Lett.* **2012**, *208*, 286.

[119] C. Greulich, J. Diendorf, J. Geßmann, T. Simon, T. Habijan, G. Eggeler, T. A. Schildhauer, M. Epple, M. Köller, *Acta Biomater.* **2011**, *7*, 3505.

[120] S. Kittler, C. Greulich, J. Diendorf, M. Köller, M. Epple, *Chem. Mater.* **2010**, *22*, 4548.

[121] K. Loza, J. Diendorf, C. Sengstock, L. Ruiz-Gonzalez, J. M. Gonzalez-Calbet, M. Vallet-Regi, M. Koller, M. Epple, *J. Mater. Chem. B* **2014**, *2*, 1634.

[122] Y. Borensztein, L. Delannoy, R. G. Barrera, C. Louis, *Eur. Phys. J. D* **2011**, *63*, 235.

[123] Y. Borensztein, L. Delannoy, A. Djedidi, R. G. Barrera, C. Louis, *J. Phys. Chem. C* **2010**, *114*, 9008.

[124] C. Lemire, R. Meyer, S. Shaikhutdinov, H.-J. Freund, *Angew. Chem. Int. Ed.* **2004**, *43*, 118.

[125] M. Haruta, *Chem. Rec.* **2003**, *3*, 75.

[126] M. Haruta, *Faraday Discuss.* **2011**, *152*, 11.

[127] M. Haruta, T. Kobayashi, H. Sano, N. Yamada, *Chem. Lett.* **1987**, *16*, 405.

[128] J. D. Gibson, B. P. Khanal, E. R. Zubarev, *J. Am. Chem. Soc.* **2007**, *129*, 11653.

[129] D. R. Lide, *CRC Handbook of Chemistry and Physics*, 84 ed., CRC Press, **2003**.

[130] G. Bredig, R. Allolio, *Z. Phys. Chem.* **1927**, *126*, 41.

[131] International Centre for Diffraction Data (ICDD), *Powder Diffraction File (PDF) 00-001-1194 (Pt)*.

[132] International Centre for Diffraction Data (ICDD), *Powder Diffraction File (PDF) 00-004-0783 (Ag)*.

[133] International Centre for Diffraction Data (ICDD), *Powder Diffraction File (PDF) 00-004-0784 (Au)*.

[134] A. J. Bard, R. Parsons, J. Jordan, *Standard Potentials in Aqueous Solution*, Marcel Dekker, Inc, New York, Basel, **1985**.

[135] Y. Sun, Y. Ren, Y. Liu, J. Wen, J. S. Okasinski, D. J. Miller, *Nat. Commun.* **2012**, *3*, 971.

[136] G. Mettela, M. Bhogra, U. V. Waghmare, G. U. Kulkarni, *J. Am. Chem. Soc.* **2015**, *137*, 3024.

[137] X. Huang, H. Li, S. Li, S. Wu, F. Boey, J. Ma, H. Zhang, *Angew. Chem. Int. Ed.* **2011**, *50*, 12245.

[138] X. Huang, S. Li, Y. Huang, S. Wu, X. Zhou, S. Li, C. L. Gan, F. Boey, C. A. Mirkin, H. Zhang, *Nat. Commun.* **2011**, *2*, 292.

[139] J. Diao, K. Gall, M. L. Dunn, *Nat. Mater.* **2003**, *2*, 656.

[140] J. Lao, D. Moldovan, *Appl. Phys. Lett.* **2008**, *93*, 093108.

[141] T. B. Massalski, H. Okamoto, P. R. Subramanian, L. Kacprzak, *Binary Alloy Phase Diagrams*, 2 ed., ASM International, **1990**.

[142] L. Vegard, *Z. Phys.* **1921**, *5*, 17.

[143] L. Vegard, H. Dale, *Z. Kristallogr., Kristallgeom., Kristallphys., Kristallchem.* **1928**, *67*, 148.

[144] V. A. Lubarda, *Mech. Mater.* **2003**, *35*, 53.

[145] V. Petkov, S. Shastri, S. Shan, P. Joseph, J. Luo, C.-J. Zhong, T. Nakamura, Y. Herbani, S. Sato, *J. Phys. Chem. C* **2013**, *117*, 22131.

[146] B. J. Plowman, B. Sidhureddy, S. V. Sokolov, N. P. Young, A. Chen, R. G. Compton, *ChemElectroChem* **2016**, *3*, 1039.

[147] A. F. Lee, C. J. Baddeley, C. Hardacre, R. M. Ormerod, R. M. Lambert, G. Schmid, H. West, *J. Phys. Chem.* **1995**, *99*, 6096.

[148] S. Devarajan, P. Bera, S. Sampath, *J. Colloid Interface Sci.* **2005**, *290*, 117.

[149] S. Link, Z. L. Wang, M. A. El-Sayed, *J. Phys. Chem. B* **1999**, *103*, 3529.

[150] G. C. Papavassiliou, *J. Phys. Condens. Matter* **1976**, *6*, L103.

[151] Z. Y. Li, J. Yuan, Y. Chen, R. E. Palmer, J. P. Wilcoxon, *Appl. Phys. Lett.* **2005**, *87*, 243103.

[152] S. Pande, S. K. Ghosh, S. Praharaj, S. Panigrahi, S. Basu, S. Jana, A. Pal, T. Tsukuda, T. Pal, *J. Phys. Chem. C* **2007**, *111*, 10806.

[153] N. Alissawi, V. Zaporojtchenko, T. Strunskus, I. Kocabas, V. S. K. Chakravadhanula, L. Kienle, D. Garbe-Schönberg, F. Faupel, *Gold Bull.* **2013**, *46*, 3.

[154] S. Grade, J. Eberhard, J. Jakobi, A. Winkel, M. Stiesch, S. Barcikowski, *Gold Bull.* **2014**, *47*, 83.

[155] S. Chen, S. Thota, G. Singh, T. J. Aímola, C. Koenigsmann, J. Zhao, *RSC Adv.* **2017**, *7*, 46916.

[156] T. A. Dao, M. D. Mott, K. Higashimine, S. Maenosono, *Sensors* **2013**, *13*, 7813.

[157] P. Hou, H. Liu, J. Li, J. Yang, *Cryst. Eng. Comm.* **2015**, *17*, 1826.

[158] L. Liu, H. Huang, A. Hu, G. Zou, L. Quintino, Y. Zhou, *Nano-Micro Lett.* **2013**, *5*, 88.

[159] S. Wojtysiak, J. Solla-Gullón, P. Dłużewski, A. Kudelski, *Colloids Surf. A* **2014**, *441*, 178.

[160] A. V. Singh, R. Patil, M. B. Kasture, W. N. Gade, B. L. Prasad, *Colloids Surf. B* **2009**, *69*, 239.

[161] M. K. Temgire, J. Bellare, S. S. Joshi, *Adv. Phys. Chem.* **2011**, *2011*, 1.

[162] I. Weber, J. Solla-Gullon, S. Brimaud, J. M. Feliu, R. Juergen Behm, *J. Electroanal. Chem.* **2017**, *793*, 164.

[163] M. Y. Gamarnik, Y. Y. Sidorin, *Phys. Stat. Sol. B* **1989**, *156*, K1.

[164] Q. Jiang, L. H. Liang, D. S. Zhao, *J. Phys. Chem. B* **2001**, *105*, 6275.

[165] B. Medasani, Y. H. Park, I. Vasiliev, *Phys. Rev. B* **2007**, *75*, 235436.

[166] C. Solliard, M. Flueli, *Surf. Sci.* **1985**, *156*, 487.

[167] H.-S. Ryu, I.-H. Bae, K.-G. Lee, H.-S. Hwang, K.-H. Lee, J.-T. Koh, J.-H. Cho, *Angle Orthod.* **2011**, *82*, 151.

[168] D. Fraenkel, C. Rickard, P. Thomas, J. Faoagali, N. George, R. Ware, *J. Crit. Care Med.* **2006**, *34*, 668.

[169] P. Boomi, H. G. Prabu, J. Mathiyarasu, *Colloids Surf. B* **2013**, *103*, 9.

[170] D. Mahl, J. Diendorf, W. Meyer-Zaika, M. Epple, *Colloids Surf. A* **2011**, *377*, 386.

[171] M. T. Otten, *J. Electron Microsc. Tech.* **1991**, *17*, 221.

[172] P. Scherrer, *Nachr. Ges. Wiss. Göttingen, Math.-Phys. Kl.* **1918**, *2*, 98.

[173] A. R. Stokes, A. J. C. Wilson, *Proc. Phys. Soc. London* **1944**, *56*, 174.

[174] E. W. Nuffield, *X-Ray Diffraction Methods*, Wiley, New York, **1966**.

[175] S. Gražulis, D. Chateigner, R. T. Downs, A. F. T. Yokochi, M. Quirós, L. Lutterotti, E. Manakova, J. Butkus, P. Moeck, A. Le Bail, *J. Appl. Crystallogr.* **2009**, *42*, 726.

[176] M. N. Polyanskiy, *Refractive index database https://refractiveindex.info, Vol. 2017*, **2008-2017**.

[177] D. Mahl, *Synthese, Löslichkeit und Stabilität von Gold-Nanopartikeln in biologischen Medien*, Thesis, University of Duisburg-Essen, **2011**.

[178] Y. Wan, Z. Guo, X. Jiang, K. Fang, X. Lu, Y. Zhang, N. Gu, *J. Colloid. Interface Sci.* **2013**, *394*, 263.

[179] E. Gharibshahi, E. Saion, *Int. J. Mol. Sci.* **2012**, *13*, 14723.

[180] T. Herricks, J. Chen, Y. Xia, *Nano Lett.* **2004**, *4*, 2367.

[181] D. S. Sheny, D. Philip, J. Mathew, *Spectrochim. Acta A* **2013**, *114*, 267.

[182] J. Chen, B. Wiley, J. McLellan, Y. Xiong, Z.-Y. Li, Y. Xia, *Nano Lett.* **2005**, *5*, 2058.

[183] M. M. Kreevoy, R. W. Jacobson, *Ventron Alembic* **1979**, *15*, 2.

[184] D. Nachtigall, S. Artelt, G. Wünsch, *J. Chromatogr. A* **1997**, *775*, 197.

[185] G. K. Inwati, Y. Rao, M. Singh, *Nanoscale Res. Lett.* **2016**, *11*, 458.

[186] F.-D. Mai, C.-C. Yu, Y.-C. Liu, T.-C. Hsu, Y.-H. Wu, *Mater. Res. Bull.* **2012**, *47*, 167.

[187] H. P. Klug, L. E. Alexander, *X-ray diffraction procedures for polycrystalline and amorphous materials.*, Wiley-Interscience, New York, **1974**.

[188] K. O'Connell, J. R. Regalbuto, *Catal. Lett.* **2015**, *145*, 777.

[189] International Centre for Diffraction Data (ICDD), *Powder Diffraction File (PDF) 00-034-0427 (LaB_6).*

[190] B. D. Chithrani, A. A. Ghazani, W. C. W. Chan, *Nano Lett.* **2006**, *6*, 662.

[191] Y. Mizukoshi, E. Takagi, H. Okuno, R. Oshima, Y. Maeda, Y. Nagata, *Ultrason. Sonochem.* **2001**, *8*, 1.

[192] K. Esumi, R. Nakamura, A. Suzuki, K. Torigoe, *Langmuir* **2000**, *16*, 7842.

[193] F. Mafuné, J.-y. Kohno, Y. Takeda, T. Kondow, *J. Phys. Chem. B* **2003**, *107*, 4218.

[194] J. Sun, J. Zhang, Y. Jin, *J. Mater. Chem. C* **2013**, *1*, 138.

[195] G. R. Desiraju, J. J. Vittal, A. Ramanan, *Crystal Engineering - A Textbook*, World Scientific Publishing Co. Pte. Ltd., Singapore, **2011**.

[196] G. Barcaro, L. Sementa, A. Fortunelli, M. Stener, *J. Phys. Chem. C* **2014**, *118*, 28101.

[197] T. Dorfmüller, K. Kleinermanns, *Gase, Nanosysteme, Flüssigkeiten*, 2., überarb. Aufl., de Gruyter, Berlin, **2006**.

[198] S.-I. Tanaka, J. Miyazaki, D. K. Tiwari, T. Jin, Y. Inouye, *Angew. Chem.* **2011**, *123*, 451.

[199] C. M. Ritchie, K. R. Johnsen, J. R. Kiser, Y. Antoku, R. M. Dickson, J. T. Petty, *J. Phys. Chem. C* **2007**, *111*, 175.

[200] I. Diez, M. Pusa, S. Kulmala, H. Jiang, A. Walther, A. S. Goldmann, A. H. E. Muller, O. Ikkala, R. H. A. Ras, *Angew. Chem. Int. Ed.* **2009**, *48*, 2122.

[201] I. Diez, R. H. A. Ras, *Nanoscale* **2011**, *3*, 1963.

[202] A. V. Girao, P. C. Pinheiro, M. Ferro, T. Trindade, *RSC Adv.* **2017**, *7*, 15944.

[203] G. Bozzolo, J. E. Garcés, G. N. Derry, *Surf. Sci.* **2007**, *601*, 2038.

[204] H. Rietveld, *J. Appl. Crystallogr.* **1969**, *2*, 65.

[205] I. Barke, H. Hartmann, D. Rupp, L. Flueckiger, M. Sauppe, M. Adolph, S. Schorb, C. Bostedt, R. Treusch, C. Peltz, S. Bartling, T. Fennel, K.-H. Meiwes-Broer, T. Moeller, *Nat. Commun.* **2015**, *6*, 6187.

[206] Q. Zhang, J. Xie, J. Yang, J. Y. Lee, *ACS Nano* **2009**, *3*, 139.

[207] E. C. Bain, *Trans. Am. Inst. Min. Met. Eng.* **1924**, *70*, 25.

[208] E. Hahn, E. Kampshoff, N. Wälchli, K. Kern, *Phys. Rev. Lett.* **1995**, *74*, 1803.

[209] B. Predel, in *Ac-Au – Au-Zr* (Ed.: O. Madelung), Springer Berlin Heidelberg, Berlin, Heidelberg, **1991**, pp. 1.

[210] V. I. Iveronova, A. A. Katsnel'son, *Kristallografiya* **1966**, *11*, 576.

[211] N. Al-Zoubi, B. Johansson, G. Nilson, L. Vitos, *J. Appl. Phys.* **2011**, *110*, 013708.

[212] J. I. Langford, *J. Appl. Crystallogr.* **1978**, *11*, 10.

[213] J. I. Langford, R. J. Cernik, D. Louer, *J. Appl. Crystallogr.* **1991**, *24*, 912.

[214] International Centre for Diffraction Data (ICDD), *Powder Diffraction File (PDF) 00-004-0788 (Ta)*.

[215] M. A. Asoro, D. Kovar, P. J. Ferreira, *ACS Nano* **2013**, *7*, 7844.

[216] Y. Ding, F. Fan, Z. Tian, Z. L. Wang, *Small* **2009**, *5*, 2812.

[217] S. V. N. Naidu, C. R. Houska, *J. Appl. Phys.* **1971**, *42*, 4971.

[218] Y. C. Venudhar, L. Iyengar, K. V. K. Rao, *J. Less-Common Met.* **1978**, *60*, P41.

[219] V. Craciun, D. Craciun, *Appl. Surf. Sci.* **2005**, *247*, 384.

[220] N. N. Sirota, V. V. Novikov, V. A. Vinokurov, Y. B. Paderno, *Phys. Solid State* **1998**, *40*, 1856.

[221] G.-L. Xu, J.-D. Chen, Y.-Z. Xia, X.-F. Liu, Y.-F. Liu, X.-Z. Zhang, *Chin. Phys. Lett.* **2009**, *26*, 056201.

[222] F. C. Nix, D. MacNair, *Phys. Rev.* **1941**, *60*, 597.

[223] I.-K. Suh, H. Ohta, Y. Waseda, *J. Mater. Sci.* **1988**, *23*, 757.

[224] M. E. Straumanis, *Monatsh. Chem.* **1971**, *102*, 1377.

[225] C. C. Yang, M. X. Xiao, W. Li, Q. Jiang, *Solid State Commun.* **2006**, *139*, 148.

[226] Y. F. Zhu, J. S. Lian, Q. Jiang, *J. Phys. Chem. C* **2009**, *113*, 16896.

[227] K. Tschulik, K. Ngamchuea, C. Ziegler, M. G. Beier, C. Damm, A. Eychmueller, R. G. Compton, *Adv. Funct. Mater.* **2015**, *25*, 5149.

[228] M. Kamundi, L. Bromberg, E. Fey, C. Mitchell, M. Fayette, N. Dimitrov, *J. Phys. Chem. C* **2012**, *116*, 14123.

[229] J. Solla-Gullon, P. Rodriguez, E. Herrero, A. Aldaz, J. M. Feliu, *Phys. Chem. Chem. Phys.* **2008**, *10*, 1359.

[230] Y. Wang, E. Laborda, C. Salter, A. Crossley, R. G. Compton, *Analyst* **2012**, *137*, 4693.

[231] L. Wei, W. Qi, B. Huang, M. Wang, *Comput. Mater. Sci.* **2013**, *69*, 374.

[232] Y. Yang, J. Liu, Z.-W. Fu, D. Qin, *J. Am. Chem. Soc.* **2014**, *136*, 8153.

[233] L. R. Holt, B. J. Plowman, N. P. Young, K. Tschulik, R. G. Compton, *Angew. Chem. Int. Ed.* **2016**, *55*, 397.

[234] Y.-G. Zhou, N. V. Rees, J. Pillay, R. Tshikhudo, S. Vilakazi, R. G. Compton, *Chem. Commun.* **2012**, *48*, 224.

[235] A. Hamelin, *J. Electroanal. Chem. Interfacial Electrochem.* **1984**, *165*, 167.

[236] J. Hernandez, J. Solla-Gullon, E. Herrero, *J. Electroanal. Chem.* **2004**, *574*, 185.

[237] R. D. Kent, P. J. Vikesland, *Environ. Sci. Technol.* **2012**, *46*, 6977.

[238] P. Munusamy, C. Wang, M. H. Engelhard, D. R. Baer, J. N. Smith, C. Liu, V. Kodali, B. D. Thrall, S. Chen, A. E. Porter, M. P. Ryan, *Biointerphases* **2015**, *10*, 031003.

[239] Z. Adamczyk, M. Ocwieja, H. Mrowiec, S. Walas, D. Lupa, *J. Colloid Interface Sci.* **2016**, *469*, 355.

[240] J. Liu, R. H. Hurt, *Environ. Sci. Technol.* **2010**, *44*, 2169.

[241] J. Liu, D. A. Sonshine, S. Shervani, R. H. Hurt, *ACS Nano* **2010**, *4*, 6903.

[242] D. Tiedemann, U. Taylor, C. Rehbock, J. Jakobi, S. Klein, W. A. Kues, S. Barcikowski, D. Rath, *Analyst* **2014**, *139*, 931.

[243] J. Wu, W. Gao, H. Yang, J.-M. Zuo, *ACS Nano* **2017**, *11*, 1696.

[244] Y. Ma, *The mechanism of silver dissolution for biomedical devices and hygienic coating applications*, Thesis, Dublin Institute of Technology, **2008**.

[245] P. Costa, J. M. Sousa Lobo, *Eur. J. Pharm. Sci.* **2001**, *13*, 123.

[246] G. A. Sotiriou, G. D. Etterlin, A. Spyrogianni, F. Krumeich, J.-C. Leroux, S. E. Pratsinis, *Chem. Commun.* **2014**, *50*, 13559.

[247] M. Hyotanishi, Y. Isomura, H. Yamamoto, H. Kawasaki, Y. Obora, *Chem. Commun.* **2011**, *47*, 5750.

[248] S. Link, A. Beeby, S. FitzGerald, M. A. El-Sayed, T. G. Schaaff, R. L. Whetten, *J. Phys. Chem. B* **2002**, *106*, 3410.

[249] J. Zheng, J. T. Petty, R. M. Dickson, *J. Am. Chem. Soc.* **2003**, *125*, 7780.

8. Appendix

8.1 High-temperature X-ray diffraction

Table 38: Linear thermal expansion coefficients of lanthanum hexaboride from RT → T_1, T_1 → T_2 and so on (differential calculation).

Temperature range / °C	Thermal expansion coefficient $\alpha \cdot 10^{-6}$ / K^{-1}
25 → 150	5.39
150 → 195	6.95
195 → 215	7.21
215 → 250	6.86
250 → 315	7.39
315 → 400	7.62
400 → 550	8.15
550 → 700	9.10
700 → 800	9.57
800 → 850	9.08

Table 39: Crystallographic data of silver-gold nanoparticles during high-temperature X-ray diffraction obtained from the (220) reflex.

Sample	FWHM / °	2 θ / °	θ / °	R Square	Cryst. size / nm	Lattice parameter *a* / Å	Micro strain *ε* / %
Ag100 RT	0.86	64.46	32.23	0.72	10.8	4.0837	0.60
Ag100 150	0.83	64.26	32.13	0.76	11.2	4.0950	0.58
Ag100 250	0.65	64.1	32.05	0.82	14.3	4.1041	0.45
Ag100 400	0.55	63.85	31.93	0.8	16.8	4.1185	0.39
Ag100 550	0.23	63.6	31.8	0.83	40.2	4.1330	0.16
Ag100 700	0.069	63.34	31.67	0.92	133.7	4.1482	0.05

Table 39: Continued.

Sample	FWHM / °	2 θ / °	θ / °	R Square	Cryst. size / nm	Lattice parameter *a* / Å	Micro strain *ε* / %
Ag80Au20 RT	2.59	64.52	32.26	0.26	3.6	4.0803	1.79
Ag80Au20 150	1.91	64.49	32.245	0.26	4.91	4.0820	1.32
Ag80Au20 250	0.85	64.19	32.095	0.86	10.9	4.0990	0.59
Ag80Au20 550	0.499	63.74	31.87	0.82	18.5	4.1248	0.35
Ag80Au20 700	0.42	63.49	31.745	0.82	22.0	4.1394	0.30
Ag80Au20 850	0.56	63.47	31.735	0.65	16.5	4.1405	0.40
Ag80Au20 RT after 850	0.49	64.55	32.275	0.92	19.0	4.0786	0.34
Ag50Au50 RT	2.75	64.9	32.45	0.13	3.4	4.0590	1.89
Ag50Au50 150	1.55	64.55	32.275	0.27	6.0	4.0786	1.07
Ag50Au50 195	1.36	64.46	32.23	0.69	6.8	4.0837	0.94
Ag50Au50 215	1.2	64.41	32.205	0.82	7.7	4.0865	0.83
Ag50Au50 250	0.94	64.35	32.175	0.88	9.9	4.0899	0.65
Ag50Au50 315	0.81	64.25	32.125	0.91	11.5	4.0956	0.56
Ag50Au50 400	0.71	64.14	32.07	0.89	13.1	4.1018	0.49

Table 39: Continued.

Sample	FWHM /°	2 θ /°	θ /°	R Square	Cryst. size /nm	Lattice parameter *a* /Å	Micro strain *ε* / %
Ag50Au50 550	0.62	63.92	31.96	0.9	14.9	4.1145	0.43
Ag50Au50 800	0.54	63.58	31.79	0.87	17.1	4.1341	0.38
Ag50Au50 RT after 800	0.52	64.59	32.295	0.95	17.9	4.0763	0.36
Ag30Au70 RT	5.33	64.75	32.375	0.002	1.7	4.0673	3.67
Ag30Au70 150	3.67	64.64	32.32	0.03	2.5	4.0735	2.53
Ag30Au70 250	2.23	64.43	32.215	0.16	4.2	4.0854	1.54
Ag30Au70 400	0.94	64.25	32.125	0.12	9.9	4.0956	0.65
Ag30Au70 550	1.47	64.12	32.06	0.02	6.3	4.1030	1.02
Ag30Au70 700	2.16	63.88	31.94	0.17	4.3	4.1168	1.51
Ag30Au70 850	0.64	63.57	31.785	0.52	14.4	4.1347	0.45
Ag30Au70 RT after 850	0.48	64.58	32.29	0.86	19.4	4.0769	0.33

Table 39: Continued.

Sample	FWHM /°	2 θ /°	θ /°	R Square	Cryst. size /nm	Lattice parameter *a* /Å	Micro strain ε / %
Au100 RT	2.1	64.75	32.375	0.72	4.4	4.0673	1.45
Au100 150	1.99	64.63	32.315	0.71	4.7	4.0741	1.37
Au100 250	1.3	64.42	32.21	0.89	7.1	4.0859	0.90
Au100 400	1.14	64.23	32.115	0.92	8.1	4.0967	0.79
Au100 550	1.06	64.04	32.02	0.92	8.7	4.1076	0.74
Au100 700	1.11	63.82	31.91	0.9	8.3	4.1202	0.78
Au100 850	0.8	63.59	31.795	0.86	11.6	4.1335	0.56
Au100 RT after 850	0.84	64.56	32.28	0.94	11.1	4.0780	0.58

8.2 Dissolution experiments

8.2.1 Silver-gold nanoparticles

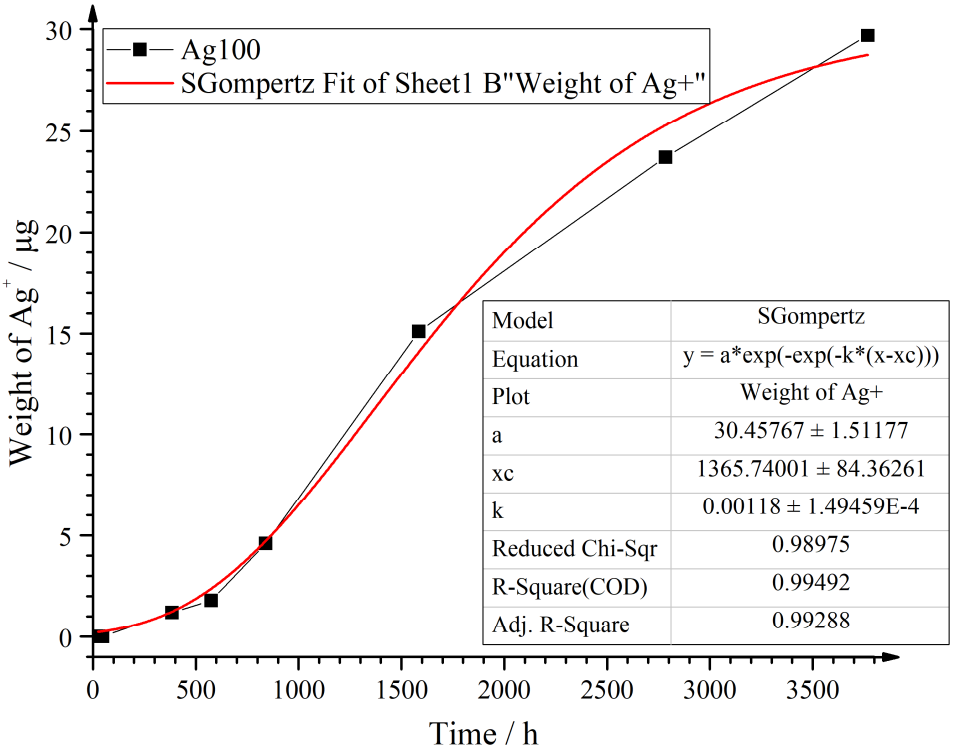

Model	SGompertz
Equation	y = a*exp(-exp(-k*(x-xc)))
Plot	Weight of Ag+
a	30.45767 ± 1.51177
xc	1365.74001 ± 84.36261
k	0.00118 ± 1.49459E-4
Reduced Chi-Sqr	0.98975
R-Square(COD)	0.99492
Adj. R-Square	0.99288

Figure 101: Gompertz fit function for Ag100.

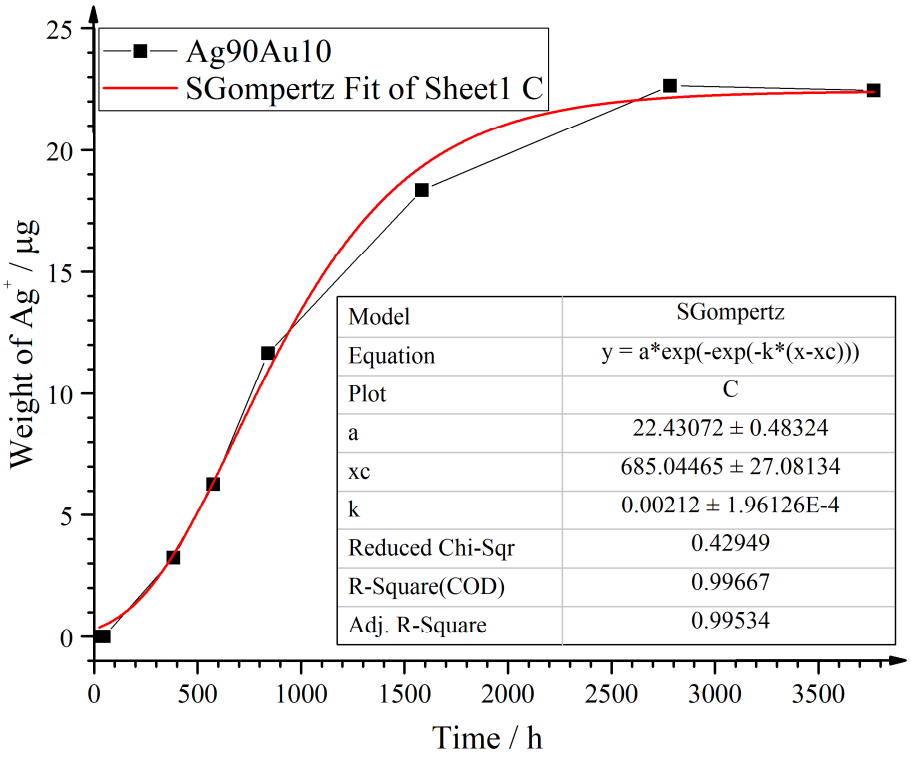

Model	SGompertz
Equation	y = a*exp(-exp(-k*(x-xc)))
Plot	C
a	22.43072 ± 0.48324
xc	685.04465 ± 27.08134
k	0.00212 ± 1.96126E-4
Reduced Chi-Sqr	0.42949
R-Square(COD)	0.99667
Adj. R-Square	0.99534

Figure 102: Gompertz fit function for Ag90Au10.

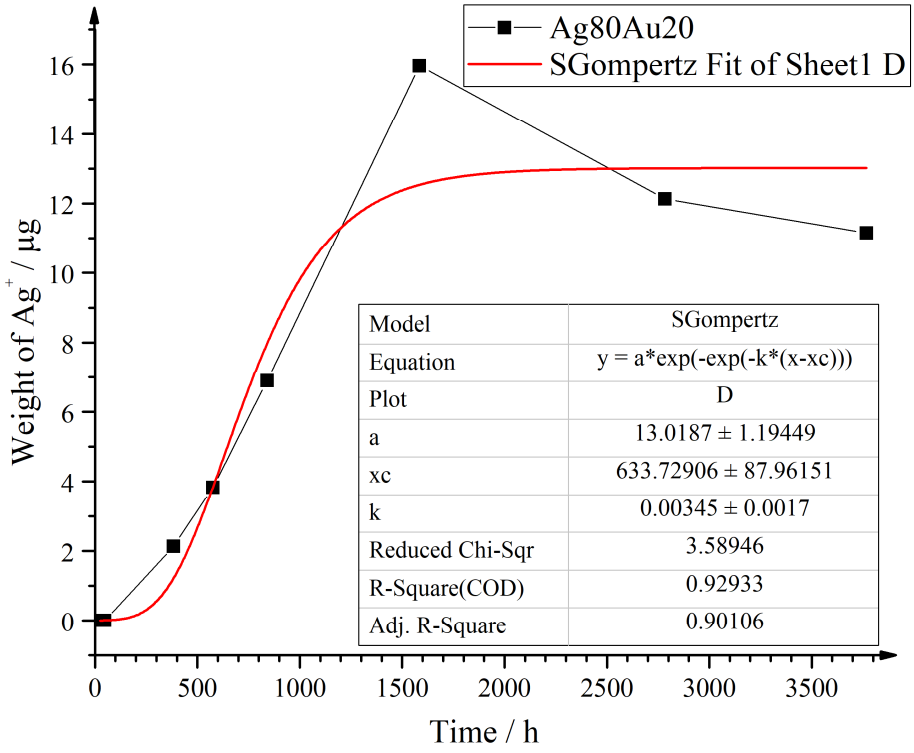

Figure 103: Gompertz fit function for Ag80Au20.

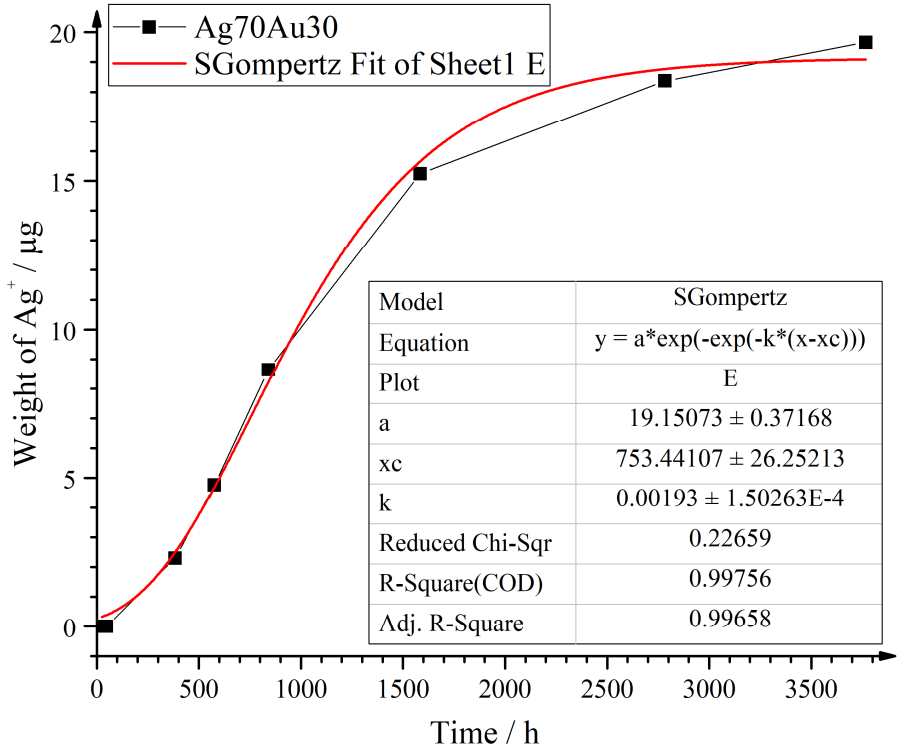

Figure 104: Gompertz fit function for Ag70Au30.

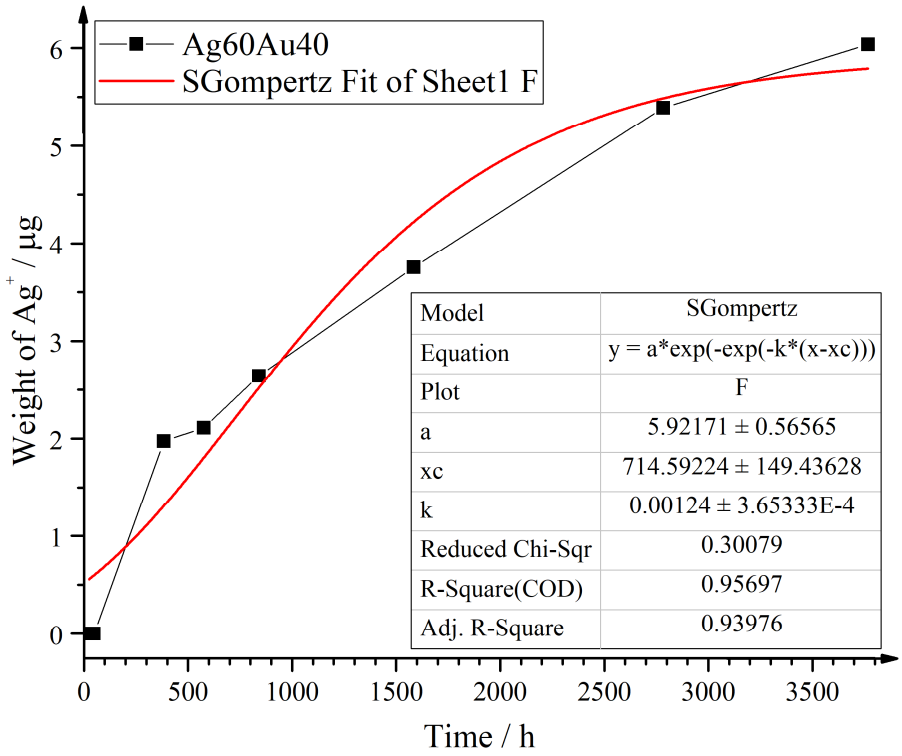

Figure 105: Gompertz fit function for Ag60Au40.

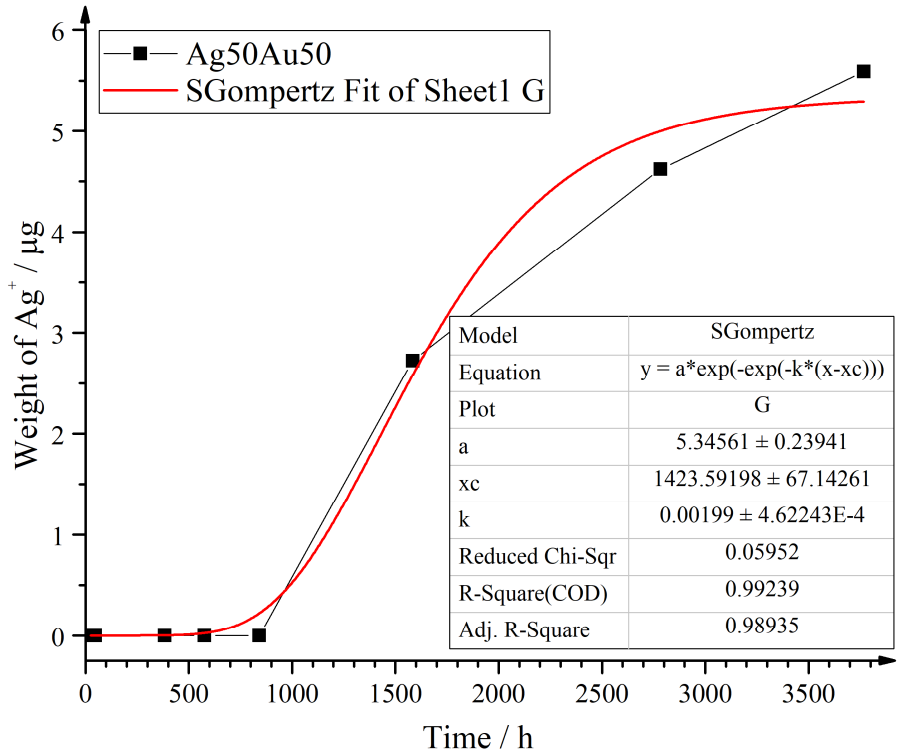

Figure 106: Gompertz fit function for Ag50Au50.

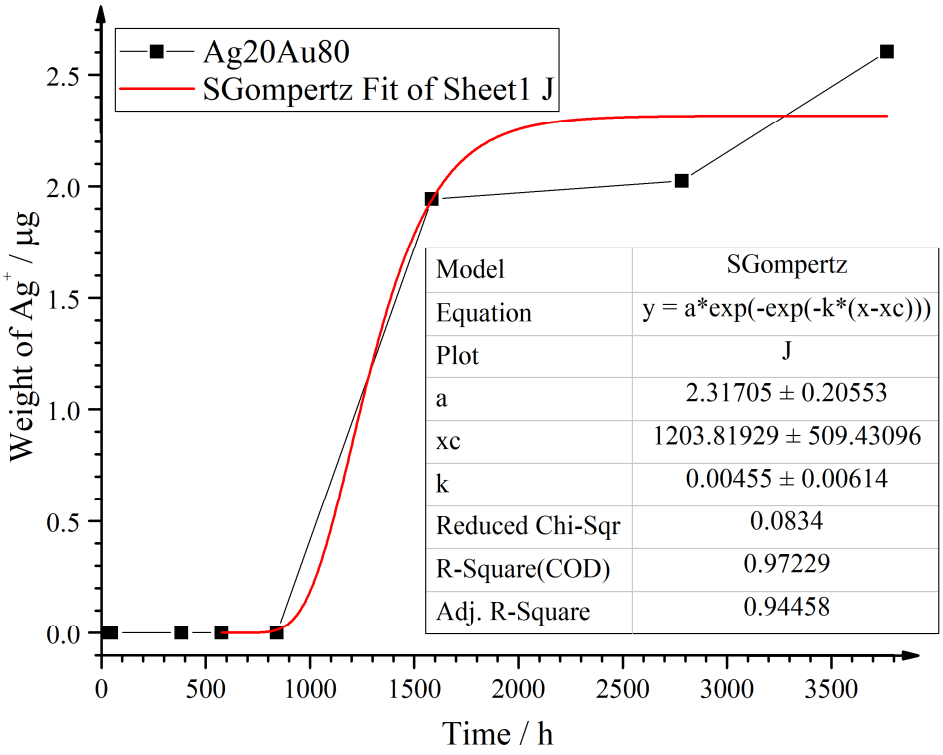

Figure 107: Gompertz fit function for Ag20Au80.

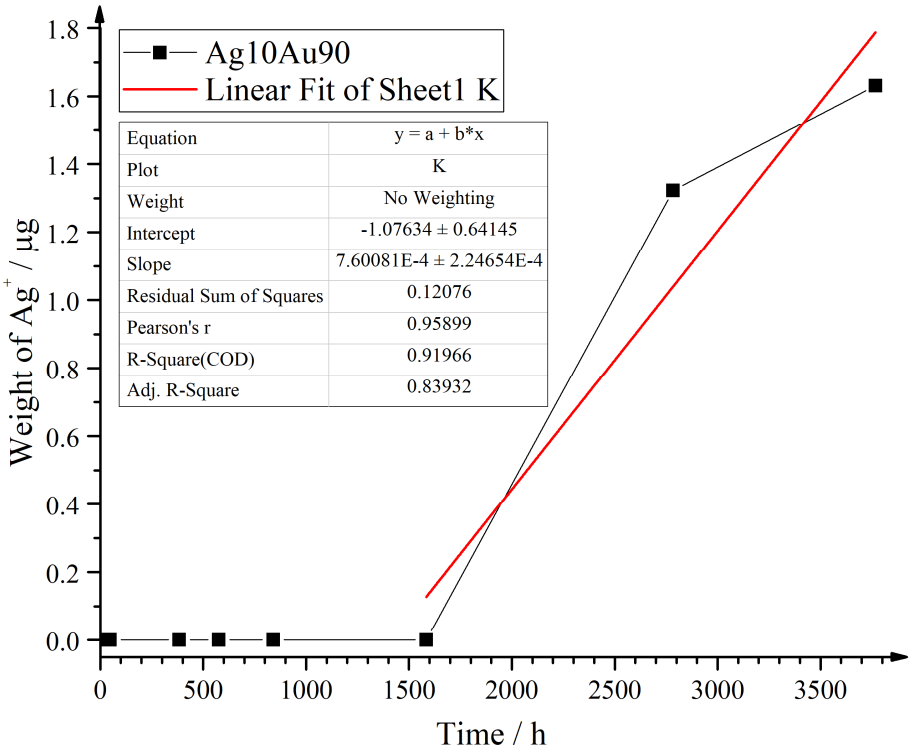

Figure 108: Linear regression for Ag10Au90.

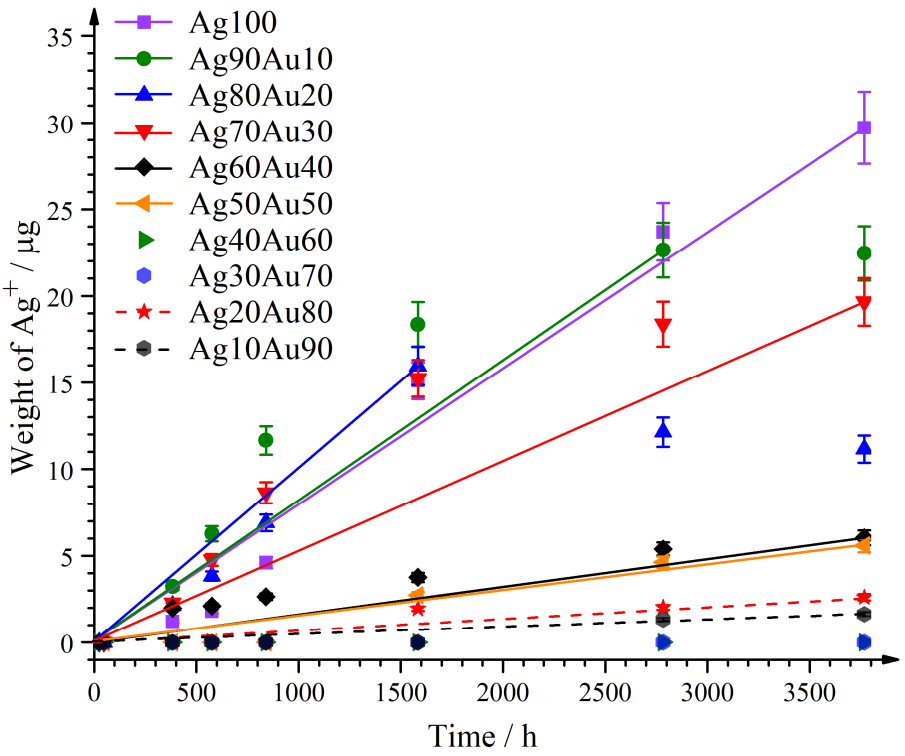

Figure 109: Graphical determination of the average dissolution rate of silver out of silver-gold nanoparticles.

8.2.2 Silver-platinum nanoparticles

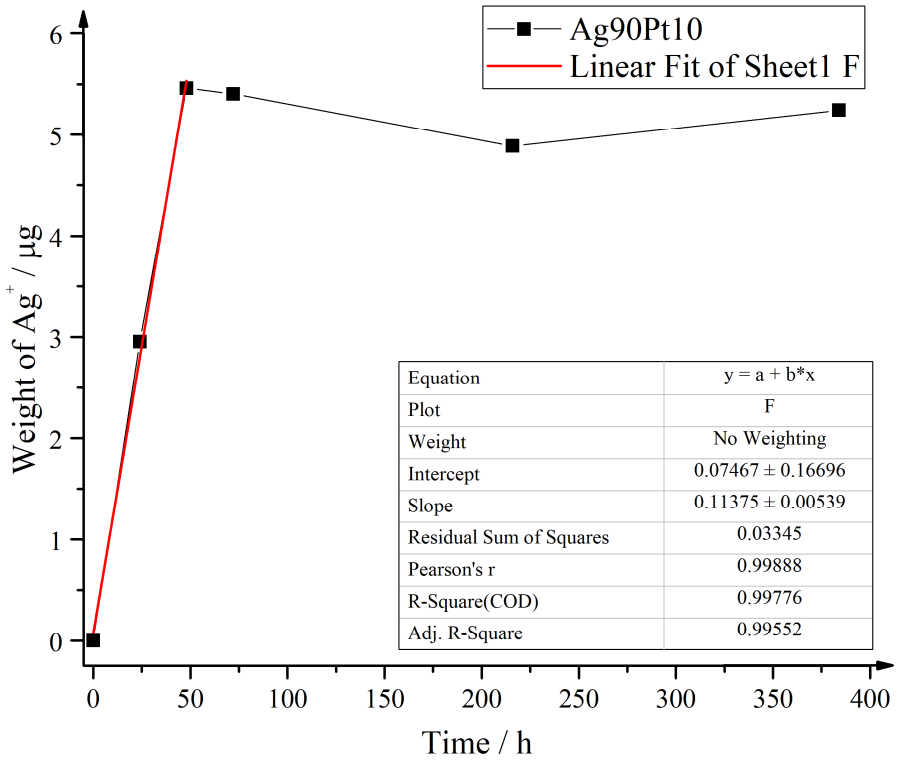

Figure 110: Linear regression for Ag90Pt10.

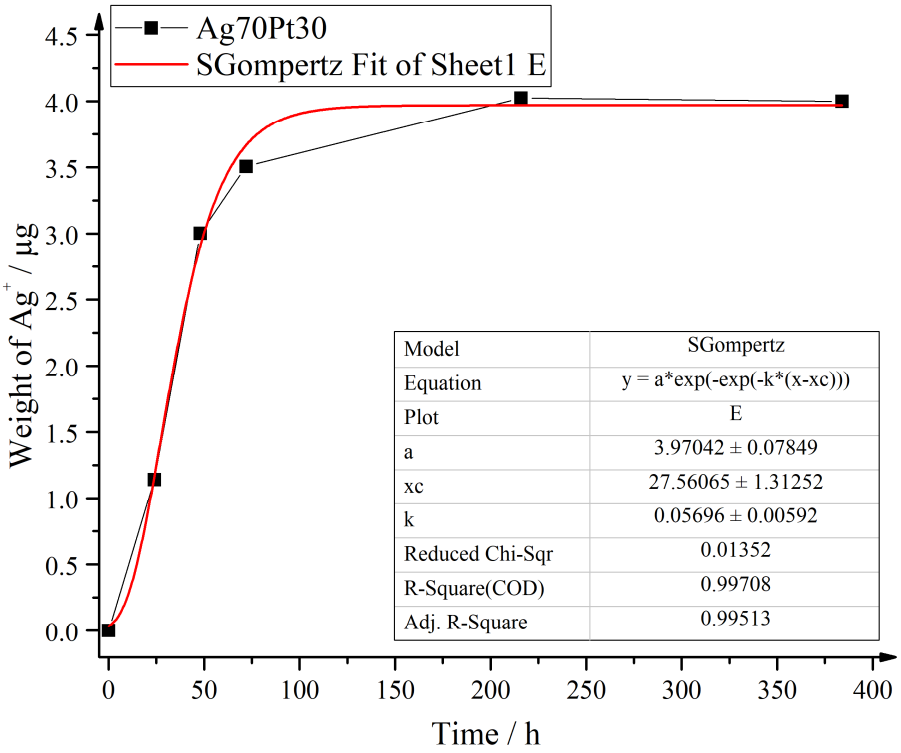

Figure 111: Gompertz fit function for Ag70Pt30.

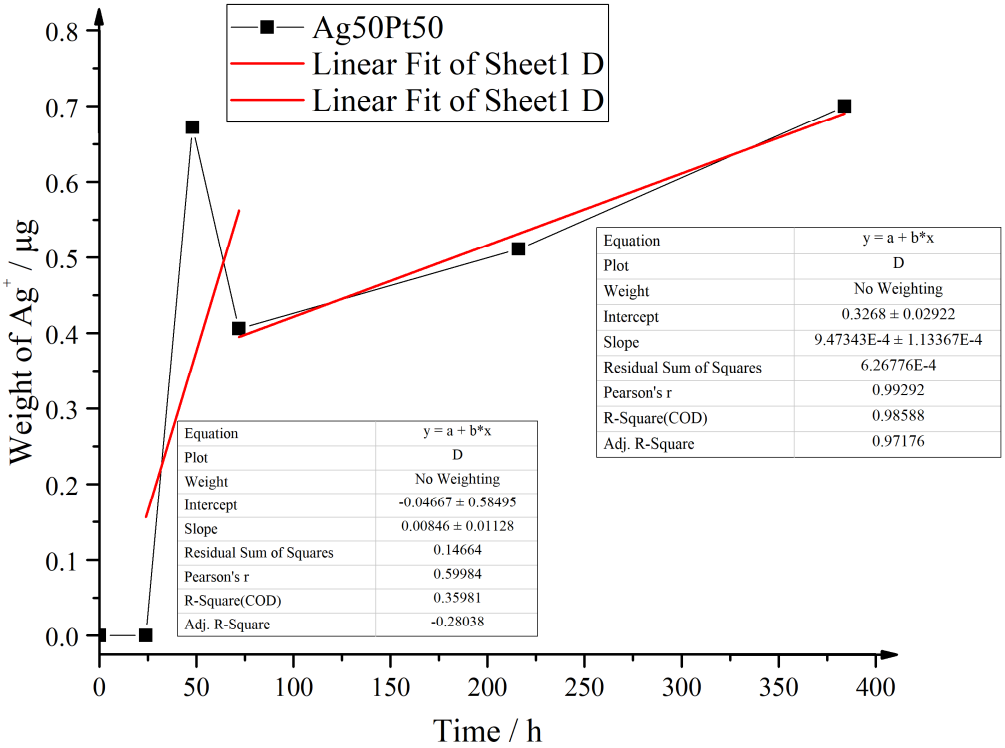

Figure 112: Linear regression for Ag50Pt50.

8.3 List of publications

E. N. Saw, V. Grasmik, C. Rurainsky, M. Epple, K. Tschulik, “Electrochemistry at single bimetallic nanoparticles - using nano impacts for sizing and compositional analysis of individual AgAu alloy nanoparticles”, *Faraday Discuss.*, **2016**, *193*, 327.

T. Alammar, I. Hamm, V. Grasmik, M. Wark, A.-V. Mudring, “Microwave-Assisted Synthesis of Perovskite $SrSnO_3$ Nanocrystals in Ionic Liquids for Photocatalytic Applications”, *Inorg. Chem.*, **2017**, *56*, 6920.

V. Grasmik, C. Rurainsky, K. Loza, M. V. Evers, O. Prymak, M. Heggen, K. Tschulik, M. Epple, “Deciphering the Surface Composition and the Internal Structure of Alloyed Silver-Gold Nanoparticles”, *Chem. Eur. J.* **2018**, doi:10.1002/chem.201800579.

P. R. A. F. Garcia, K. Loza, S. Daumann, V. Grasmik, K. Pappert, A. Rostek, J. Helmlinger, O. Prymak, M. Epple, C. L. P. Oliveira, “Combining Small-Angle X-Ray Scattering and X-Ray Powder Diffraction to Investigate Size, Shape, and Crystallinity of Silver, Gold, and Alloyed Silver-Gold Nanoparticles“, **2018** (submitted).

S. Banerjee, C.-H. Liu, J. D. Lee, A. Kovyakh, V. Grasmik, O. Prymak, C. Koenigsmann, H. Liu, L. Wang, S. S. Wong, M. Epple, C. B. Murray, S. J. L. Billinge, “Improved models for metallic nanoparticle cores from atomic pair distribution function (PDF) analysis“, **2018** (submitted).

8.4 Posters and presentations

23rd Annual Conference of the German Crystallographic Society, Göttingen, Germany, March 2015, V. Grasmik, K. Merz, "Influence of H/D exchange on the crystallization process of oxalyl dihydrazide" (**poster contribution**).

Materials Chain International Conference, Bochum, Germany, May 2016, V. Grasmik, E. N. Saw, K. Tschulik, M. Epple, "Electrochemical characterization of PVP-functionalized silver nanoparticles, gold nanoparticles and silver-gold nanoalloys" (**poster contribution**).

DAAD exchange with the University of Sao Paulo, Sao Paulo, Brazil, October 2016, V. Grasmik, E. N. Saw, O. Prymak, K. Tschulik, M. Epple, "Synthesis and characterization of bimetallic nanoparticles" (**oral presentation**).

DAAD exchange with the University of Notre Dame, South Bend, USA, December 2017, V. Grasmik, M. Breisch, K. Loza, C. Rurainsky, O. Prymak, M. V. Evers, K. Tschulik, M. Heggen, C. Sengstock, M. Köller, M. Epple, "Silver-based nanoparticles: Synthesis and characterization of bimetallic silver-platinum and silver-gold nanoparticles" (**oral presentation**).

CENIDE conference, Bergisch-Gladbach, Germany, February 2018, V. Grasmik, K. Loza, C. Rurainsky, O. Prymak, K. Tschulik, M. Heggen, M. Epple, "In-depth characterization of alloyed silver-gold nanoparticles and their dissolution behaviour" (**oral presentation**).

26th Annual Conference of the German Crystallographic Society, Essen, Germany, March 2018, V. Grasmik, K. Loza, O. Prymak, M. Heggen, M. Epple, "Silver-platinum nanoparticles in the miscibility gap: Characterization by X-ray diffraction" (**oral presentation**).

8.5 Curriculum Vitae

Der Lebenslauf ist in der Online-Version aus Gründen des Datenschutzes nicht enthalten.

8.6 Acknowledgements

I would like to express my gratitude to Prof. Dr. Matthias Epple for providing me with a really interesting research topic, scientific support during my graduate phase, the opportunity of many research stays abroad, and the possibility of presenting my results at various conferences.
I also thank Prof. Dr. Malte Behrens for the assessment of my thesis.

Furthermore, my thank goes to our cooperation partners Jun.-Prof. Dr. Kristina Tschulik, Mr. Christian Rurainsky, Mr. En Ning Saw, and Mr. Mathies V. Evers from Ruhr-University Bochum; Prof. Dr. Manfred Köller, Jun.-Prof. Dr. Christina Sengstock, and Ms. Marina Breisch from Bergmannsheil university medical center; Prof. Dr. Cristiano L. P. Oliveira and Mr. Paulo R. Garcia from University of Sao Paulo; Prof. Dr. Simon J. L. Billinge and Mr. Soham Banerjee from Columbia University in the city of New York; and Dr. Marc Heggen from the Ernst-Ruska Centre in the Forschungscenter Jülich for outstanding collaborations and the insight into various research fields.

I would like to offer my special thanks to Dr. Oleg Prymak for assistance in powder X-ray diffraction and Dr. Kateryna Loza for transmission electron microscopic investigations as well as fruitful discussions and scientific support.

Mr. Smail Boukercha and Ms. Ursula Giebel helped me to get acquainted with the scanning electron microscope, whereas Mrs. Veronika Hiltenkamp, Mrs. Kerstin Brauner, and Mr. Robin Meya provided me with atomic absorption spectrometry analyses for which I am very grateful.

I also wish to acknowledge the help provided by Ms. Sabine Kiefer, Mrs. Carola Fischer, Mr. Dietrich Tönnes and Mrs. Sabine Bollmann with organization of various types and technical assistance.

Very special gratitude goes to Mr. Kevin Pappert who accompanied me since our first semester, who always helped me with word and deed, and with whom I spent countless hours discussing scientific questions.

My special thanks are extended to Dr. Bernhard Neuhaus and Mr. Sebastian Kollenda for a pleasant time as lab mates, to Ms. Selina van der Meer, Dr. Benjamin Schütze, Dr. Sascha Büscher, Dr. Sven Range, Dr. Jens N. Helmlinger, Dr. Sabrina Daumann, Dr. Jens Nelsen, Mr. Alexander Rostek, Mrs. Alwina Lübke, Ms. Karolin Wey, Ms. Tatjana Ruks, Mr. Leonardo Rojas-Sanchez, Dr. Mathis Kopp, Mr. Mateusz Olejnik, Ms. Shabnam Hosseini, Mr. Nataniel Bialas, Ms. Xin Sun, and Mr. Oliver Wetzel for an enjoyable working atmosphere, scientific advice, and pleasant lunch breaks.

I thank Mr. Shishir Dhakal who provided me with samples during his research stay under my supervision.

Finally, I would like to express my very great appreciation to my family and friends for their helpfulness and support.

8.7 Eidesstaatliche Erklärung

Hiermit versichere ich, die vorliegende Arbeit mit dem Titel

„Silver-based nanoparticles: Synthesis and characterization of bimetallic silver-platinum and silver-gold nanoparticles“

selbst verfasst und keine außer den angegebenen Hilfsmitteln und Quellen verwendet zu haben.

Zudem erkläre ich, dass ich die Arbeit in dieser oder einer ähnlichen Form bei keiner anderen Fakultät eingereicht habe.

Essen,

Viktoria Grasmik